GEOMETRIC AND SPECTRAL ACCURACY OF AIRBORNE REMOTE SENSING

Amanuel Tsehaye

Master of Philosophy

ASTON UNIVERSITY

January 2008

ASTON UNIVERSITY

GEOMETRIC AND SPECTRAL ACCURACY OF AIRBORNE REMOTE SENSING

Summary

This research examined the use of airborne remote sensing that has been acquired in the West-Midlands near Lichfield and Brownhills in March 2002. Image data considered in the study consisted of Airborne Thematic Mapper (ATM) and Compact Airborne Spectrographic Imager (CASI), with a spatial resolution of 1.8 metres. No atmospheric correction was done in this research. The spectral response of the ATM and CASI sensors were carefully examined to investigate if the sensors pick up the same radiation from the same land cover at different places in the imagery, enabling qualitative classification of the area. To supply the same geometric integrity as a map, original raw images must be geometrically corrected and the distortions, such as variations in altitude, and Earth curvature, must be compensated for. It was found that the RMS of location error was 11.01 metres. It was discovered that the same land cover on different parts of the imagery gave different spectral responses and their qualitative classification was not reliable.

Keywords: Thermal band, Spectral Accuracy, Geometric Accuracy.

Acknowledgments

I would like to express my gratitude to my supervisor, Dr. John Elgy, whose expertise, understanding, and patience, added considerably to my graduate experience. I appreciate his vast knowledge and skill in many areas. I would like to thank my family for all their support during the whole period of my research.

Table of Contents

List of Figures

List of Tables

Tables **Page**

1 INTRODUCTION

1.1 INTRODUCTION

Remote sensing may be broadly defined as "the science and art of obtaining information about an object, area, or phenomena through the analysis of data acquired by a device that is not in contact with the object, area, or phenomena under investigation" (Lillesand and Kiefer, 1994). This thesis is concerned with passive remote sensing from the blue to the thermal wavelengths of the electromagnetic spectrum, which are reflected or emitted from the surface. This information is stored as a digital image composed of a two dimensional array of pixels. Each pixel has a digital number value associated with a measurement of the electromagnetic radiation at the sensor from the surface, sensed over a particular spectral bandwidth through the atmosphere.

The methodologies behind the research have been based upon considerations of the spectral fidelity, geometric accuracy and the use of multi-temporal and multi-spectral airborne remote sensing including the information content of the night time thermal imagery. The research recognises the requirement that airborne remotely sensed imagery be referenced to an Earth-based coordinate system prior to its usage.

1.2 AIMS AND OBJECTIVES

The main aim of this thesis is to access the accuracy and reliability of airborne remote sensing and to obtain a detailed understanding of the information carried within the thermal band. This thesis will attempt to resolve the following questions:

1) Is the digital number (DN) obtained at different points across a scan line the same for the same land cover at all wavelengths?

2) What is the potential for the day and night time thermal imagery of the same area?

3) Are geo-rectification techniques suitable to mosaic images and co-registering night time and daytime flights?

4) Is the ATM data in the form supplied suitable for land cover classification?

1.3 THESIS STRUCTURE

All chapters in the thesis are devoted to answering the questions posed in section 1.2. The chapter titles are Introduction, Literature review, Data sources and methodology, Spectral accuracy, Geometric accuracy, Discussion and Conclusion.

Since a large part of this thesis involves the use of day and night thermal imagery, Chapter 2 starts by reviewing the literature that has attempted to define, describe and explain the principles of thermal airborne remote sensing. This chapter also states the terminologies most relevant to thermal airborne remote sensing. This is followed by stating the properties and advantages of day and night time thermal images. Finally, a review of the methods of assessing the spectral, spatial and geometric accuracy of satellite and airborne remote sensing images is discussed.

Chapter 3 illustrates the location and nature of the study area in addition to the data collection procedures used in the research. This is followed by detailed specifications and data acquisition modes for the Airborne Thematic Mapper (ATM) and the Compact Airborne Spectrographic Imager (CASI). How the hierarchical data format (HDF) stores the scientific data, and how it was applied to the ATM data is also explained. Finally, this chapter explains how the data are extracted, and both extreme edges of each flight line are trimmed in making the data useful for quantitative and qualitative analysis. This chapter also discusses the classification procedures, which automate as much as possible of the photo-interpretation process, and its usefulness for different application, such as comparison between the day and night thermal flights.

Chapter 4 explains that before multi-temporal data can be used, it is essential that the spectral response received at the sensor from the same land cover is understood relative to its position of the scan line. Moreover, this chapter studies the distribution of DN values across the swath of the image. Finally, in the data quality analysis, the frequency distribution of DN values needs to be examined to study the spectral differences at different points in the scan line. This research is looking for any trends in the data such as referenced by Gregory (2001).

Chapter 5 describes the geo-correction procedure of the data provided by NERC using the AZGCORR software. The processes of geometric correction and registration, which are generally carried out in parallel, and can be classified into parametric and non-parametric techniques, are discussed in this chapter. Colour composite images were created by displaying different coloured guns for different overlapping flights. This technique was useful in assessing the registration accuracy, and the colour images provide an immediate qualitative indication of the nature of registration errors between the imagery. The errors are measured relative to a map. Finally, the geometric accuracy of the flights was illustrated by carrying out mosaic and overlaying procedures.

Chapter 6 discusses the main results that have evolved through the course of this research project.

Finally, in Chapter 7, the entire work is summarised and recommendations are made.

2 LITERATURE REVIEW

2.1 INTRODUCTION

Remote sensing refers to the acquisition of information from digital geospatial data acquired from overhead perspective, using sensors which sample and record electromagnetic radiation in one or more regions of the electromagnetic spectrum that is reflected or emitted from the surface of the Earth (Avery and Berlin, 1992). A broader definition might include analogue data, other force fields (seismic, acoustic, or gravitational) and non-terrestrial applications (lunar and planetary surfaces and astronomical investigations). However, the above definition provides sufficient scope to describe the data and methods that are commonly considered under the heading of remote sensing.

Remotely sensed imagery acquired from an airborne platform has the potential to offer far greater spatial and spectral resolution than is currently available from any satellite platform based system. The system implemented by NERC using the Airborne Thematic Mapper (ATM) can achieve a ground resolution of 0.8 metres (Wilson, 1997), and the spatial resolution may be chosen by altering the altitude of the aircraft (Atkinson and Curran, 1997). Airborne remote sensing offers the ability to collect radiation throughout the visible and infrared spectrum, including thermal infrared at high spatial resolution. Image acquisition is possible at any time required by the user, enabling scientific studies to investigate topics that have previously been difficult to undertake; satellite imagery is only available for the pre-determined times at which the satellite passes over a given portion of the Earth, when the target area is not covered by cloud. These factors combine to make airborne platforms and sensors a very attractive remote sensing system. However, they are not without their problems. During image acquisition, the aircraft is subject to atmospheric turbulence affecting its orientation throughout the flight. Despite the pilot's best efforts, it can be impossible to keep the aircraft exactly on the desired path with the correct orientation. The aircraft varies in its pitch, roll and heading throughout the duration of image acquisition; its attitude changing constantly as the aircraft encounters varying atmospheric conditions (Roy *et al,* 1997). The constant changing of the aircraft's attitude has a direct effect on the geometric properties of the data acquired. As a result, extensive post-processing of the data is required to produce fully geo-referenced digital data (Wilson, 1997 and Gregory, 2001).

Various components of the landscape such as vegetation, soil, rock, water, concrete, and asphalt have predictable thermal characteristics based on how they selectively absorb, transmit, reflect and emit solar energy. Thermal infrared remote sensing systems record thermal infrared images that can be used to determine the type of material in certain instances, based on its thermal emission characteristics, and/or to evaluate if significant changes have taken place in the thermal characteristics of these phenomena through time. In this manner, it is possible to identify stress in plants, thermal pollution in water bodies, or the loss of heat from buildings. Applications of thermal infrared imagery include; fire fighting resources during a forest fire (Lytle, 1996) or to target enemy facilities as in the Gulf war in 1991 (McDaid and Oliver, 1997).

2.2 THERMAL AIRBORNE REMOTE SENSING

A body's temperature can represent one thermal state but be expressed by two temperatures: the first is its internal temperature (from the kinetic motion of its atoms) as measured by an inserted thermometer, whereas the second is the external temperature measured by its emitted radiation. The radiant flux F_B (rate of flow of electromagnetic energy, commonly measured as Watts per square centimetre) emanating from a blackbody is related to its internal (kinetic) temperature T_K by the Stefan-Boltzmann Law, which in simplified form is given by Sabins (1987);

$$F_B = \sigma T_K^4 \tag{2-1}$$

where σ is a constant given as 5.67 x 10^{-12} W × cm^{-2} × K^{-4}. Strictly, this equation holds only for perfect blackbodies; for other bodies (so-called real or "grey bodies") the radiant flux will always be less than the blackbody flux, as calculated by:

$$F_R = \varepsilon \sigma T_K^4 \tag{2-2}$$

where ε is emissivity, the quantity of radiant emission. The effective temperature is measured externally as radiation and depends on the emissivity ε of the object in the spectral region of interest as well as temperature. Emissivity establishes the radiant temperature of an object (Avery and Berlin, 1992). Emissivity is a dimensionless number that expresses the ratio of the radiant flux of a real material F_R to the radiant flux of a perfect blackbody F_B calculated as (Sabins, 1987);

$$\varepsilon = \frac{F_R}{F_B} \tag{2-3}$$

Emissivity is a measure of the efficiency of emitted radiance of any real body to that of a perfect radiator (for which $\varepsilon = 1.0$). Values of ε vary from 0 to 1 and are spectrally dependent, i.e., can change with the electromagnetic wavelength (λ). Becker and Li (1993) reviewed a number of methods for deriving emissivity. Figure 2-1, shows an example comparison of the spectral radiant emittance of the common mineral quartz to a perfect blackbody when they are at thermal equilibrium at a given temperature (here, at 600 °K).

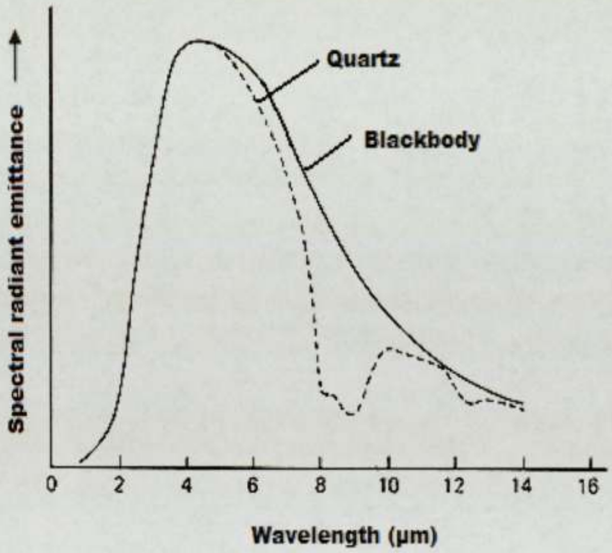

Figure 2-1: Spectral radiant emittance for quartz heated to 600 K compared with blackbody at the same temperature (Adapted from Salisbury and D'Aria, 1992).

The sharp decrease in emissivity (ε_λ) in the 8-10 μm region, noted for quartz and other silicates, is a "reststrahlen" effect (decreased emission) related to thermally induced stretching vibrations within silicon-oxygen bonds (Lillesand and Kiefer, 2000). In general, for opaque materials,

$$\varepsilon_\lambda = 1 - \rho_\lambda \tag{2-4}$$

where, ρ is the material's optical reflectance at wavelength (λ). Therefore, as $\rho_\lambda \rightarrow 1$, with high reflectance of radiation (poor absorption), the emittance will be lowered (thus, thermal radiation decreases). Water, which has a high emissivity in the thermal infrared in the 8-10 μm interval, is a poor reflector over that range; quartz (and many silicate rocks) is a good emitter at lower thermal wavelengths but poor in this interval. From this, one might predict that rock surfaces would appear darker than water in the 8-10 μm interval, even though they are at the same temperature. The radiant (sensed) temperature T_R differs from a body's kinetic (internal) temperature T_K according to the relation:

$$T_R = \varepsilon^{1/4} T_K \tag{2-5}$$

For real bodies (grey bodies) radiant temperatures are always less than kinetic temperatures. Thus, the radiant temperature is significantly higher for a blackened surface (high emissivity) than for a white surface (lower emissivity), even if the two materials are at the same kinetic temperature.

Salisbury and D'Aria (1992) computed the emissivity for a variety of terrestrial materials in the 8–14 µm region, including igneous, metamorphic, and sedimentary rocks, desert varnish, soil, vegetation, water, and ice. Snyder *et al*., (1997) provided additional information on the bidirectional reflectance measurements of sand and soils in the 3–14 µm region. One must take in to account an object's emissivity when using remote radiant temperature measurement to measure the object's true kinetic temperature. For the range of Earth temperatures (except fires and volcanoes), maximum radiometric emission is found in the infrared spectral region, which contains the middle wave infrared (MWIR: 3.4-5.2 µm), and long wave infrared (LWIR: 7.5-14 µm, also referred to as thermal infrared). Moreover, radiance measurements made in these two windows allow emissivity estimation, which is a thermo-optical intrinsic property of the surface and of its physical state. Recent spaceborne thermal infrared multispectral sensors, such as the Advanced Spaceborne Thermal Emission and Reflection Radiometer (ASTER) sensor on the National Aeronautics and Space Administration (NASA)'s Earth Observing System TERRA satellite (Yamaguchi *et al.,* 1998), are carrying out such measurements at regional and global scale.

Decorrelation of emissivity and temperature from infrared measurements is not a trivial task. Since the surface is characterized by its temperature and by one emissivity for each spectral band, there always remain more unknowns than measurements. Inversion methods have to make assumptions to bypass this difficulty. Some of these methods are described in Becker and Li (1990, 1995), Hook *et al*., (1992), Sobrino *et al*., (1994), Wan and Li (1997), Li *et al.,* (1999), Ma *et al.,* (2000) and reviewed by Dash *et al.,* (2002). In particular, the Temperature Emissivity Separation (TES) algorithm, developed for ASTER data by Gillespie *et* *al.,* (1998), combines the iterative removal of atmospheric radiance and an empirical relationship allowing absolute emissivity recovery.

Land surface temperature (LST) is an important factor controlling most physical, chemical and biological processes of the Earth. Knowledge of LST is necessary for many environmental studies and management activities of the Earth's resources (Becker and Li, 1993). In order to monitor macro-scale spatial changes of surface temperature, scanners designed for sensing in the thermal bands are placed onboard platforms for remote sensing of the Earth's resources from space (Sabins, 1987). The extensive application and significant importance of temperature in environmental studies and management is the main force driving the study of LST in remote sensing. Under the availability of thermal sensing data such as channels 4 and 5 of Advanced Very High Resolution Radiometer (AVHRR) data as well as Landsat Thematic Mapper 6 (TM6), the study of LST has become one of the hottest topics in remote sensing during the last two decades (Vogt, 1996). Many studies have been carried out on LST and the related ground emissivity from both technological aspects and application to specific areas (Prata and Platt, 1991; Prata *et al.*, 1995; Vogt, 1996; Vidal, 1991; Seguin *et al.*, 1994; Choudhury *et al.*, 1995, Schultz and Halpert, 1995; Cracknell and Xue, 1996; Caselles *et al.*, 1997).

LST is generally defined as the skin temperature of the ground. For the bare soil surface, LST is the soil surface temperature. However, the ground of the Earth is far from a skin or homogeneous surface with two dimensions (Vogt, 1996). Usually, it is composed of various objects on the surface and some of them such as vegetation may be best described in three dimensions. This situation makes the understanding of LST obscure, such as the case of vegetated ground. The remote sensing of LST is based on the thermal spectral (long wave) radiation from the ground. Thus, LST of dense vegetated ground can be viewed as the canopy surface temperature of the vegetation, and in sparse vegetated ground, it is the average temperature of the vegetation canopy, vegetation body and the soil surface under the vegetation. Another factor leading to the difficult understanding of LST is that the surface is not homogeneous at the spatial resolution (pixel scale) of remote sensing data.

Usually, LST changes obviously in a small distance such as 1 metre (Ottlé and Vidal-Madjar, 1992). However, the spatial resolution of most remote sensing data for LST is low compared with the difference of LST on the ground. For example, the pixel size for NOAA-AVHRR is 1.1 km, and for Landsat TM channel 6 it is 120 metre. Thus, LST in remote sensing means the average surface temperature of the ground under the pixel scale mixed with different fractions of surface types (Kerr *et al.,* 1992). The theoretical basis for the remote sensing of LST is that total radiative energy emitted by ground surface increases rapidly with increase in temperature. The spectral distribution of the energy emitted by a ground object also varies with temperature.

According to Wien's Displacement Law on the relationship between spectral radiance and wavelength, for the Earth with an ambient temperature of 300 K, the peak of its spectral radiance occurs at about 9.6 μm (Lillesand and Kiefer, 1994). Therefore, theoretically, the thermal energy in relation to the physical temperature of the ground surface can be remotely observed by using sensors operating at wavelength around 10 μm, which have been defined as thermal channels in remote sensing systems. The obtained temperature of the ground surface on the satellite level is called the brightness temperature (Reutter *et al*., 1994).

On the other hand, the spectral characteristics of the atmosphere indicates that there is an atmospheric window in the spectral region 8-14 μm, where atmospheric absorption is minimum and through which the energy source of ground surface can transmit without great losses. Thus, ground surface temperature can be remotely sensed using the channels within the atmospheric window at the thermal spectral wavelength. Data from NOAA-AVHRR channels 4 and 5 operating respectively at 10.5-11.3 μm and 11.5-12.5 μm as well as Landsat TM channel 6 operating at 10.4-12.5 μm can be used to estimate surface temperature.

In the thermal wavelength, usually the atmosphere has three very important effects on the spectral radiation transmission: absorption, upward atmospheric radiance and bi-directional reflection of the downward atmospheric radiance (Franc and Cracknell, 1994). Therefore, the spectral radiance reaching the sensors are not only that emitted by ground objects and attenuated by atmospheric absorption, but also includes the radiance emitted by the atmosphere and the reflected component of the downward atmospheric radiance. At the same time, different viewing angles of the sensor and the characteristics of the ground objects also have significant effects on the observed radiance from space (Ignatov and Dergileva, 1995; Wan and Dozier, 1996).

LST is one of the key parameters in the physics of land surface processes on regional and global scales. It combines the results of all surface–atmosphere interactions and energy fluxes between the atmosphere and the ground. The LST retrieved from satellite data may be used to validate and improve the global meteorological model prediction after appropriate aggregation and parameterization (Diak and Whipple, 1993). The remotely sensed LST has been used in land cover and land cover change analysis (Ehrlich and Lambin, 1996; Lambin and Ehrlich, 1997), and in the production of the MODIS land cover product. It has been also used in monitoring drought and estimating surface soil moisture (Feldhake *et al.*, 1996, McVicar and Jupp, 1998), evaluating water requirements of wheat (Jackson *et al.*, 1977).

Refinements and improvements were made to the new version of MODIS LST product generation executive code. Using both Terra and Aqua MODIS data for LST retrieval improves the quality of the LST product and the diurnal feature in the product due to better temporal, spatial and angular coverage of clear-sky observations. The absolute radiometric accuracy of MODIS TIR channel data was evaluated with in situ data collected in a vicarious calibration field campaign (Wan *et al.,* 2002, 2004).

The MODIS LST products have been validated within 1K in multiple validation sites in relatively wide ranges of surface and atmospheric conditions. Refinements and updates were made to improve the quality of the LST product and to use both Terra and Aqua MODIS data in the LST retrieval (Vermote and Roy, 2002). The major advantages of the additional Aqua MODIS data for the LST product include the increase in quantity and the improvement in quality of the surface emissivity and temperature science data over the global land due to the increasing number of MODIS observations in clear-sky conditions. With the MODIS observations four times a day for nearly every spot on the Earth and more frequently in high latitude regions, the diurnal variation feature will be kept in the LST product. Because, of the Aqua overpass time around 1:30 pm, the afternoon LSTs retrieved from the MODIS data will be close to the maximum temperature of the land surface so that it is more suitable for regional and global change studies, especially in applications for estimating soil moisture condition and water requirements of crops, and for monitoring drought (Ma *et al*., 2000, 2002).

The hot spot is the term used to describe the increased directional reflectance that occurs over most land surfaces when the solar and view directions coincide. Under these viewing conditions, shadows cast on the surface are minimized, resulting in increased reflectance. This phenomenon has been observed in laboratory measurements (Sandmeier *et al*., 1998), airborne data (Vermote *et al*., 1997, 2002) and multi-angular satellite sensor data by systems such as POLDER (Hautecoeur and Leroy, 1998). MODIS has seven reflective bands for land studies, two 250m bands and vs. 500 m bands.

Hot-spots are evident in successive MODIS scans as the solar and view directions coincide and observed forest canopy shadows decrease. Failure to account for these directional reflectance effects implies a commensurate reduction in the capabilities of certain applications, for example change detection (Roy *et al*., 2002), and fails to exploit the full range of information available in these data. The large number of daily global MODIS observations that are available at moderate spatial resolution encourage the development of inversion procedures (e.g. Lacaze and Roujean, 2001) that retrieve physical parameters describing those land cover features that manifest themselves in the hot-spot amplitude and width (Fang *et al.,* 2004).

At the same time, the MODIS onboard Terra is providing data for surface reflectance, BRF and albedo products because of its large field of view (FOV) (Vermote and Vermeulen, 1999). Surface reflectance and albedo can also be obtained from Landsat Enhanced Thematic Mapper (ETM) data after removing the atmospheric effects (Liang, 2001). These reflectance products are important inputs for the generation of other land products such as vegetation indices (VI), land cover, and the Fraction of Photosynthetically Active Radiation/Leaf Area Index (FPAR/LAI). Users of these products need to know the relative uncertainties associated with the sources of information. The comparison of information products from different satellites has been an important part of validating these products before the information is provided to the user community (Liang *et al*., 2002).

The hemispherical–directional reflectance factors (HDRF), BRF, bi-hemispherical reflectance (BHR), and directional–hemispherical reflectance (DHR) land surface products are considered by this comparison. DHR is the radiant exitance divided by irradiance under illumination from a single direction. BHR is the radiant exitance divided by irradiance under the same illumination conditions (Diner *et al*., 1999). BHR can be directly determined through field measurements while the DHR needs numerical integration calculation after the BRF is obtained. BRF is defined as the surface-leaving radiance divided by radiance from a Lambertian reflector illuminated from a single direction. HDRF is defined as the surface-leaving radiance divided by radiance from a Lambertian reflector with the same illumination (Diner *et al*., 1999). The differences between BRF and HDRF have been detailed by Gu and Guyot (1993).

Previous work has compared the bidirectional reflectance and albedo of MODIS and MISR (Lucht, 1998) using simulated data. The satellite data use includes the examination of spatial and temporal product trends, comparison of data products, comparisons with in situ data collected over a range of validation sites, and comparisons with data and products from other spaceborne sensors.

2.2.1 ENERGY- MATTER INTERACTION WITH THE TERRAIN

The rate of radiant energy onto, from or through a surface per unit time is called radiant flux (ϕ), and is measured in Watts per metres square. The characteristics of radiant flux and what happens to it as it interacts with the Earth's surface is of critical importance in remote sensing. By carefully monitoring the exact nature of the incoming radiant flux in selective wavelengths and how it interacts with the terrain, it is possible to learn important information about the terrain.

The simple radiation budget equation, which states that the total amount of radiant flux in specific wavelengths (λ) incident on the terrain ($\phi_{\lambda i}$) is accounted for by evaluating the amount of energy reflected from the surface (r_{λ}), the amount of energy absorbed by the surface (α_{λ}), and the amount of radiant energy transmitted through the surface (τ_{λ}) (Jensen, 2000);

$$\phi_{\lambda i} = r_{\lambda} + \alpha_{\lambda} + \tau_{\lambda} \tag{2-6}$$

Anisotropy of thermal infrared (TIR) radiance exists and is observed for many natural surfaces, particularly for three-dimensional (3D) vegetated areas (Lagouarde *et al.,* 1995). The magnitude and sign of this anisotropy depend, on one hand, on macroscopic structural parameters and thermal heterogeneities, on the other hand, on canopy geometric structure, density, and optical properties. It is also time-dependent because of sun illumination effects and sensitivity to ambient conditions (Lagouarde *et al.*, 1995). This is important in the imagery used in this project, as anisotropy makes it difficult to obtain reliable surface temperature measurements, but also provides an opportunity to extract component temperatures of the surface elements (Ottermann *et al.,* 1992). Several experimental studies have been conducted to document this anisotropy over a wide range of surfaces and to validate different models developed to interpret observations of anisotropic thermal infrared radiance (Caselles *et al.*, 1992, Norman *et al.,* 1994).

However, actual existing experimental systems designed to measure the anisotropic TIR radiance with a TIR radiometer in the field suffer from two major difficulties:

(1) the projected area on the surface for a constant instantaneous field of view of the radiometer changes with different view angles for a thermally heterogeneous surface, this implies that different elements and different proportions of the elements are viewed in different view angles; and (2) since multidirectional measurements in the field often take several to thirty minutes, the heat balance on the surface, i.e. surface temperature, changes during the period of the measurement due to the variations of atmospheric turbulence and of local meteorological conditions (Menenti *et al.,* 2001). These two difficulties have hampered understanding of the mechanism of directional thermal radiation and quantitative modelling of directional TIR radiation.

2.2.2 HEMISPHERICAL REFLECTANCE, ABSORPTANCE AND TRANSMITTANCE

This section will not be limited to thermal radiation only; it will range from the visible to the thermal infrared wavelengths of the electromagnetic spectrum.

Hemispherical Reflectance (r_λ) is defined as the dimensionless ratio of radiant flux reflected from the surface to the radiant flux incident to it (Jensen, 2000).

$$r_\lambda = \frac{\phi_{reflected}}{\phi_{\lambda i}} \tag{2-7}$$

Hemispherical Transmittance (τ_λ) is defined in Jensen (2000) as the dimensionless ratio of the radiant flux transmitted through a surface to the radiant flux incident to it.

$$\tau_\lambda = \frac{\phi_{transmited}}{\phi_{\lambda i}} \qquad \textbf{(2-8)}$$

Hemispherical Absorptance (α_λ) is the dimensionless relationship given by Jensen (2000):

$$\alpha_\lambda = \frac{\phi_{absorbed}}{\phi_{\lambda i}} \qquad \text{Or}$$

$$\alpha_\lambda = 1 - (\tau_\lambda + r_\lambda) \qquad \textbf{(2-9)}$$

2.2.3 IRRADIANCE AND EXITANCE

Irradiance (E_λ) is the total amount of radiant flux incident per unit area (A) of a plane surface from all directions above. Irradiance weighted with the response curve of the human eye gives ***Illuminance*** (Richards, 1993).

$$E_\lambda = \frac{\phi_\lambda}{A} \qquad \textbf{(2-10)}$$

Exitance (M_λ) explains the total amount of radiant flux leaving per unit area of a surface into all directions above (Jensen, 2000).

$$M_\lambda = \frac{\phi_\lambda}{A} \qquad \textbf{(2-11)}$$

Both quantities are measured in watts per metre square (W m^{-2}).

Radiant Flux Density is the amount of radiant flux intercepted divided by the area of the plane surface, the average radiant flux density (ϕ) (Elachi, 1987).

2.2.4 RADIANCE

Unlike irradiance, radiance is a property solely of a radiation field, not of the orientation of the surface. Its density per solid angle defines the amount of power density scattered in a particular direction, since equal amounts are scattered into equal cones of solid angle. (Solid angle is the angle that, seen from the centre of a sphere, includes a given area on the surface of that sphere. The value of the solid angle is numerically equal to the size of that area divided by the square of the radius of the sphere). This quantity is called solid radiance and has units of W m^{-2} sr^{-1} (Richards, 1993). Irradiance for any surface is the integral of radiance over a hemisphere of directions above or below that surface. The photometric equivalent of radiance is luminance, obtained by integrating spectral radiance weighted by luminous efficiency over the visible spectrum. The focus is on the radiant flux in certain wavelengths (L_λ) leaving the projected source area (A) within certain directions ($ACos\theta$) and solid angle (Ω) was given by Jensen (1996);

$$L_\lambda = \frac{\theta}{\Omega * ACos\theta} \qquad \textbf{(2-12)}$$

2.3 THERMAL PROPERTIES

Avery and Berlin (1992) discussed the importance of an objects thermal properties in controlling the internal distribution of heat energy as a function of time and depth. This distribution pattern, in turn, controls the surface temperature of a given object. A thermal sensor detects radiant energy from a surface target, heated through radiation, convection (atmospheric circulation) and conduction (through the ground). Most sensed heat from surfaces has its origin in solar illumination, that varies with diurnal and seasonal changes, as well as cloud cover, but there is also a small, nearly constant, contribution from internal heat flux from the Earth's interior (mostly from radioactive decay). Heat transfers into and out of near surface layers because of external heating by the thermal processes of conduction, convection, and radiation.

A primary objective of temperature measurements and related thermal responses is to infer something about the nature of the composition and other physical attributes of materials at the Earth's surface and in its atmosphere. For any material, certain internal properties play important roles in governing the temperature of a body at equilibrium with its surroundings.

Some factors have fixed or constant effects, while others vary with each sensor overpass. It may be possible to correct for the influence of some of the variable factors, but this is difficult to do routinely. Diurnal variation in solar heating accounts for temperature differences up to 1 m below the earth's surface, whilst seasonal heating accounts for temperature differences up to depth of 10-20 m below the Earth's surface (Elachi, 1987).

2.4 INTERPRETING THERMAL SCANNER IMAGERY

Thermal airborne remote sensing data are useful to map the water turbidity in an area. However, they require robust quantification algorithms that include conversion of the water-leaving signal into concentrations of the water constituents. In this domain, recently obtained results are encouraging: (e.g. Doxaran *et al.,* 2002 and 2003) and the fitted models can be used to predict suspended solids and dissolved organic matter concentrations from above-water optical measurements (e.g. Bowers *et al.,* 2000 and 2004, D'Sa and Miller, 2003). Unlike the reflected light from surfaces in which only the topmost layers (a few molecular layers thick) are involved, thermal remote sensing includes energy variations extending to varying shallow depths below the ground surface. This takes time and is the normal consequence of heating during the day and cooling at night. Jensen (2000) explains the most critical consideration in analyzing and interpreting thermal data and imagery is that of knowing the physical and temporal conditions that heat the near surface layers. Over the seasons, minor shifts in the mean temperature in bedrock can occur to depths of 10 metre or more.

Solar radiation and heat transfer from the air significantly heat materials at and immediately below the surface during the day. Temperatures usually drop at night primarily by radiative cooling (maximum radiative cooling occurs under cloudless conditions), accompanied by some conduction and convection. During a single daily (diurnal) cycle, the near surface layers (commonly, unconsolidated soils) experience alternate heating and cooling to depths typically between 50 and 100 cm. The daily mean surface temperature is commonly near the mean air temperature. Observed temperature changes are induced mainly by changes during the diurnal heating cycle, but seasonal differences (averages and range) in temperature and local meteorological conditions also affect the cycle response from day to day.

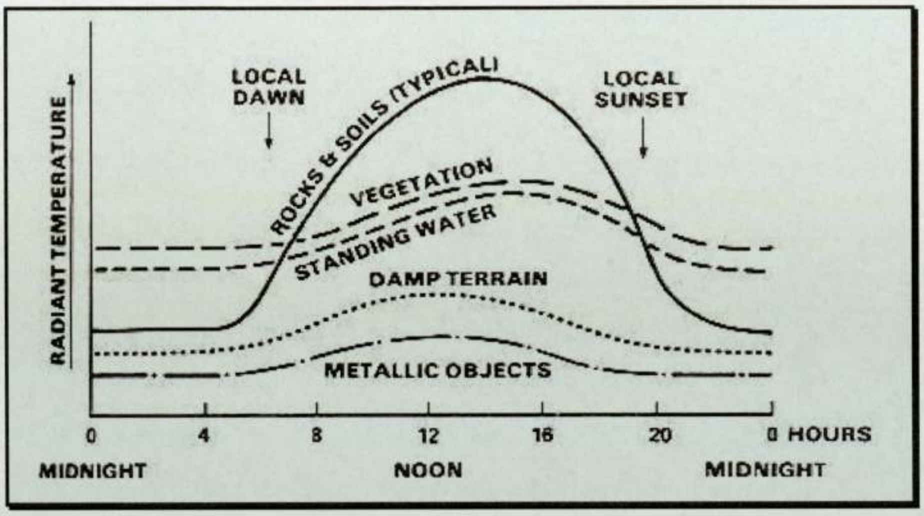

Figure 2-2: Changes in radiant temperatures of five surface-cover types during a 24-hour thermal cycle. From F.F. Sabins, Jr., Remote Sensing: Principles and Interpretation 2nd Ed., © 1987.

Sabins (1987) plotted the curve of Figure 2-2 to summarize the qualitative changes in radiant temperature during a 24-hour cycle, for five general classes of materials found at the surface. Given two thermal images of the same locale, taken 12 hours apart, about noon and about midnight, it may be possible to determine the identities of co-registered pixels, based on their temperatures and thermal inertias.

2.5 SPECTRAL ACCURACY

2.5.1 INTRODUCTION

In this section, the spectral characteristics, image sensor, image motion and radiometric effect and characteristics of the airborne sensor will be discussed, and hence the research tries to address the following questions;

i. Is there any error in the spectral response?

ii. Does the sensor pick-up the same radiation from the same material at different places in the imagery?

Urban and rural areas are characterized by a very specific spatial architecture (Dana *et al.,* 1999). Indeed, the complexity of the environments makes it more difficult to automatically classify different urban materials directly from airborne radiance measurements than rural environments. Pre-processing is usually required to extract ground surface intrinsic properties like reflectance, which are independent of the irradiance conditions.

Some works have already analysed spectral reflectance (Hook, 2000; Ben-Dor *et al.,* 2001; and Herold *et al.,* 2004) or bidirectional properties (Meister *et al.,* 2000) of some urban and rural materials. Spectral measurements not only allow estimation of the spectral reflectance of materials, but also the quantification of their spatial variability. The spectral range may be adjustable or set, with the number of channels (discrete wavelength intervals) and bandwidth (internal range) varying considerably.

One of the advantages of airborne scanners is the ability to configure the sensor to record spectral features of a particular interest. Another advantage of airborne scanners is the ability to adjust flight times to avoid adverse weather or atmospheric conditions or, to respond to a crisis. One can adjust the instrument to vary the spatial/spectral resolution, scale, etc.

Image scanners are available with spectral bands throughout the visible short infrared (SWIR, or near IR), and thermal IR range. The spatial resolution of airborne scanners is a function of the instantaneous field of view (IFOV) and the aircrafts altitude. The spatial resolution of the dataset used in the project is 1.8 metres. The spectral resolution is also an instrumental parameter and can be designed narrow (10 nm or less) to wide (4 microns or more).

2.5.2 SPECTRAL CHARACTERISTICS

Broad-band multi-spectral instruments such as the Thematic Mapper on airborne platforms measure emitted or reflected energy over spectral bands that are on the order of 0.1 μm (in the visible region) to 2 μm (in the mid- and thermal IR regions) wide, for a total of up to six or eight spectral bands. Imaging spectrometers have spectral resolutions on the order of 0.01 μm and up to 200 or more spectral bands, for example Eagle/Hawk. These narrow spectral bands do not have sharp cut-offs however, and the measured signal generally includes some out-of-band response (Herold *et al.,* 2004).

2.5.3 IMAGE SENSORS

2.5.3.1 Cameras

Electro-optical sensors differ from photographic sensors in that they do not capture an instantaneous snapshot of the Earth, but rather the image is built by viewing individual scan lines contiguously. The shutter of the camera opens for a fraction of a second, allowing light energy to fall on the solid-state imaging sensor (CCD-matrix chip). The incident light energy (photons) is absorbed, raising the energy level of electrons in the chip materials that jumps to the outer shells. The spatial resolution in digital cameras is variable, depending on the number and size of the photo-site of the sensor chips. The signal to noise ratio, it is related to target contrast, illumination, lens aperture and spectral band (Gupta, 2003).

Electro-optical and spectral imaging scanners produce digital images with the use of detectors that measure the brightness of reflected electromagnetic energy. Scanners consist of one or more sensor detectors depending on the type of sensor system used and can be used on airborne or space platforms. There are two different types of multispectral scanners: (1) Across-Track Scanners (whiskbroom), and (2) Along-Track Scanners (pushbroom).

2.5.3.2 Across-Track Scanners

The whiskbroom scanners also referred to as across-track scanners, uses rotating mirrors to scan the scenery below from side to side perpendicular to the direction of the sensor platform. The width of the sweep is referred to as the sensor swath. The rotating mirrors redirect the reflected light to a point where a single or just a few sensor detectors are grouped together. Whiskbroom scanners with their moving mirrors tend to be large and complex to build. The moving mirrors create spatial distortions that must be corrected with pre-processing by the data provider, before image data is delivered to the user.

The whiskbroom scans the terrain along lines that are at right angles to the flight path. A large instantaneous field of view (IFOV) means there is: (1) a greater quantity of energy on any detector, (2) a more sensitive scene radiance measurement due to higher signal levels been received, and (3) an improved radiometric resolution (Wadsworth, *et al.*, 1992). It also benefits the quality of the image due to the signal being greater than background noise, so there is a higher signal-to noise ratio, thus meaning less distortion to the image. A high IFOV enables a higher dwell time, which means that a stronger signal is received, and a greater range of sensed signal, leading to better spatial and/or radiometric resolution. However, narrowing the wavelength band, over which a detector operates, increases the signal-to-noise ratio and so radiometric resolution is sacrificed. The whiskbroom scanner has fewer sensor detectors to keep calibrated, compared to other types of sensors (Avery and Berlin, 1992).

2.5.3.3 Along-Track Scanners

Pushbroom sensors use a linear array of charged coupled devices (CCD's) to scan the surface enabling a complete scan to be recorded instantaneously. This sensor type relies on the forward motion of the platform to provide one direction of scan (the so called along track direction), allowing successive scan lines to be recorded.

Pushbroom scanners are also referred to as along-track scanners. For more detailed review of airborne imaging systems refer to Lillesand and Kiefer (1994 and 2000).

2.5.3.4 CCD-TDI Sensors

A Time Delay and Integration (TDI) charge-coupled device (CCD) is widely used for observation of high speed moving objects undetectable by classic CCD. TDI is a specialized detector readout mode that is used in machine vision applications where there is fast relative movement between the camera and the object being imaged. CCD's can be linear arrays (as in scanners) or area arrays (as in cameras). Clearly, an area array system is more powerful and can collect a lot more information in a given time than an area array, but the applications of TDI are usually more like scanning than single-image photography.

The primary advantage of TDI operation is the greatly increased image integration period it affords. TDI increases the integrated signal proportional to the number or rows on the detector (512 on the Image Stream 100). The practical limit on the number of rows is determined by the accuracy of the cell velocity measurement, since velocity errors result in cumulative tracking errors (Holst, 1998). Therefore, despite of the movement of the object, always the same part of object is scanned, so the integration time is multiplied by the number of TDI stages. For this reason, TDI-sensors offer advantages compared to standard linear sensors. This can be an advantage at applications with quickly moving objects, if the exposition times are too short for normal linear sensors. TDI sensors are for e.g., used for scanning documents at very high speed, as it is for example needed for sorting postage letters, but in this context they allow a sensor to move over the ground at high speed, as in a aircraft, and still records low energy emissions from the ground.

2.5.4 RADIOMETRIC CHARACTERISTICS

Several properties of electromagnetic radiation can be measured: intensity, phase, and polarization. Of these, intensity is most frequently used. The radiometric resolution of digital intensity data is recorded in bits, between 6 bits (i.e. 64 quantization levels) and 10 bits (1024 levels) for most remote sensing instruments. In general this quantization effect is small relative to the signal-to-noise ratio (SNR) of the receiver, which in turn is limited by the fact that the target area is distant and heterogeneous, and the dwell time is short. In addition, measured radiance is a function not only of surface reflectance, but of other factors, including topographic shading and atmospheric transmission (Negahdaripour, 1998).

Scattering and absorption of radiation by aerosols are the most significant and variable atmospheric effects at short wavelengths (visible and near IR) Speckle (coherent scattering) is the primary limitation on the radiometric resolution of radar images.

2.5.5 SPATIAL CHARACTERISTICS

A sensor integrates the energy received across the instantaneous field of view (IFOV) to produce an electronic signal whose magnitude depends on the nature of the observed scene (the average radiance in the prescribed spectral band) and on the dwell time (Wilson, 1997). Hyperspectral and multispectral instruments include a dispersion element (a diffraction grating or an interferometer) to separate out the components of this signal by wavelength.

The imaged swath from an aircraft may also be several kilometres although this will require a large angular sweep and high altitude. Satellite systems are outside of the atmosphere, and hence not subjected to atmospherics disturbances and hence relatively predictable in altitude and position as compared to airborne sensors (Gupta, 2003).

2.6 GEOMETRIC ACCURACY

2.6.1 INTRODUCTION

Pre-processing of the airborne remote sensing data must precede interpretive tasks. Spatial or geometric distortion in the image arises from several sources. These include the wide field of view and platform instability, and panoramic effects of scanning instruments. Geometric correction of remotely sensed imagery is the process of eliminating, to a satisfactory degree, errors of a geometric nature resulting from sensor imperfections, surface relief and the relative motion of the sensor platform and underlying scene. This procedure is also referred to as image rectification, geo-rectification and geometric enhancement (Jacobsen, 1993). Image registration is the transformation of a raw image so its pixels conform to a specified geometry, provided typically by a map co-ordinate system. The advantage of registering imagery to a map co-ordinate system is that pixels can be referenced in terms of co-ordinate rather than row and column addresses. Furthermore, registration to a map provides the imagery with a measurable scale, enabling areas and distances to be calculated quickly and accurately (Davies and Wang, 2001).

While the theory behind the correction of geometric distortions is usually straightforward, its implementation may not be. One problem is registering the image to a rectified grid. The same problem arises when two or more images or maps from different sources are overlain, another common preliminary to data analysis. The current generation of high spatial resolution imagery using previously proven technology (Konecny, 2000) provides an interesting source for topographic mapping as well as thematic applications such as agriculture, and forestry. Petrie (2002) gives a review and comparisons of the characteristics of the generation of high spatial resolution satellite imagery. Consequently, multi-source data integration (raster and vector) for mapping application requires geometric and radiometric models and processing adapted to the nature and characteristics of the data, in order to recover the original information from each image in the composite geo-coded image.

Before a remotely sensed image can be integrated with other sources of geographical data, it must first undergo a transformation to remove the many distortions caused by errors inherent to the methods of image acquisition which affect its geometry.

2.6.2 SOURCE OF IMAGE DISTORTION

The source of distortion can be related to two general categories: (1) the observer or the acquisition system i.e. platform and imaging sensor (see Ehlers, 1997 and

Mather, 1999) and, (2) the observed (atmospheric and Earth). In addition to these distortions, the deformations related to the map projection have to be taken in to account, because the terrain and most of GIS end users applications are generally represented and performed with respect to referenced topographic maps produced to some map projection.

The distortions caused by the imaging sensor are:

- Error due to calibration parameter such as the focal length
- Distortion due to too wide instantaneous field of view (IFOV)
- Imperfection of the scanning mirror, and
- Offset errors.

The distortions caused by the non-imaging sensor are:

- Due to variation in the altitude of the aircraft
- Due to terrain effect
- Due to motion of the underline surface, and
- Atmospheric (e.g. refraction).

2.6.3 IMAGE CORRECTION MODELS

All these geometric distortions require models and mathematical functions to perform the geometric correction of an image: either with 2D/3D non-parametric models or with rigorous 3D parametric models. With 3D parametric models, the geometric error can be corrected systematically with a mathematical function for each distortion or all together with a "combined" mathematical function (Pala and Pons, 1995). Since 2D polynomial functions do not reflect the sources of distortion during the image formation and for the relief, they are limited to images with few or small distortions, such as nadir-viewing images, small images, systematically corrected images, flat terrain. They also are very sensitive to input errors (Hanley and Fraser, 2001). The 2D polynomial functions were mainly used in the 70's and 80's on images whose systematic distortions, excluding the relief, were already corrected by the image providers.

There are many, seemingly disparate, approaches to the geometric correction process (Janssen *et al*., 1994). The purpose of this section is to clarify the geometric correction process and to introduce some relevant terminology and concepts. This section reviews methodologies developed to geometrically correct airborne scanner imagery; where appropriate a more detailed review is given (Richards and Jia, 1999). The geometric correction of airborne scanner imagery can be achieved by the following approaches:

i. Parametric Models

ii. Non-Parametric Models

iii. Platform stabilisation, and

iv. Level flight.

2.6.3.1 Parametric Models

Parametric methods of geometric correction require information concerning the sensor geometry and the sensor exterior orientation (attitude and position) (Toutin, 2004). Parametric correction methods are based upon fundamental, analytical photogrammetric concepts and use principles of projective geometry and the collinearity condition which arises from them. Parametric correction of line scanner imagery is developed from photogrammetry and uses the principles of projective geometry and the collinearity equation which arise from them. Central to photogrammetry are the concepts of interior and exterior orientation (Gregory, 2001). The collinearity condition serves as the basis of the collinearity equations, which relate two dimensional image, coordinates to corresponding three dimensional scene coordinates. Two dimensional aerial photographs, sensed at a single instant, may be rectified into Earth coordinates using a variety of well established analogue or analytical photogrammetric techniques (see Barnsley *et al.,* 2004 and Davies and Wang, 2001).

The collinearity equation is a physical model representing the geometry between a sensor (projection centre), the ground coordinates of an object and the image coordinates. The collinearity equation gives the geometry of a bundle of rays connecting the projection centre of a sensor, an image point and an object on the ground. This concept is used to develop the collinearity equations, usually in the form where the image coordinates of an object are expressed as functions of the interior orientation parameters, the exterior orientation parameters, and the space coordinates of the object (Strausz, 2001). These equations are shown below:

$$X = X_a - f\left[\frac{a_1(x_A - x_C) + a_2(y_A - y_C) + a_3(z_A - z_C)}{a_7(x_A - x_C) + a_8(y_A - y_C) + a_9(z_A - z_C)}\right]$$

$$Y = Y_a - f\left[\frac{a_4(x_A - x_C) + a_5(y_A - y \quad) + a_6(z_A - z_0)}{a_7(x_A - x_C) + a_8(y_A - y_C) + a_9(z_A - z_C)}\right] \qquad \textbf{(2-13)}$$

In these equations X and Y are an object image coordinates; x_A, y_A, z_A are the object's coordinates in object space; x_C, y_C, z_C are the object space coordinates of the camera position; a_1 - a_9 are the coefficients of the orthogonal transformation between the image plane orientation and object space orientation, and are functions of the rotation angles ω, φ, κ; X_a, Y_a, and f are the interior orientation parameters of the image, the image coordinates of the photo principal point and the camera focal length, respectively.

Although each sensor has its own specificity, one can draw generalities for the development of 3D parametric functions, in order to fully correct all distortions described previously. The 3D parametric functions should model the distortions of the platform (position, velocity, and attitude), the sensor (viewing angles, panoramic effect), the Earth (ellipsoid and relief) and the cartographic projection (Richards and Jia, 1999). The geometric correction process can address each distortion one by one and step by step or all together. In fact, it is better to consider the total geometry of viewing: platform + sensor + Earth + map, because some of the distortions are correlated (Toutin, 1995 and 2001). It is theoretically more precise to compute one "combined" parameter than each individual component of this "combined" parameter, separately.

Examples of combined parameters include:

- The orientation of the image is a combination of the platform heading due to orbital inclination, the yaw of the platform, and the convergence of the meridian for satellite sensor
- The scale factor in along-track direction is a combination of the velocity, map projection, the altitude and the pitch of the platform, and
- The levelling angle in the across-track direction is a combination of roll, the viewing angle, and the orientation of the sensor.

The 3D parametric functions are generally the well-known collinearity condition and equations (Lillesand and Kiefer, 2000), which are only valid for a scan line acquisition. However, the parameters of neighbouring scan lines of scanners are highly correlated, it is thus possible to link the exposure centres and the rotation angles of the different scan lines with supplemental information. Ephemeris and attitude data can be integrated using 2^{nd} order polynomial functions (Richards and Jia, 1999), or benefiting from theoretical work in celestial mechanics (Toutin, 1995).

2.6.3.2 3D Polynomial Models

The 3D polynomial functions are an extension of the 2D polynomial function by adding Z-term related to the third dimension of the terrain. However, they are subjected to the same problems related to 2D non-parametric functions: application to small images, need a lot of ground control points (GCPs) regularly distributed, very sensitive to input errors, lack of robustness, etc difficulties with whiskbroom and pushbroom scanners. Their use should be thus limited to small images or to systematically-corrected images, where all systematic distortions except the relief were corrected. They were applied with geo-referenced images, such as SPOT-HRV (level 1B) (Pala and Pons, 1995) and IKONOS Geo-products (Hanley and Fraser, 2001).

For the 3D polynomial functions, *P3D:*

$$P3D(XYZ)=\sum_{i=0}^{m}\ \sum_{j=0}^{n}\sum^{p}a_{ijk}X^{i}Y^{j}Z^{k} \tag{2-14}$$

Where:

X, Y, and Z are the terrain or cartographic coordinates

i, j and k are integer increments

a_{ijk} is transformation coefficient.

m, n and p are integer values

$m+n+p$ is the order of the polynomial functions.

The term RMSE related to terrain elevation in the 3D polynomial functions could be reduced to a Z for high-resolution images, whatever the order of the polynomial functions used.

2.6.3.3 Rational Models

3D rational functions have recently drawn interest in the civilian photogrammetric and remote sensing community due to the launch of new civilian high spatial resolution sensors. The major reason for their recent interest is that some image vendors, such as Space Imaging (Davies and Wang, 2001); do not release information on the satellite and the sensor position and altitude.

For the 3D rational functions, R3D:

$$R3D(XYZ) = \frac{\sum_{i=0}^{m}\sum_{j=0}^{n}\sum_{k=0}^{p} a_{ijk} X^i Y^j Z^k}{\sum_{i=0}^{m}\sum_{j=0}^{n}\sum_{k=0}^{p} b_{ijk} X^i Y^j Z^k} \qquad \textbf{(2-15)}$$

Where:

X, Y, and Z are the terrain or cartographic coordinates

i, j and k are integer increments

a_{ijk} and b_{ijk} are transformation coefficient.

m, n and p are integer values

$m+n+p$ is the order of the polynomial functions.

The 3D rational functions can be used with two approaches:

i. To approximate an already-solved existing 3D parametric model, and

ii. To determine by least-squares adjustment the coefficients of the polynomial functions (equation 2-15) with GCPs.

The first approach is performed in two steps. A 3D regular grid of the imaged terrain is first defined and the image coordinates of the 3D grid ground points are computed using the already-solved existing 3D parametric model (Jia, 2003 and Yao, 2001). These grid points and their 3D ground and 2D image coordinates are then used as GCPs to resolve the 3D rational functions and compute the unknown term of polynomial functions.

This approach has been proven adequate for aerial photographs or satellite images by Tao and Hu (2001). However, they found that the results are sensitive to GCP distribution with satellite images. When the image is too large, the image itself has to be subdivided and separate 3D rational functions are required for each subdivided image.

As in the 3D polynomial functions, the rational functions mainly correct locally at the GCPs, and errors and inconsistencies between GCPs can be found (Davies and Wang, 2001). They should not be used with raw and large-size images but only with small-size or geo-referenced/geo-coded images. Otherwise, a piecewise approach as described previously should be used for large raw images, and the number of GCPs should be increased proportional to the number of sub-images (Yao, 2001).

2.6.3.4 Geometric Correction by Matching Delaunay Triangles

Geometric correction of scanner data by matching Delaunay triangles involves three steps. The first step is the selection of GCPs. The selection of GCPs for the Delaunay triangulation procedure is achieved using exactly the same principles as those which apply to polynomial-based methods. However, it is frequently the case that on the relatively large-scale images produced by ATM and other airborne scanners, there is a lack of corresponding detail on associated maps. This can make the identification of accurate map locations for GCPs a problem. In extreme cases it has been necessary to circumvent this problem by using aerial photography as a source of GCPs in addition to primary data as collected from large scale Ordnance Survey (OS) sheets. Assuming the OS locations are correct it is possible to generate a root mean square error (RMSE) for prediction from the stereo model.

Once an acceptable model has been defined it is possible to predict the OS map locations of features which appear on the stereo model but not on the map (Devereux, *et al.,* 1990). Using this mechanism, large numbers of accurate GCPs can be generated for input into the geometric correction process. In the case of ATM imagery, where air photos are collected at the time of imagery, the stereo model is an invaluable adjunct to the correction process because even relatively transient image features can be used as GCPs with relative safety. Nevertheless, in most circumstances, there is no necessity for the photography to be acquired at exactly the same time as the image data.

Once an accurate set of GCPs has been found, the next stage in the process is to derive an augmented set of GCPs from the original accurately located set. This is achieved by simultaneously constructing the Delaunay triangulation of the original data set in both the map and the image space. The Delaunay procedure is described by McCullagh and Ross (1980) and involves constructing triangles from the control point distribution such that no triangle's circumcircle contains a vertex of another triangle. It thus has the properties of generating the most equilateral set of triangles from a given random data set and also guaranteeing the same triangulation will be produced from a given data set, regardless of the starting point for the triangulation construction. The capacity for generating equilateral triangles is important in this application because subsequent matching of equilateral triangles in image and map space is likely to yield greater accuracy and fewer computational problems than matching any other triangular shapes. Furthermore, always being able to ensure arriving at the same triangulation for a given data set guarantees reproducible results for different images of a site processed at different times and possibly at different installations.

Once an initial triangulation has been constructed, a secondary set of GCPs is computed by estimating a new point for each of the original triangles. This point is located within a given triangle by finding the intersection formed by two lines which bisect any two triangle edges and their opposite angles. The estimated image and map locations for this point are computed straightforwardly by linear interpolation. After each initial triangle has been processed there is a set of estimated GCPs, which are used to augment the measured set. By pooling the points and recalculating the triangulation it is possible to repeat the process. This is done iteratively until every triangle on the image is less than some pre-specified area. Once a given triangle is less than this area, it is removed from consideration as a source of new GCP estimates (Settle and Drake, 1987).

When the triangle area constraint has been met for the entire image, the process outputs a set of Delaunay triangles for both map and image space which match geometrically but which differ in shape to a degree dependent on the level and distribution of distortion in the image relative to the distribution of GCPs. These triangles are then used as a basis for computing the input image locations of the pixels to be found for the geometrically corrected output image.

Finally, it is now possible using the pairs of image/map space Delaunay triangles, to reconstruct a geometrically more correct output image. The following description assumes that the dimensions of the map output image domain have been defined and that the output pixel size has been selected.

2.6.4 LEVEL FLIGHT AND PLATFORM STABILISATION

The last two geo-correction approaches, level flight and platform stabilisation provide only partial solutions. Neither can guarantee that platform motion effects will be totally removed, and they cannot take into account scanning geometry and surface relief effects. Platform stabilisation approaches attempt to remove platform motion effects and are usually achieved by mounting the sensor upon a stabilisation rig fixed only on a small aircraft undercarriage (Kindelan *et al.,* 1981; Dowman *et al.,* 1984). Simple stabilisation systems are passive and damp attitude perturbations using springs and shock absorbers, whereas more advanced systems incorporate active components which measure changes in the sensor attitude using inertial gyro systems and then compensate them by changing the attitude of the rig via servo motors (Crabtree and Bown, 1989). Stabilisation systems are limited because they cannot take into account changes in the sensor position, and because they cannot guarantee stabilisation of very rapid attitude perturbations. For this reasons, the level flight and platform stabilisation approaches are not discussed any further.

2.7 CLASSIFICATION

2.7.1 INTRODUCTION

Remotely sensed imagery interpretation, or more generally the term 'classification', is an important process, which translates the raw image data into more meaningful and understandable information. Normally, the classification process can be categorized into two broad categories known as supervised and unsupervised classification, respectively (Mather, 1999 and 2004). Multi-spectral classification is the process of sorting pixels into a finite number of individual classes, or categories of data, based on their digital numbers (Blonda *et al.*, 1996). If a pixel satisfies a certain set of criteria, the pixel is assigned to the class that corresponds to those criteria. This process is also referred to as image segmentation. Depending on the type of information the analyst wants to extract from the original data, classes may be associated with known features on the ground or may simply represent areas that look different to the computer. An example of a classified image is a land cover map, showing vegetation, bare land, pasture, urban, etc.

Classification pattern recognition is the science and art of finding meaningful patter ns in data, which can be extracted through classification (Tso and Mather, 2001). By spatially and spectrally enhancing an image, pattern recognition can be performed with the human eye; the human brain automatically sorts certain textures and colours into categories.

2.7.2 SUPERVISED CLASSIFICATION

The first task for most applications of remote sensing is classification of pixels or regions in the scene into information classes that are meaningful for the task at hand. Unlike the spectral classes obtained by cluster analysis, useful information classes can generally be determined only with the use of a training set, so supervised classification methods are used. Statistical algorithms include methods based on maximum likelihood or nearest-neighbour decision rules and classification trees. Maximum likelihood methods may require the estimation of separate covariance matrices for each class or may use a pooled covariance matrix (Yu *et al.*, 1999).

Rules of thumb indicate the number of training samples per class should be 10 to 100 times the number of discriminating variables; otherwise the overall performance of a classifier can actually degrade. This is referred to as the "Hughes phenomenon", after Hughes, 1968. Jeon and Landgrebe (1999) have experimented with several methods for alleviating this problem, including manual identification of training samples from spectral information alone (Hoffbeck and Landgrebe, 1996). Other problems with training sets for remote sensing data include the difficulty of finding unmixed pixels and of ensuring that all of the classes of interest are represented and the addition of unlabeled samples using an Endmember (EM) algorithm (Tajudin and Landgrebe, 2000). On the other hand, Jeon and Landgrebe (1999) were able to obtain satisfactory results for the case where training samples were available for only the class of interest.

2.7.3 UNSUPERVISED CLASSIFICATION

Unsupervised classification mechanism automatically clusters the image data into several groups according to some predefined criterion or cost function (for example, clustering data based on minimum distance). Those groups are then mapped into classes. Unsupervised methods are more attractive in the sense that they do not require as much intervention. As the data volume collected by a variety of air-borne and space sensors increases dramatically, unsupervised classification can bring considerable benefit in enhancing imagery processing speed to the extent that a stable and high classification accuracy is achieved. Unfortunately, traditional unsupervised classification methodology, such as k-means clustering using imagery spectral data alone, does not generally produce high classification accuracy (Tso and Mather, 2001). This is due to the fact that, in common and traditional clustering mechanisms; each pixel in an image is treated as spatially independent. This, in turn, makes the output image after clustering unlikely to form a patch-like and easily interpretable pattern. In order to achieve better classification outcomes, the validity of such an inter-pixel independency assumption should be concerned. More robust ways of modelling pixel interactions are needed.

3 DATA SOURCES AND METHODOLOGIES

3.1 INTRODUCTION

This chapter will discuss and investigate the reliability of airborne remote sensing, with a series of flights from the Natural Environmental Research Council (NERC) airborne remote sensing facility were used. This chapter presents the details of the scanners used, the area flown and pre-processing necessary for preparing the data further analysis.

3.2 STUDY AREA AND FLIGHT DETAILS

The study will investigate ATM and CASI data provided by the Natural Environmental Research Council (Wilson, 1994). The study area (Figure 3-1) is in the West Midlands near Lichfield and Brownhills, England. There are seven flight paths for both the day and night time flights, each of which was flown on 25th and 26th of March 2002 respectively, within a period of less than forty minutes. The site lies between Longitude 1.79^{0} to 1.87^{0} West and between Latitude 52.6^{0} to 52.69^{0} North. The flight condition was some haze and high layer of thin cloud with reasonable visibility. The area is relatively flat throughout, there is one main urban area in the centre of the scene, the village of Shenstone, and otherwise the land cover is mainly rural farmland. A motor-way is being constructed across the north of the imagery.

©Copyright 2005 OS map

Figure 3-1: Study Area.

3.3 TRACK OF FLIGHT LINES

The sensors incorporate a GPS and inertial navigation system to record precise scene centres and roll, pitch, and yaw information during flight. This accurately assigns coordinates to each pixel in an image during processing. Figures 3-2 and 3-3 illustrate the track of the aircraft for the day and night time flights respectively. The aircraft starts to fly from North to South and then back from South to North, thus half of the flights are North to South and the rest South to North.

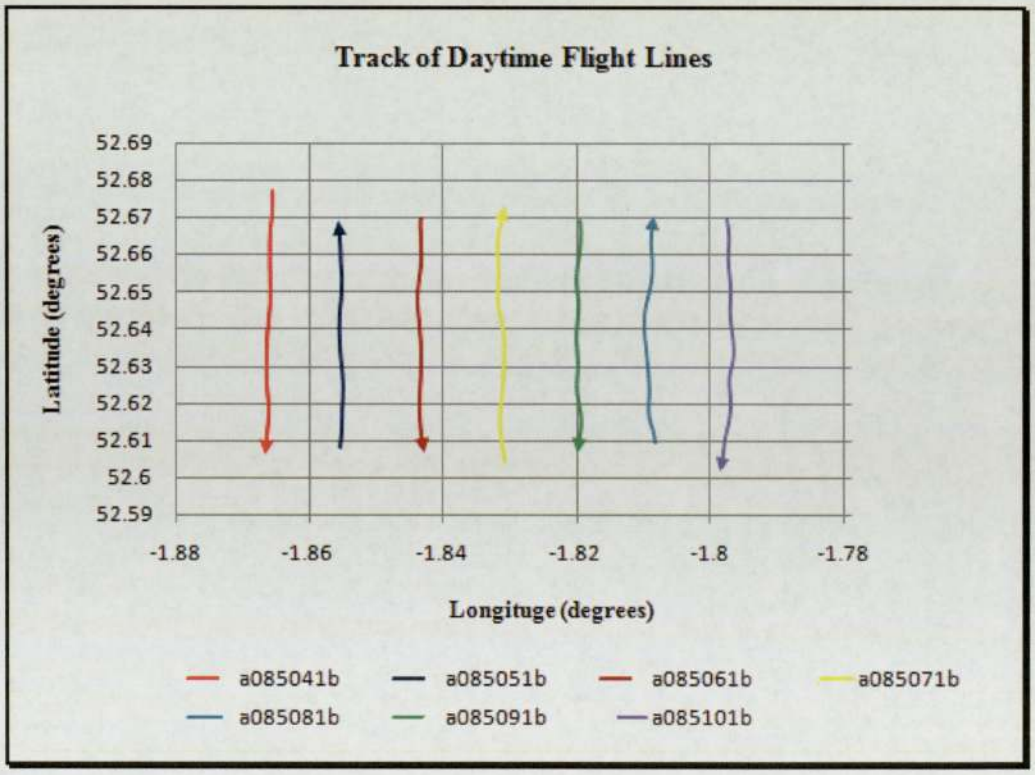

Figure 3-2: Track of daytime flight lines.

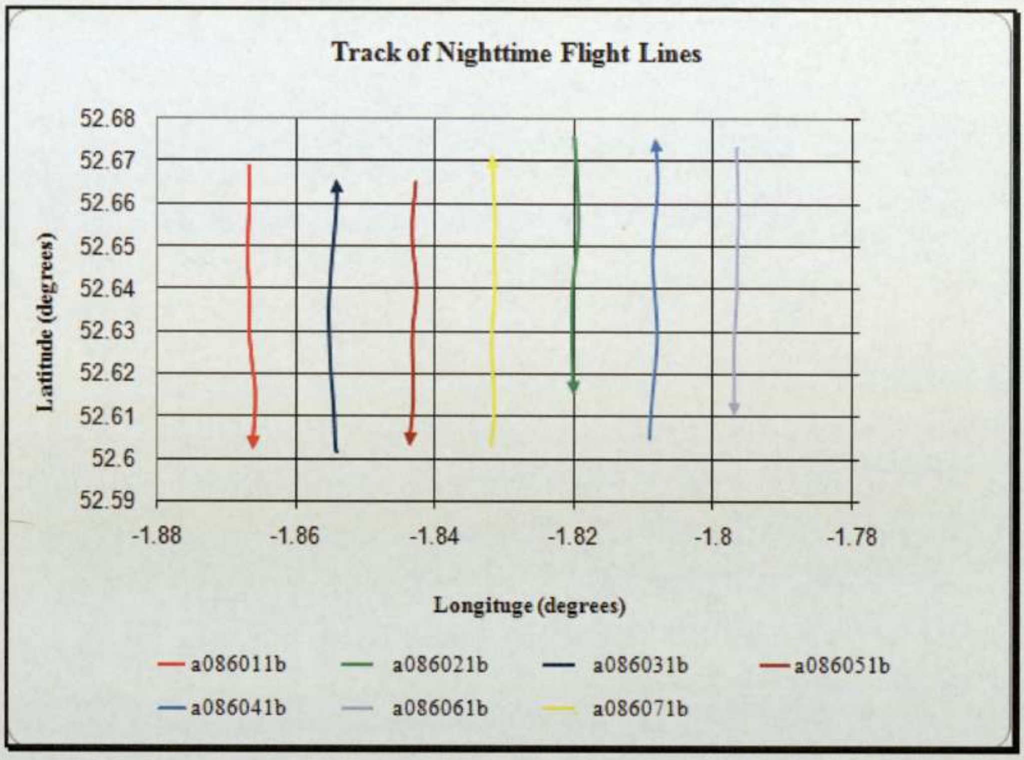

Figure 3-3: Track of night time flight lines.

3.4 DATA HISTORY

The raw data sets used in the study were provided by Natural Environment Research Council (NERC) in HDF format. The daytime data were flown at 15:00 on 25th March 2002, while the night time data were flown at 03:00 on the next day. The ATM contains 11 bands while the CASI has 15 bands as shown in Table 3-1 and Table 3-2 respectively.

In this research the multi-spectral scanner, Airborne Thematic Mapper (ATM-Daedalus-1268) used had a bandwidth range from 420-13000 nm. The ATM scanner has a view angle of 90.0° and 938 pixels, while the CASI-2 scanner has a FOV of 53.2° and 512 pixels. (see Appendix 1 for the layout of optics and detectors in the Daedalus AADS1268).

The aircraft is arranged with a core instrument suite comprising RC-10 Metric Camera, Daedalus-126 Airborne Thematic Mapper (ATM) plus Azimuth System AZ16, and Compact Airborne Spectrographic Imager (CASI-2). The instruments are carefully assembled on the plane according to their most favourable positions. The spectral bandwidth encompassed by the instruments is from 400 up to 13000 nanometres (nm) (Wilson, 1994).

ATM Bands	Spectral Range (nm)	Spectral Response	Equivalent Landsat TM Bands
1	420-450	Blue	
2	450-520	Blue	1
3	520-600	Green	2
4	605-625	Red	
5	630-690	Red	3
6	695-750	Near IR	
7	760-900	Near IR	4
8	910-1050	Near IR	
9	1550-1850	Middle IR	5
10	2080-2350	Middle IR	7
11	8500-13000	Thermal IR	6

Table 3-1: ATM's spectral range approximation, ground resolution, comparison to the Landsat Thematic Mapper instrument, and its spectral response.

The performance of the aircraft is extremely important when using it for remote sensing. The platform must remain as level as possible and maintain the velocity during the process of acquiring the data. If the aircraft pitches, rolls and yaws, then the image will be distorted. The aircraft vibration noise needs to be kept to a minimum level in order to minimise the disturbance of the image.

The sensors or instruments used in the study are:

i. The Multi-Spectral scanner which the Airborne Thematic Mapper (ATM-Daedalus-1268) uses has a bandwidth range from 420-13000 nm, see Table 3-1

ii. The Compact Airborne Spectrographic Imager (CASI-2) uses a bandwidth with a range of 405-945 nm, see Table 3-2, and

iii. Wild RC-10 analogue Camera is used in the visible spectrum.

CASI Bands	Spectral Range (nm)	CASI Bands	Spectral Range (nm)
1	450-490	**9**	740-750
2	490-552	**10**	750-762
3	552-607	**11**	762-780
4	607-651	**12**	780-820
5	651-669	**13**	820-865
6	669-700	**14**	865-940
7	700-710	**15**	940-945
8	710-740		

Table 3-2: Spectral channels of Compact Airborne Spectrographic Imager (CASI).

3.5 THE AIRBORNE THEMATIC MAPPER

3.5.1 SPECIFICATIONS OF ATM

The Daedalus 1268 (Airborne Thematic Mapper-ATM) is a passive remote sensor designed to collect radiation from the Earth's surface from an airborne platform. It separates the incoming radiation into 11 spectral bands ranging from the visible blue to the thermal infrared.

The scan head optics and detector layout provide 11 spectral channels (see Table 3-1). These cover the visible and near infrared (Channel: 1-8), short wave infrared (SWIR) (Channel: 9 & 10) and thermal infrared (TIR) (Channel: 11). ATM channels that closely match the seven spectral channels of the Landsat Thematic Mapper are shown on Table 3-1.

Radiation, captured by the rotating scan mirror is split by dichroic filters into a number of light paths, which are imaged onto detectors. A prism splits visible and near-infrared radiation before being imaged onto an array of silicon detectors (Channel 1-8). Middle- (Short-wave), and thermal-infrared radiation is split, imaged and recorded on single detector elements held within three individual, liquid nitrogen (LN2) cooled dewars (Channel 9,10 and 11).

The scan mirror has three synchronised speeds (12.5, 25, and 50 Hz) to optimise the scan-rate to more closely match data acquisition and coverage over the ground at various altitudes, thus avoiding any under-sampling or over-sampling of the data in the along-track (flight-line) direction. An approximately 10% overlap of successive scans is normally used to avoid missing areas on the ground caused by changes in aircraft velocity or attitude. Actual pixel size (ground spatial resolution) will be dependent on the flying altitude of the aircraft since the ATM sensor has a fixed

Instantaneous Field of View (IFOV) of 2.5 mrad.

3.5.2 INTEGRATED DATA SYSTEM (IDS)

Since 1996, the NERC ARSF has flown an upgraded version of the Daedalus 1268 ATM. This system - the Azimuth Systems AZ-16 - is an integral component of the Integrated Data System (IDS), which was developed for the ARSF to enable geometric registration of the multispecteral ATM data and hyperspectral CASI data by eliminating, during post-processing of the acquired data, the effects of changes in aircraft attitude during flight. The AZ-16 also has increased sensitivity with the upgrade from 8-bit to 16-bit resolution (256 DN to 65536 DN levels).

The data generated by the ATM may require pre-processing to account for atmospheric effects and problems that arise from the instability of the platform (Richards, 1986). An important step when analysing geospatial data is in the integration of the data into geographical information systems, which require accurate geometric rectification of the imagery. This is also a major requirement of multi-temporal data. Unfortunately, achieving this with ATM imagery is extremely difficult. Whereas satellite data can be effectively rectified using polynomial equations, aircraft motion causes disturbances of too great a magnitude to be compensated for even by high-order polynomials.

The fully automated Integrated Data System was finally commissioned in late 1998 or early 1999 and can now routinely provide geometrically registered, radiometrically calibrated data for both the multi-spectral ATM and the hyper-spectral CASI systems as operated by the NERC Airborne Remote Sensing Facility (now re-designated the Airborne Research and Survey Facility-ARSF).

The AZ-16 (ATM) is the result of a significant upgrade and enhancement of the original Daedalus sensor, carried out within the Integrated Data System development program, providing new data acquisition and recording capabilities. The IDS has been developed to integrate the imagery provided by the scanners with the navigation and attitude data to provide fully geo-referenced digital data without the use of ground control point. Comparative Specifications of the Airborne Thematic Mapper - in its Daedalus 1268 and AZ-16 configurations is provided in Table 3-4.

Specification	Daedalus 1268	AZ-16
Operational Period	1982-1995	1996-present
IFOV	2.5 mrad	2.5 mrad
Pixel Swath	716	938
Total Digitized FOV	85.92^0	90^0
Scan Rate	12.5,25,50 Hz	12.5,25,50 Hz
Resolution	8-bit (0-255)	16-bit (0-65535)
Data Visualisation	Oscilloscope of digitized signal	Waterfall image of selected band(s) on colour monitor
Data Recording	1" HDDT tape drive	9 GB removable HD
Black Bodies	1 digitised pixel	16 digitised pixels

Table 3-3: The specifications of the Daedalus 1268 and AZ-16 of the Airborne Thematic Mapper (by NERC, accessed on December 2004).

During its development the IDS underwent a series of upgrades in its components. The ATM original mechanical gyro was disconnected and replaced by the Litef LCR-92 Attitude and Heading Reference System (AHRF). This fibre-optic gyros system provides 64 Hz attitude information on pitch/roll angles and magnetic heading. In 2000 the Ashtech 3DF GPS was upgraded to the Javad AT-4 20 Hz GPS attitude and position reference system, which synchronises the GPS information with scan line acquisition time from both the Daedalus 1268 scan-head and the CASI system.

The 11 spectral channels of the Daedalus 1268 are digitised, by the Azimuth Systems (AZ16) hardware, and together with an accurate measure of scan line acquisition time, are recorded on one the of 9 GB removal HDs. These are removable to enable easy transfer of data to CD at base, prior to data transcription by the ground processing system.

Time labelled information on GPS satellite ephemeris at 20Hz (0.05 second intervals) is also recorded in the data stream for later navigation processing and merging with ground-station GPS for differential correction of absolute position. Although the CASI is operated independently of the IDS the asynchronous image frame acquisition timing of the CASI is recorded, via a coaxial cable port on the CASI providing a timing pulse, and an RS-232 serial line providing a scan count parameter.

The IDS/ATM system also has an increased sensitivity with the upgrade from 8-bit to 16-bit resolution (256DN to 65536DN levels). This latter enhancement, in the number of digitised 'bits' of the A/D converter, eliminates the need for the operator to set up 'gain-settings' for each channel to maximise recorded sensitivity in any one channel for a particular target.

Unlike the first 10 channels, which are calibrated using a pre-, or post-mission laboratory test bench procedure, the thermal channel is calibrated by comparison in 'real-time' to two onboard black-bodies, which can be set to just above and just below the maximum and minimum temperatures expected in the scene (-15°C to +50°C) (see section 2-5 for the changes in radiant temperatures of different cover types during a 24-hour thermal cycle). The sensor images these during every scan, immediately before and after the scene pixels. The two blackbody temperatures and the sensor responses are recorded in the data stream for later radiometric calibration processing.

3.6 COMPACT AIRBORNE SPECTROGRAPHIC IMAGER (CASI)

3.6.1 SPECIFICATIONS OF CASI

The CASI is designed to provide a flexible spectrographic imaging system. The system is a "pushbroom" configuration, i.e. the full swath width is imaged instantaneously, in a large number of spectral wavebands. This can be used to construct "Hyperspectral" image datasets for detailed studies of the spectral characteristics.

Light reflected from the ground is received by the CASI optical system and focused on a diffraction grating. This has an effect analogous to a glass prism, splitting the light up into its component wavelengths. The light then falls onto a two dimensional array of Charge Coupled Devices (CCD's) which electronically measure the amount of radiation falling on them.

The array consists of rows of detectors, with each row containing 512 individual CCD units. The rows are positioned with respect to the diffraction grating such that each row sees a different wavelength of light. The 512 detectors in each row image a line on the ground, enabling a swath width 512 pixels across to be imaged on the ground (Wilson, 1997). As the aircraft moves over the ground, the CCD array is repeatedly read out, and a two dimensional image is slowly built up. The along-track spatial resolution of the image is governed by the speed of the aircraft and the frame rate at which the CCD array is read out. The flying altitude governs the across-track spatial resolution. Detailed specifications of the CASI sensor are given in Table 3-4.

Properties of CASI	**Detailed Specifications**
Field of View	59.9^0 across track
Aperture	f/2.8-f/11 (Automated iris control)
Spectral Rage	401-915nm
Spatial Sampling	512 spatial pixel
Spectral Sampling	288 at 1.8 nm intervals (3 nm FWHM @650 nm)
Dynamic Range	12 bit (4096 levels)

Table 3-4: The specification of the CASI Sensor (by NERC, accessed on December 2004).

3.6.2 DATA ACQUISITION MODES

One dimension of the 578x288 element array is used to obtain an image frame of 512 spatial pixels of the surface that builds up a flight line of data as the aircraft moves forward (see Figure 3-3). On the front of the CASI camera head is a custom fibre-optic lens with 54.4° FOV which has been designed to provide optimum focussing across the CASI wavelength range (achromatic focus). Light levels entering the spectrometer through the lens can be varied by the operator via an automated iris control (Settings 1 to 5) which is approximately equivalent to apertures of f11, f8, f5.6, f4, and f2.8. Setting 0 causes the iris to close completely for use in collecting in-flight dark-current readings, prior to and after a flight line. After passing through a 15mm wide spectrographic slit, a reflection grating disperses the light from each pixel over the 405 to 950nm spectral range and is recorded by the 288 detectors on the orthogonal dimension of the CCD. The row spacing on the CCD equates to a spectral sampling of 1.8 nm. However, the effective bandwidth of a single row has an approximate value of 2.2 nm FWHM (Full Width at Half its Maximum value) at 650 nm, resulting from the optical system and convolution of the slit width and detector size.

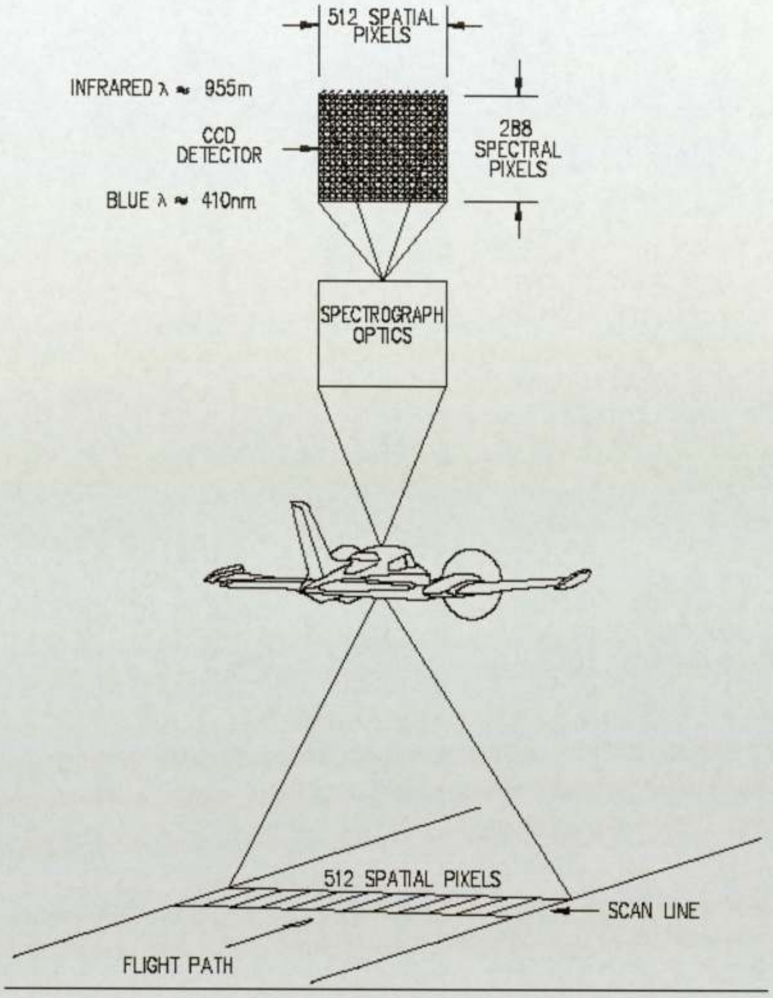

Figure 3-4: Imaging concept of the CASI-2 CCD Push-broom spectrograph (from NERC, accessed on December 2005).

A section of the array, masked off from imaging scene pixels, is used to record electronic noise, frame shift smear and scattered light contributions for use in post processing calibration. Additionally, a portion of this hidden section is used to image light, transmitted via a fibre optic bundle, from a down-welling Incident Light Sensor (ILS) mounted in the roof of the aircraft. Light from the ILS is dispersed, imaged onto the CCD, and recorded in spectral bands identical to those from the scene viewed by the CASI. The analogue signals from the complete CCD array are digitised by a 12-bit A/D converter providing 4096 digital levels and recorded on a removable 9Gbyte hard drive. Signal levels can be adjusted via control of both the auto-iris aperture and the integration time of the CCD, maximising use of the full 12-bit range without saturating the detectors. The sensor operator controls the CASI system via a keyboard and a monitor, that displays the instrument settings, signal levels, and a scrolling real-time window of the data as it is collected.

3.7 THE HIERARCHICAL DATA FORMAT

ATM data is provided in a HDF file; a file format for storing scientific data. The HDF file format was developed to provide a machine independent file format for scientific data, allowing data exchange between users without the need for any technical considerations such as byte swapping, compression or loss of precision. It provides a means of efficient storage and access to large datasets for types commonly used by scientists, and very importantly in terms of this project, it provides a means of storing large amounts of meta data: numerical or textual to accompany the data. The HDF file format is accomplished through a set of I/O libraries developed for many different computer platforms that provide a consistent means for writing and accessing scientific data stored in HDF files.

To accommodate the different types of scientific data, HDF provides several different data structures that can be created and customised by the user to store their data: *raster image, palette, scientific data set, annotation, vdata*, and *vgroup*. The two data structures that this project deals with are *vdata* and *scientific data set*. The vdata data structure is essentially a table; the user can construct a vdata item with as many fields as they need to model each data item in the chosen class, and then add as many records as needs be to the table. This vdata data structure is the common method for storing numerical data, a single value may be stored in a 1-row x 1-column vdata.

The scientific dataset data (SDS) structure allows storage of multidimensional numerical data (NCSA, 2004). There are several required components to a SDS that must be defined when the SDS is created; an *SDS array*, a *name*, a *data type*, and the *dimensions*. It is the SDS array in which the data is stored, in the case of the ATM data, a three dimensional array is used where the first two dimensions represent the rows and columns of the flight, and the third dimension represents the band. Attributes associated with the SDS may also be defined, providing a means of assigning metadata that is directly linked and stored alongside the data that it is describing.

A HDF file is created via a set of software libraries provided by the National Centre for Supercomputing Applications (NCSA). In computer science, software libraries of this kind are referred to as Abstract Programming Interfaces (API); a group of programmed routines defined and made available for use by programmers to integrate into their own software (NCSA, 2004). For each type of HDF data structure, a different set of routines (or API) is provided to construct and add data to a data structure of that type to a given HDF file. A HDF file is completely self-describing; it contains within it all information needed to access the various data structures that have been created. The supplied APIs can access any given HDF file and extract data based on the information stored within it (NCSA, 2004).

3.7.1 THE AZIMUTH HDF'S

The HDF files that store the ATM data are created by the processing software developed by Azimuth Systems. This project involved working with the mainly level 1 and 3 HDF files. Although similar in structure to the level 1b HDF files, the level 3 files contain the geo-corrected ATM data along with geo-referencing information (refer to appendix 3-B, section 1 for the definition of levels). The scanned ATM data is stored in a scientific data set (SDS), with the *SDS array* having 3 dimensions as discussed in section 3-7, and the *data type* is of type 'unsigned 16 bit' (one of the modifications performed by NERC ARSF was to increase the Digital Number resolution from 8 bit to 16 bit for the Daedalus scanner). A vast amount of metadata and data concerning the flight and the processing is stored in the HDF file, using the *vdata* data structures. Among the ATM metadata, are the coordinates of the corners of the ATM data in the British National Grid projection and the normal pixel size.

3.7.2 HDF'S IN MATLAB

The HDF APIs have been made available for the Matlab language, allowing the manipulation of HDF files through the use of predefined functions that interact with the files. These provide the Matlab programmer with a sufficient degree of abstraction, although knowledge of the conceptual format of the data structures as described above is still needed by the programmer to read and write data to a file. The APIs available for Matlab map directly to those defined for the C programming language. These are described in detail on the NCSA HDF website (NCSA, 2004). The access routines in the APIs have a specific sequence in which they need to be called; each routine retrieves information from the HDF file that needs to be supplied as input to others (also described in detail on the NCSA HDF website). The consequence of using this method of file access and creation allows great flexibility for the user to design and implement data structures to model and store almost any data they wish, and also a reliable way to retrieve data. However, the disadvantage is that it can take considerable effort to retrieve only a few simple data items; indeed looking at code to retrieve a single vdata item using this method appears to be very long winded.

Fortunately, Matlab provides a graphical user interface tool that allows one to browse through the data structures stored within a chosen HDF file and extract them into the Matlab environment. This proves very useful for quickly browsing through the HDF file to determine the data one wants to retrieve. The Azimuth Systems HDF files all have the same format, so once customised code is written to access certain data from one of these HDF files, it can be used to access data from any HDF file with this format.

3.8 OVERVIEW OF AZGCORR SOFTWARE

AZGCORR combines scanner image data and post processed navigation data recorded or interpolated at each scan, and interpolates a map projection referenced rectilinear output image corrected for aircraft position, attitude and ground surface separation computed from aircraft spheroid height, digital elevation data and geoid-spheroid separation estimates. Inputs to AZGCORR are run time parameters from the command line, Level 1B HDF, Level 2 HDF or a combined Level 1B HDF and related BIL (band interleaved by line)/BSQ (band sequential) image file. Outputs are a brief run listing and a Level 3A (default with or without DEM) or 3B HDF (with use of field GPS observation of GCPs) file. Navigation and image data input to AZGCORR must have been processed using the correct programs in the Azimuth Systems package to ensure that all data items are present and as expected (Azimuth, 2005). The one exception is Level 2 data, the basis of which is image data extracted from a Level 1B file with AZEXHDF; messaged by a user program and input to AZGCORR still in BIL or BSEQ format along with its originating Level 1B HDF file. AZGCORR does all image processing in rectilinear coordinates; therefore the first step is to convert the navigation from geographic coordinates on GPS satellite datum to a suitable survey map projection. It is important to note that all appropriate data items (DEM, etc) must be on the same datum and projection. A summary of command line options and parameters can be obtained by running AZGCORR -help with no parameters.

3.8.1 CONCEPTS AND GOALS OF CORRECTION

Stated simply the purpose of the program is to produce an output image which overlays an existing map. The rotating mirror (ATM) or push-broom (CASI) scans have positions calculated for every pixel and then the image is interpolated to a rectilinear grid, which may be projected to a plane relative to the aircraft or related to existing topographic data. It is important to note that this ground referencing is only achieved by using observed scanner (aircraft) position and attitude and referencing scan positioning to elevation (DEMs) information. Ground control points are only used for 'calibrating' DEMs and geoid-spheroid separation data.

3.8.2 NAVIGATION-RELATION TO DATUM AND SPHEROIDS

All navigation on the Earth's surface is referenced to a set of axes and a model which describes the static and dynamic geometry of the Earth and navigation platform; this is a geodetic datum. For the sake of this discussion we can ignore all parameters except Earth geometry and time. For the sake of brevity a datum is given a name or even a mnemonic; throughout the world there are several hundred different data. The current GPS datum is called WGS84 (World Geodetic System agreed in 1984). However, the Airy 1834 datum is used for the Great Britain (GB) national grid, and all heights for a locality are then relative to this reference point.

In the UK the datum point is at Newlyn, Cornwall and the height zero is related to mean sea-level at that point. A locality height (topographic) map in grid form is also known as a digital elevation model. It is important to note that before the days of GPS, heights and positions on maps were obtained separately. Heights were obtained by bubble or optical levelling and thus relate to the local gravity normal. Positions were obtained by angular triangulation or optical or microwave trilateration. Both sets of observations have varying errors which are minimised (not removed) by network adjustment. A network of observed points, both position and height can then be 'filled-in' on the ground with more levelling or other techniques, or used to scale a series of stereographic aerial photographs from which height and position details can be measured using a stereogrammetric plotter.

In general, height is an order of magnitude less accurate than position. On the other hand, GPS surveying observes both position and height simultaneously; in fact the observation is the 3D axis position of the observation site relative to the centre of the satellite orbit (Earth centre). With appropriate equipment and techniques it is possible to make this 3D observation to an accuracy of a few millimetres. More importantly each GPS survey is essentially independent from other observations, errors being related mainly to satellite constellation geometry and atmospheric conditions. This allows static site and vehicle positions to be independently observed whilst retaining a very high degree of relative accuracy. As can be expected there is a problem relating positions obtained from GPS observations and those from traditional geodetic surveying. For purely economic reasons the correct solution for a whole country will never be performed, i.e. re-observe all original ground points by GPS and recompile all maps.

3.8.3 MAP PROJECTIONS

The procedure for the UK outlined above does a one-step conversion from WGS lat/long/height to UK National Grid map projection coordinates. The more usual method of transformation does this in two steps allowing more flexibility. First the GPS position (latitude, longitude and spheroid height) on satellite datum (WGS84) is transformed to a local datum (lat, long, height). Then the geographic (spheroidal) coordinates are transformed to a suitable rectilinear coordinate set using a map projection (Azimuth, 2005). Representing points on a spheroid by points on a flat surface is at best, a compromise.

3.8.4 DIGITAL ELEVATION DATA

From the above discussions on datum and map projections it should be clear that elevation data is a measure of heights above some datum on a given spheroid, and without transformation or other messaging can only be used in the context of this spheroid. If the data is also positioned in map projection grid coordinates it is even more closely linked. Consequently, care must be taken that selected datum shifts, map projection and DEM data are all self-consistent.

Elevation data may be input to the program as AZGCORR internal format grids, NTF contour or grid files or a flat file. NTF files must comply with the appropriate OS format description for layout and content. AZGCORR saves or creates a grid from these files, to cover the image area requiring correction. Previously gridded data may not be altered in grid spacing. NTF contour files are converted internally using a user requested grid interval to form the required grid. The requested grid interval must be chosen to be equal to or greater than the output pixel spacing. If too small an interval is used the program run time will increase considerably, and the processor may run out of memory and thus no improvement in image correction will be achieved; two times the pixel spacing is more than adequate. In the case where the DEM does not completely cover the image grid, the missing parts are filled with default or user supplied fill values before the geoid-spheroid correction is made. In the case of completely offshore sites where geoid-spheroid correction is required, the program will create a zero filled grid and apply the correction; ignore the 'no data' message (Azimuth, 2005).

3.8.5 IMAGE INTERPOLATION

Once the coefficients for the mapping polynomial have been determined, the final stage of the correction procedure is to estimate the digital numbers (DNs) associated with each location in the corrected image space. The assignment of DNs to the pixel co-ordinates in the output image is known as Resampling, and is carried out through two approaches; direct (forward) and indirect (reverse) interpolation. With the direct interpolation, the DNs to be registered in the input image are transferred on a pixel-by-pixel basis to the output data set, so that the new position of every input pixel is calculated. However, using this technique it is possible that a number of output pixel locations will not be addressed at all, leaving gaps which later need to be filled through interpolation (Mather, 1999). The indirect resampling method generates the output image on a pixel-by-pixel basis by determining which input pixel maps the closest to the output pixel or interpolations between neighbouring pixels. This method is the preferred method of resampling; since every output pixel is referenced ensuring gaps do not occur. However, since pixel centres in the raw imagery will rarely project to exact pixel centres in the corrected image, interpolation is required to estimate a representative DN for placement in the new grid. Interpolation is carried out using one of three main techniques; nearest neighbour resampling, bilinear interpolation, and cubic convolution.

Nearest neighbour resampling is the simplest and quickest method for estimating DNs, since the pixel centres in the corrected grid take the actual value of the nearest projected pixel from the raw image. This is the most commonly used method of resampling since the final corrected image consist of the original DNs, simply rearranged into the correct image geometry. However, nearest neighbour resampling is criticised for the 'blocky' appearance of the output image. Bilinear interpolation and cubic convolution draw DNs from the surrounding four or sixteen pixels respectively (Wilson, 1994).

Images taken with a Charge-Coupled Device (CCD) are the electron distribution over the chip, generated by incoming radiation. Electrons generated in a pixel area are not necessarily collected by the same pixel, but can diffuse into neighboring pixels because the electric field that collects the charge does not penetrate the entire chip (Ralf *et al.,* 2003). In these field-free regions, charge can diffuse randomly. Knowing the size of the field-free region helps to improve manufacturing and determine the modulation transfer function for a chip. In 2002, Ralf *et al.* developed a technique for probing the diffusion of charge and to investigate the size of the field-free region. First, a source to obtain a light spot of less than one micrometer in diameter was created. The idea was to take a glass fiber tip, similar to a Scanning Near Field Microscope (SNOM), which permits an easy change of wavelength. Different etch processes with hydrofluoric acid were used on a glass fiber to form a tip. After coating the tip with metal, a focused ion beam was used to cut the end giving an aperture size of less than one micron. Different wavelengths, absorbed at different distances within the CCD, generate carriers at different distances from the pixel depletion region. The ability of carriers to diffuse will be less for wavelengths penetrating deeper, and thus a variety of wavelengths can be used to independently determine the field-free region. The response of a pixel was measured, depending on the location of the tip over the pixel.

Point Spread function (PSF): There are two principal effects that broaden the PSF in thick sensors, the charge diffusion and the divergent optical beam in silicon. At short wavelengths the photons are absorbed near the entrance window creating electron-hole pairs. These electrons or holes (depending on the doping polarity configuration of the sensor) drift under the influence of the electric field across the full thickness of the sensor to the buried channel in a CCD or to the pixel junction in a hybrid PIN-CMOS sensor, and the PSF is determined by their thermal diffusion (Tonry *et al.,* 2005). At long wavelengths photons may be absorbed at any depth in the sensor, and their initial spreading is determined by the divergence of the optical beam. The resulting electrons or holes diffuse less than those from short wavelength photons depending on the distance from the point of conversion to the charge collecting region. The PSF is then a convolution of these two effects. The divergence of the optical beam is given by the basic optical design of the telescope. Fortunately, the divergence is reduced by the high index of refraction of silicon (Holland *et al.,* 2003).

3.8.6 RUNNING THE AZGCORR PROGRAM

The data provided by NERC were not geo-corrected, but were provided with the post-processed navigation data to enable the imagery to be geo-rectified later. They also supplied the AZGCORR software to geo-correct the data. The DEM (Digital elevation model) used in this study was downloaded from Edina Digimap (Edina, 2005). The Ordnance Survey has used the dataset to derive mathematically a Digital elevation model from 1:10000 contour data. Contours were at 5 metre vertical intervals and 10 metre vertical intervals in some mountain and moor land areas. The model also used spot heights, and high and low water marks were available. The ATM level 1 data including attitude and position from the flight path was used to create a map projection referenced output image to HDF level 3 (refer chapter five for details).

With the amount of data and calculation required, correction of all bands for even a moderate sized site can take several hours. Roughly, the correction program took between one hour to hour and half to geo-correct a flight. The program allocates dynamically many large buffers depending on the direction of the data and the output pixel size. Memory is inversely related to the pixel size. The program will halt with an error message if too little memory is available. The program gives the total size of buffers allocated in the summary listing. The command used to geo-correct the raw data is:

```
azgcorr -1 /ATM/a085061b.hdf –3 level3/a085063b.hdf –d95 –mUKNG –br 1
11 –ism –eh dem.ascii.txt -p 0.8 0.8 > result63 &
```

The parameters used are:

-1 this is input file (provided by NERC by compact disc).

-3 the output file, the file name should end in 3B.

-d95 this uses the BNG data to get an accuracy of a few metres.

-mUKNG outputs the data to the UK national grid.

-p this is the pixel size (m); in this case 0.8 m is chosen because it yields a good compromise between good resolution file size and processing time yet accurately reflects the original image resolution. It is a simple matter to resample the image to lager pixel sizes if required.

-br which band to extract (day time flights extract band 1 to 11 and night time only extract band 11)

-il uses bilinear interpolation.

-eh uses the dtm data to obtain higher accuracy.

-v this uses verbose listing to give details of what is happening.

3.9 NON-PARAMETRIC MODELS

Non-parametric geometric correction methods can correct all types of image distortion and do not require information concerning the sensor, the sensing conditions, or the surface relief (Negahdaripour, 1998). For these reasons non-parametric methods are very commonly used, and will always be useful because they can correct archived imagery when only a map of the scene is available. The geometric description in non-parametric correction methods is inferred from the spatial relationship between corresponding features identified upon the sensed image and a map of the scene (Perplant and McKeown, 1990). Conventionally these features are clearly distinguishable point-like features termed ground control points (GCPs) and only their planimetric coordinates are used. The map GCPs should be selected from an accurate cartographic map of similar scale as the image, as the map compilation accuracy will limit the accuracy of the map GCP coordinates and hence limit the accuracy of the geometric description (Yao, 2001). Alternatively, rather than use a map product, the image can be non-parametrically corrected to another remotely sensed image which acts as the `map' (although it may not necessarily be geometrically correct). This process is termed image registration and in some cases, when the images are reasonably similar, it is possible to match the GCPs from both images automatically (Ton and Jain, 1989).

The first stage of the procedure is to define a mathematical relationship between the raw image data and map co-ordinate system pertinent to the region. The coefficients for the mapping polynomials are calculated from GCPs selected in the imagery. GCPs are well-defined and spatially small features, which can be located both within the image and on the corresponding map of the study area. Typically GCPs might include road intersection, corners of buildings, or airport runways (Jia, 2003).

By comparing the measured map co-ordinates with the pixel address for each GCP, the coefficients of the mapping functions can be determined using the least-square regression approach. The order of mapping function directly influences the number of GCPs required. First order polynomials require at least three GCPs, second order transformations require at least six GCPs, and third order functions need at least ten. It is however, better to have many more than this and estimate the parameter using a least square approach. Mather (1999) suggested GCPs should be evenly distributed to limit the extrapolation errors at the extremes of the image when employing high order polynomials.

Once the GCPs have been selected, the accuracy of the resulting transformation can be estimated by calculating the root-mean-square-error (RMSE) of the residuals between the actual and predicted position for each GCP in the test. RMSE is calculated as:

$$RMSE = \sqrt{\frac{1}{n}\left(\sum_{i=1}^{n} \sigma_i^2\right)} \tag{3-1}$$

Where n is the number of GCPs, σ is the Planner distance between the estimated and actual position of each control point. The RMSE is a statistical measure of how accurate the polynomial transformation can fit GCPs to their true map co-ordinates, and is generally expressed in terms of metres or number of pixels. If the positional residuals at GCPs are small the RMSE will consequently be small, indicating a relatively accurate transformation. If the geometry of a raw imagery is severely distorted, positional residuals at GCPs are likely to be higher indicating a less accurate transformation.

Devereux *et al.,* (1990) geometrically corrected Daedalus ATM imagery by Delaunay triangulating map GCPs and then mapping each map triangle into its equivalent image triangle. This technique was shown to correct badly distorted images significantly more accurately than using polynomial mapping functions. Devereux attempted to reduce the effect of discontinuities in the mapping function along the triangle edges by refining the triangulation topology using synthetic GCPs placed at triangle centroids.

The 3D non-parametric models can be used when the parameters of the acquisition systems or a rigorous 3D parametric model are not available. Since these models do not require a priori information on any component of the total system (platform, sensor, Earth, map projection), they do not reflect the source of distortions described previously. Consequently, due to the lack of physical meaning, the interpretations of the parameters are difficult (Madani, 1999).

3.10 DATA MODIFICATION

3.10.1 INTRODUCTION

Since there are seven overlapping flights available from the airborne remote sensing compiling an analysis of the overlapping areas will give an insight into the magnitude and structure of geometric error. An overlap of flight 'a085061b' and 'a085071b' is shown in Figure 3-5. The study area covers an area from 408000E to 413825E and 302353N to 306747N on the British National Grid. The area is relatively flat throughout, there is one small urban area in the centre of the scene, the village of Shenstone, and otherwise the land cover is mainly rural farmland.

The plane's attitude will vary between the recording of each pixel; to record the attitude of the plane throughout the flight a fibre-optic gyros system is used to record the pitch, roll and heading changes of the aircraft. A GPS device is used to record the aircraft's position throughout the duration of the flight. To derive fully geo-referenced and corrected data, the raw data collected by the scanner and the attitude and positional information need to undergo significant post processing. This is implemented by several pieces of software developed by Azimuths Systems running on UNIX (Wilson, 1997), (see section 3.8).

3.10.2 PRELIMINARY INSPECTION OF THE DATASET

The dataset that will be used in this research was acquired in an area of the West Midlands near Lichfield and Brownhills, England. The aircraft flew nearly from north to south, and then from south to north, thereby providing a considerable coverage as well as 25% overlaps between the adjacent flight lines as shown in Figure 3-5 (see Chapter 5 for geocorrection and removed edges section 3.10.4). Despite the good overlap between the adjacent flights, an overlay of the north to south and south to north flight covering the same area showed a difference in the brightness level. The reason for this could be due to the flights being carried out at 15:00 hours in the afternoon, and hence the sun was heading towards the west at about 125°. The raw imagery used in this project was found to suffer from an inconsistent intensity variation across the flight path.

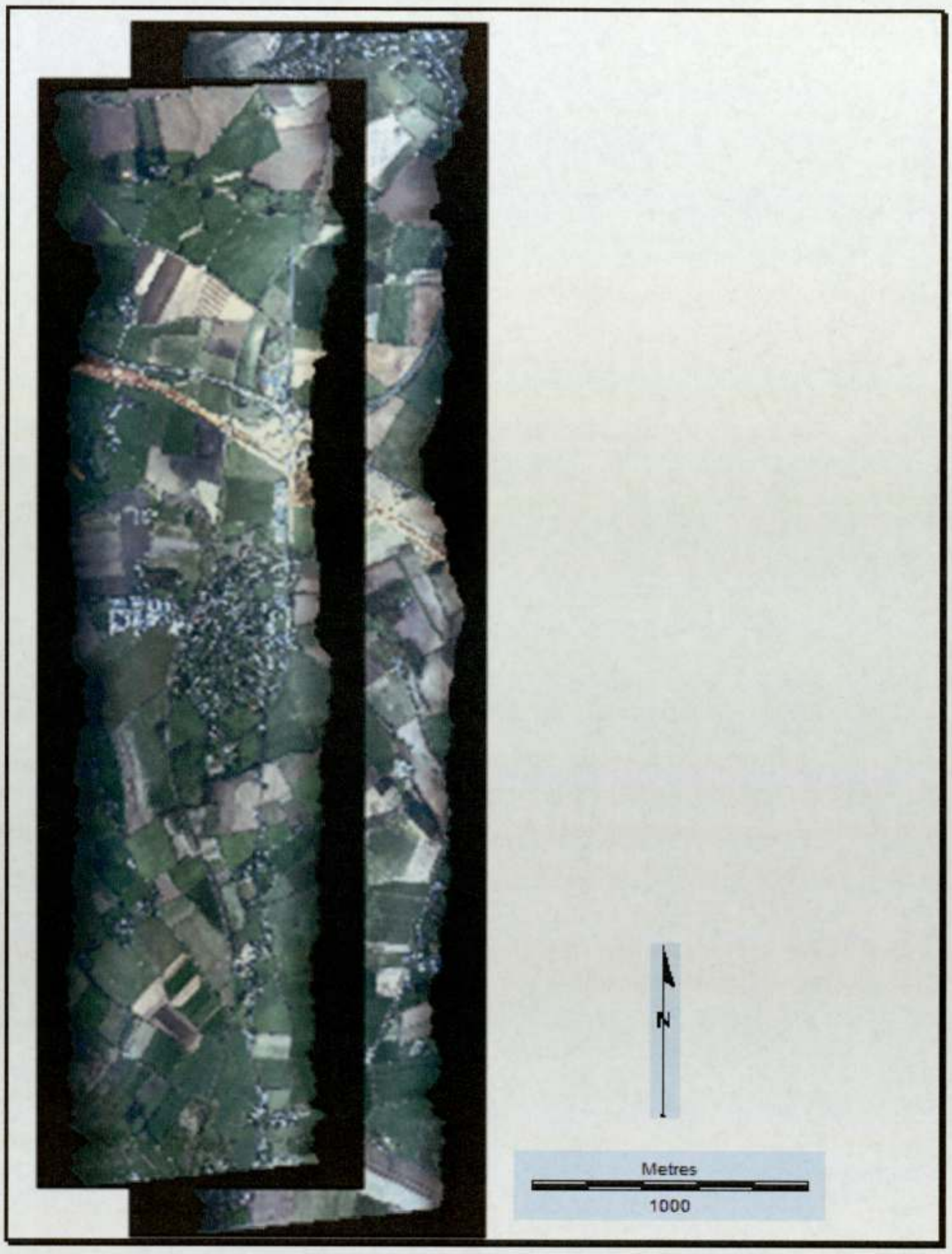

Figure 3-5: Flights a085061b and a085071b showing overlap between the adjacent flight lines.

The image brightness either increased towards one side or exhibited an increase or decrease down the centre of the image. This variation in pixel value across the image in known as the "scan angle effect", and is related to the wide scan angle of the ATM (Barnsley and Barr, 1993). Further documentation of the scan angle effect can be found in Danson (1986). This indicates that the amount of energy recorded by the sensor from the same land cover with adjacent flight line is different because of the position and direction of the aircraft. From section 3-5, the gain settings should be the same on each flight.

Despite the fact both flights were acquired not long after 15:00 hours, at some locations the spectral reflectance differs greatly between flights. It appears that flight a085061b was scanned when the sun was much brighter than it was at the time of acquisition for flight a085071b; an example of this is shown in Figures 3-6 and Figure 3-7. These figures show a group of houses in the south of the study area in both flights. The difference in spectral reflectance of the roofs of these houses as well as the surrounding fields is very apparent.

Figure 3-6: A brighter group of houses in flight a085061b, with no enhancement.

Figure 3-7: A darker group of houses in flight a085071b, with no enhancement.

The fact that different features on the ground have different reflectance properties means the same area taken from both flights in a given band might show up very differently; it is not the simple case of the reflectance in the 'brighter' image being a constant quantity greater than those in the other. Reflectance values will change by differing amounts depending on the surface and properties of the feature on the ground. This does not bode well for accuracy assessment methods that rely on pattern matching of reflectance values in data windows taken from the flights.

There are several characteristics of this data set that have been identified through simple visual analysis of colour composites of the flights that arouse suspicion in terms of its spatial accuracy. Towards the north of the scene, a massive spatial distortion occurs at the same location in adjacent flights (see Figures 3-8 and Figure 3-9). Linear features such as the roads and field boundaries indicate a massive shift in the datasets, after which point, the two flights match up very poorly in the overlapping region. The shift appears to have been much more severe in the a085061b flight than in the a085071b flight. This anomaly is a bit of a mystery; the fact that the shift appears at exactly the same point, possibly due to a change in height or ground elevation. This could be most likely an error in the DEM.

Figure 3-8: Unexplained 'jump' in flight a085061b.

Figure 3-9: Unexplained 'jump' in flight a085071b.

3.10.3 DIURNAL HEATING EFFECTS

It has been implied earlier in the section 2.2, that thermal images will vary considerably in appearance depending on whether they are acquired during the warm part of the day or after a night of absence of the sun and resultant cooling of the atmosphere, as well as heat loss from the surface and shallow depths beneath.

In the daytime thermal image, contrasts between heated buildings and streets, and areas in shadow create a scene that resembles an aerial photo, Figure 3-11. However, in the pre-dawn image (night time), the differences in temperature have decreased sharply (no shadows) although a part of that image is brighter, representing a local "heat island" effect (see Figure 3-10). In addition, in the pre-dawn image, many streets are evident because, being asphalt paved (being black bodies); they emit more radiation through the night.

Figure 3-10: Night time thermal imagery of Shenstone village.

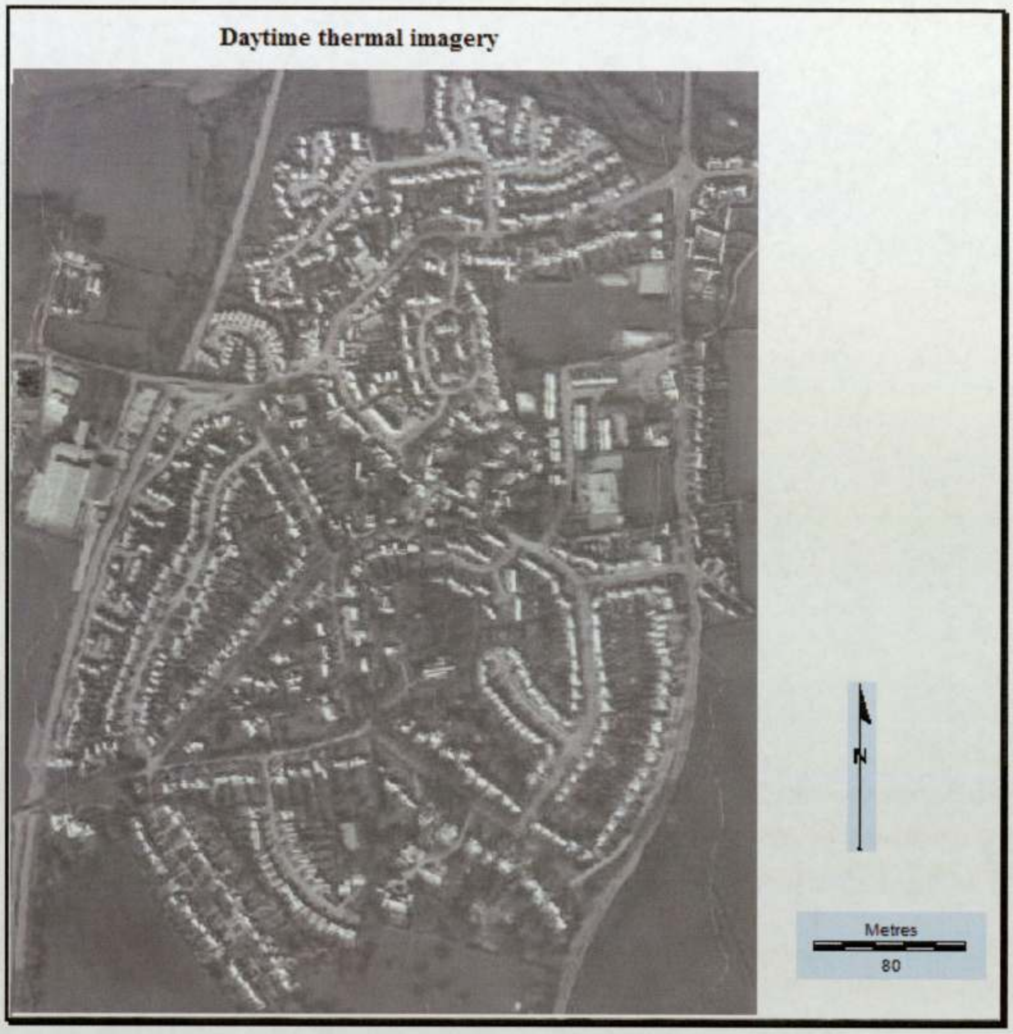

Figure 3-11: Daytime thermal imagery of Shenstone village.

3.10.4 EDGE TRIMMING OF THE DATA

The ATM is a whisk broom sensor; the data is collected by the means of an oscillating mirror, swinging perpendicular to the direction of flight. The plane's attitude will theoretically vary between the recordings of each pixel. To derive fully geo-referenced and corrected data, the raw data collected by the scanner and the attitude and positional information need to undergo significant post processing. Barnsley and Barr (1993) advised not to rely on the extreme edges of the scan line.

There was considerable overlap between the flights, necessitating changes to the DN values of both extreme edges of each flight line. Within the Matlab programming environment, the first and last 100 pixels were padded or altered to one from their original values without making any changes to the data as shown in Figure 3-12 (refer to Appendix 3 for details of Matlab program used). By so doing, it became possible to remove some odd values from the overlapping area and improve the difference in brightness level of the adjacent flight lines. This is essential because the concept of the spectral response received at the sensor from the same land cover is understood and can be corrected for position of the scan line. It is also important that the data can be accurately overlaid and geometrically correct.

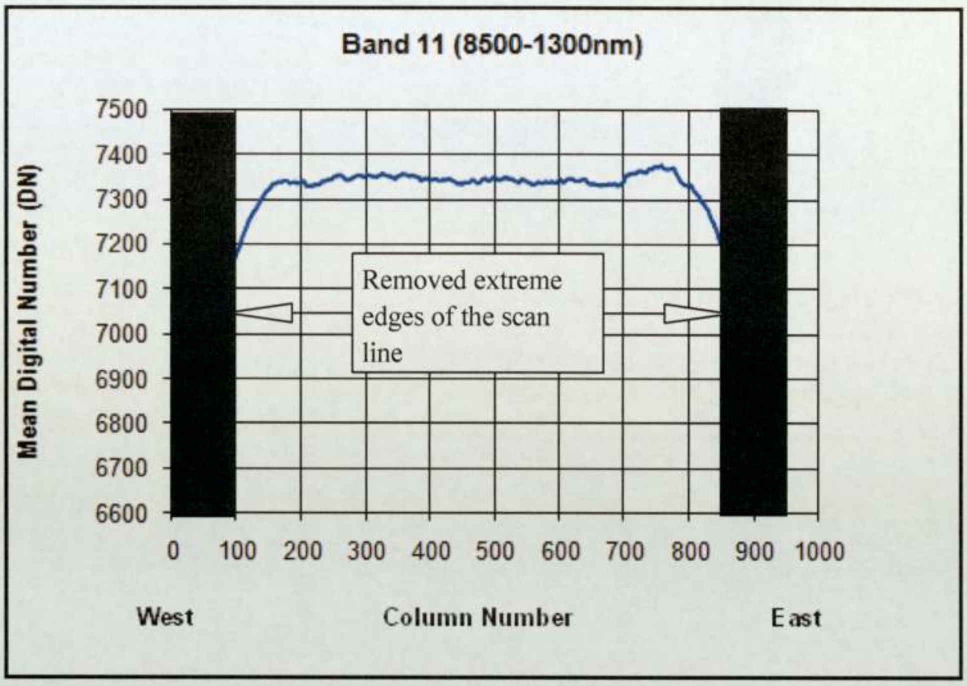

Figure 3-12: The distribution of mean DN values across swath for thermal band.

3.11 QUALITATIVE AND QUANTITATIVE USE OF THE ATM DATA

3.11.1 CLASSIFICATION OF THE ATM DATA

Unsupervised classification methodology applied to remote sensing image processing can provide benefits in automatically converting the raw image data into useful information so long as higher classification accuracy is achieved. The main aim of this section is to illustrate if mosaiced raw DN imagery is appropriate for classification. Scott (1994) compares the use of multi-spectral airborne video-graphy and manual method of classification. Scott achieved a very good distinction between roads, roofs and permeable areas. Table 3-5, shows the wavelength of ATM bands with its application of each band by Wilson (1995).

ATM Bands	Spectral Range (nm)	Equivalent Landsat TM Bands
1	420-450	Bathymetry, soil/vegetation differentiation
2	450-520	Coniferous/Deciduous differentiation
3	520-600	Green reflectance by health vegetation
4	605-625	Secondary green reflectance band
5	630-690	Plant species differentiation by chlorophyll absorption
6	695-750	Geo-botanical surveys, water bodies delineation
7	760-900	Bio-mass surveys, water body delineation
8	910-1050	Secondary near infrared band
9	1550-1850	Altered rock mapping, vegetation moisture measurement
10	2080-2350	Hydro-thermal mapping
11	8500-13000	Plant heat stress detection, thermal mapping

Table 3-5: The band wavelengths of the Airborne Thematic Mapper (Wilson, 1995).

A composite image was created from different band combinations to carry out the cluster classifications. In theory, the order in which a set of bands are composited (in composite) should make no difference to the result produced by cluster. However, in practice, the results of a cluster analysis may be different depending upon the order of the bands input to the composite routine and positioning of the seed value.

Figure 3-13 displays the test area in the form of false colour (IR) composite generated by projecting Band 3 (630-690 nm) as green, Band 5 (630-690 nm) as blue, and Band 7 (760-900 nm) as red and shows a variety of landscape types. The agricultural fields around the area are planted. The area is relatively flat throughout, there is one main urban area in the centre of the scene, and otherwise the land cover is mainly rural farmland. A motorway is being constructed across the north of the imagery.

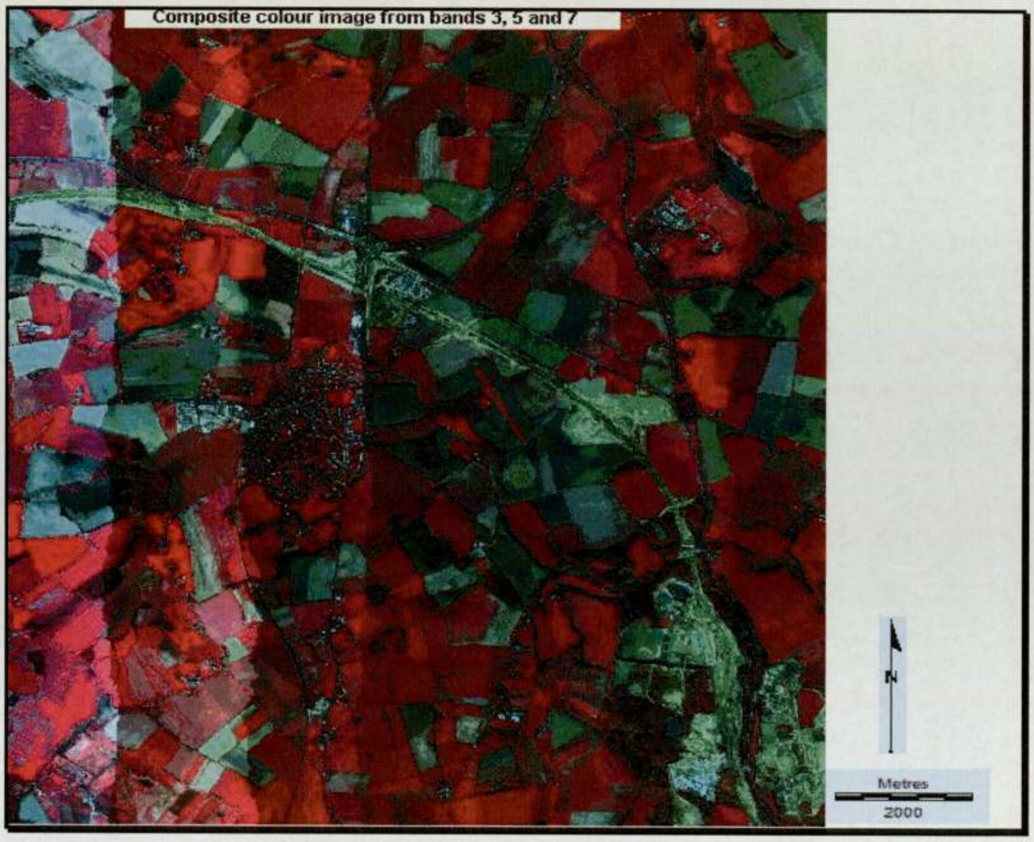

Figure 3-13: A 8-bit false colour composite image from three bands (Band 3, 5 and 7).

When dealing with unsupervised classification, each class may contain more than one cluster. Pre-experimental clustering experiments could be conducted for detecting the relationship between the clusters and the ground data so as to determine the suitable number of clusters and the information classes. This will facilitate further the classification accuracy comparisons among the different methods. The information classes are shown in Table 3-6.

No.	Class name
1	Vegetation
2	Water
3	Forest
4	Bare soil and living area
5	Dry grass and low sprout

Table 3-6: Selected information classes for unsupervised classification clustering mapping.

One of the parameters in an unsupervised classification is the number of pixels groups (clusters) the user requires. These are then classified after the map is produced, by using ground truth or aerial photography. With unsupervised classification, the resulting map will generally have a higher number of distinct classes, since some are clearly members of the same class.

A pixel may be incorrectly classified for one of several reasons. One reason is that it may simply be mis-classified because its spectral response does not uniquely identify the land cover. A more likely reason is that the pixel is mixed –meaning it contains a certain percentage of one class and certain percentage of another. As a result it may not fit into any of the classes defined, but some other mixed class. Likewise, in supervised classification, the operator must decide which class certain indistinct groups of pixels belong to. This is certainly an area where error in the classification is introduced.

In broad classification, a class must contain a frequency higher than all of its non-diagonal neighbours. Whereas, in the fine classification thus is relaxed, permitting one non-diagonal neighbour to have a higher frequency. This accommodates true peaks which are otherwise missed because a nearby peak of greater magnitude obscures the usual dip between the peaks. Thus, in this first test broad cluster classification is carried-out and it produced six classes as shown in Figure 3-14. The broad classification gives a general picture of spectral classes.

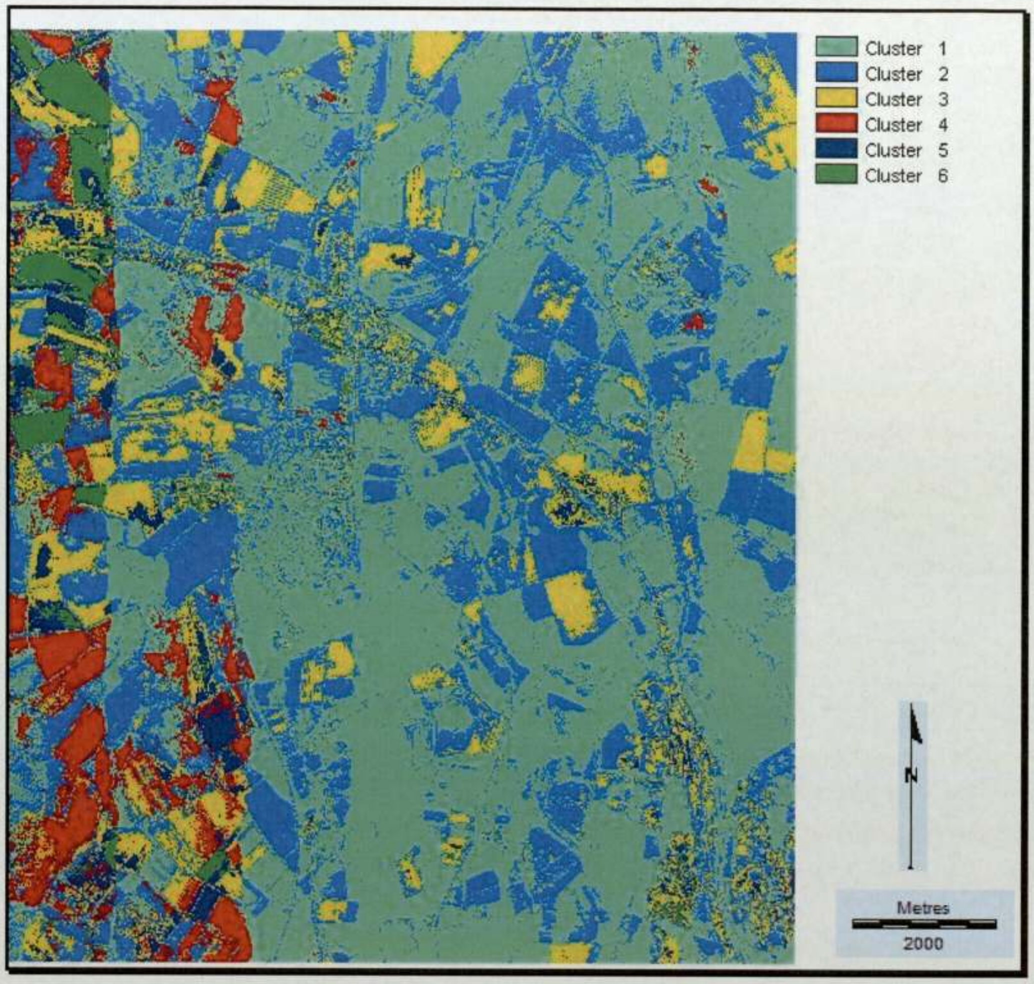

Figure 3-14: Unsupervised broad cluster classification from bands 3, 5 and 7, 6 Classes.

The fine cluster classification used the same colour composite image as the broad one, but produced 16 classes as shown in Figure 3-15. With unsupervised classification, the resulting map will generally have a fewer number of distinct classes, since some are clearly members of the same class. For example the pixel that makes up the road class may be spread across several groups that should be combined if a class representing road is to be produced. As a consequence, 16 groups were selected from the initial classification. These could be subsequently combined to give five distinct classes.

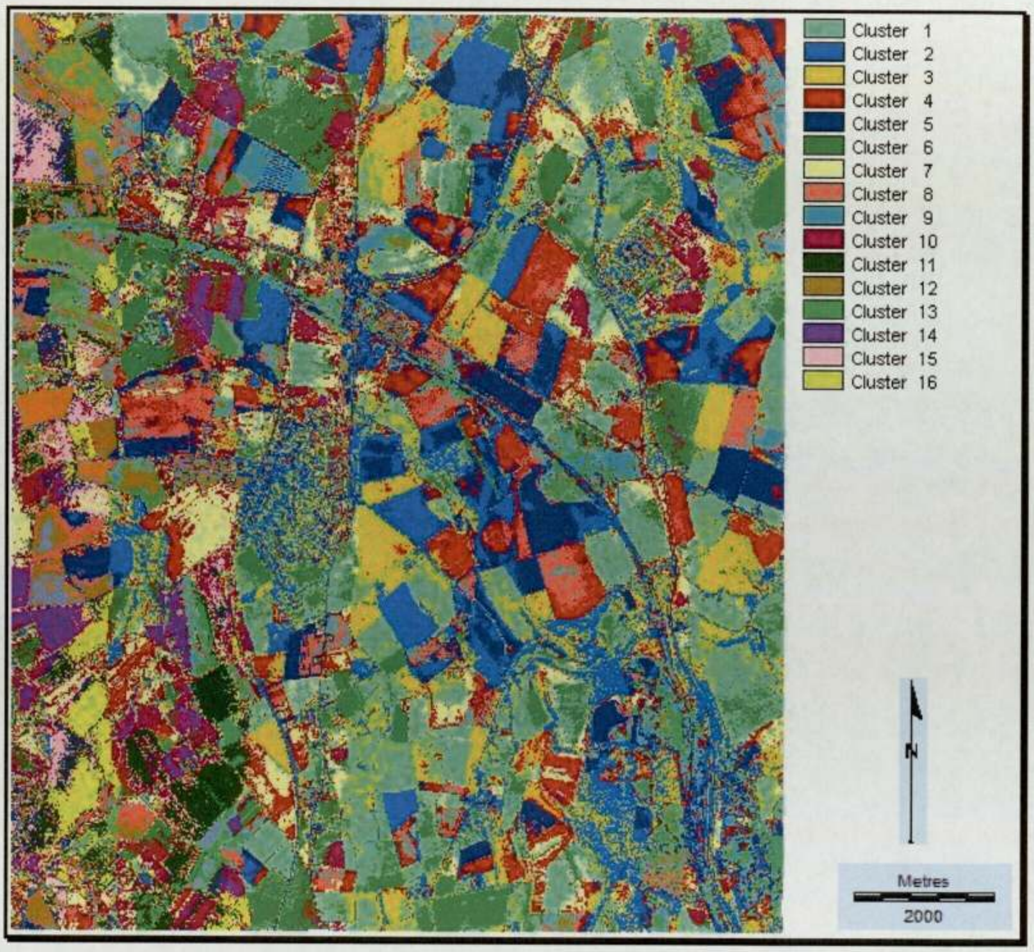

Figure 3-15: Unsupervised fine cluster classification from bands 3, 5 and 7, 16 Classes.

3.11.2 COMPARISON BETWEEN DAY AND NIGHT THERMAL BANDS

The band 11 of ATM imagery records energy emitted by the Earth surface in the thermal infrared part of the spectrum (8500-13000 nm; note that there is no equivalent band in CASI imagery and so this component of the research is limited to ATM imagery only). The energy emitted at these wavelengths is generally related to variations in soil/ground moisture and micro-topography, which together affect the temperature of the ground. Analysis of the thermal band of ATM data has proven particularly effective at identifying archaeological features (Winterbottom and Dawson, 2005). Where possible, comparison of night-time and daytime thermal images to gauge diurnal heat capacity has been shown to provide additional information (Rowlands and Sarris, 2007). Data available for the present research includes both daytime and night time thermal images; these will be examined individually in order to identify archaeological and geomorphological features and assess the efficacy of thermal imagery for archaeological prospection in alluvial environments.

Figure 3-16, shows the difference between the day and night time thermal bands. Both bands were recorded from the same spectral range (8500-13000 nm). The difference was calculated by simple Idrisi overlay (subtraction) function and hence the result is promising.

Figure 3-16: The difference between the day and night time thermal band.

The difference of the day and night time thermal bands, (Figure 3-16) can be reclassed further for the identification of building roof without any problem. Thus all DN values less than 2000 were assigned to zero and greater than 2000 to 1, to produce an image shown in Figure 3-17. Thus, one can also make a distinction between roof types: metal roofs from industrial buildings which looked brighter than the house-hold or residential roofs (clay or concrete roofing). More importantly there is clear demarcation between the roofs of the buildings and roads. This will be more helpful for environmental modelling and determination of heat loss from the roofs of industrial and residential house.

Figure 3-17: The roofs of building from industrial and residential from the difference between day and night time thermal bands.

3.11.3 QUANTITATIVE ANALYSIS OF DAY AND NIGHT IMAGERY

The detailed quantitative analysis of the day and night thermal imagery was carried out by overlaying the day and night thermal flights, to obtain an indication of the information contained within the flights. Day flight line 6 and night flight line 5 more or less cover one another and cover our field survey area. Initial processing of the data required reclassing the day flight, and windowing common to both to reduce computation effort. This was done by;

- multiplying the two images together to find the common area;
- converting this to a mask and apply the mask to get the areas in each image common to the other, and
- finally, the statistics for the day and night thermal common area were calculated (see Table 3-7).

Statistics		Night Flight	Day Flight
Maximum		7819	12229
Minimum		4292	193
Range		3527	12036
Mean		5818.25	7394.59
Std. Error of Mean		0.049	0.121
Mode		5841	7268
Median		5832	7331
Standard Deviation		177.79	432.40
1st Quartiles		5720	7196
2nd Quartiles		5832	7331
3rd Quartiles		5927	7513
Correlation Coefficient		-0.090(*)	-0.090(*)
Variance		31610.23	186973.39
Skewness	**Statistic**	-0.300	-1.768
	Standard Error	0.001	0.001
Kurtosis	**Statistic**	3.418	55.063
	Standard Error	0.001	0.001

*Correlation is significant at the 0.01 level (2-tailed).

Table 3-7: Quantitative analysis of day and night imagery.

The scattered diagram given in Figure 3-18 shows a very low correlation between the day and night thermal common imagery, which agrees with the correlation coefficient (-0.09) obtained from the statistical analysis (see Table 3-7). The DNs for the day and night flights are very different and hence correlation between them is almost zero. Thus, it is not possible to forecast nighttime thermal emission from day flights alone.

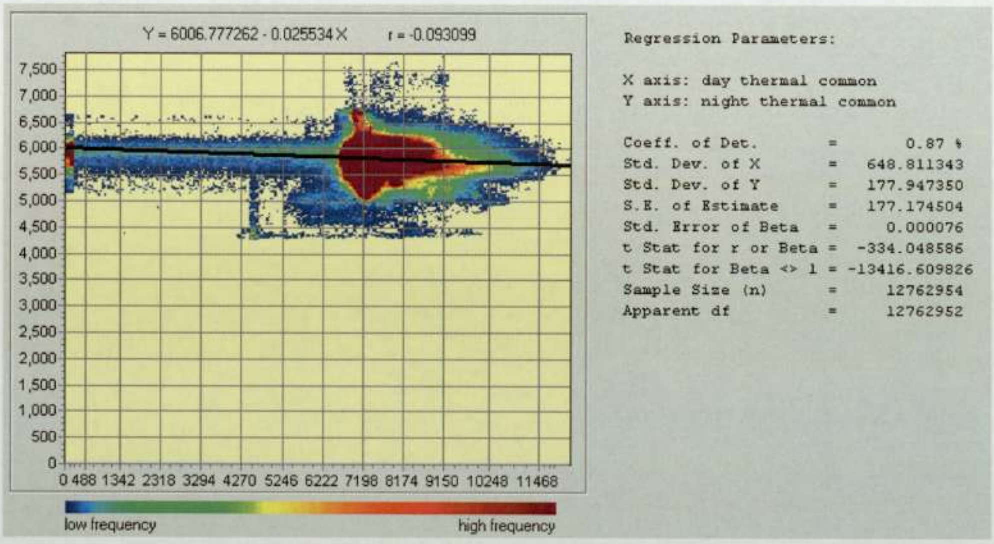

```
Regression Parameters:

X axis: day thermal common
Y axis: night thermal common

Coeff. of Det.          =         0.87 %
Std. Dev. of X          =   648.811343
Std. Dev. of Y          =   177.947350
S.E. of Estimate        =   177.174504
Std. Error of Beta      =     0.000076
t Stat for r or Beta =  -334.048586
t Stat for Beta <> 1 = -13416.609826
Sample Size (n)         =     12762954
Apparent df             =     12762952
```

Figure 3-18: Scattered diagram of the day and night thermal bands.

3.12 CONCLUSION

Chapter 3 illustrated the location and nature of the study area in addition to the data collection procedures used in the research. This was followed with the detailed specifications and data acquisition modes for the Airborne Thematic Mapper (ATM) and the Compact Airborne Spectrographic Imager (CASI). In addition, chapter three discussed the hierarchical data format (HDF), which stores the scientific data and how it was applied to the ATM data, and also explained how the data was extracted. The extreme edges of all the flight lines under consideration were trimmed thereby making the data useful for quantitative and qualitative analysis by not relying on the extreme edges of the scan line.

Chapter 3 also examined how useful were data for a quantitative and qualitative use. Mosaiced raw DN imagery is inappropriate for classification, and it was discovered that the same land cover on different parts of the imagery gave different spectral responses and their qualitative classification was not reliable and tangible. However, the nighttime thermal band suffer from a problem called gain effect from different flights lines. This gain effect had caused problems in identifying objects throughout the whole imagery. The use of ratio reduces the gain problem with different flights and hence, it is recommended to use a band ratio rather than absolute values. This procedure cannot be done for night flights; it can only be done for day flights with more bands.

Finally, the result from the difference between the day and nighttime thermal bands was promising, because it is very useful in detecting water bodies: rivers, ponds and roofs of houses. One can also make a distinction between roof types: metal roofs from industrial, which looked brighter than the household or residential roofs (clay or concrete roofing). More importantly, there is clear demarcation between the roofs of the buildings and roads.

4 SPECTRAL ACCURACY

4.1 INTRODUCTION

Substantial research has been undertaken to automate the analysis of the detailed spectral accuracy associated with individual pixels in hyperspectral and multispectral data sets (Kruse and Lefkoff, 1992). This chapter will discuss the spectral accuracy of the Airborne Thematic Mapper and the Compact Airborne Spectrographic Imager under the following sub sections.

The first section in this chapter discusses the quantification of edges of Airborne Thematic Mapper. In this, the whole image is visually studied and, despite the good overlap between the adjacent flights and the removal of the edges of the image, flight lines covering the same area showed a difference in brightness level. The quality of the data is assessed by considering the spectral response received at the sensor from the same land cover.

The second section discusses the cross scan variation of the whole imagery. This section calculates the angular view and shows a comparison between the Airborne Thematic Mapper and Compact Airborne Spectrographic Imager by considering the FOV (Field of View) for both scanners.

The third section looks into the quality analysis of Airborne Thematic Mapper data and its relative standard deviation. Here the focus of the study is the distribution of DN values across the swath of the image. Moreover, it also investigates whether these variations could have arisen by chance or not. Finally, in this sub section, the standardized mean is discussed for all bands throughout the flight.

Finally, this chapter discusses the frequency distribution of the DN values. Thus, it examines how frequently DN values occur by considering the centre, west and east side of the image and subsequent by conclusions are drawn with regard to the width discussed in the depth and some recommendations are made.

4.2 CROSS SCAN VARIATION

4.2.1 QUANTIFICATION OF EDGES FOR ATM BANDS

In this research before multi-temporal data can be used, it is essential that the spectral response received at the sensor from the same land cover is understood and can be corrected for the position of the scan line. It is also essential that the data can be accurately overlaid and geometrically correct.

In the case of ATM the scanning FOV (Field of View) is typically about 90°. Such a large angle is necessary to acquire an acceptable swath width from typical aircraft altitudes. The consequence of the larger FOV with aircraft scanning is that significant distortions in the image can occur at the edges of the scan lines. Often these have to be corrected by digital processes.

To examine whether there is any systematic variation across the scan line, the average digital numbers for each column will be used (as studied by Gregory, 2001). In order to study the spectral differences, when working on raw un-rectified data, all flights from south to north were flipped to north to south within the Matlab programming environment, and the mean of the columns was taken for each flight line. The average of just over forty thousand rows was calculated to see the pattern and characteristics for each band. Theoretically, because of the huge number of lines it may be assumed that each land-cover is sampled almost equally down each column, and the resulting plot (the distribution of mean DN values across swath) is a nearly horizontal line across the swath of the flight line as shown in Figure 4-1 (thermal band) below. The extreme edges of the scan line are discarded or removed (see Section 3.10.4 for details).

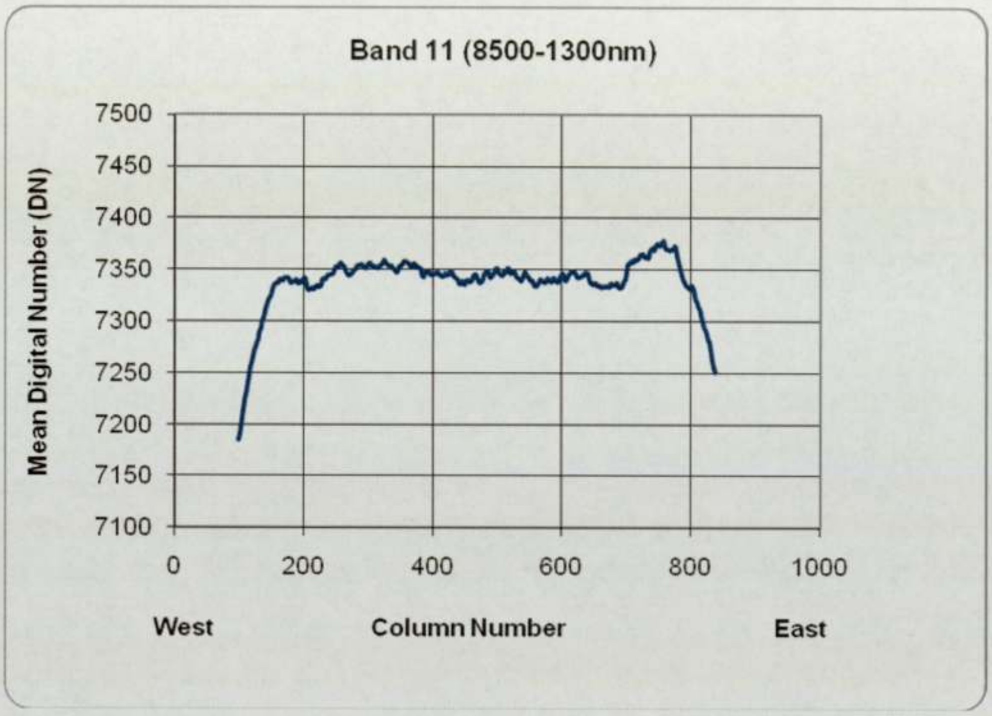

Figure 4-1: The distribution of mean DN values across swath for band 11.

The thermal Band 11 (8500–13000 nm) shows an almost a horizontal line with minimal fluctuations of the average digital number across the scan line. Towards the east side of the image there is an increase in digital value (7375) before it drops.

However, Band 3 (Figure 4-2) reaches its peak (1385) on the west side of the scan line. This drop within a few pixels, and dip to the middle before it finally rises to reach a peak in the east, and subsequently decreasing at the end of the line. The high DN values (1420) at both ends could be due to scanner failure to record the correct radiance at the far view angle, resulting in some anomalous values. The dip in the middle is quite difficult to explain since no simple explanation is immediately obvious. Its cause can only be speculative as shown below.

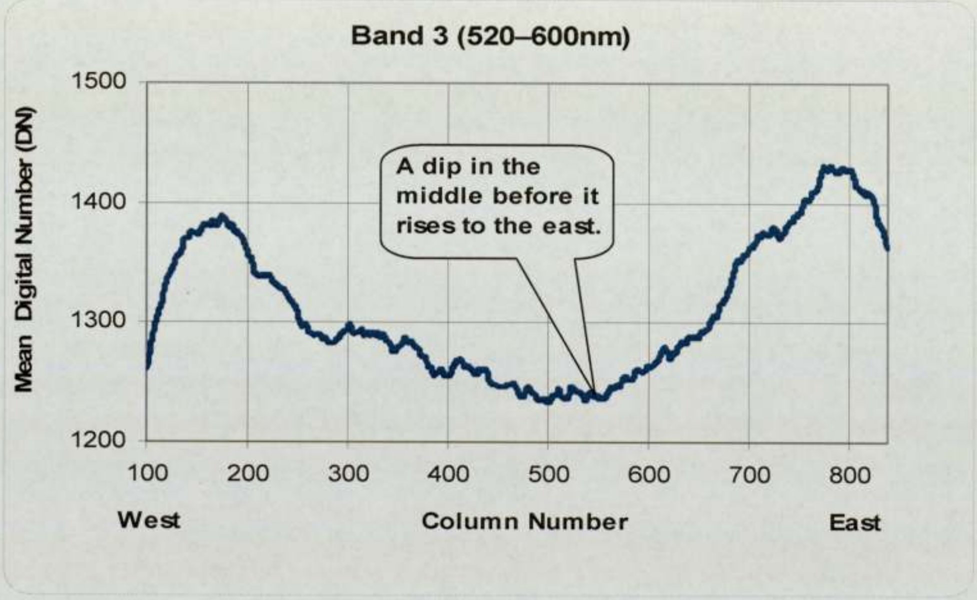

Figure 4-2: The distribution of mean DN values across swath for band 3.

Clearly each column has a distribution of values, but these distributions are difficult to compare for each of 938 columns. A method of summarizing the central spread of the distribution is required. The mean value of a column offers the simplest single statistic to describe the central property of that column distribution. The standard deviation is also used to describe the spread of the distribution. Using these two statistics (mean and standard deviation) a workable description of the variation of the distribution across the scan line is available. If the variation was caused by land cover then certain bands would show high values for specific land cover types. For example, bare soil for an infrared would show high values for vegetation. Independent data sources could be used to correct for the variation in land cover, but they are either not available or are subject to the following problems:

1) Land cover map required at the time of the flight to show time dependent variations such as bare earth, emerging vegetation etc.
2) Classifying from aerial photograph is difficult due to requirement for geo-referencing all the photographs and assuming there is no vignetting etc in the camera, and inadequate quality.
3) OS maps typically show land use not land cover, and
4) Satellite data is at too coarse a resolution for land cover maps.

For these reasons no independent land cover data was available to correct the variation.

The results from all the visible and infra-red bands are completely different from the thermal band. In all bands except the thermal band, the mean DN value showed similar trends and patterns, but all bands differed in the range and magnitude of mean DN values. In almost all bands (1 to 10) the lowest mean DN value recorded occurred between column numbers 450 and 600. Interestingly, Band 1 and Band 2 showed smooth curve when plotted and compared with rest of the bands, which showed more unsettled graph, as shown in Figure 4-3 to Figure 4-11.

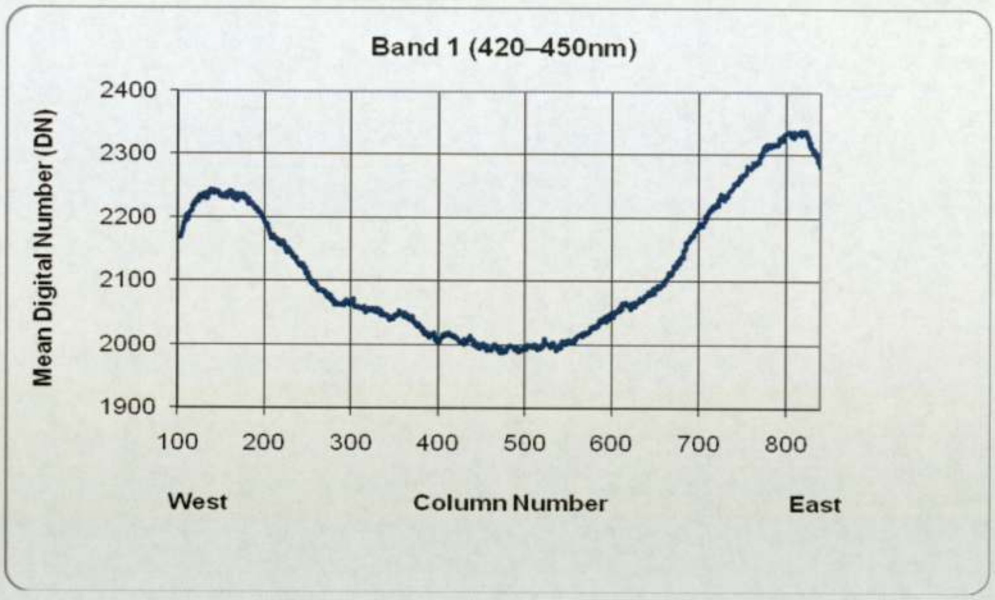

Figure 4-3: The distribution of mean DN values across swath for band 1.

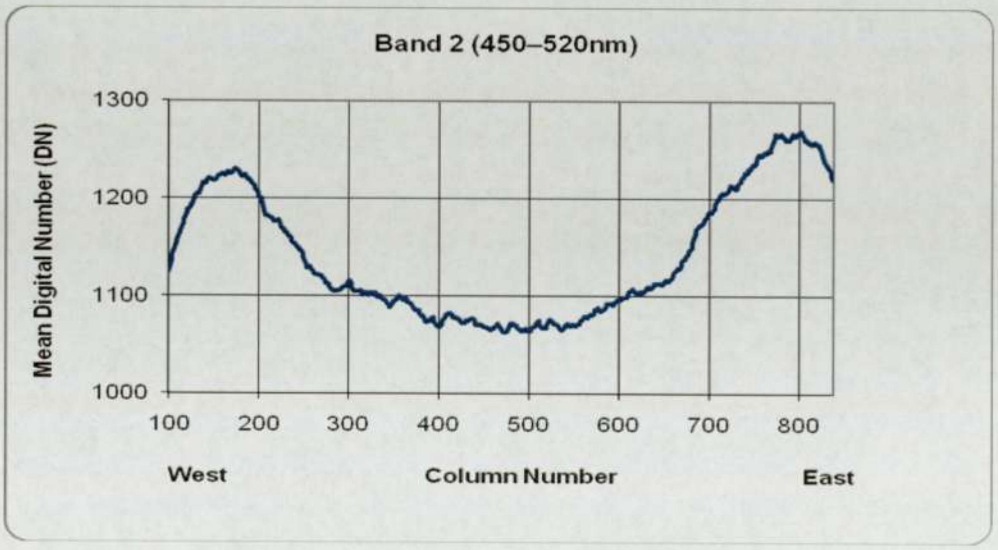

Figure 4-4: The distribution of mean DN values across swath for band 2.

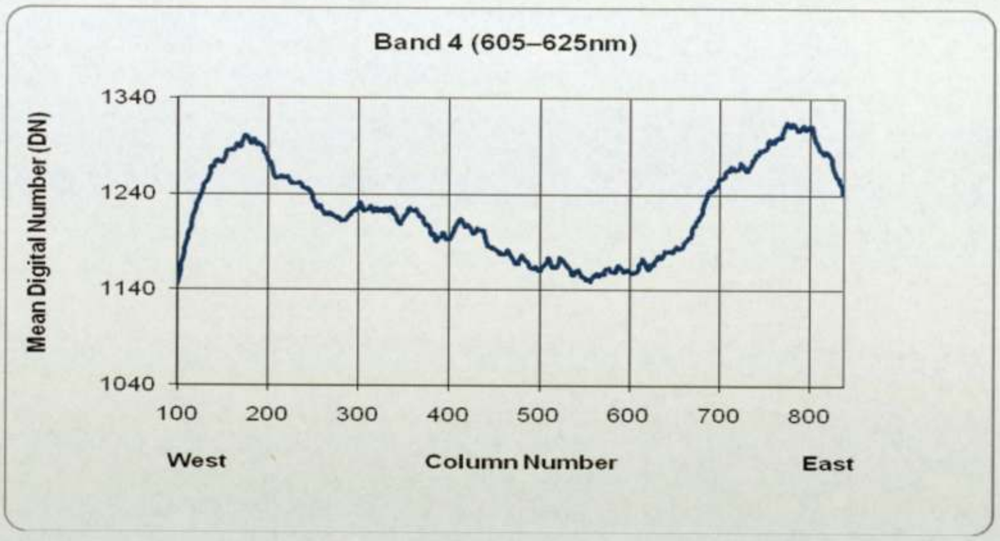

Figure 4-5: The distribution of mean DN values across swath for band 4.

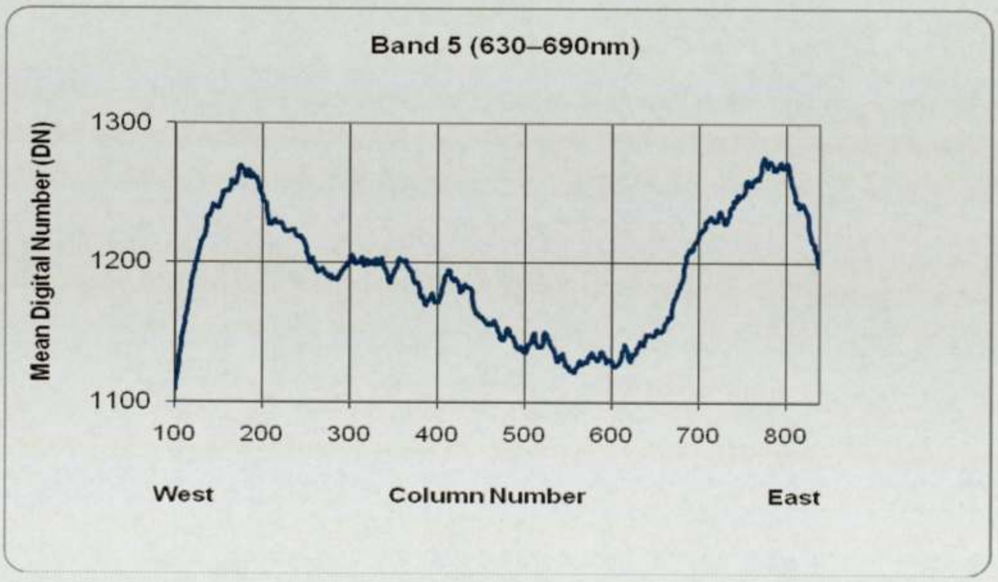

Figure 4-6: The distribution of mean DN values across swath for band 5.

Figure 4-7: The distribution of mean DN values across swath for band 6.

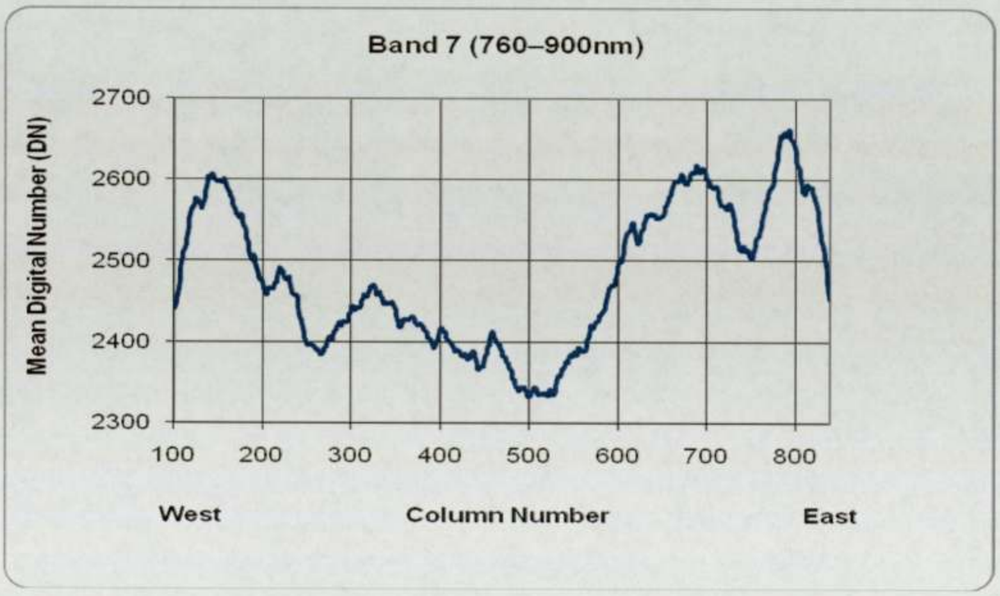

Figure 4-8: The distribution of mean DN values across swath for band 7.

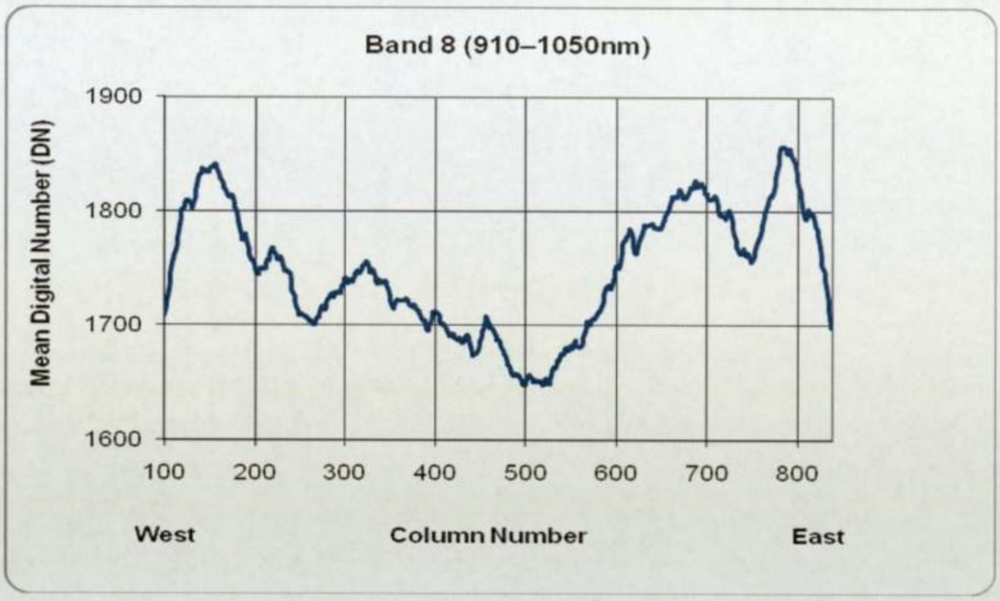

Figure 4-9: The distribution of mean DN values across swath for band 8.

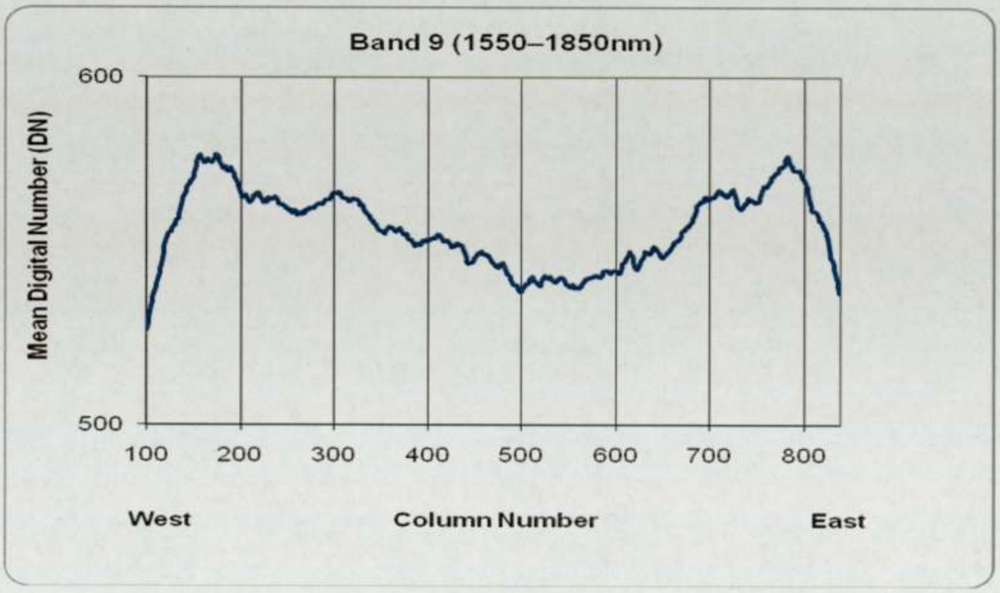

Figure 4-10: The distribution of mean DN values across swath for band 9.

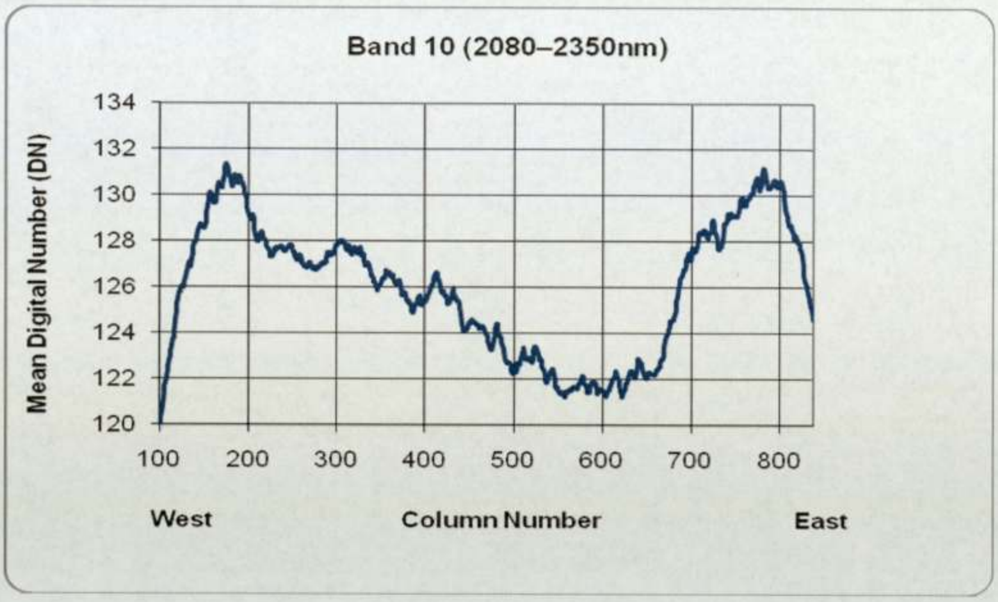

Figure 4-11: The distribution of mean DN values across swath for band 10.

4.2.2 ANGULAR VIEW COMPARISON BETWEEN ATM AND CASI

A model was developed to compare the DN values obtained by the Airborne Thematic Mapper (ATM) and Compact Airborne Spectrographic Imager (CASI) scanners. This model looks mainly at field of view (FOV) for both scanners (see Figure 4-12). Both were mounted on the same aircraft, covering the same land cover and scanning at the same time. Whilst, the CASI scanner had FOV of 53.2° and 512 pixels, the ATM scanners have a wider view angle of 90.0° and 938 pixels.

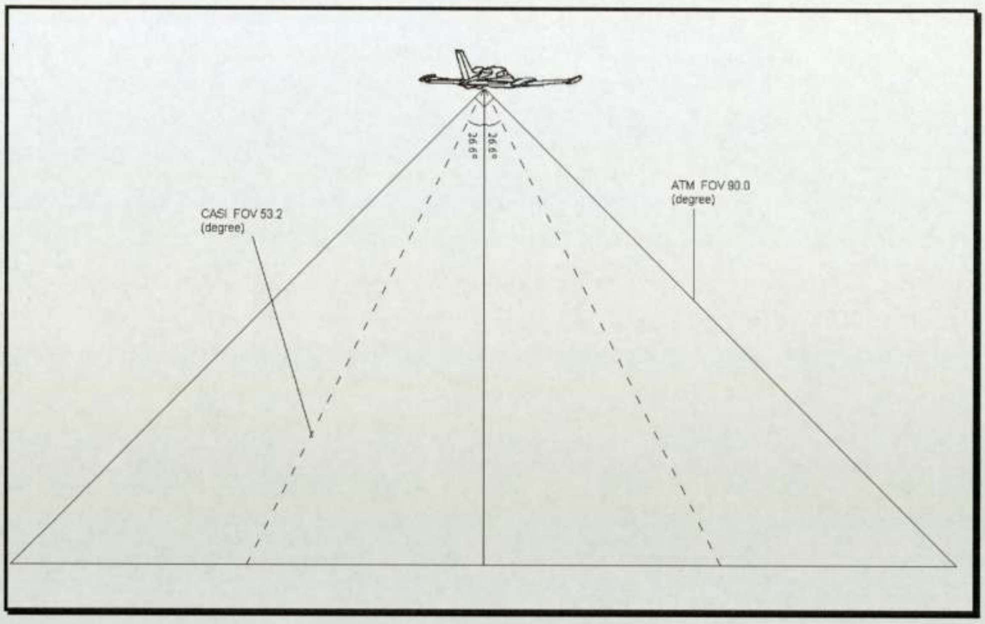

Figure 4-12: The comparison of the FOV between the ATM and CASI.

After examining the distribution of mean DN values across swath, the next step is to study the pattern and the variability in magnitude of the DN values across the scan line. With a FOV of θ radians, equation 4-1 is derived to calculate the angular view in degrees for both sensors by considering the field of view and number of pixel for each sensor. Theoretically, both sensors should show a similar pattern and shape within the same band width.

$$\kappa = -\left(\frac{\theta}{2}\right) + \left[\frac{(P_i) * \theta}{n}\right] \tag{4-1}$$

Where:

κ = Angular view (in radians)

θ = FOV (in radians)

n = Swath width in pixels

P_i = Individual pixel number

The CASI bands do not correspond to the ATM bands, for example Band 7 (760–900 nm) of the ATM corresponds Bands 10, 11, 12, 13, and 14 (750–940 nm) of the CASI sensor. The data available did not give the point spread function for either scanner so a simple aggregation function was devised by simply taking the arithmetic mean of the DN values for all CASI bands covered by a single ATM band. The best possible range of the wavelength is used to correlate the ATM and CASI sensors are shown in Table 4-1 and how they averaged. The range between the lower and upper wavelength is not an exact range for ATM and CASI, it could be out in one and/or both sides of the range. More than 90% of the wavelength ranges used in the CASI corresponds with the ATM bands.

ATM Bands	ATM Spectral Range (nm)	CASI Bands	CASI Spectral Range (nm)
1	420-450	**1**	450-490
2	450-520	**1** **2**	450-552
3	520-600	**2** **3**	490-607
4	605-625	**4**	607-651
5	630-690	**4** **5** **6**	607-700
6	695-750	**6** **7** **8** **9**	669-750
7	760-900	**10** **11** **12** **13** **14**	750-940
8	710-740	**15**	940-945

Table 4-1: Band correlation between the ATM and CASI.

Thus, all bands in the CASI will be corresponded to the ATM by considering the wavelength of each band and will be discussed below.

In Figure 4-13, CASI Band 4 (607–651nm) was compared with Band 4 of the ATM (605–625 nm). To the west side the CASI Band 4 showed higher in DN values compared with the ATM Band 4, but in east side the sensors showed almost identical DN value throughout the area covered. This variation could be due to the difference in frequency sampled.

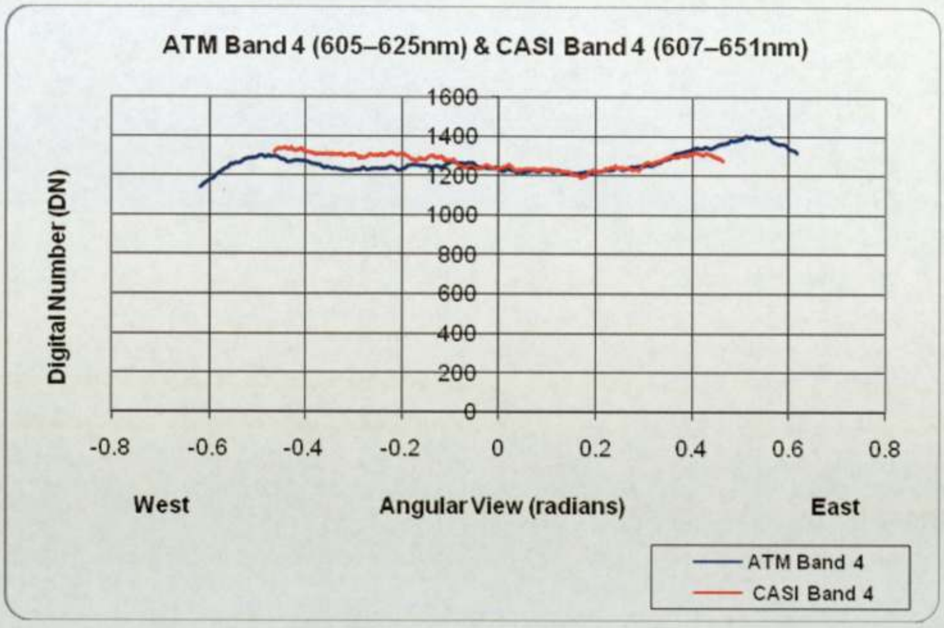

Figure 4-13: The comparison of the angular view between ATM band 4 and CASI band four.

In another example, the ATM near-infrared Band 6 (695-750 nm) is plotted against the aggregate average values of Band 6, 7, 8, and 9 of the CASI with a spectral range of 669–750 nm as shown in Figure 4-14. From Figure 4-14, it can be seen that although the overall pattern is similar for the CASI and the ATM, but the actual values are different. The difference in the gap between the ATM and the CASI DN values gets wider and wider as one goes from west to east. The aggregate CASI values seemed flatter throughout whole angular view as compared to the ATM which showed an increase in DN value from west to east.

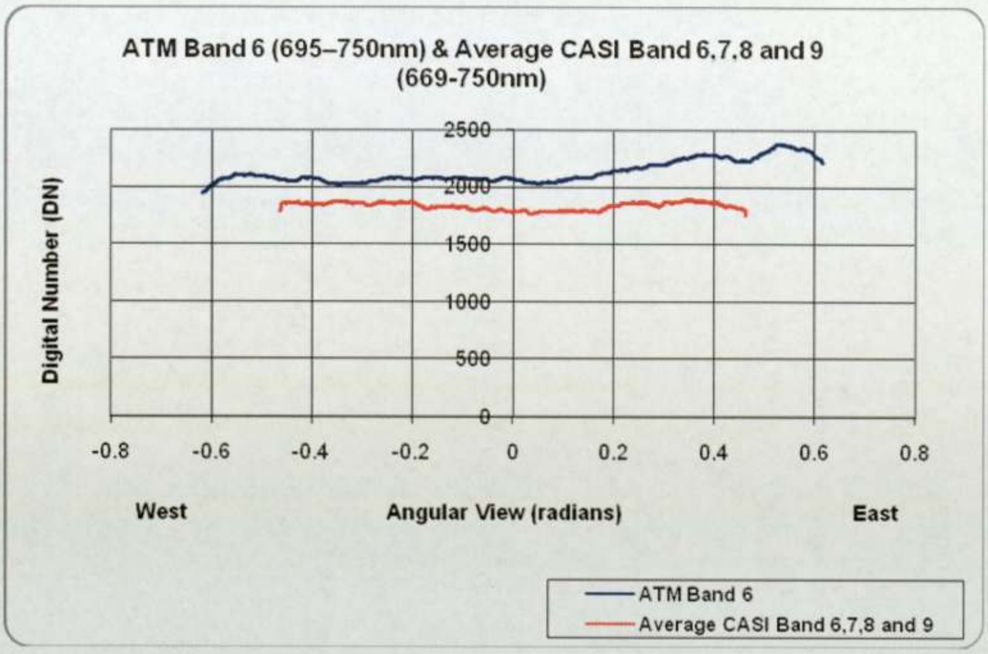

Figure 4-14: The comparison of the angular view between ATM band 6 and average CASI band 6, 7, 8 and 9.

Figure 4-15 shows a comparison between ATM Band 1 (420–450 nm) and CASI Band 1 (450–490 nm). In this plot, the ATM Band 1 shows a higher DN value than the CASI Band 1, but showed a similar pattern throughout the scan line. The difference in the gap between the ATM and the CASI is almost constant from west to east throughout the whole angular view. The aggregate CASI seemed to have a slight dip in the middle, but kept similar magnitude at the extreme east and west side. The ATM band showed an increase in DN value from west to east.

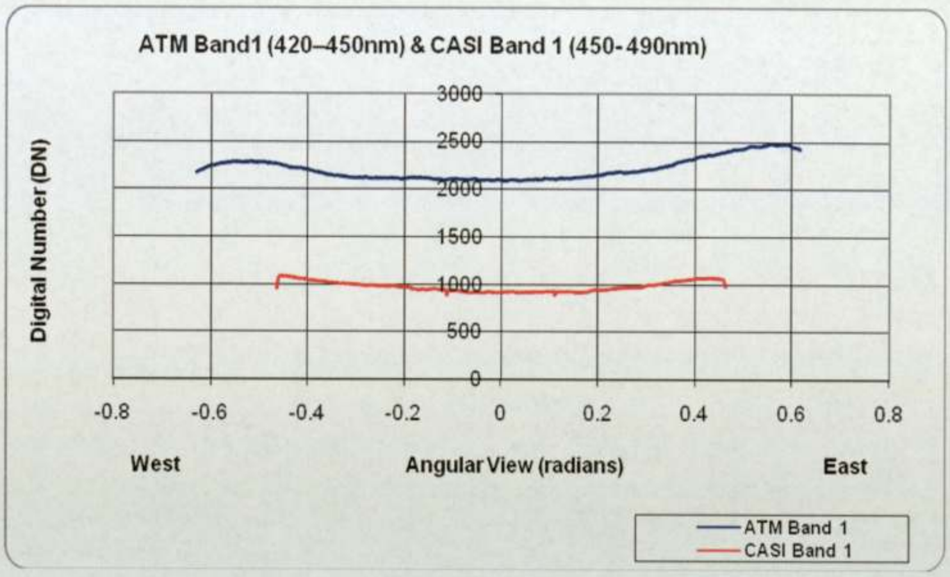

Figure 4-15: The comparison of the Angular view between ATM band one and CASI band one.

The comparison of ATM Band 2 (450–520 nm) with the average of the CASI Band 1 and 2 (450–552 nm) shows a similar pattern and shape as shown in Figure 4-16. In this graph, the average CASI recorded lower DN than the ATM Band 2. In the CASI sensor there is a drop off in the limb in the west and east side of the imagery, this could be due a sudden dropping off of the CASI sensor or failure in collecting DN values from the extreme edges of the scan line.

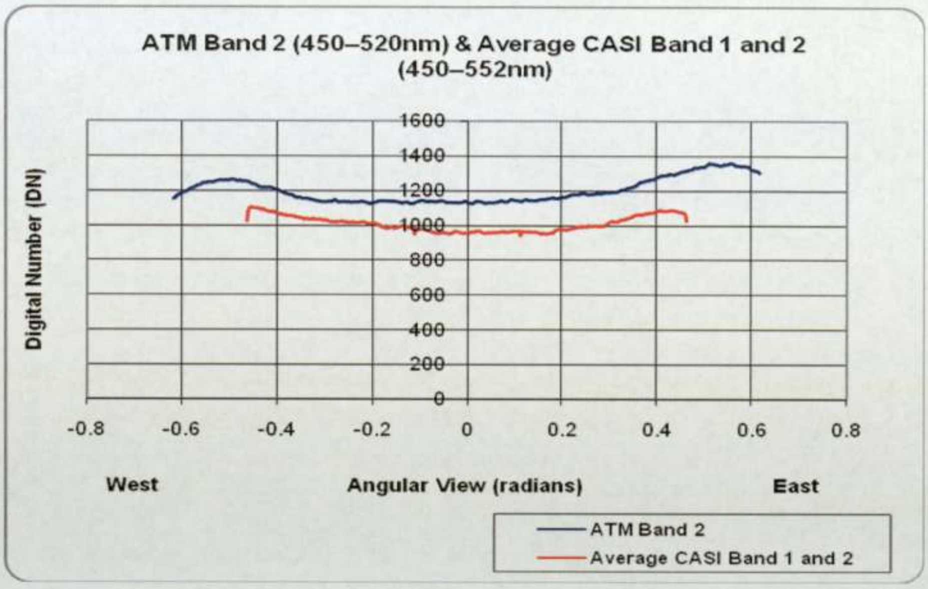

Figure 4-16: The comparison of the angular view between ATM band two and average CASI band one and two.

Figure 4-17 depicts a comparison between ATM Band 3 (520-600 nm) with the average of CASI Band 2 and 3 (490–607 nm); the ATM band recorded higher DN values as compared to the aggregate CASI 2 and 3. In addition to the above it also showed a similar pattern and shape throughout the scan line as resulted below. No dropping off in the limb in the west and east side of the imagery is observed in the aggregate CASI 2 and 3. The difference in the gap between the ATM band and the aggregate CASI bands gets slightly wider as one goes from west to east.

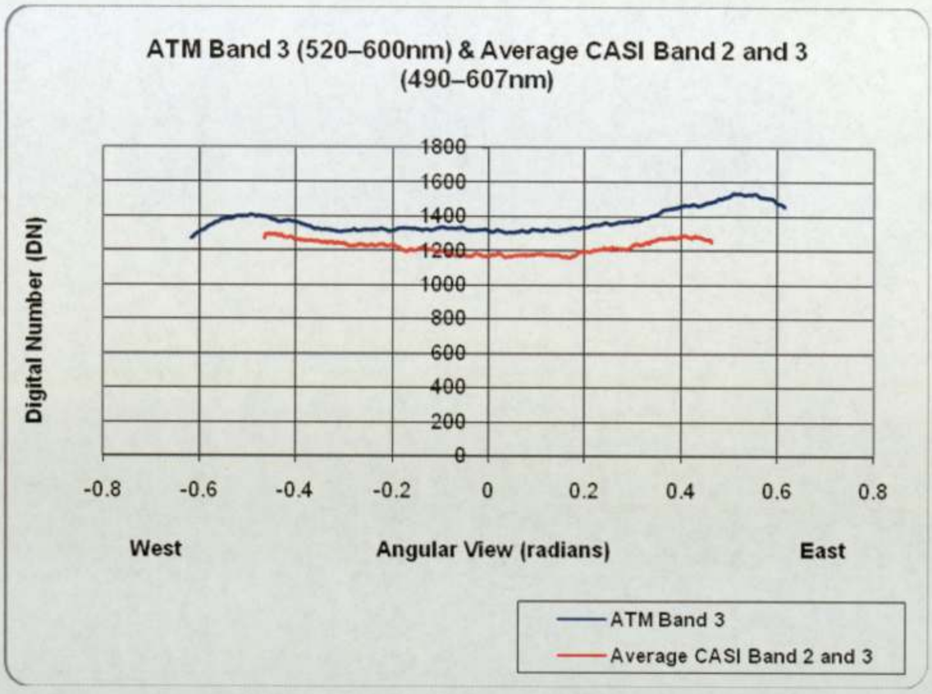

Figure 4-17: The comparison of the angular view between ATM band three and average CASI band two and three.

The aggregate of the averages CASI Band 4, 5, and 6 (607–700 nm) had showed almost the same magnitude of the digital numbers when compared to Band 5 of the ATM (630–690 nm). The plot in Figure 4-18 shows a similar pattern and shape in their angular view for both scanners. The aggregate CASI 4, 5 and 6 showed a gradual decreased from west to east side of the imagery. This could be due to lower DN values being recorded at the eastern side as compared to the west. Both sensors recorded almost identical digital numbers in the west side as compared to east.

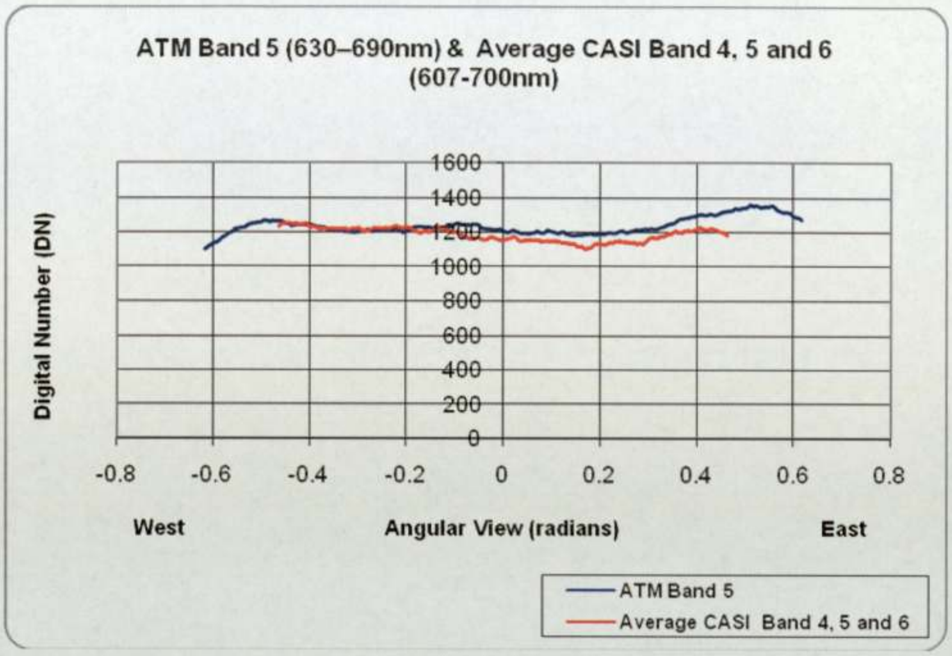

Figure 4-18: The comparison of the angular view between ATM band 5 and average CASI band 4, 5, and 6.

However, in Figure 4-19, the comparison of the angular view between ATM Band 7 (760–900 nm) and average of CASI Band 10, 11, 12, 13, and 14 (750–740 nm), shows a similar pattern and shape in the angular view, but with the CASI exhibiting a slight lower magnitude of digital number as compared to the ATM. In the CASI sensor there is a drop off of in the limb in the west and east side of the imagery, this could be due a sudden dropping off of the CASI sensor or failure in collecting DN values from the extreme edges of the scan line. The aggregate CASI showed similar pattern and trend in the west side of the imagery with ATM, but in far east side, there is a sudden drop off in DN values in the CASI as compared to the ATM. In the middle also the CASI showed slight lower magnitude of digital number as compared to the ATM.

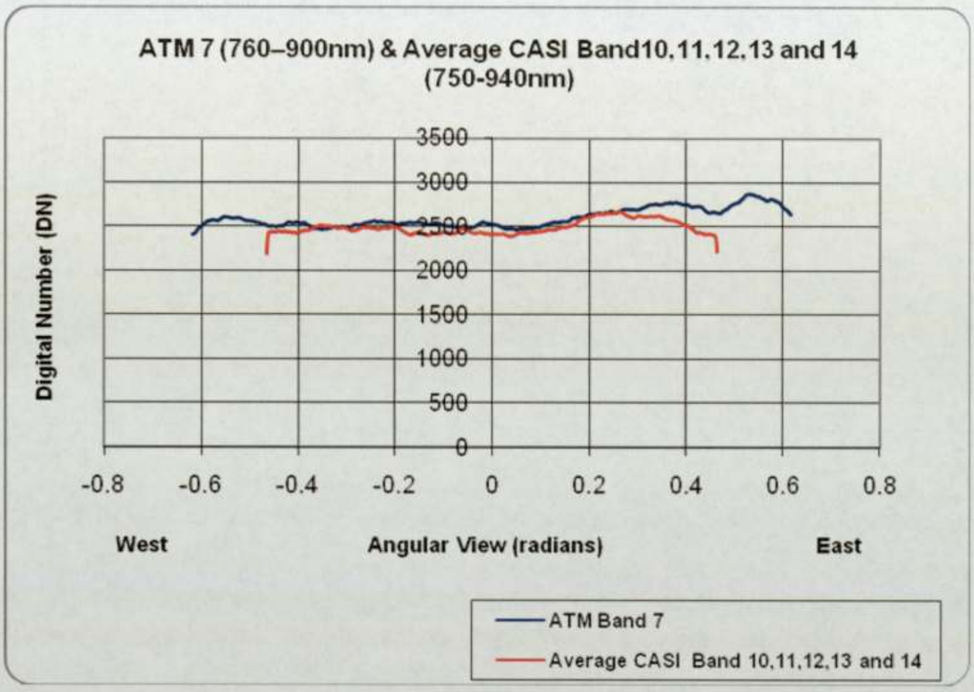

Figure 4-19: The comparison of the angular view between ATM band 7 and average CASI band 10,11,12,13 and 14.

In Figure 4-20, the comparison of ATM Band 8 (910–1050 nm) with the CASI Band 15 (940–945 nm) showed a similar pattern and shape, but the ATM band is higher in magnitude than the CASI one. Similarly, there is a drop off in the limb in the west and east side of the imagery in the CASI 15, which could be the sensor failing to record DN values from the extreme sides of the imagery as compared to the ATM Band 8.

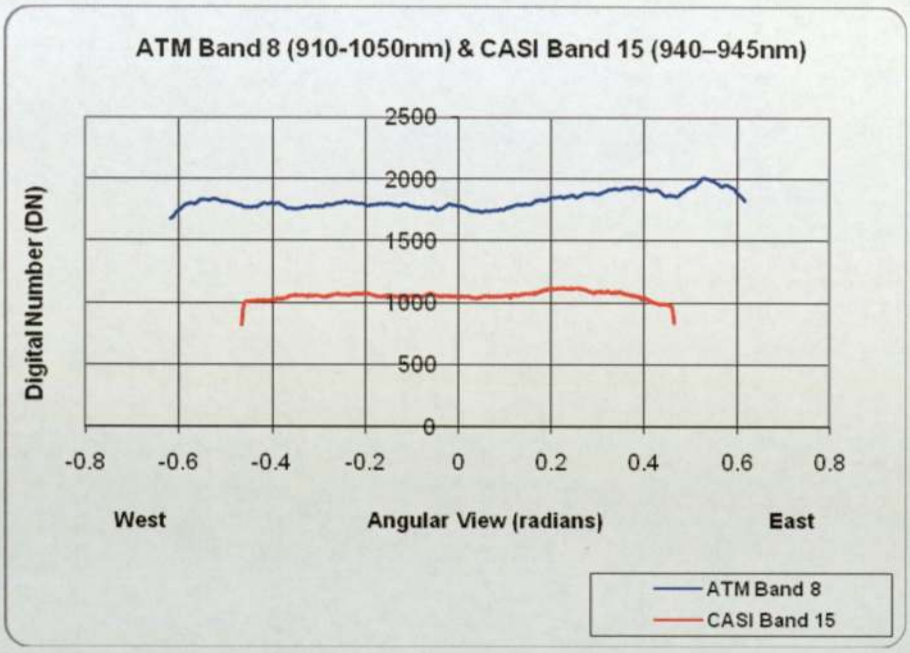

Figure 4-20: The comparison of the angular view between ATM band 8 and average CASI band 15.

Figure 4-13 to 4-20, all depicted the relationship between similar CASI and ATM wavebands with respect to their angular view. In all cases the values represent raw digital values not radiance and hence similar patterns were expected and observed, but none showed the same values or the same shape. This could be due to:

i. Error in the sensor – possibly not responding in a linear fashion

ii. The ATM or CASI sensor not giving the same response to all frequencies in the given wavelength range, and

iii. The slightly different spectral range of each scanner for similar wavebands.

The ATM and CASI, because of the scaling effect do not show the same DN values but should be the same shape. Clearly the curves from Figure 4-13 to Figure 4-20, showed there is a discrepancy of the digital number based on its location across the image. If the variance of the DN's for over forty thousand pixels is large then this variation could be due to the chance of encountering more of one feature type, say water at the centre of the image than at the edges. For example, if column 150 encounters less water than column 460, then this will increase the mean DN for that column.

4.2.3 THE QUALITY ANALYSIS OF ATM BY STANDARD DEVIATION

The next step of the quality analysis is to study the distribution of DN values across the swath of the image. From this point on, only the ATM data is considered. To investigate whether these variations could have arisen by chance, e.g. one scan column could contain a disproportionably high amount of water (which has a low emitted radiation) the standard deviation of each scan column is also considered.

Overall, analysis shows that there is a pattern to these standard deviations with a slight rise towards the ends of the scan line. The standard deviations are an order of magnitude lower than the variation in mean across the columns. This suggests that the variation cannot be attributed to chance inclusions of particular land-cover types and is a property of the sensor.

The green or Band 3 (520–600 nm), shows an increase in mean DN values in the west side, they then decline with a dip in the middle of the image. Towards the east side of the image there is an increase in mean DN values reaching a peak (1430) before a decrease in value toward the end of the line. In a similar situation, the standard deviation show a similar increase at the start, stabilizing in the middle, then reaching a peak in the east side of the image, before a decrease towards the end as shown in Figure 4-21.

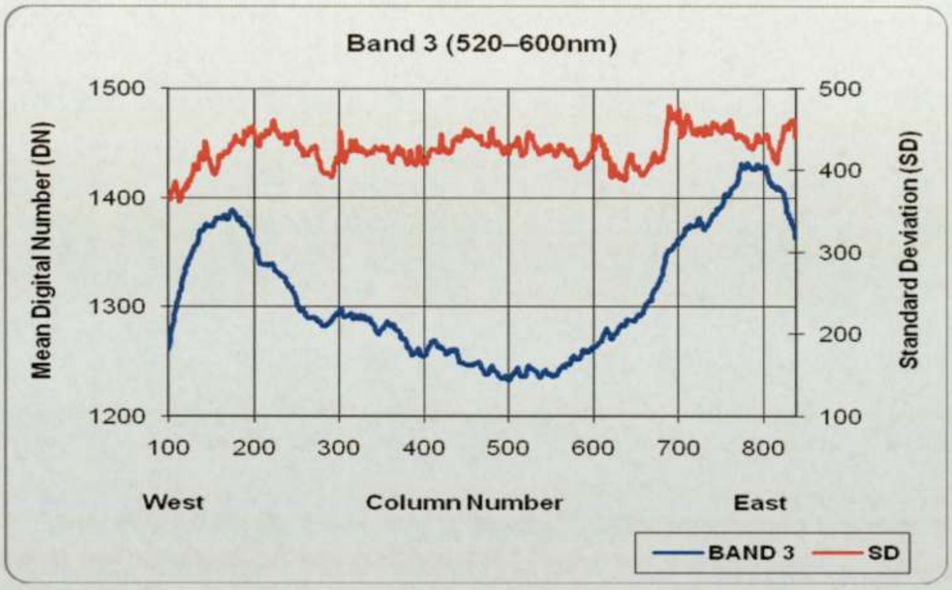

Figure 4-21: The distribution of mean DN value across the swath and standard deviation for band 3.

Like Band 3 (green), the near infrared Band 7 (760–900 nm), shows a similar pattern, see Figure 4-22. The shape and graphical patterns of both plots are more or less similar. However, in Band 7 the individual values are showing higher variance and it is clearly seen that there is lot of fluctuation in DN values when comparing it with Band 3. At pixel 500, a lowest value of digital number (2350) is recorded. The standard deviation has shown a similar pattern to the mean DN, but with lower fluctuations between individual values and a slight dip in the middle. This could indicate that the differences are not arising by chance.

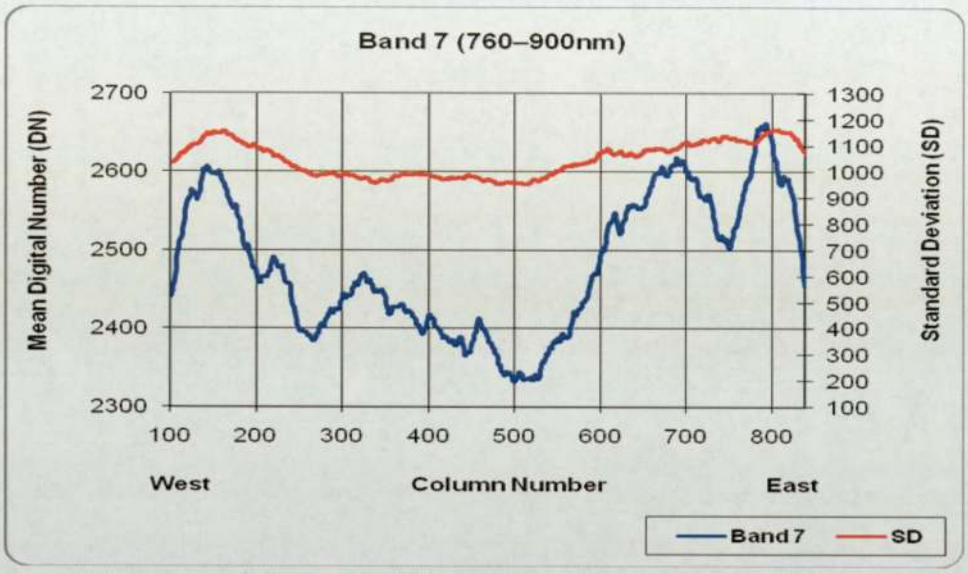

Figure 4-22: The distribution of mean DN value across swath and standard deviation for band 7.

Band 1 (420–450 nm) DN values had shown a dip in the middle of the image in Figure 4-23, and from the west side of the image. It started with a sharp increase in value reaching a peak value up to 2250, before it starts to decline in value reaching its minimum of 2000 at pixel 500. From pixel 550 onwards it rises in value up to 2350 towards the west side on the image. The standard deviation shows a steady fluctuation across the scan line with an average value around 500 throughout the whole imagery

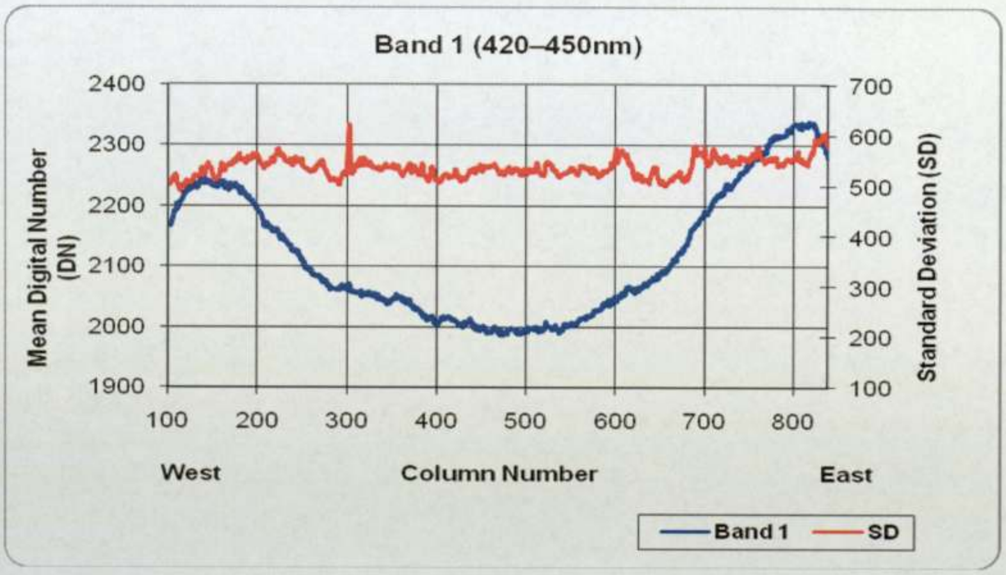

Figure 4-23: The distribution of mean DN value across the swath and standard deviation for band 1.

Like Band 1, Band 2 with (450–520 nm), shown in Figure 4-24, exhibits a similar patterns except different in values. The standard deviation shows a steady fluctuation across the scan line with an average value around 400 throughout the whole imagery and the distribution of DN value across the swath dips in the middle, with a minimum digital value (1075) at around pixel 500.

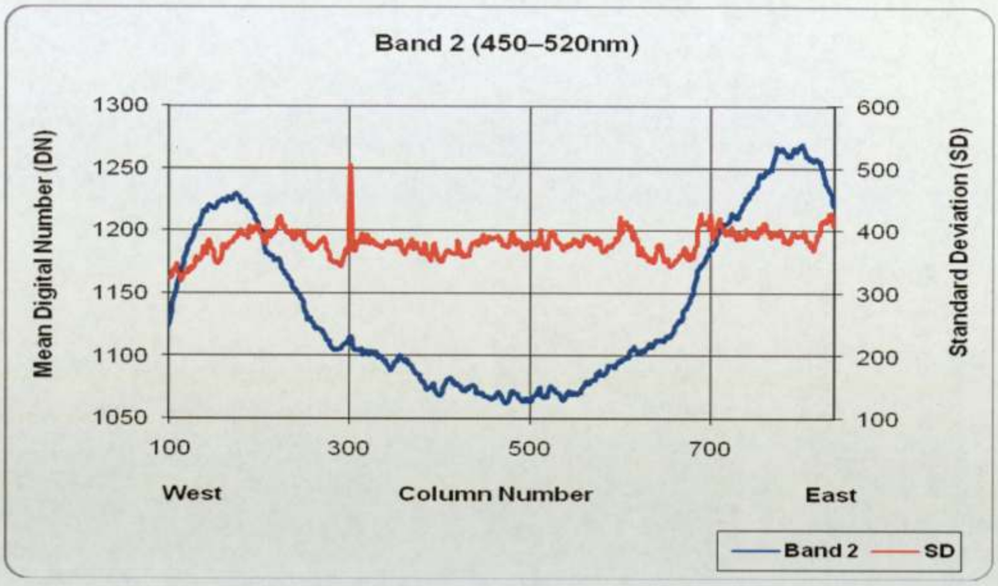

Figure 4-24: The distribution of mean DN value across the swath and standard deviation for band 2.

On the other hand, both Band 4 (605–625 nm) and Band 5 (630–690 nm), Figures 4-25 and 4-26, showed a shift of the dip (lowest digital number to 1160 and 1120 respectively) in middle of the image from pixel 500 towards pixel 600, but with a similar pattern. In both cases the standard deviation is steady with a maximal value of 600 and minimal value is 500 throughout the whole image.

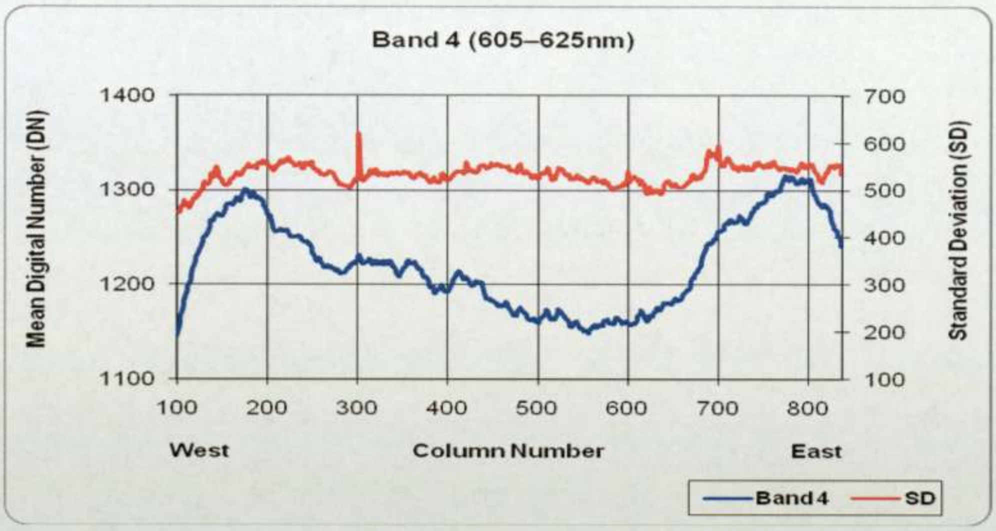

Figure 4-25: The distribution of mean DN value across the swath and standard deviation for band 4.

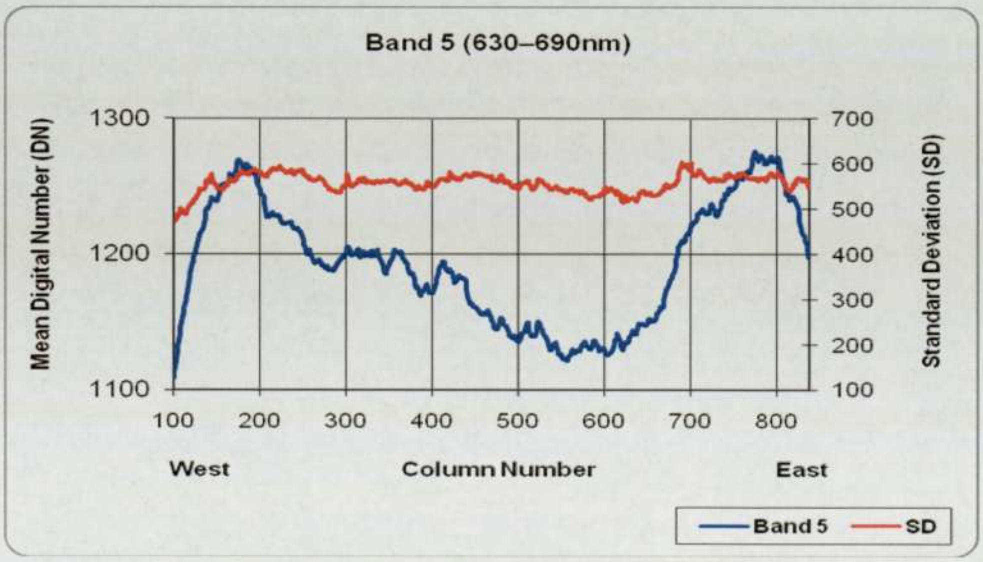

Figure 4-26: The distribution of mean DN value across the swath and standard deviation for band 5.

Figure 4-27, shows the distribution of DN values across the swath and the standard deviation for Band 6 (695–750 nm). For DN values there a dip in the middle of the image. The west side of the image started with a sharp increase in value reaching a peak value up to 2125, before it starts to decline in value reaching its minimum 1925 at around pixel 500. From pixel 550 onwards it rises to 2350 towards the east side of the image. The standard deviation showed a steady fluctuation, with a dip midway across the scan line, with an average value around 600, but an increase in value towards the east side of the image to 700.

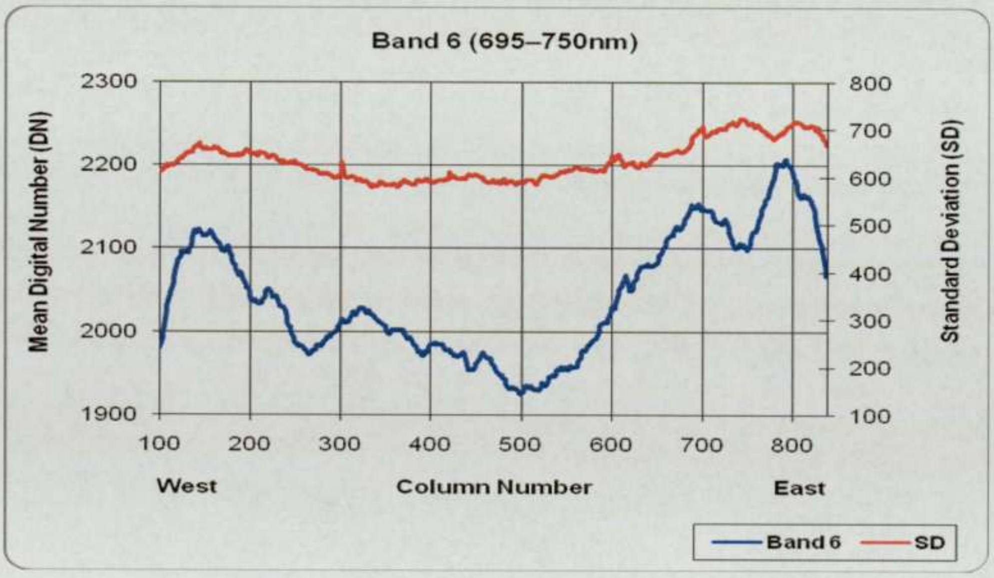

Figure 4-27: The distribution of mean DN value across the swath and standard deviation for band 6.

Figure 4-28, depicts the distribution of mean DN value for Band 8 (910–1050 nm), across the swath and its standard deviation. The strange thing observed is that both the distribution of mean DN value and the standard deviation showed an almost similar fluctuation in pattern and shape throughout the whole scan line. This pattern is unique and never seen in other bands. From the west, the mean DN value and standard deviation increases reaching peaks (1875 and 750 respectively), and then declined and with a dip in the middle of the image at around pixel 500. Towards the east side of the image there is an increase in DN values and standard deviation with a similar pattern and shape.

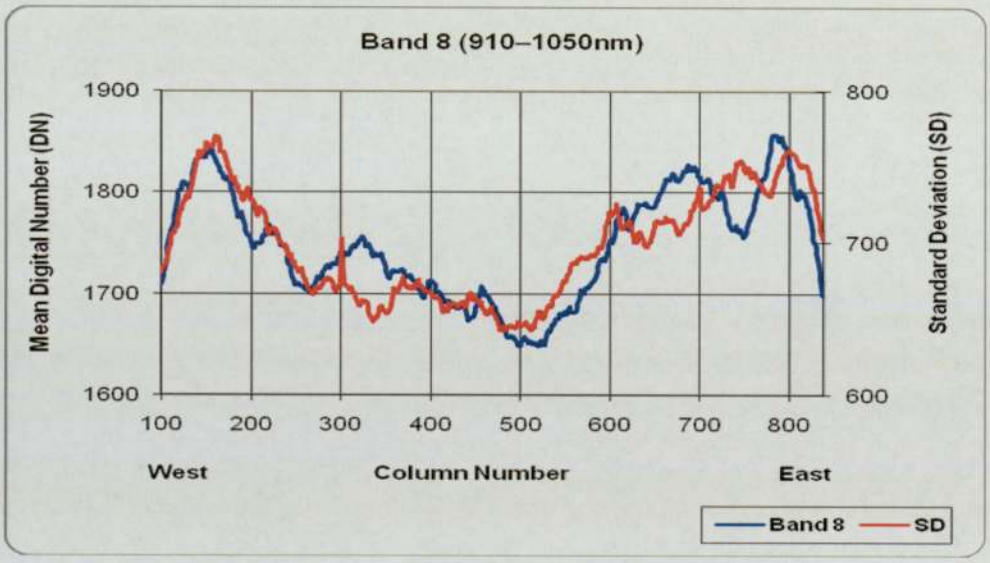

Figure 4-28: The distribution of mean DN value across the swath and standard deviation for band 8.

The plot for Band 9 (1550-1850 nm) is shown in Figure 4-29. In Band 9, an initial increase in DN values in the west side is observed and then it declines with a dip in the middle of the image at around pixel 500. Towards the west side of the image there is an increase in DN value reaching its peak (575) before a decrease in value toward the end. In a similar situation, the standard deviation also shows an increase at the start, stabilizing in the middle with more fluctuations throughout the image. The standard deviation ranges from 100 to 130.

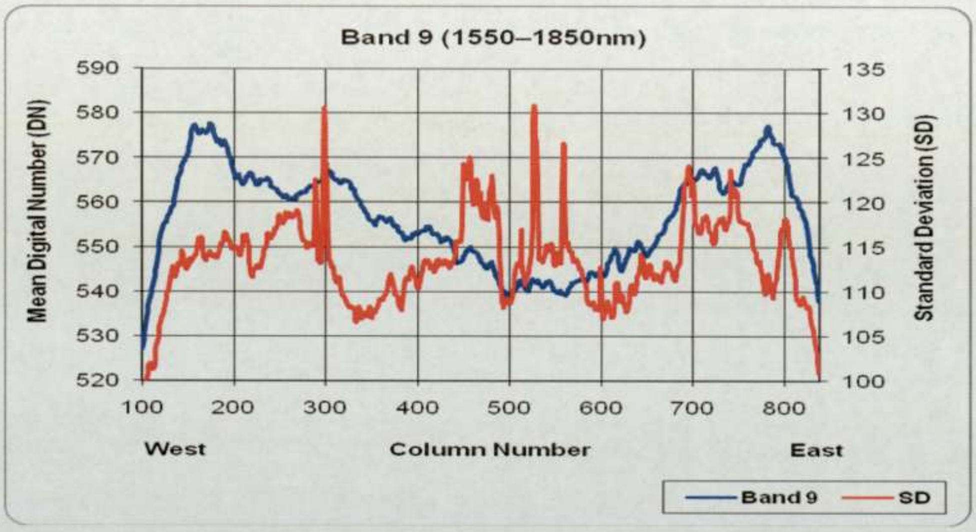

Figure 4-29: The distribution of mean DN value across the swath and standard deviation for band 9.

Band 10 (2080–2350 nm) is shown in Figure 4-30, and has the lowest digital value recorded of all bands through-out the scan line. It shows a similar pattern to Band 9. An initial increase in DN values in the west side is observed, followed by a shift of the dip in the middle of the image towards pixel 600, with a lowest value of 121. The DN values rise towards the west side of the image reaching a peak (131) before it drops at end of the image. Like-wise the standard deviation shows a steady fluctuation with a range of 35-43 and horizontal pattern across the scan line.

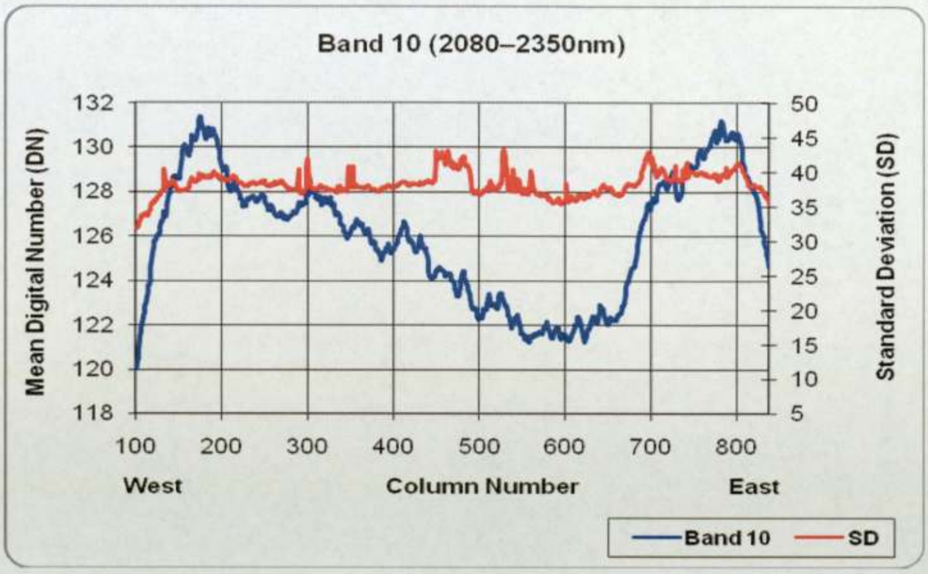

Figure 4-30: The distribution of mean DN value across the swath and standard deviation for band 10.

The thermal Band 11 starts with an increase in DN values (see Figure 4-31), reaching its peak as seen in all other bands, then levels off with an almost horizontal line in the middle, but rises sharply toward the end reaching 7375, before it decreases in value to the east side of the image. The sharp rise in DN values toward the end of the west side could not be plausibly explained; it could be due the angle of the sun. A similar situation is observed in regard to the standard deviation with values ranging from 250-350 throughout the image.

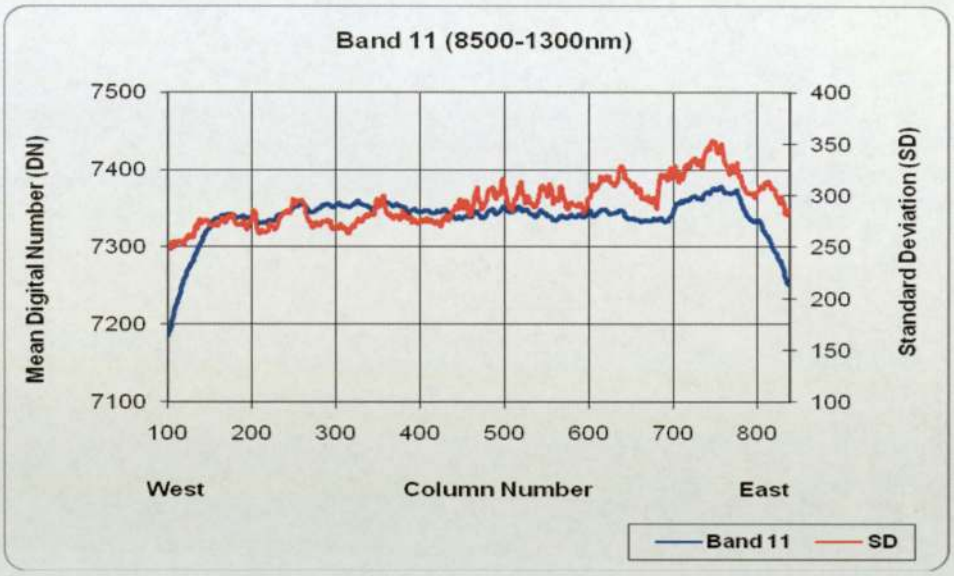

Figure 4-31: The distribution of mean DN value across the swath and standard deviation for band 11.

A 2 tail t-test was applied to all bands to compare the probability of the mean being the same as any another column chosen at random. The results are tabulated from Table 4-2 to Table 4-12 for all bands. All bands adjacent columns showed a higher probability of being the same as compared with the rest. For example, in Band 2 the probability of adjacent column 301 and 302 being the same is 0.953 (Table 4-3), which was very high. But the probability of column 150 from west and column 800 the east being the same is zero.

Band One

2 tail t-test for comparing probability of mean being the same in the sensor position

Column	150	217	301	302	320	510	628	800
150	1	0.767	0	0	0	0	0	0
217	0.753	1	0	0	0	0	0	0
301	0	0	1	0.594	0	0	0	0
302	0	0	0.593	1	0.001	0	0	0
320	0	0	0	0	1	0	0	0
510	0	0	0	0	0	1	0	0
628	0	0	0	0	0	0	1	0
800	0	0	0	0	0	0	0	1

Table 4-2: Shows a 2-tail t-test comparing probability of mean being the same in the sensor position for band one.

Band Two

2 tail t-test for comparing probability of mean being the same in the sensor position

Column	150	217	301	302	320	510	628	800
150	1	0.189	0	0	0	0	0	0
217	0.151	1	0	0	0	0	0	0
301	0	0	1	0.953	0.002	0.011	0	0
302	0	0	0.953	1	0.001	0.009	0	0
320	0	0	0.001	0.001	1	0.773	0	0
510	0	0	0.004	0.004	0.75	1	0	0
628	0	0	0	0	0	0	1	0
800	0	0	0	0	0	0	0	1

Table 4-3: Shows a 2-tail t-test comparing probability of mean being the same in the sensor position for band two.

Band Three

2 tail t-test for comparing probability of mean being the same in the sensor position								
Column	**150**	**217**	**301**	**302**	**320**	**510**	**628**	**800**
150	1	0.24	0	0	0	0	0	0
217	0.014	1	0	0	0	0	0	0
301	0	0	1	0.779	0.008	0	0	0
302	0	0	0.777	1	0.003	0	0	0
320	0	0	0.007	0.003	1	0.001	0	0
510	0	0	0	0	0	1	0	0
628	0	0	0	0	0	0	1	0
800	0	0	0	0	0	0	0	1

Table 4-4: Shows a 2-tail t-test comparing probability of mean being the same in the sensor position for band three.

Band Four

2 tail t-test for comparing probability of mean being the same in the sensor position								
Column	**150**	**217**	**301**	**302**	**320**	**510**	**628**	**800**
150	1	0	0	0	0	0	0	0
217	0	1	0	0	0	0	0	0
301	0	0	1	0.743	0.054	0	0.001	0
302	0	0	0.741	1	0.024	0	0	0
320	0	0	0.05	0.023	1	0	0.152	0
510	0	0	0	0	0	1	0.011	0
628	0	0	0.001	0	0.138	0.014	1	0
800	0	0	0	0	0	0	0	1

Table 4-5: Shows a 2-tail t-test comparing probability of mean being the same in the sensor position for band four.

Band Five

2 tail t-test for comparing probability of mean being the same in the sensor position

Column	150	217	301	302	320	510	628	800
150	1	0	0	0	0	0	0	0
217	0	1	0	0	0	0	0	0
301	0	0	1	0.671	0.228	0	0.011	0
302	0	0	0.669	1	0.104	0	0.003	0
320	0	0	0.222	0.101	1	0.013	0.175	0
510	0	0	0	0	0.01	1	0.235	0
628	0	0	0.009	0.002	0.168	0.245	1	0
800	0	0	0	0	0	0	0	1

Table 4-6: Shows a 2-tail t-test comparing probability of mean being the same in the sensor position for band five.

Band Six

2 tail t-test for comparing probability of mean being the same in the sensor position

Column	150	217	301	302	320	510	628	800
150	1	0	0	0	0	0	0	0
217	0	1	0.004	0.006	0.226	0	0	0
301	0	0.007	1	0.903	0.087	0	0	0
302	0	0.009	0.903	1	0.113	0	0	0
320	0	0.261	0.089	0.116	1	0	0	0
510	0	0	0	0	0	1	0	0
628	0	0	0	0	0	0	1	0
800	0	0	0	0	0	0	0	1

Table 4-7: Shows a 2-tail t-test comparing probability of mean being the same in the sensor position for band six.

Band Seven

2 tail t-test for comparing probability of mean being the same in the sensor position

Column	150	217	301	302	320	510	628	800
150	1	0	0	0	0	0	0	0
217	0	1	0.47	0.402	0.75	0	0.978	0
301	0	0.482	1	0.908	0.298	0	0.505	0
302	0	0.415	0.908	1	0.248	0	0.437	0
320	0	0.756	0.297	0.247	1	0	0.739	0
510	0	0	0	0	0	1	0	0
628	0	0.978	0.487	0.418	0.729	0	1	0
800	0	0	0	0	0	0	0	1

Table 4-8: Shows a 2-tail t-test comparing probability of mean being the same in the sensor position for band seven.

Band Eight

2 tail t-test for comparing probability of mean being the same in the sensor position

Column	150	217	301	302	320	510	628	800
150	1	0	0	0	0	0	0	0
217	0	1	0	0	0	0	0	0.001
301	0	0	1	0.784	0.895	0	0	0
302	0	0	0.784	1	0.887	0	0	0
320	0	0	0.895	0.887	1	0	0	0
510	0	0	0	0	0	1	0	0
628	0	0	0	0	0	0	1	0
800	0	0	0	0	0	0	0	1

Table 4-9: Shows a 2-tail t-test comparing probability of mean being the same in the sensor position for band eight.

Band Nine

2 tail t-test for comparing probability of mean being the same in the sensor position

Column	150	217	301	302	320	510	628	800
150	1	0	0	0	0	0	0	0
217	0	1	0	0	0	0	0	0
301	0	0	1	0.608	0	0	0	0.197
302	0	0	0.609	1	0	0	0	0.402
320	0	0	0	0	1	0	0	0
510	0	0	0	0	0	1	0	0
628	0	0	0	0	0	0	1	0
800	0	0	0.144	0.341	0	0	0	1

Table 4-10: Shows a 2-tail t-test comparing probability of mean being the same in the sensor position for band nine.

Band Ten

2 tail t-test for comparing probability of mean being the same in the sensor position

Column	150	217	301	302	320	510	628	800
150	1	0	0	0	0	0	0	0
217	0	1	0	0	0	0	0	0
301	0	0	1	0.708	0.014	0	0.804	0
302	0	0	0.709	1	0.004	0	0.551	0
320	0	0	0.019	0.006	1	0.206	0.052	0
510	0	0	0	0	0.165	1	0.001	0
628	0	0	0.79	0.521	0.029	0.001	1	0
800	0	0	0	0	0	0	0	1

Table 4-11: Shows a 2-tail t-test comparing probability of mean being the same in the sensor position for band ten.

Band Eleven

2 tail t-test for comparing probability of mean being the same in the sensor position

Column	150	217	301	302	320	510	628	800
150	1	0	0	0	0	0	0	0
217	0	1	0	0	0.843	0.71	0.25	0.024
301	0	0	1	0.732	0	0	0	0
302	0	0	0.73	1	0	0	0	0
320	0	0.855	0	0	1	0.859	0.337	0.038
510	0	0.726	0	0	0.856	1	0.432	0.057
628	0	0.271	0	0	0.321	0.427	1	0.255
800	0	0.027	0	0	0.028	0.048	0.244	1

Table 4-12: Shows a 2-tail t-test comparing probability of mean being the same in the sensor position for band eleven.

The general observation and conclusions for all bands, from the 2 tail t-test comparing the probability of mean being the same with respect to the sensor position was that adjacent columns showed a higher probability of being the same as compared with other columns in all bands. However, the probability that the west and east side columns are the same showed this one not likely; with the probability of the same mean value arising by chance being effectively zero. As the wavelengths increase, the probability of columns being the same was higher in the east as compared to the west side of the imagery. The east side of thermal band is more likely to be the same as compared to the same side of Band 1. In addition to this, in all bands the west side of the imagery showed a lower probability of being the same than the east side of the imagery.

In other-words the probability of pixel 150 (west side) and pixel 800 (east side) being the same but the sample estimates giving different values by chance is 4.6×10^{-56}. This is less than 1000th of the probability of finding an individual atom on the Earth. Clearly this difference could not have arisen by chance alone.

Before quality analysis of mean DN values across the swath of the image is concluded, the standardized mean for all bands, except the thermal band, is plotted against the band wavelength. The thermal band is excluded because of its higher wavelength range and will result in a straight line. Standardized mean is calculated for each band from the average of just over forty thousand rows for each column by Equation 4-2.

$$\textbf{Standardized Mean} = \left[1 - \left\{\frac{Max(bandmean) - (mean)}{(Max(bandmean)) - (Min(bandmean))}\right\}\right] \qquad \textbf{(4-2)}$$

A 2D contour plot for the centre of the band wavelength for each band versus the pixel numbers was created (see Figure 4-32). It is observed that the central dip effect is reduced as the wavelength increases and the centre part of this dip tends towards the east part of the scan line. It also shown, that the edge effect is still pronounced in the final 150 pixels for each edge. The edge effect is largely independent of wavelength.

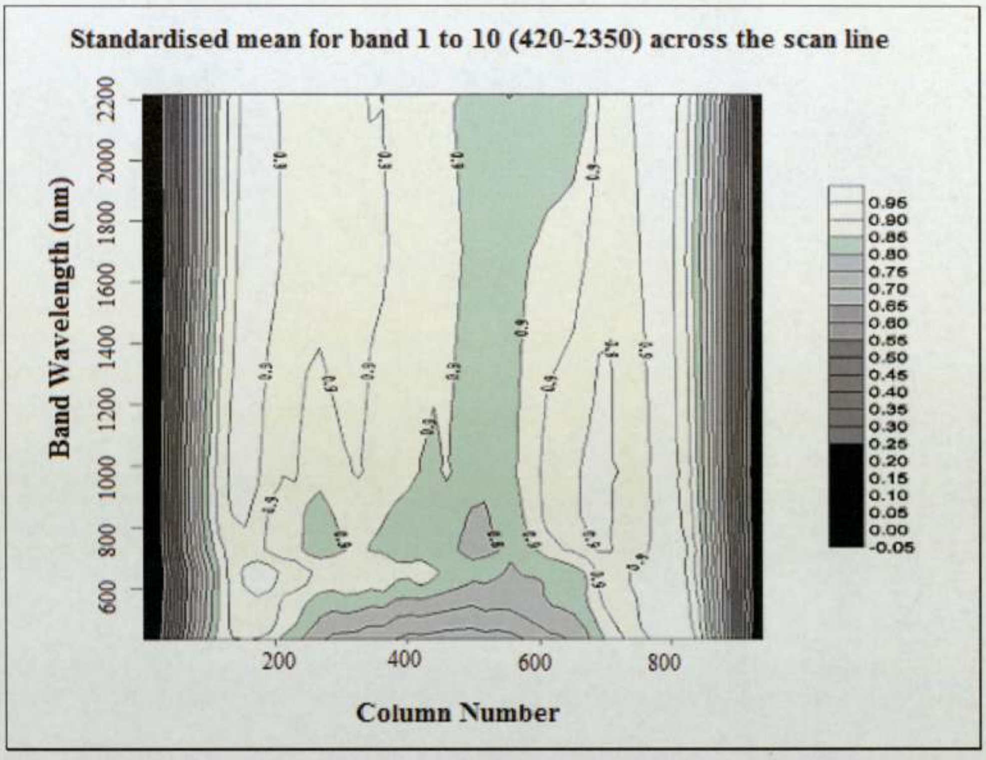

Figure 4-32: A contour of standardised mean plotted against median of the bandwidth vs. Column number of the scan line.

4.2.4 FREQUENCY DISTRIBUTION OF THE DN VALUES

Finally, in the cross track analysis, the frequency distribution of DN values needs to be examined. In order to do so, the centre (column number 502), the west (column 220) and east edge (column number 718) of the image are considered for all bands. All bands had shown an almost similar shape and pattern in the centre, west and east sides of the imagery. Figure 4-33 to 4-43 shows the variation for all bands, but only Bands 5 and 7 will be discussed and interpreted.

In Figure 4-33, Band 7 (760-900 nm), the centre (column 502) shows a rise then drops off suddenly before a reaches the maximum which gradually drops off. On the other hand the east side (column 718) shows a rise then drops unexpectedly at the edge of the scan line. The edge lines also have a larger number of high DN values, which is difficult to explain from the land cover. The west side (column 220) of the image also showed a similar trend and pattern to the east side.

There is a rises in DN value in the middle of the scan line; but it then drops unexpectantly at the edge of the scan line. The edge lines also have a larger number of high DN values, which cannot be explained by the land cover. These few extremely high values could probably be excluded from the image by capping the max DN value to about 7000.

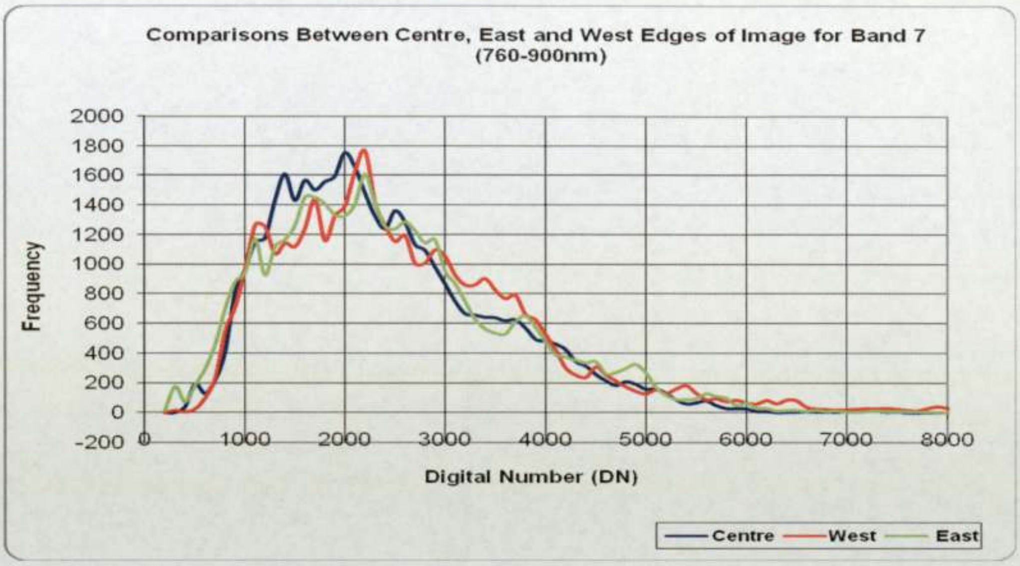

Figure 4-33: Illustrates comparisons between the centre, west and east edge of the image for band 7.

Band 5 (630-690 nm) follows the trend of Band 7 shown in Figure 4-34. In the eastern side there is a similar mode of rise then drops un-expectantly at the edge of the scan line. The edge lines also have a larger number of high DN values, which is hard to explain by specific land cover type.

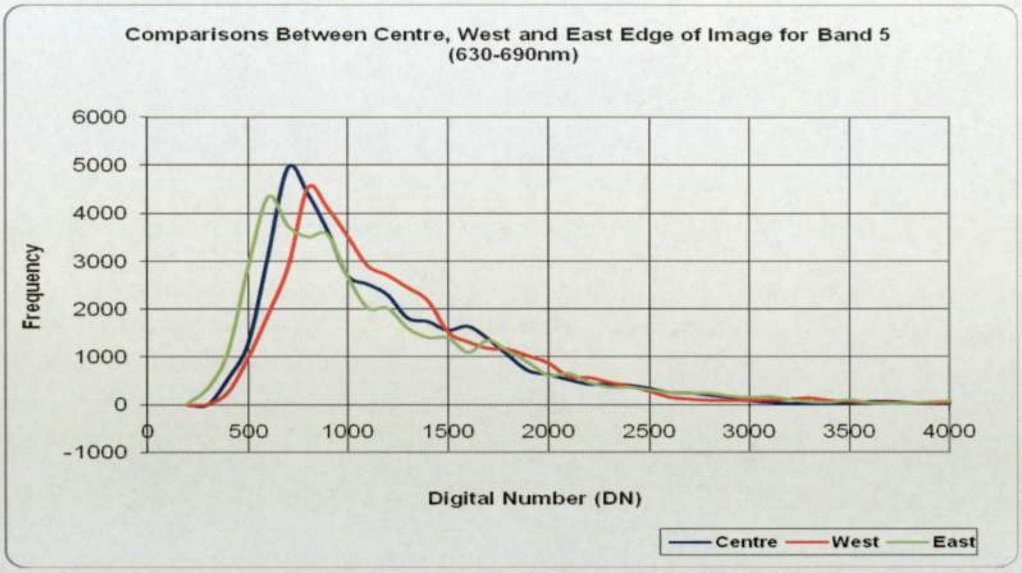

Figure 4-34: Illustrates comparisons between the centre, west and east edge of the image for band 5.

Figure 4-35 for Band 1, showed a lot of fluctuation in the distribution of DN values. The fluctuation was seen in the east, centre and west sides of the imagery and could be caused due to noise and poor quality of the band is seen by visual inspection of the actual imagery. Because of its poor quality, it is difficult to interpret the distribution of DN values throughout the whole imagery of Band 1.

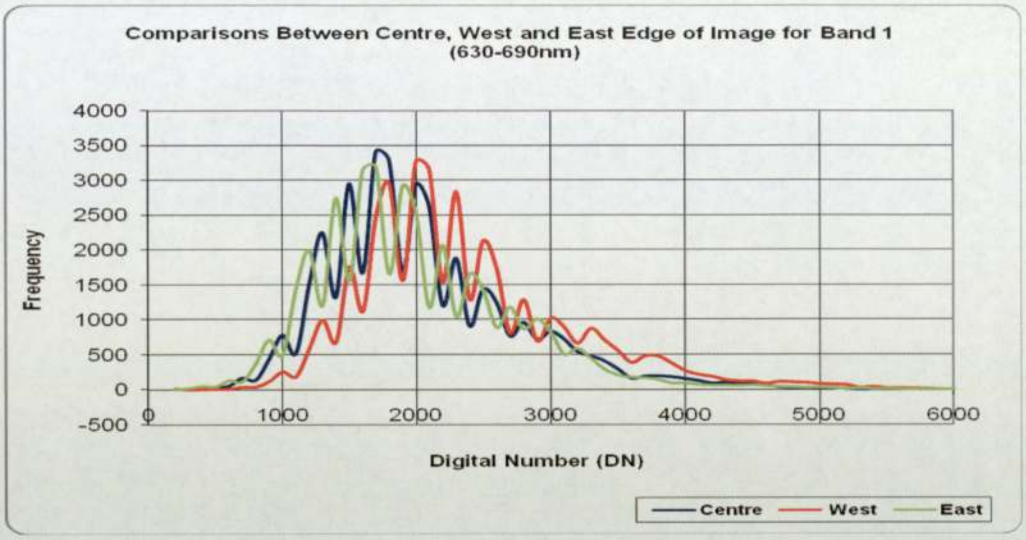

Figure 4-35: Illustrates comparisons between the centre, west and east edge of the image for band 1.

Note: Band 1 is very noisy and its values cannot be relied upon.

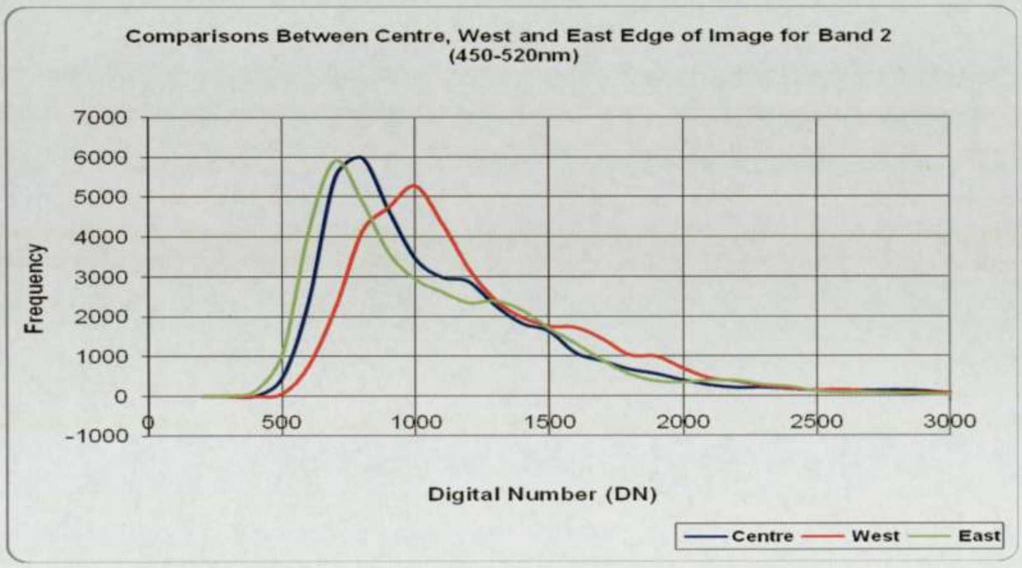

Figure 4-36: Illustrates comparisons between the centre, west and east edge of the image for band 2.

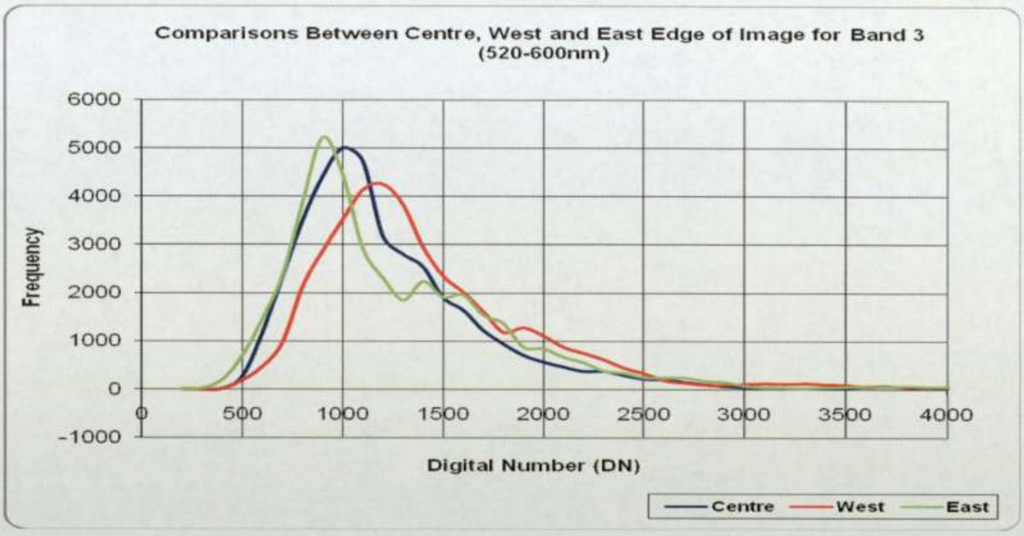

Figure 4-37: Illustrates comparisons between the centre, west and east edge of the image for band 3.

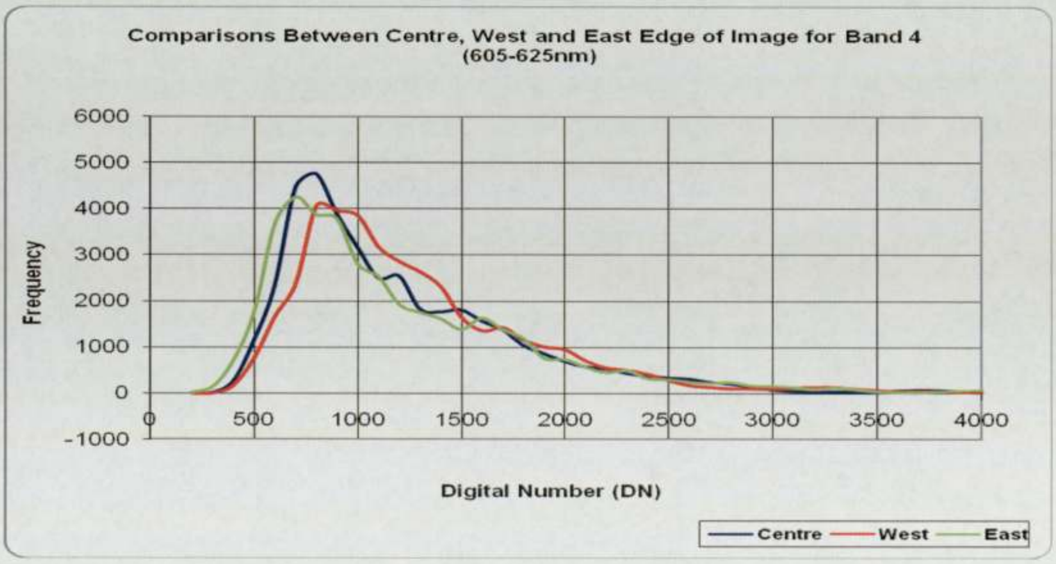

Figure 4-38: Illustrates comparisons between the centre, west and east edge of the image for band 4.

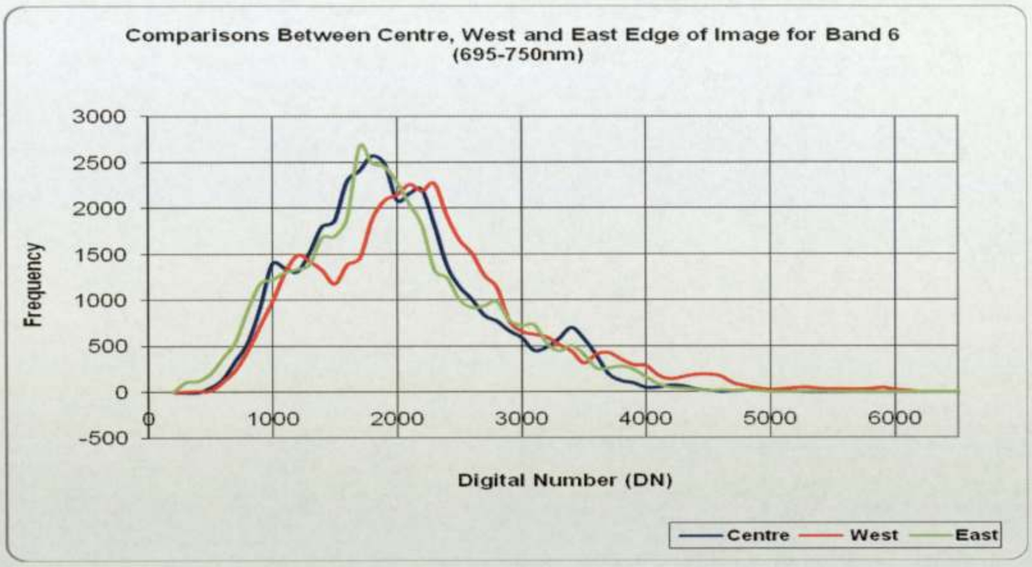

Figure 4-39: Illustrates comparisons between the centre, west and east edge of the image for band 6.

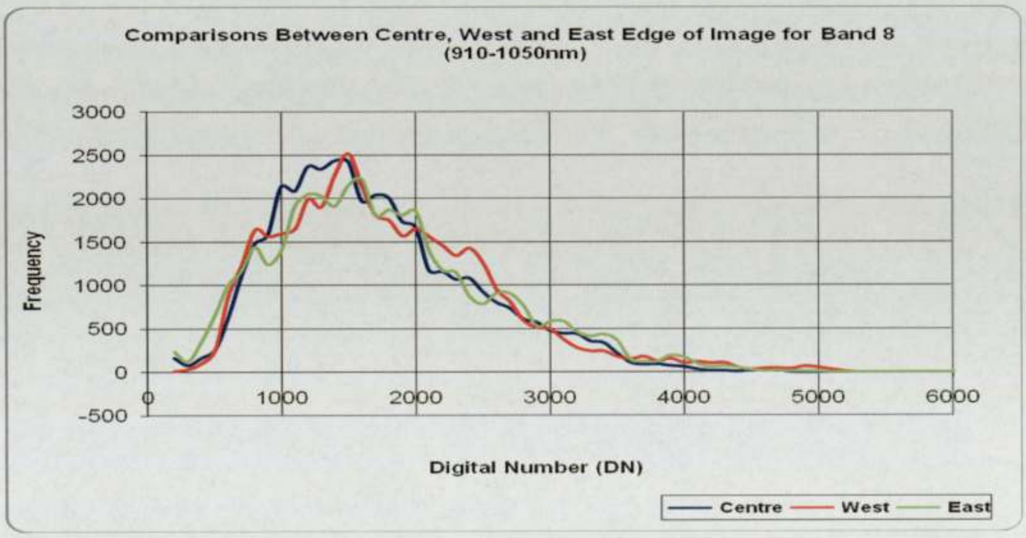

Figure 4-40: Illustrates comparisons between the centre, west and east edge of the image for band 6.

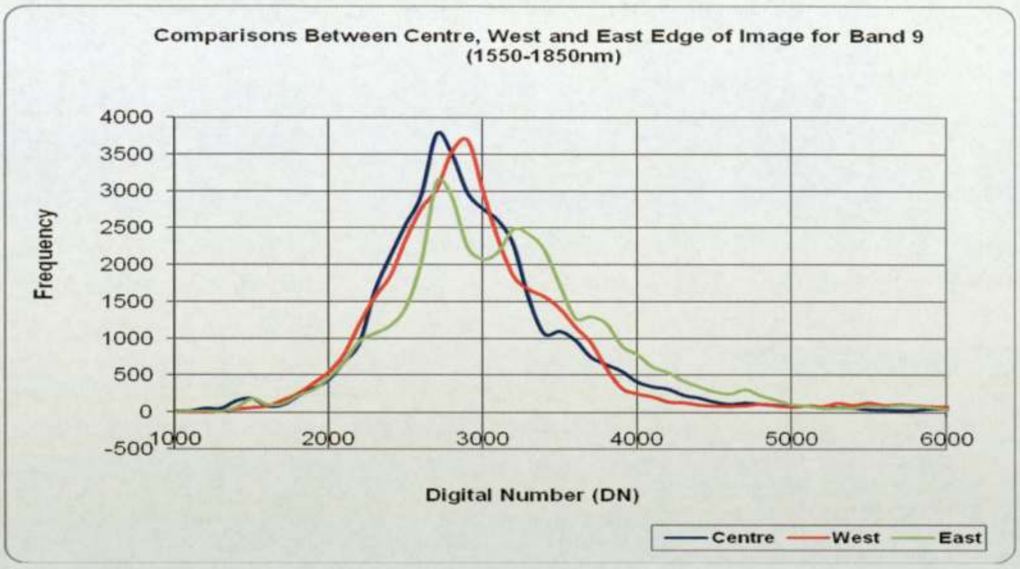

Figure 4-41: Illustrates comparisons between the centre, west and east edge of the image for band 9.

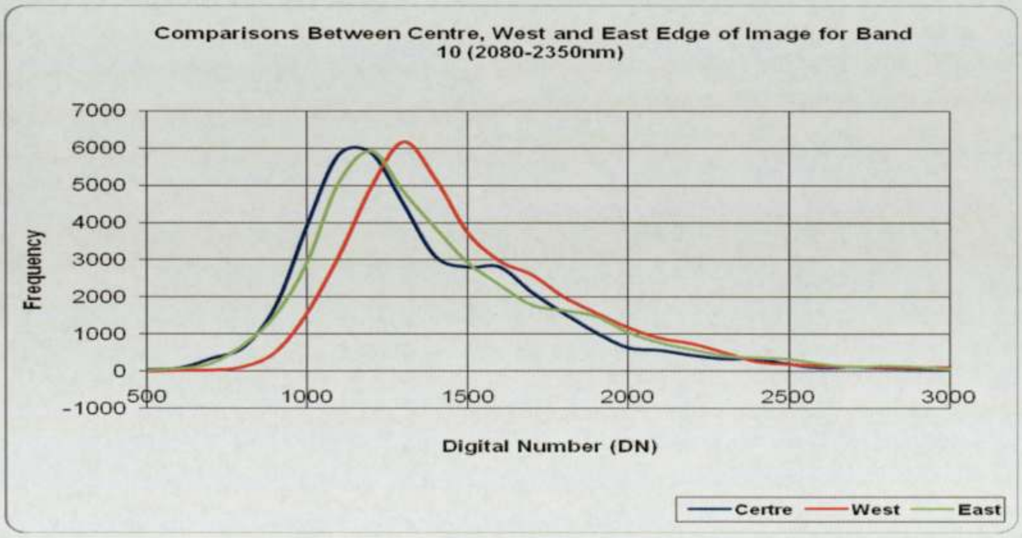

Figure 4-42: Illustrates comparisons between the centre, west and east edge of the image for band 10.

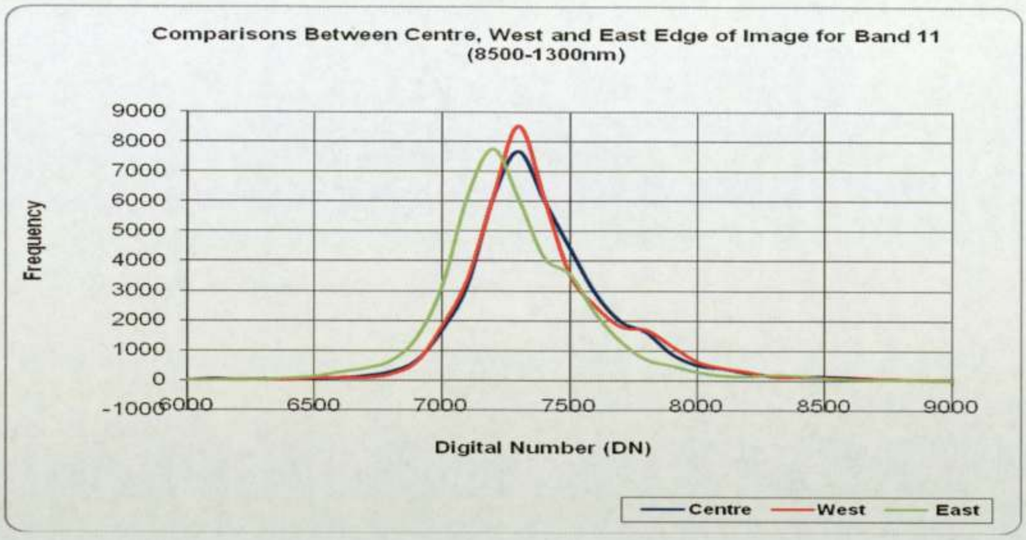

Figure 4-43: Illustrates comparisons between the centre, west and east edge of the image for band 11.

4.3 CONCLUSION

The amount of energy recorded by the sensor from the same land cover at the same location within adjacent flight lines is different because of the position and direction of the aircraft. It is essential that the spectral response received at the sensor from the same land cover is understood and can be corrected for position of the scan line. It is also essential that the data can be accurately overlaid and geometrically corrected.

Section 4.2 discussed the cross scan variation. First, the whole image was studied, and examined for systematic variation across the scan line. The extreme 100 pixels of both edges of the scan line were removed due to anomalous values. These values could be due to the scanner's failure to record correct values at wide view angle.

Secondly, section 4.2.2 showed a comparison between the Airborne Thematic Mapper and Compact Airborne Spectrographic Imager by considering the field of view. The values represented were raw digital values not radiances, and hence in all cases a similar pattern was expected and observed, but none showed the same values or the same shape. This could be due to either error in the sensor – possibly not responding in a linear fashion or the ATM sensor not giving the same response to all frequencies in the given wavelength range. There is a discrepancy of the digital number based on it location across the image. If the variance of the DN's of forty thousand pixels is large then this variation could be due to the chance of encountering more of a particular land cover, say water, at the centre of the image, than at the edges. Theoretically, both sensors should show a similar pattern and shape within the same band width and roughly they do.

Section 4.2.3, examined the quality of the Airborne Thematic Mapper data. This mainly involved a study of the distribution of DN values of the ATM only, across the swath of the image. Moreover, it also investigated whether these variations could have arisen by chance or not. There is a pattern to these standard deviations with a slight rise towards the ends of the scan line. The standard deviations are an order of magnitude lower than the variation in DN values across the columns. This suggests that the variation cannot be attributed to chance inclusions of particular land-cover types and is a property of the sensor. A T-test was applied to all bands to compare the probability of the mean of one column being the same as another column chosen at random. Adjacent columns showed a higher probability of being the same as compared with the rest in all bands. As the wavelength increases, the probability of columns being the same was higher in the east as compared to the west side of the imagery. The standardized mean was considered and it was observed that the central dip effect is reduced as the wavelength increases, and the centre part of this dip tends towards the east part of the scan line.

Finally, this chapter looked at the frequency distribution of the DN values. Thus, it examined how frequent DN occurs by considering the centre, east and west side of the image. There is a rises in DN value in the middle of the scan line; but it then drops un-expectantly at the edge of the scan line. The edge lines also have a larger number of high DN values, which cannot be explained by the land cover. These few extremely high values could probably be excluded from the image by capping the max DN value to about 7000.

In Band 1, fluctuation was seen in the east, centre and west sides of the imagery and could be caused due to noise and poor quality of the band as visible in the actual imagery. For Band 1 because of its poor quality, it was difficult to interpret the distribution throughout the whole imagery.

5 GEOMETRIC ACCURACY

5.1 INTRODUCTION

This chapter will discuss the geometric accuracy of the Airborne Thematic Mapper (ATM). Geometric correction can be termed as the processes of removing geometric distortions and reconstructing remotely sensed images so that they may be treated as a map (Ehlers, 1997). Aircraft usually provide unstable remote sensing platforms because they are flown at relatively low altitude, where air turbulence and fluctuating winds buffet the aircraft, despite the pilot's best efforts to control the manoeuvres. Thus, it is necessary that ATM data undergoes more complex geometric correction and other accuracy assessments techniques, if the data are going to be used any further.

The first section in this chapter discusses the geometric correction. Geometric correction is a process of eliminating, to a satisfactory degree, errors of a geometric nature resulting from sensor imperfections, surface relief and the relative motions of the sensor platform and the underlying scene. The data provided by NERC was not geo-corrected, but can be processed using AZGCORR software supplied by NERC (see Chapter 3). This section looks at both non-parametric and parametric geometric correction of airborne remotely sensed scanner imagery, and subsequently it checks the geometric accuracy of linear features, such as the roads and field boundaries. Each stage of the generic geometric correction process is described. Geometrically correct images are required for the integration of the image data with other information in a spatially referenced database. Applications that require geometrically correct images include land cover mapping, image mosaicing incorporation of other geographic data, and multitemporal studies. The second and third sections discuss in detail geometric accuracy and mosaicing of the images.

Finally, the entire chapter on geometric accuracy is concluded with some recommendations for its suitability for further applications being made.

5.2 UNPROCESSED FLIGHTS

On receipt from NERC, the raw data from the flight was Level 1. The HDF format contained all the attitude and positional information at a per scan line frequency along with the uncorrected scanned data. The data can be processed using AZGCORR (see Section 3.8.6) to geo-correct the data to Level 3. This software takes the ATM image data from the flight path and with this information it creates a map projection referenced output image.

Level 1B data products are reconstructed, unprocessed instrument data at full resolution, time-referenced, and annotated with ancillary information. This includes radiometric and geometric calibration coefficients and geo-referencing parameters, e.g. platform ephemeris, external and internal sensor orientation parameters. Platform/sensor exterior orientation parameters appear both in unprocessed and dGPS-corrected format (if base station GPS time-series were available). Consequently, the Level 1B file is a completely self-descriptive file, enabling a full geometric correction.

The images are oriented with the vertical image axes, from top to bottom, lying approximately north to south. Figure 5-1 shows the flight line 7 of the near infrared band (760-900 nm). Bands 5 of flight line 4 (630-690 nm) and Band 10 of flight line 10 (2080-2350 nm) are shown in Figure 5-2 and Figure 5-3 respectively.

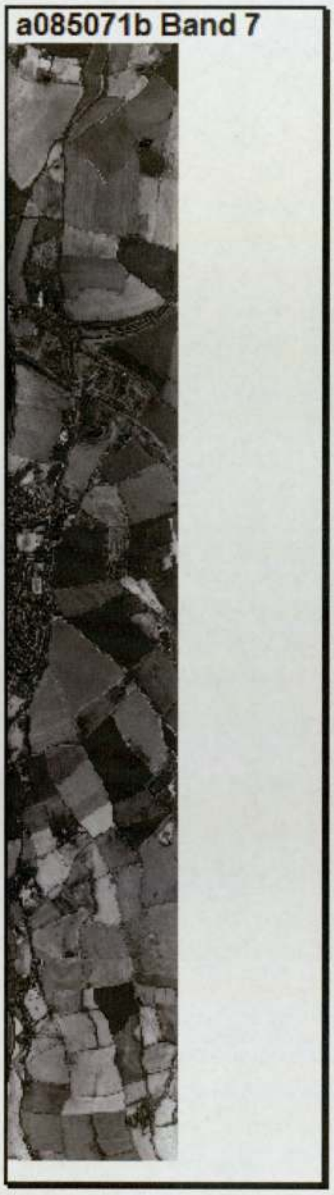

Figure 5-1: Unprocessed image data for near infrared band (760–900 nm).

Figure 5-2: Unprocessed image data for bands five of flight line four (630-690 nm).

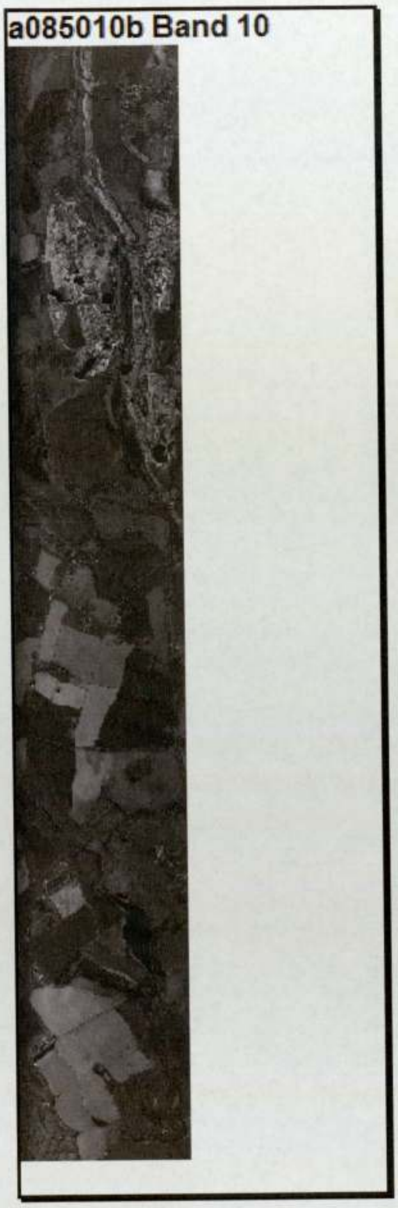

Figure 5-3: Unprocessed image data for band ten of flight line ten (2080-2350 nm).

5.3 THE CONCEPT OF GEOMETRIC CORRECTION

A general concept for geometric correction must be oriented towards a holistic philosophy that takes into account all available auxiliary information. The aim is to get an optimal solution, even if the initial information is sketchy. Generally, a geometric correction is divided into two main processing steps. These are: first, the establishment of a three-dimensional coordinate frame based on the reference system; and second, the resampling of the hyperspectral or multi-spectral image data. Sometimes purists prefer to do without the interpolation of values because they want to keep the radiometric information unchanged.

5.3.1 PARAMETRIC CORRECTION

The proposed geometric correction relies on a parametric approach taking into account the viewing geometry and geometric distortion due to the sensor, platform and topography. Potentially, this method provides high accuracy, robustness and consistent results over the full image. The performance of the geometric correction is validated relative to a geo-located digital map. A physical model can mathematically describe all distortions of the platform (position, velocity, orientation), the sensor (view angles, IFOV, panoramic effects), the Earth (ellipsoid, relief) and the cartographic projection. Such a model needs sensor information and a small number of ground control points (GCPs) to compute and refine the parameters of the mathematical model (Toutin, 2004). The sensor information required comprises sensor altitude, actual inclination, sensor across- and along track angle and IFOV. Required image scene information is pixel spacing at nadir, the approximate scene centre, as well as the underlying ellipsoid and a digital elevation or surface model (Barnsley *et al.,* 2004).

During the first step, the coordinates for each pixel of the hyperspectral data set are determined. To do this a three-dimensional coordinate frame is established and filled during the subsequent processing. The best case would be if the position and the attitude of the flight path were directly measured with high precision during the mission.

The parametric correction is carried out by the AZGCORR software. The geo-correction program uses the data file coordinates to guide the resampling of the sensed image onto a regular Earth-based coordinate grid and produces a parametrically corrected image (see Figure 5-4 and Figure 5-5). This can be computed for all the ATM image bands, at different image scales and surface coverage and using different resampling techniques without the need to re-compute the coordinates.

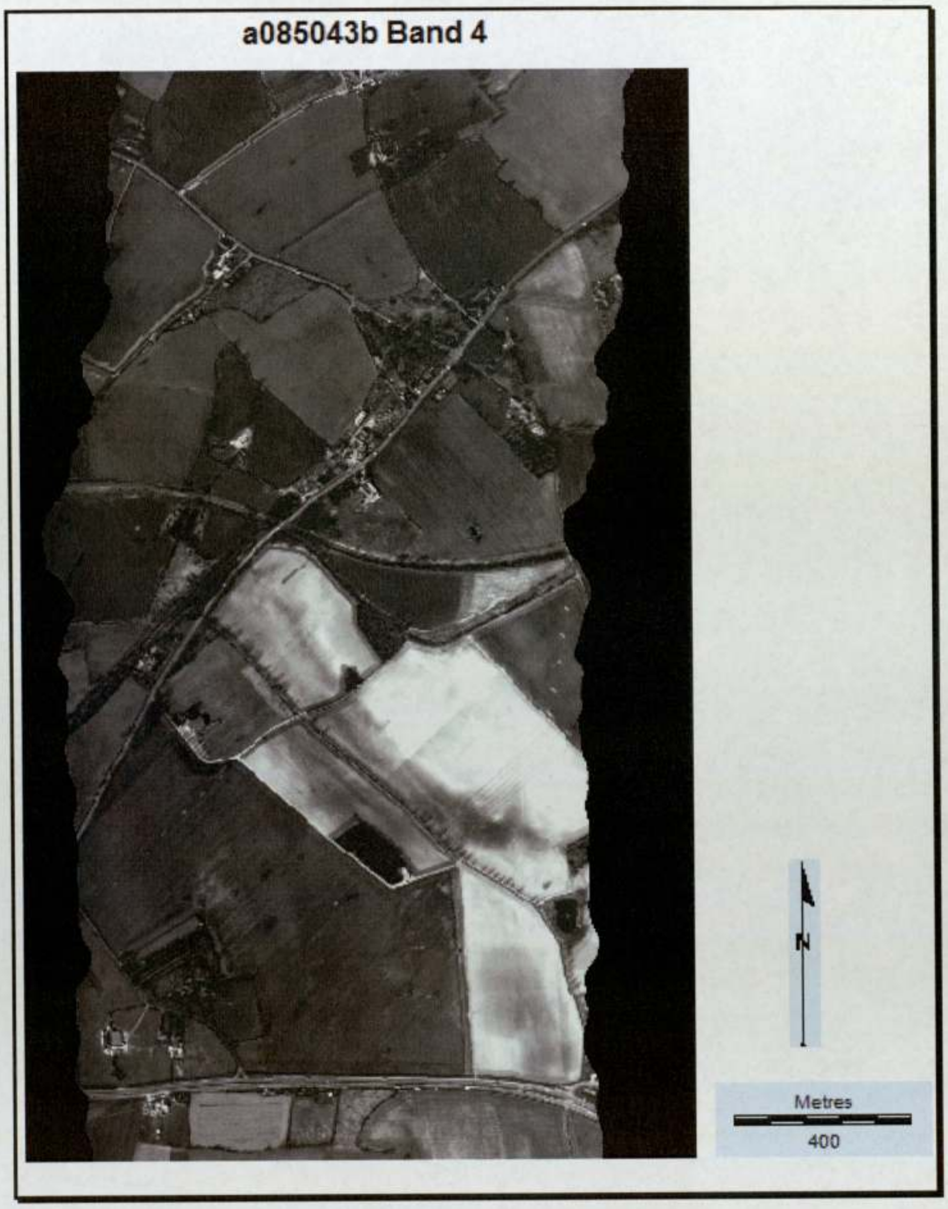

Figure 5-4: A parametrically corrected image for flight four of the red band (605-625 nm).

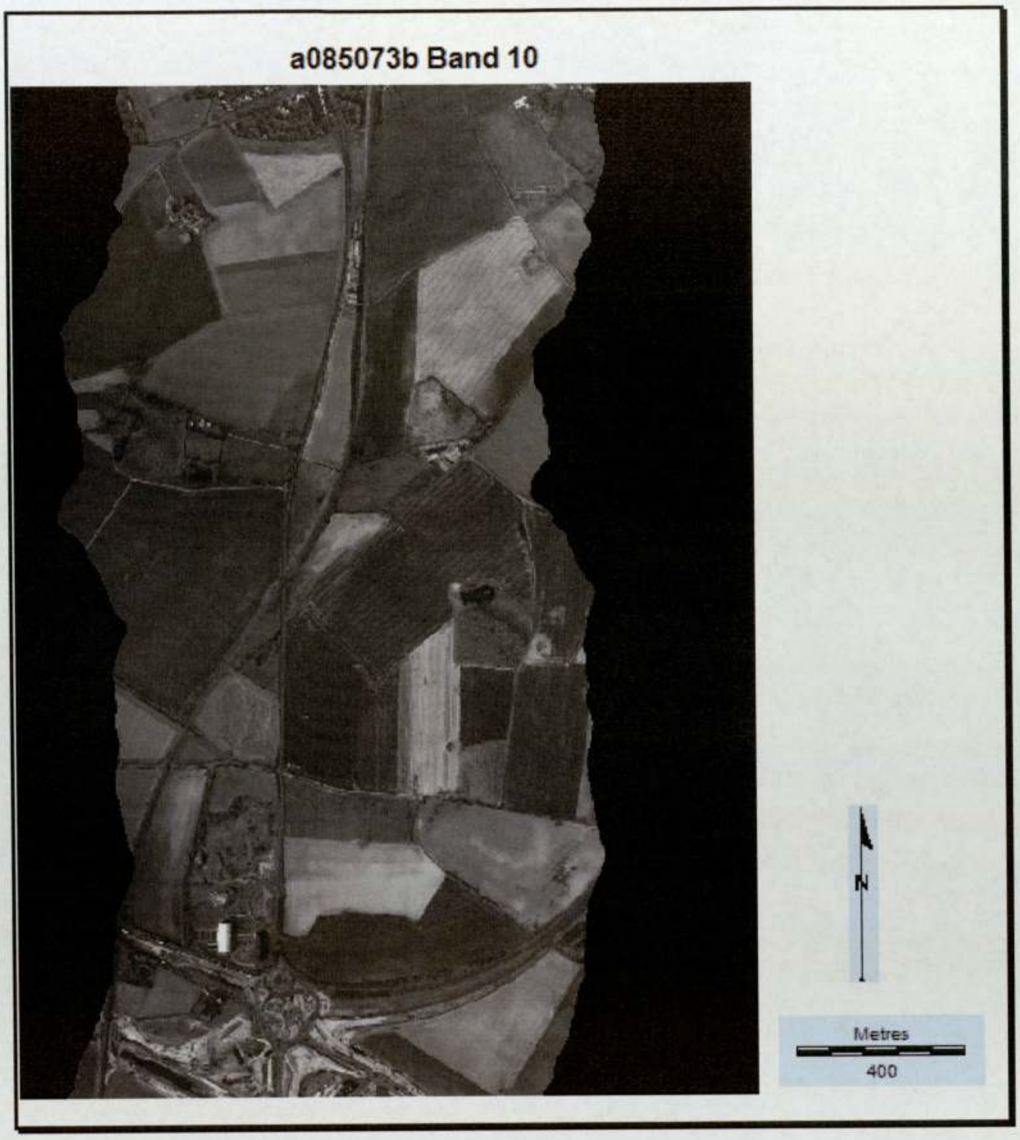

Figure 5-5: A parametrically corrected image for flight seven of the middle infrared band (2080-2350 nm).

Within a parametric approach, all parameters of the time-variant image capturing process can be modeled rigorously. Normally this is done within an adjustment procedure, which allows the modeling of error propagation. With a parametric approach, it is possible to model the inherent disturbing effects individually because of the fact that even correlation between observations can be modeled, if they are known. However, these methods need adequate initial auxiliary information like position and attitude data, a DEM and/or a reference Ordnance Survey (OS) map. The level 3 imagery was not in OS coordinates with error in rotation throughout the imagery.

5.3.2 NON-PARAMETRIC CORRECTION

The level 3b ATM data will be geocorrected to real world coordinates using the resampling module of Idrisi. Geocorrection involves the identification of multiple GCP on the imagery for which real world coordinates are known or can be deduced from existing data. In common practice, the image data will be geocorrected using OS 1:10,000 scale base maps as a source for GCP. All image processing (vegetation indices, transforms, statistical analysis, etc.) will take place using uncorrected imagery, with the outputs of analysis being geocorrected using a set of standard GCP for each image. However for multitemporal imagery and mosaicing images together, individual bands need geometric corrections. The geocorrection of each image will be error checked and constrained to a target root mean square error (RMSE) of 4.0 metres or less.

During the second of the resampling steps, the image data were transformed to the regular grid of the reference frame. The non-parametric correction is carried out using GCP. This coordinate system transformation can be achieved by transforming the coordinates. In this manner the image need only be re-sampled once by the nearest neighbour method, reducing image degradation effects due to successive application of resampling procedures. When the image is geo-corrected with the GCPs, a report is generated after the transformation indicating how much the image had to been changed and the accuracy of the new image using the RMSE.

5.3.3 QUANTITATIVE ANALYSIS OF GEOMETRIC CORRECTION ERRORS

The resampling process includes two steps. The first is determination of polynomial mapping function and applying least square method to the set of GCPs selected. The GCPs are used to create an equation indicating how far in the X and Y directions each pixel should be moved to rectify the image. The polynomial mapping functions of second order is established and it is formulated as follows (Shaker et al., 2002).

$$X = b_0 + b_1 X_0 + b_2 Y_0 + b_3 X_0 Y_0 + b_4 X_0^{\,2} + b_5 Y_0^{\,2}$$

$$Y = a_0 + a_1 X_0 + a_2 Y_0 + a_3 X_0 Y_0 + a_4 X_0^{\,2} + a_5 Y_0^{\,2} \qquad \textbf{(5-1)}$$

Where, X_0 Y_0 are image coordinates and X, Y are ground coordinates. Both $a_0 \sim a_5$ and $b_0 \sim b_5$ are unknown coefficients determined by minimizing the sum of squared error. Using the mapping functions, the resampling procedure is carried out in the final step. The resampling was performed by transformation of pixel locations in the navigated image to corresponding locations in the resulting output image. In the transformation, the nearest neighborhood interpolation technique is used.

5.3.4 RMSE FROM MAP TRANSFORMATION

The estimated parameters describing the upwards transformation, together with the DEM of the area, were used to rectify the image. Then the OS map at 1:10,000 scale was overlaid, resulting in the product shown in Figure 5-6 and Figure 5-7.

Figure 5-6: Rectified ATM (a085073b) image with OS map.

Figure 5-7: Zoomed section of rectified ATM (a085073b) image with OS map.

In this phase of the analysis, the data is Level 3 and it simply needs to be repositioned to BNG. GCPs that had the best distribution and gave the minimum errors were chosen for geometric transformation (see Figures 5-8 and 5-9 for a085073b, band 7 and a085063b, band 7 respectively). Airborne images sensed with low geometric distortion can be adequately corrected using low order polynomials. Polynomials are usually not suitable to correct airborne line scanned imagery. This is because of the global nature of the least squares technique, where local image distortions and GCP position errors are not accurately modelled but are averaged out across the image. Generally, polynomial functions suffer inherent limitations, due to the requirement for large numbers of GCPs in high order polynomial models, difficulties in assessing where to place GCPs, sensitivity to GCP placement near the edges of the image, and computational problems.

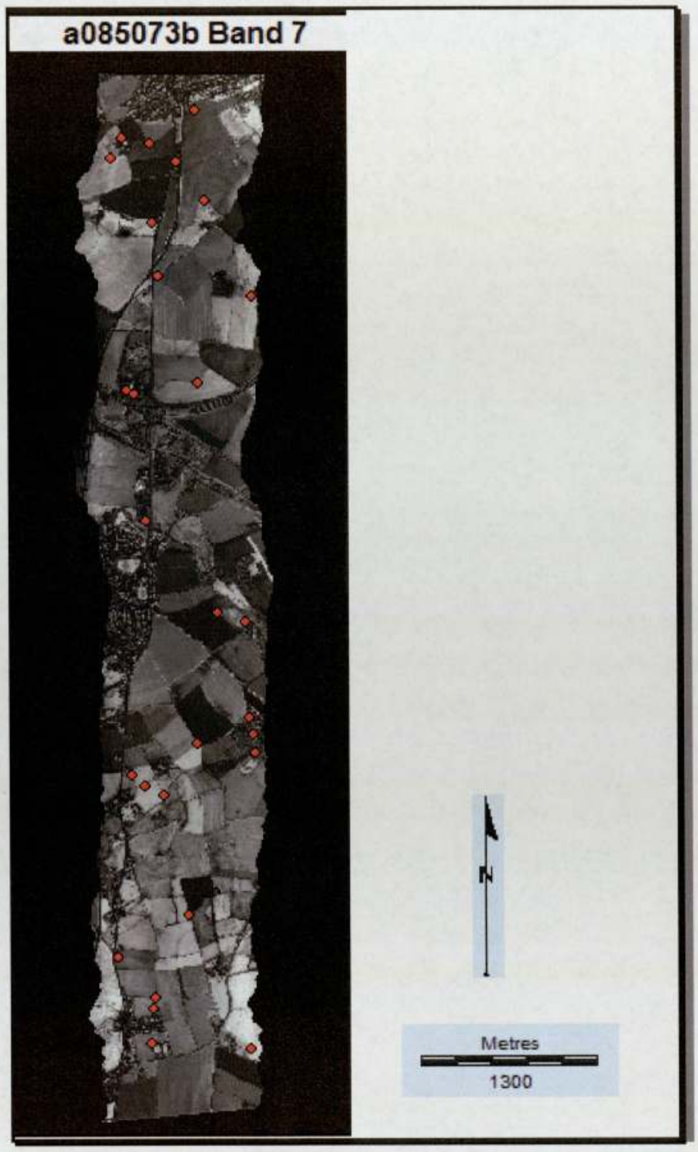

Figure 5-8: GCPs used for map transformation for a085073b, band 7.

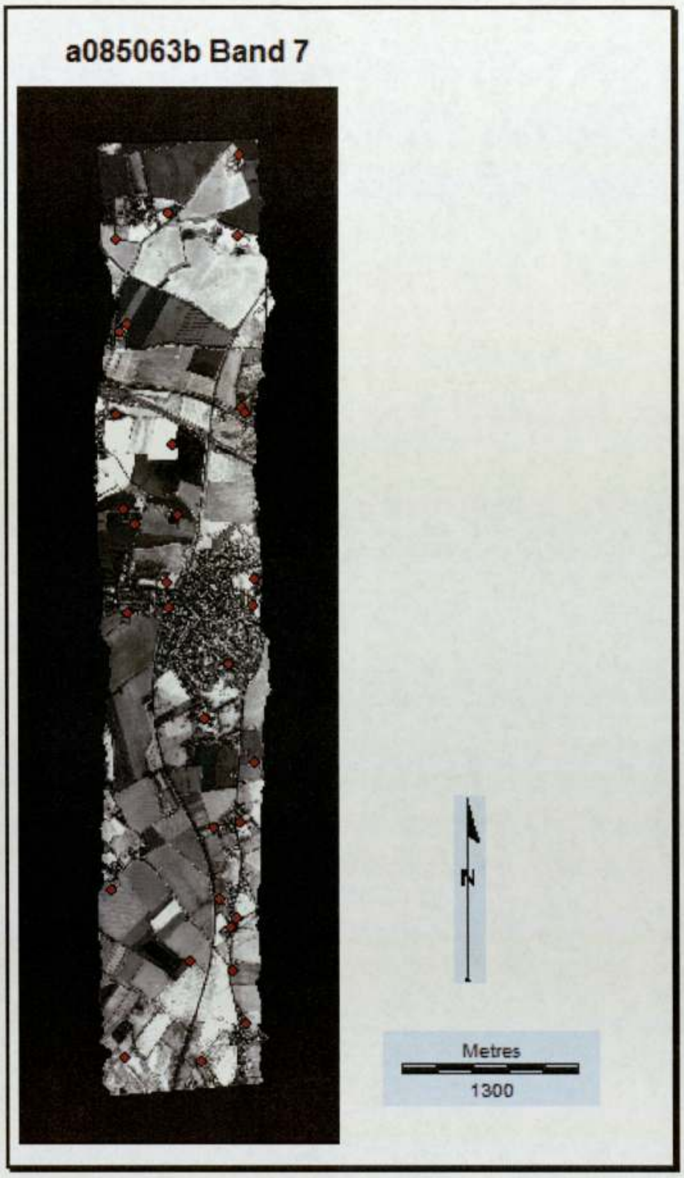

a085063b Band 7

Figure 5-9: GCPs used for map transformation for a085063b, band 7.

There is an iterative process that takes place. First, all of the original GCPs (e.g. 20 GCPs) are used to compute an initial set of coefficients. The root mean squared error (RMSE) associated with each of these initial 20 GCPs is computed. Then, the individual GCPs that contributed the greatest amount of error are identified and deleted (see Figures 5-10 and 5-11 for the omitted GCPs for a085063b and a085073b, band 7 in green colour). After the first iteration, this might only leave 16 of 20 GCPs. A new set of coefficients is then computed using the remaining 16 GCPs. The process continues until the RMSE reaches a user-specified threshold (e.g. 4.0 metre error). Figure 5-12 depicts the zoomed distributions of GCPs for a085073b.

The goal is to remove the GCPs that introduce the most errors into the multiple-regression coefficient computation and maintain a sensible distribution. When the acceptable threshold is reached, the final coefficients and constants are used to rectify the input image to an output image in a standard map projection. When ground control points are selected, they need to be from various locations, i.e. the centre of the image, the corners and the edges of the image. Figure 5-10 and Figure 5-11 illustrate the distributions all GCPs used to calculate RMSE for independent checkpoints, for map transformation and omitted GCPs in the affine transformation for flight seven (a085063b), and flight a085073b, band 7 respectively.

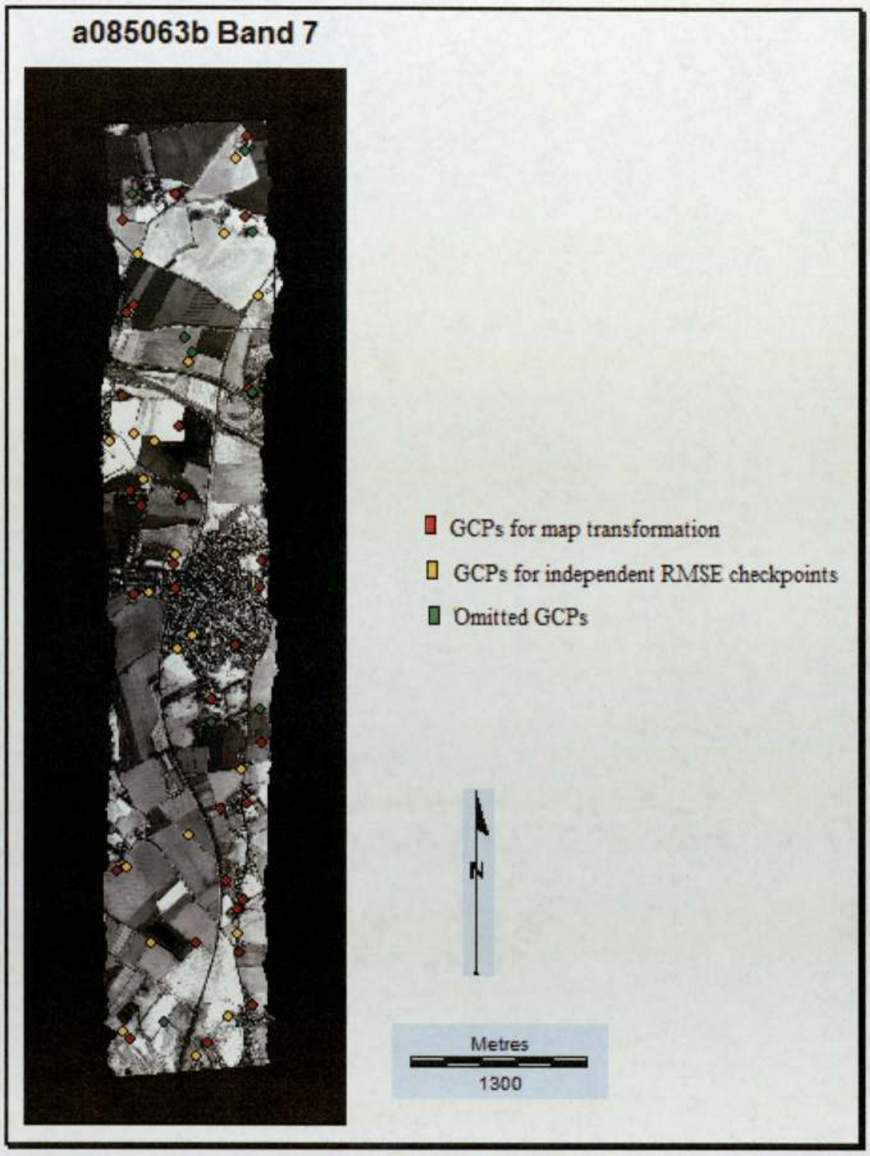
a085063b Band 7

Figure 5-10: GCPs used to calculate RMSE for independent checkpoints (yellow colour), for map transformation (red colour) and omitted GCPs (green colour), for a085063b, band 7.

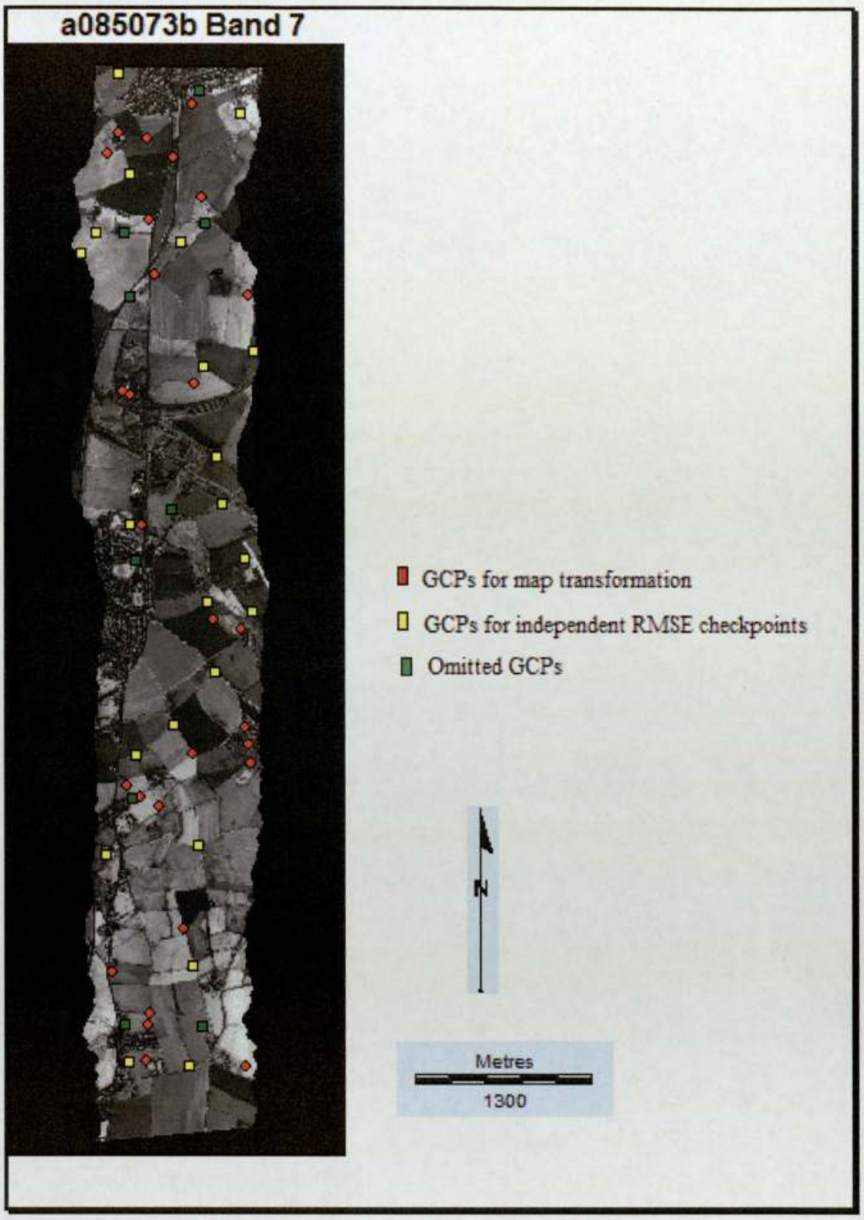

Figure 5-11: GCPs used to calculate RMSE for independent checkpoints (yellow colour), for map transformation (red colour) and omitted GCPs (green colour), for a085073b, band 7.

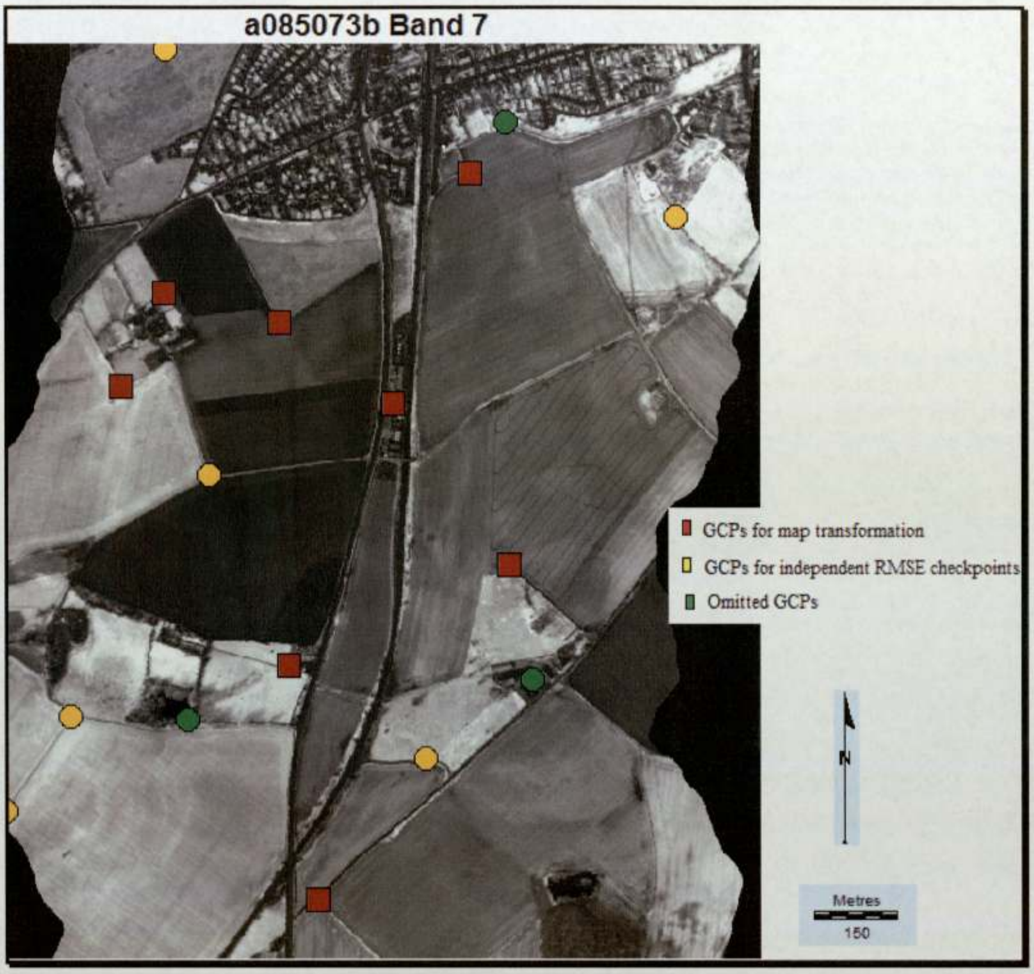

Figure 5-12: Zoomed GCPs used to calculate RMSE for independent checkpoints (yellow colour), for map transformation (red colour) and omitted GCPs (green colour), for a085073b, band 7

Often one might see that majority of GCPs have residuals, but that one or two have much larger errors. These GCPs with large errors may have been incorrectly located and one should go back and recheck them or omit them before executing the equation. RMSE is calculated on the fit of the points; if there is a good connection between the points then the RMSE will be low. A low RMSE could be masking the fact that the image does have large errors, but it generally gives an indication of the amount of inaccuracy. In all flights the RMSE ranges from 2.2-4.3 metres (see Table 5-1), which is considered to be a good accuracy. The day time appears to be a lot better than the night time flight, due the fact that it is easier to identify more accurate and clearer GCPs in the day time than in the night flights.

Flights	Image RMSE(m)	Ground Control Points used
Day 85 flight 4	2.456768	19
Day 85 flight 5	3.869167	24
Day 85 flight 6	3.997012	30
Day 85 flight 7	2.922208	28
Day 85 flight 8	3.966447	25
Day 85 flight 9	3.929155	25
Day 85 flight 10	4.222610	24
Day 86 flight 1	3.929155	25
Day 86 flight 2	3.977579	17
Day 86 flight 3	4.247019	21
Day 86 flight 4	2.296062	17
Day 86 flight 5	3.782730	30
Day 86 flight 6	3.819920	23
Day 86 flight 7	3.797801	36

Table 5-1: RMSE for the day and night flight and ground control points used.

Note: Day 85 was daytime flight and Day 86 was night time flight.

Coefficients determined from the affine transformation are tabulated in Tables 5-2 and 5-3 for the night and day flight respectively. Coefficients a_0 and b_0 are simply translations to British National Grid (BNG), while a_1 and b_1 refer to rotation and shear. These tables show the direction and magnitude change in the X and Y axis from the original image to the output image. The whole detailed affine transformation with each GCP can be found in Appendix 5. It is difficult to attach specific physical meanings to these coefficients in a second order polynomial.

Night Time Flights

Resample: Summary of Transformation a086013b
Computed polynomial surface: Quadratic (based on 25 control points)

Coefficient	X		Y
b_0	2360005.0	a_0	-1632834.0
b_1	-13.2	a_1	5.3
b_2	0.6589458304644609	a_2	2.2
b_3	0.0000182189900889	a_3	-0.0000053787121878
b_4	-0.0000019086402773	a_4	-0.0000029562634467
b_5	0.0000002095561353	a_5	0.0000003609247798

Overall RMSE = 3.929155

Table 5-2: Shows quantitative analysis of geometric correction errors for night time flights.

Resample: Summary of Transformation a086023b
Computed polynomial surface: Quadratic (based on 17 control points)

Coefficient	X		Y
b_0	-4241632.2	a_0	-3154053.7
b_1	20.5	a_1	13.9
b_2	-1.5	a_2	0.6586970218195347
b_3	-0.0000247319167622	a_3	-0.0000175538696450
b_4	0.0000038526839841	a_4	0.0000019301267302
b_5	-0.0000000982802638	a_5	-0.0000003339745451

Overall RMSE = 3.977579

Resample: Summary of Transformation a086033b
Computed polynomial surface: Quadratic (based on 21 control points)

Coefficient	X		Y
b_0	96164.0	a_0	-428218.6
b_1	-1.5	a_1	0.1726647162704467
b_2	-0.2284064378011692	a_2	1.3462765169458635
b_3	0.0000032756685393	a_3	0.0000000336646402
b_4	0.0000000781003708	a_4	-0.0000006129545661
b_5	0.0000003217447756	a_5	0.0000002524092772

Overall RMSE = 4.247019

Table 5-2 Continued

Resample: Summary of Transformation a086043b
Computed polynomial surface: Quadratic (based on 17 control points)

Coefficient	X		Y
b_0	-3044834.0	a_0	-936200.9
b_1	11.5	a_1	2.1
b_2	2.8	a_2	1.9
b_3	-0.0000092347852071	a_3	-0.0000022275324706
b_4	-0.0000086698179353	a_4	-0.0000011140198343
b_5	0.0000012879580811	a_5	-0.0000004157129386

Overall RMSE = 2.296062

Resample: Summary of Transformation a086053b
Computed polynomial surface: Quadratic (based on 30 control points)

Coefficient	X		Y
b_0	2338853.7	a_0	-1540757.6
b_1	-12.2	a_1	5.2
b_2	-0.4894796421499450	a_2	1.8
b_3	0.0000159432987145	a_3	-0.0000059124736110
b_4	0.0000011836112348	a_4	-0.0000011541788006
b_5	0.0000000051954502	a_5	-0.0000001661108291

Overall RMSE = 3.782730

Table 5-2 Continued

Resample: Summary of Transformation a086063b
Computed polynomial surface: Quadratic (based on 23 control points)

Coefficient	X		Y
b_0	-45710.4	a_0	-864496.9
b_1	-0.5218169443432998	a_1	1.6
b_2	-0.6775497493126750	a_2	2.3
b_3	0.0000021085263265	a_3	-0.0000010788769556
b_4	0.0000000820604118	a_4	-0.0000022465939855
b_5	0.0000010553492158	a_5	-0.0000001805789616

Overall RMSE = 3.819920

Resample: Summary of Transformation a086073b
Computed polynomial surface: Quadratic (based on 36 control points)

Coefficient	X		Y
b_0	318472.7	a_0	-59787.4
b_1	-2.7	a_1	-1.9
b_2	-0.1220581566494730	a_2	1.8
b_3	0.0000047587409792	a_3	0.0000026807243794
b_4	0.0000000891862604	a_4	-0.0000007498608640
b_5	0.0000001392256718	a_5	-0.0000003862780644

Overall RMSE = 3.797801

Table 5-2 Continued

Day Time Flights

Resample: Summary of Transformation a085043b
Computed polynomial surface: Quadratic (based on 19 control points)

Coefficient	X		Y
b_0	179904.0	a_0	1497933.9
b_1	-2.1	a_1	-9.1
b_2	0.0832887107553688	a_2	1.2
b_3	0.0000040975112327	a_3	0.0000111363010752
b_4	0.0000000203669696	a_4	0.0000001073078403
b_5	-0.0000001507656495	a_5	-0.0000000039802040

Overall RMSE = 2.456768

Resample: Summary of Transformation a085053b
Computed polynomial surface: Quadratic (based on 24 control points)

Coefficient	X		Y
b_0	5194836.1	a_0	532908.2
b_1	-26.1	a_1	-5.0
b_2	-0.5503454602222178	a_2	2.0
b_3	0.0000330443244845	a_3	0.0000065676519377
b_4	0.0000009061000764	a_4	-0.0000011553181259
b_5	0.0000002939460112	a_5	-0.0000004816995283

Overall RMSE = 3.869167

Table 5-3: Shows quantitative analysis of geometric correction errors for daytime flights.

Resample: Summary of Transformation a085063b
Computed polynomial surface: Quadratic (based on 30 control points)

Coefficient	X		Y
b_0	-1209025.6	a_0	-269021.9
b_1	4.8	a_1	-0.6326516420449480
b_2	-0.1750547223521153	a_2	1.4
b_3	-0.0000041761868717	a_3	0.0000006202678460
b_4	-0.0000005790305423	a_4	0.0000004422302638
b_5	0.0000006776180000	a_5	-0.0000005207951749

Overall RMSE = 3.997012

Resample: Summary of Transformation a085073b
Computed polynomial surface: Quadratic (based on 28 control points)

Coefficient	X		Y
b_0	-306653.8	a_0	-2003528.2
b_1	0.1526556569115201	a_1	8.1
b_2	0.1316914344265570	a_2	0.9188644197438407
b_3	0.0000017773460632	a_3	-0.0000102052639265
b_4	-0.0000012043552035	a_4	0.0000009327707669
b_5	0.0000005959111308	a_5	-0.0000000873348395

Overall RMSE = 2.922208

Table 5-3 Continued

Resample: Summary of Transformation a085083b
Computed polynomial surface: Quadratic (based on 25 control points)

Coefficient	X		Y
b_0	2955428.7	a_0	-2265450.4
b_1	-16.1	a_1	9.4561347535782261
b_2	0.7696548451003764	a_2	0.8188601361434849
b_3	0.0000218904472991	a_3	-0.0000120778065988
b_4	-0.0000023762150195	a_4	0.0000017335019822
b_5	0.0000003449525006	a_5	-0.0000004658942518

Overall RMSE = 3.966447

Resample: Summary of Transformation a085093b
Computed polynomial surface: Quadratic (based on 25 control points)

Coefficient	X		Y
b_0	2360005.0	a_0	-1632834.0
b_1	-13.2	a_1	5.3
b_2	0.6589458304644609	a_2	2.5
b_3	0.0000182189900889	a_3	-0.0000053787121878
b_4	-0.0000019086402773	a_4	-0.0000029562634467
b_5	0.0000002095561353	a_5	0.0000003609247798

Overall RMSE = 3.929155

Table 5-3 Continued

Resample: Summary of Transformation a085103b
Computed polynomial surface: Quadratic (based on 24 control points)

Coefficient	X		Y
b_0	-1947652.3	a_0	213048.0
b_1	9.1	a_1	-3.4
b_2	-1.3	a_2	2.0
b_3	-0.0000107472872071	a_3	0.0000050881900627
b_4	0.0000033549978935	a_4	-0.0000025988537779
b_5	-0.0000002082274753	a_5	0.0000005106566367

Overall RMSE = 4.222610

Table 5-3 Continued

5.3.5 RMSE FROM INDEPENDENT CHECK POINTS

As a next phase of this study, accuracy was assessed by using GCPs collected at independent checkpoints. It is reasonable to measure geometric correction quality for the overall image by RMSE obtained from the GCPs different from those used to determine the mapping functions. Therefore the estimation approach, in which the accuracy of the geometric registration method was evaluated by calculation of RMSE and mean deviations of the GCPs for samples and lines when a geometrically corrected image was overlaid on the reference overlay image, was used. The reference overlay image was generated from the OS map and the 22 GCPs were used for flight 6 (a085063b) and flight 7 (a085073b). The result is compared with the accuracy of the image corrected by map transformations and GCPs (Table 5-4). The mean deviation for pixels $RMSE_{independent}$ is calculated by;

$$RMSE_{independent} = \sqrt{\sum_{i=1}^{n} \frac{(X_i^a - X_i^m)^2 + (Y_i^a - Y_i^m)^2}{n}} \qquad \textbf{(5-2)}$$

Where X_i^a and Y_i^a are X and Y pixels of i^th GCPs detected from the rectified ATM imagery, X_i^m and Y_i^m are the corresponding X and Y pixels in the OSmap and n is the number of GCPS.

Flights	# of GCPs	RMSE (m) from Map Transformation	RMSE (m) from Independent Check point
a085073b	28	2.922	
	22		9.87
a085063b	30	3.997	
	22		12.05

Table 5-4: RMSE calculated by map transformation and independent checkpoints.

RMSE values calculated from the independent checkpoint were greater in magnitude than the map transformation. In addition, one can see a marginal difference in magnitude of the error even with the same flight; say flight a085073b with 28 GCPs having an error of 2.922 metres compared to 9.87 metres from the independent checkpoints. The parameters (X^i_a-X^i_m) and(Y^i_a-Y^i_m) have been selected so that the sum of squares of error is a minimum hence, the image is a best fit to the ground control points. Any other set of points will in general have a greater error than this. The parameters of the transformation are selected so that the RMSE is a minimum; any other measure of accuracy will be worse than this. With 1.8 m pixels size, a localized error of ~10 m or five pixels is surely a major problem for many applications of the ATM dataset. GCPs used for the independent checkpoint are tabulated and each GCP error is calculated (see Appendix 6 for details). Figures 5-13 and 5-14 show the even distribution of GCPs used to calculate the RMSE for the independent checkpoint for flights a085063b, and a085073b, band 7 respectively.

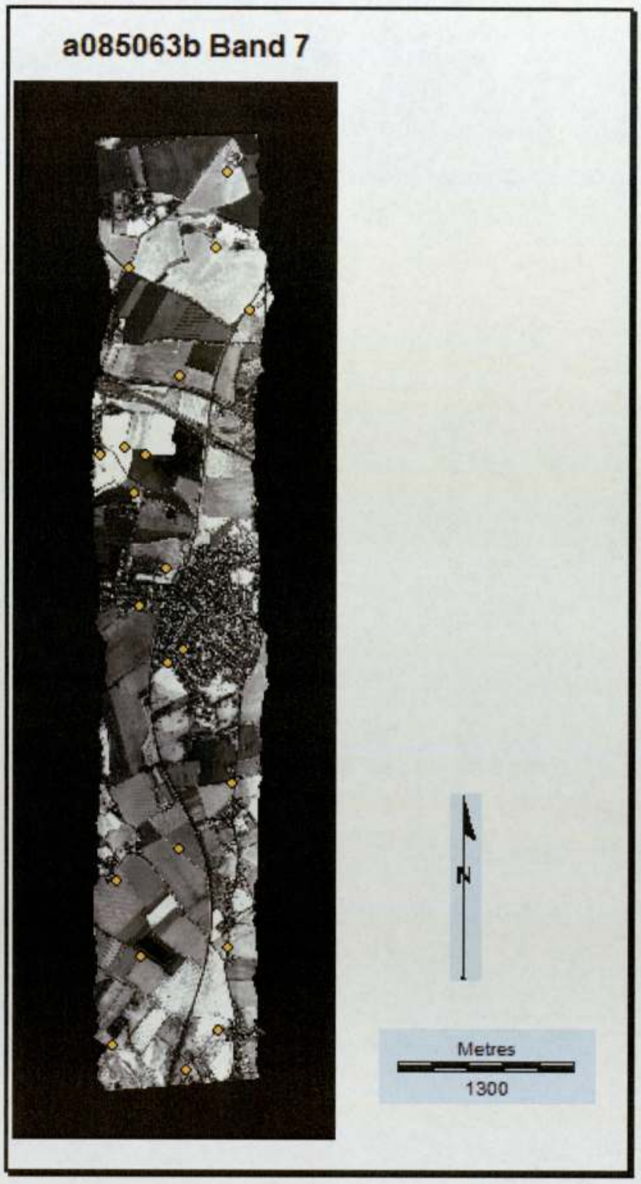

Figure 5-13: GCPs used for independent checkpoints for a085063b, band 7.

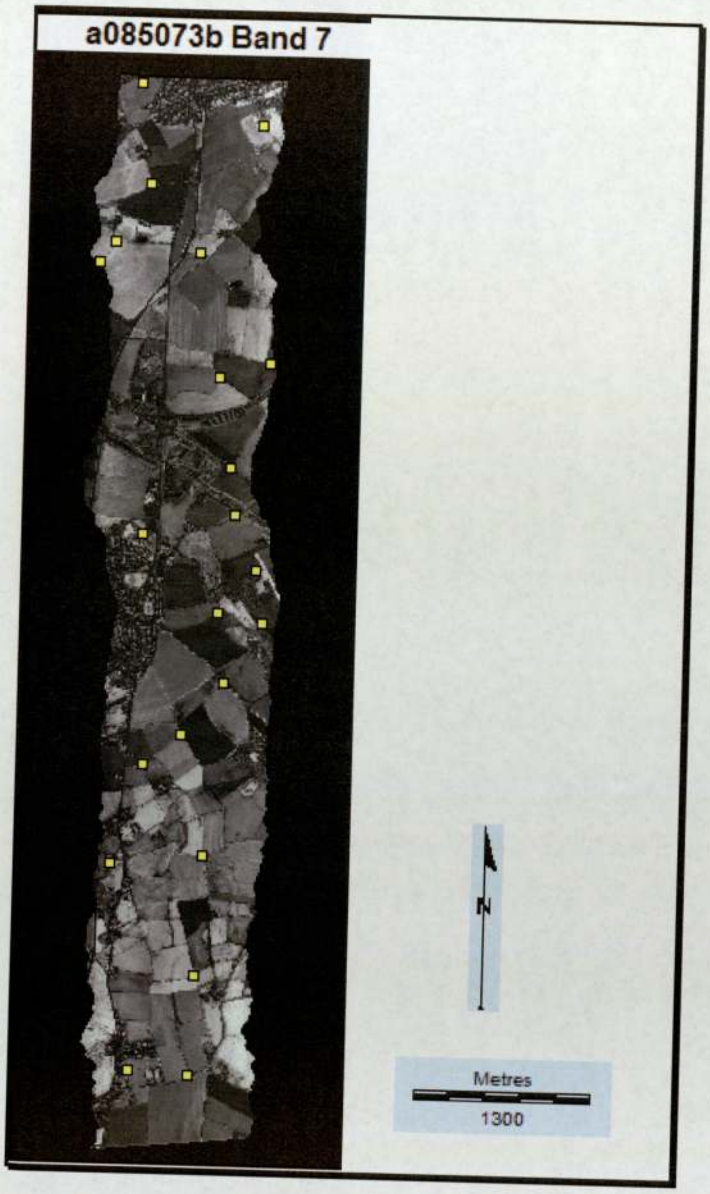

Figure 5-14: GCPs used for calculating the RMSE by independent checkpoints for a085073b, band 7.

In this section, the geometric accuracy of ATM images has been tested with transformation by using GCPs collected/used in map transformation and independent checkpoints. From the comparison results, it was seen that the polynomial non-parametric models gave reasonable results and the geometric accuracy of ATM images is very satisfactory and this leads to the conclusion that they can be efficiently used in land use mapping. It also shows that ATM images continue to provide more valuable and cost-effective spatial information that could help planning development in urban areas. 10 m on 1: 10000 map represents an error of 1 mm in map accuracy and distribution.

5.4 GEOMETRIC ACCURACY

5.4.1 ACCURACY ASSESSMENT OF THE GEO-CORRECTED IMAGERY

Both, parametric and non-parametric correction techniques produced lesser distorted imagery and hence linear features, such as the roads and field boundaries, showed lesser or almost no shift in the datasets. The flights match up very precisely in the overlapping regions (see Figure 5-15). The adjacent flights have shown a very minimal distortion and the orientation of the positional error is reduced to almost one metre or even less at some points. Considering the width of pixels, very minimal error is still encountered between the flights, but it is the best or closest accuracy achievable at this point. It will be shown that the images can be overlaid and for multi-temporal data use. This indicates that the imagery is consistent with but different from the map


Daytime flightline 4, 5 and 6

Flights 4, 5 and 6 match up very precisely in the overlapping regions.

Very precise joining between field boundaries of the adjacent flight lines.

Figure 5-15: Geo-corrected image for day flight 4, 5 and 6.

5.4.2 QUALITATIVE NUMERICAL ANALYSIS

The flights were compared by considering if the images lined up very well by using the composite function from Idrisi. Composite produces a colour composite image from three bands of 8-bit binary imagery. A composite function was projected for flight 5 as blue, flight 6 as green, and flight 7 as red bands, as shown in Figure 5-16.

Colour composite images were created by displaying through different coloured guns. When the red and blue combine they make cyan, and red and green make yellow. This technique was useful in assessing the registration accuracy, and colour images were produced extremely rapidly and provide an immediate indication of the nature of registration and errors within the imagery.

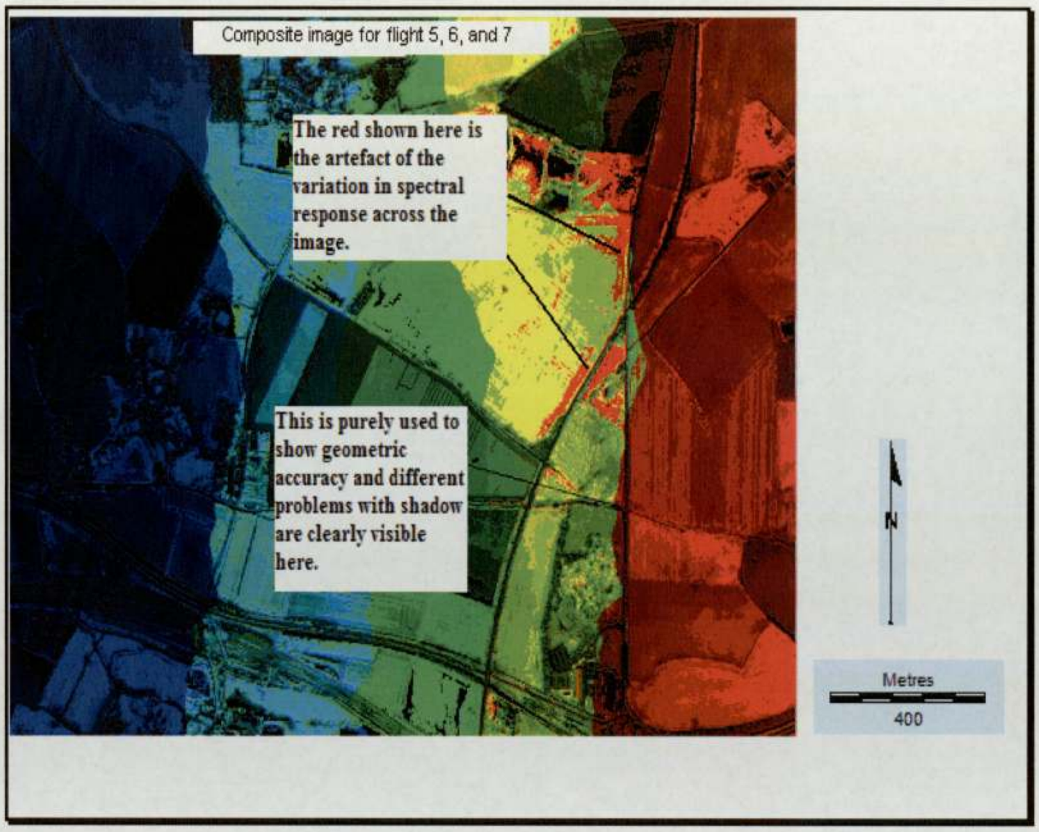
Composite image for flight 5, 6, and 7

The red shown here is the artefact of the variation in spectral response across the image.

This is purely used to show geometric accuracy and different problems with shadow are clearly visible here.

Figure 5-16: A composite image of flight 5(blue), 6(green), and 7 (red) of the north-west of Shenstone village.

This is purely used to show geometric accuracy and different problems with shadow are clearly visible here. The red shown here is an artefact of the variation in spectral response across the image. This is shown in Figure 5-16 and Figure 5-17.

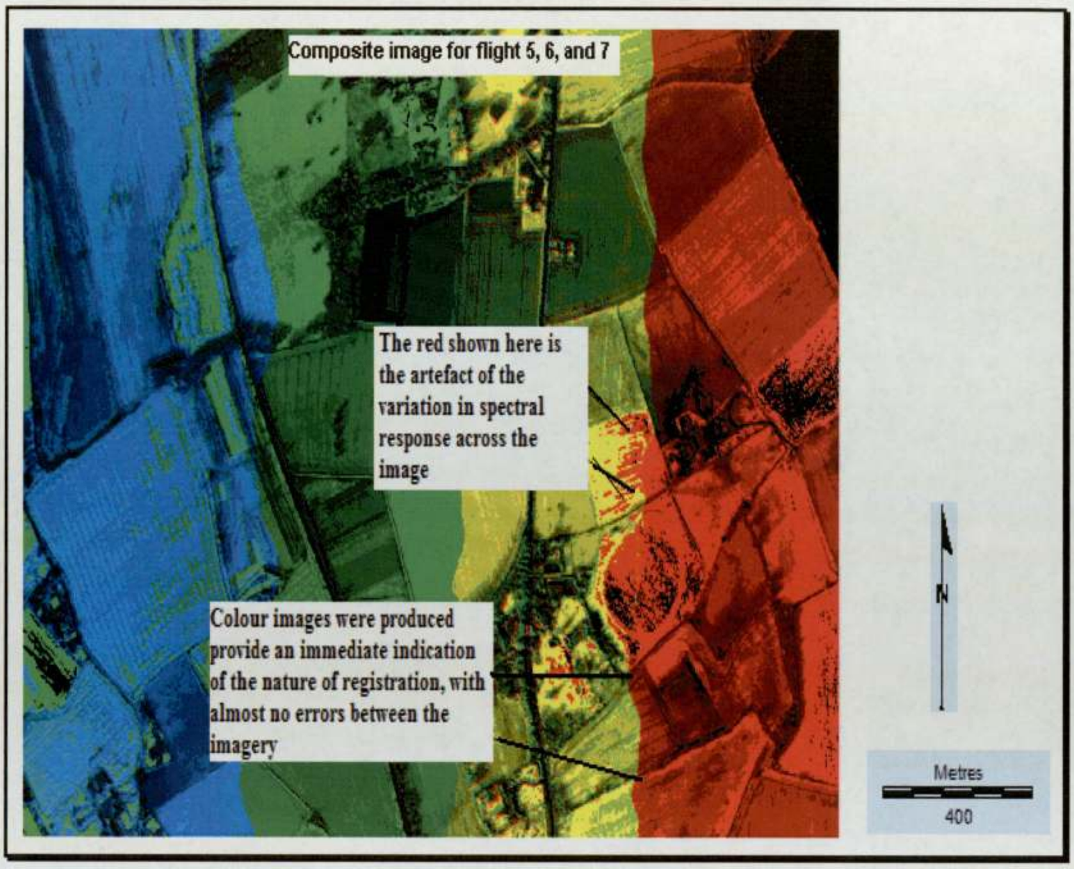

Composite image for flight 5, 6, and 7

The red shown here is the artefact of the variation in spectral response across the image

Colour images were produced provide an immediate indication of the nature of registration, with almost no errors between the imagery

Figure 5-17: A composite image of flight 5(blue), 6(green), and 7(red) of Shenstone village.

The results from composite image can be summarized as follows:

- Field boundaries align correctly or no mis-alignments
- Reduction in both horizontal and vertical errors throughout the image
- Almost all roads and roundabouts align well between adjacent flights
- Towards the bottom of the image, the rotation is reduced to a significant level, which is indicated as the features lines show almost parallel, and
- Radial distortion of objects (roads and crossroads) is less noticeable in varying in size.

From the above images it is clear to see that the images line up very well and any error is very slight and not noticeable. So from analysis of the images the result of the transformation seems very successful.

5.5 MOSAIC

5.5.1 INTRODUCTION

The flights were compared to see if the images lined up very well or how well joined were the adjacent flights by using mosaic function from Idrisi. Only the areas of overlap are used in the grey level matching process. While the module will produce an output image no matter what the area of overlap, a sufficient amount of overlap is required to develop good statistics to balance the images.

A master image is the image that will set the grey level characteristics and is used to adjust the grey level of a slave image before joining the mosaic image. The first input image is the first master image. The first slave image is the image which has the largest overlap area with the master image. The slave image will be adjusted to match the grey level characteristics of the master image and then join the mosaic image. The next slave image is chosen, which has the largest overlap area with one of the previously processed two images, and so on, until all the images are joined. The final image will extend to the overall maximum x; y coordinates of the input images.

Mosaic will ignore the background values when developing statistics for grey level matching. If no flag definition is defined and uniform background values exist across all input images, the user can specify the default background value during module operation. If multiple flag background values exist and are documented, the output background value option will specify a uniform background value in the result. Also, all background values will be ignored in assigning final values in the overlap areas.

If the operator chooses to match the grey levels, then indicate whether to use the cover or average method of assigning values in the area of overlap. With the cover option, the adjusted values of the slave image are recorded in the overlap area (i.e., it covers the master image values in the overlap area). With the average option, the average of the adjusted values of the slave image and the values from the master image are recorded in the overlap area. The averaging method will yield a smoother transition between images than the cover method. However, the averaging option may cause problems if geo-registration is not precise for all the images. A linear feature such as a road, for example, may appear as a double road in the averaged area if the two images are not exactly co-registered. In this case it is better to use the cover option. The images will have to be built up gradually as only two images can be combined at a time. So the previous overlaid files need to be overlaid together.

5.5.2 MOSAIC OF THE DAY TIME THERMAL IMAGE

Mosaics images created using averaging statistics from the overlapping images and using the raw data overlaid to show the difference and importance of what is happening. Average looks better than cover, and since the actual radiance values have already been lost, it makes no real difference. The mosaic function on full images is shown in Figure 5-18.

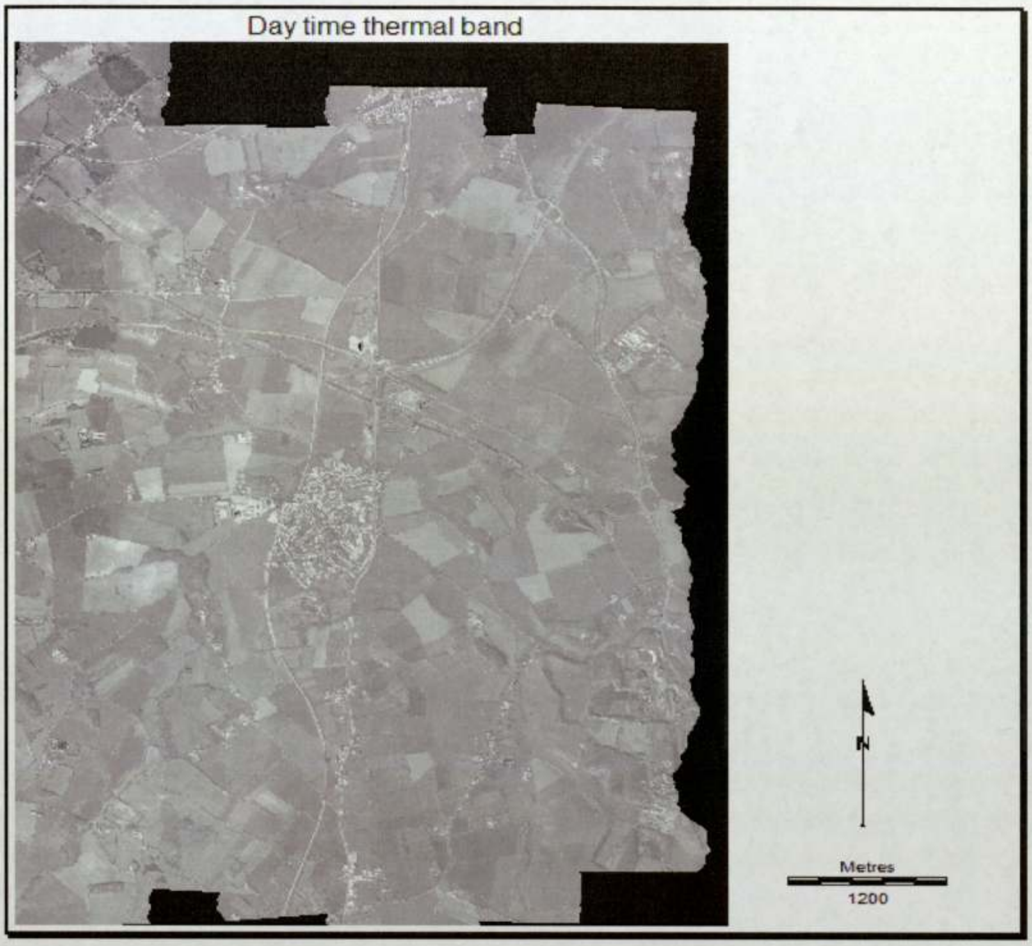

Figure 5-18: A full mosaic of the daytime thermal of the whole study area.

The mosaic of the day thermal showed a very good result in joining all the flights, but the line of joining is noticeable as shown in Figure 5-19 and Figure 5-20.

Daytime mosaiced imagery

Noticeable white line of joining between flights

Field boundaries showed precise joining

Figure 5-19: A mosaic of the daytime thermal of the northeast of Shenstone village.

Figure 5-20: A mosaic of the daytime thermal of the northwest of Shenstone village.

5.5.3 MOSAIC OF THE NIGHT TIME THERMAL IMAGERY

For the night thermal, mosaicing with no matching in overlapping areas, grey scale matching with overlay, and grey scale matching with averaging of the overlaid areas were tried, but it does not appear to make much difference. The overlaps are too small to calculate meaningful statistics. The overlay function itself creates a seamless mosaic for the night time thermal band. The night time mosaic showed a slightly disappointing result because all the joins were very noticeable and the grey level matching did not seem to work so well (see Figure 5-21). In the night time thermal imagery, there is high gain effect for different flight lines as compared to the day time thermal. The night time flights showed a worst result than the day time flights. However, in the night time thermal, the images line up very well with higher accuracies so that they can be used for creating maps or for other uses. The radial distortion is also reduced to a usable level, as images maintain the same shape and size.

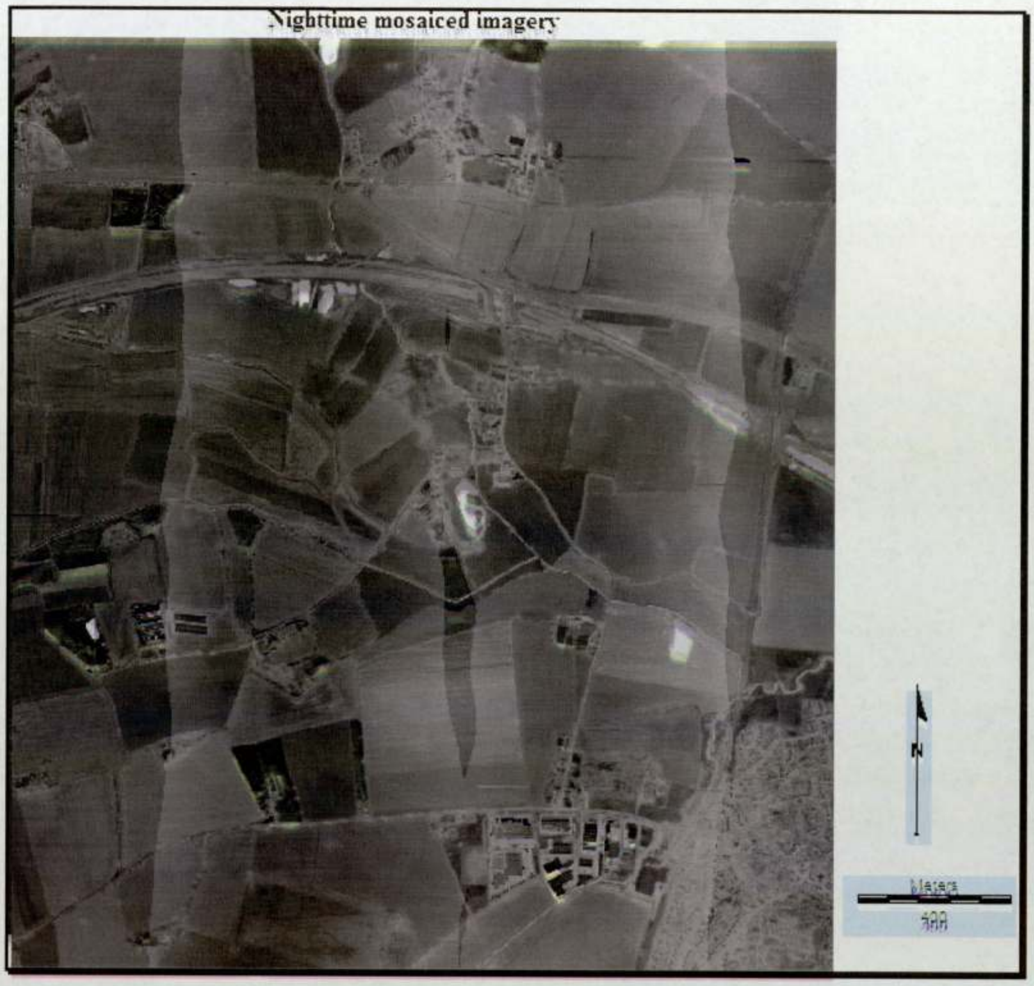

Figure 5-21: A mosaic of the night time thermal of Shenstone village.

5.6 CONCLUSION

This chapter discussed the geometric accuracy on the ATM imagery. Geometric correction of airborne scanner imagery has conventionally been performed by parametric and a non-parametric techniques to acquire best accuracies between adjacent flights. The first aim of this chapter was to check how well the geo-correction software performs in conjunction to the affine transformation. Thus, the geometrically corrected image showed a lesser distortion and therefore linear features, such as the roads and field boundaries, showed lesser or almost no distortion than the raw datasets. The parametric techniques acquired good accuracies by using finer scale of the digital elevation model.

The first accuracy test was achieved by testing the data's qualities using the overlaying method and checking the accuracy using GCPs. The objective was to examine the existing correction techniques to identify sources of error, and investigate potential methods for overcoming them. The most commonly used measure of geometric accuracy is root mean square error (RMSE). The RMSE tells the observer neither where the errors exist, nor provides any information regarding the relative errors between two or more images. In all flights the RMSE from the map transformation ranges from 2.0-4.3 metres, which is considered to be a good accuracy, as compared to three times the value from the independent check point. Although the day time flights appear to be a lot better than the night time flights, small errors still occurred. In fact, after the non-parametric correction there was a little error.

The second accuracy test of the data's quality is done using the composite function (this overlaps the data, and error between the images can be noticed). Colour composite images were created by displaying adjacent flight through different coloured guns. This technique was useful in assessing the registration accuracy, and the result showed a very precise registration with minimal errors between the adjacent flights of the imagery. In addition, the chapter consisted of assessing the corrected imagery further by creating a seamless mosaic. Hence, the images were corrected using the parametric and non-parametric correction techniques with a considerable number of GCPs selected from the imagery. The results of the affine transformation enabled the images to align very well and the mosaic functions seemed a lot more plausible. Some image processing was carried out after the mosaics were created to improve the images, but there was a very little difference in the results, so this may be because all the processing is best done at the start before the image gets stretched.

The large amount of miscalculations all over the images had been minimized; this was largely due to yaw rotation. Now, the images line up well and can be mosaiced, especially for function of order of 1 to 3 pixels, such as creating a map up to a scale of 1: 10000. Moreover, almost all the features in the image do maintain the same shape and size, which is an indication of less radial distortion.

6 DISCUSSION

This chapter provides a discussion of the main issues that arose during the course of this research and will summarize key research findings, contribution to knowledge and a reflective assessment of what could have been done with more time and a better dataset. The key research findings are a cross-swath variation within the ATM and CASI sensors, the inappropriateness of ATM raw imagery for mosaicing, and the dip in values of thermal data at the centre of a swath.

First, both ATM and CASI sensors showed a similar pattern and trend, but a difference in magnitude and shape across the swath. The variation in the swath between the ATM and CASI sensors could be due to a slight difference in the spectral range of each band recorded by each sensor. Thus, the spectral range considered is slightly different in upper and lower units of the band width, when correlating the wavelengths between the ATM and CASI. Also, this variation could be because the ATM sensor was not giving the same response to all frequencies in the given wavelength range, and because of the difference in the scaling factor between the ATM and CASI sensors.

The second findings were the inappropriateness of ATM raw imagery for mosaicing. The difference in viewing angles could have caused ATM sensor to respond in the same linear fashion. Differences in the brightness values among the individual images still remain, and the internal illumination gradient residue in some of the images existed to a degree that disturbed artefacts in the mosaic. The methodology for correcting this problem should be further developed based on the actual causes of the phenomenon. Along with problems caused by wide angle views and failures in the sensors, these problems restrict stretching operations and the interpretation of delicate reflectance patterns in the whole swath area. Furthermore, the geographic precision of the mosaic may be unsatisfactory at places. Finally, because the ATM sensors did not pick up the same radiation from the same land cover at different places in the imagery, quantitative classification of the imagery was not possible. Therefore a mosaiced raw DN imagery is inappropriate for classification.

The third research finding was a dip in values of DN data at the centre of the swath. This dip in value was observed in all bands of the ATM except the thermal band. The thermal band showed less severity in the deepness of the dip when compared to the other bands, even though the distribution of land cover is on average the same across the swath. The dip in values in the visible, near infrared and far infrared bands is more severe at the centre of the image than at the edges. This dip could be mainly more a property of the sensor, not by the chance dominance of a particular land cover. The dip in the middle has no simple explanation. Its cause can only be speculative. The dip in values can also be displayed by the standardized mean for all bands, except the thermal band. The thermal band is also excluded in this case because of its higher wavelength range; it will come as a straight line. Its exclusion will not make or add any difference for the comparison of the rest of bands. The standardized mean showed the variation and the magnitude in dipping and its decrease as the wavelength increased. In other words, bands with lower wavelength range dipped more than the higher range. It is observed that the central dip effect is reduced as the wavelength increases and the centre part of this dip is skewed towards the east part of the scan line. For the thermal band no dip was observed thought out the scan line. To verify whether the difference could not have arisen by chance alone, a t-test was applied to all bands to consider the probability of the mean being the same for random columns. The result showed adjacent columns showing a higher probability of being the same in all bands when compared to east and west columns. In other words, the probability of west and east pixel columns being different purely by chance is almost less than 1000th of the probability of finding an individual atom on the Earth.

The quantification of edge pixel problems in all ATM bands is one of the main contributions to knowledge in this thesis. The ATM is a whisk broom sensor; the data is collected by the means of an oscillating mirror, swinging perpendicular to the direction of flight. The ATM scanners have a larger field of view (about 90^o), and such an angle is necessary to acquire an acceptable swath of data from typical aircraft altitudes. However, the consequence of the larger FOV with aircraft scanning is that significant distortions in the image can occur at the edges of the scan line.

There was considerable overlap between the flights, necessitating changes to the DN values of both extreme edges of each flight line. The first and last 100 pixels were padded or altered to one from their original values without making any changes to the data. Barnsley and Barr (1993), advised not to rely on the extreme edges of the scan line. Thus, it became possible to remove some odd values from the overlapping area and improve the difference in brightness level of the adjacent flight lines. This is essential because the concept of the spectral response received at the sensor from the same land cover is understood and corrected for position of the scan line. It is also important that the data can be accurately overlaid and geometrically correct. It is recommended that the extreme edges of all the flight lines under consideration are trimmed in making the data useful for quantitative and qualitative analysis by not relying on the extreme edges of the scan line.

The operational recommendations for data acquisition with multiple sensors that have different swath angles are another of the contributions to knowledge in this thesis. It will be more reasonable and economical to capture data simultaneously for CASI /ATM. This will enable defining the total area coverage of the study area and the possible overlap between adjacent flight lines. For the ATM sensors it is recommended that the swath angle is narrowed to improve data quality. With wide angles in the ATM sensor it failed to record digital values at the extreme edges of the sensor. Similarly both narrow and wide sensor pairs should not fly separately when data acquisitions are required for each sensor. The recommended overlaps between adjacent flight lines in ATM coverage should be 45%. This will enable the analyst to carry out significant pre-processing steps without losing any data.

Differences in sun illumination (also including shadowing), atmospheric conditions and sensor response may cause significant variations in pixel radiance values for a target on remotely sensed images acquired at different dates. These effects are usually higher between archived airborne images than for sun-synchronous satellite images. Aerial photographs, for example, are often available only from different seasons and from different times of the day. Automatic analysis of land surface changes at pixel level on multi-temporal raw images would therefore be greatly hampered by non-ground specific conditions. On optical remote sensing images in general, these variation effects may be corrected either by absolute calibration of the single images or by pixel brightness normalisation between the images. For aerial photographs, only the latter approach appears feasible. Different land covers emit and/or reflect different proportion of radiation in different directions. Thus, the need for data normalisation before processing day/night ATM thermal image pairs is more important.

Finally, a reflective assessment of what could have been done with more time and a better dataset is discussed. Due to the poor quality of the ATM data, it was not possible to explore the full potential and carry out classification of the day and night thermal bands for quantitative and qualitative land use analysis and planning. Moreover the estimation of soil moisture content from the day and night thermal bands was not possible because of the inappropriateness of the ATM data. As the flights were carried out long before the start of the thesis, it was not possible to suggest the direction of the flights. Flights were to be flown from north to south or vice-versa. To avoid differential illumination it is recommended that flight should be towards the sun. However, in light of the studies carried out so far, it is possible to recommend a number of key areas which, given more time, would have benefited from further investigation. This includes:

- Radiometric correction of the day and night time imagery
- Classification of the geometrically and radiometrically corrected imagery for land use planning and other uses, and
- Independent data sources could be used to correct for the variation in land cover by doing a field work.

7 CONCLUSION

Many questions have been raised in this research as to the integrity of the ATM dataset under investigation and the extent to which it can be used in quantitative scientific work. The aim and objectives of this research project were described in Chapter 1: (a) is the digital number (DN) obtained at different points across a scan line the same for the same land cover at all wavelengths, (b), what is the potential for the day and night time thermal imagery of the same area, (c) are geo-rectification techniques suitable to mosaic images and co- registering night time and day time flights, and (d) is the ATM data in the form supplied suitable for land cover classification. In line with this, Chapter 2 discussed the main literature review of the use of Airborne Thematic Mapper and the proprieties of thermal infrared data. These were followed by Chapter 3, which had ranged from the initial observations, management of the data and description of the types of sensor used to acquire the data.

Chapter 3 illustrates the location and nature of the study area in addition to the data collection procedures used in the research. This is followed with the detailed specifications and data acquisition modes for Airborne Thematic Mapper (ATM) and Compact Airborne Spectrographic Imager (CASI). In addition, Chapter 3 discussed the hierarchical data format (HDF), which stores the scientific data and how it was applied to the ATM data. Finally, the chapter explained how the data are extracted, and both extreme edges trimmed to make the data useful for quantitative and qualitative analysis.

The results presented in section 3.10 showed that the same land cover showed different spectral response and varied digital number within individual flight lines. There were also differences in brightness level between adjacent flights on their adjoining line. Thus, because the ATM sensors did not pick up the same radiation from the same land cover at different places in the imagery, quantitative classification of the imagery was not possible. It was also discovered that the same land cover on different parts of the imagery gave different spectral responses and their quantitative classification was not reliable and tangible.

Finally Chapter 3 discussed the identification of water bodies from the day and night thermal images. In the night time image, the water bodies are brighter and more evident because water bodies tend to retain higher temperatures than their surroundings and emit more thermal energy than their surroundings when compared to the day time. This unique property has made the water bodies easily detectable and identifiable within the content of night time thermal.

Chapter 4 examined the spectral response of the ATM and CASI sensors, and it also considered if the sensors pick up the same radiation from the same land cover at different places in the imagery. Despite good overlap between the adjacent flights, flights covering the same area showed a difference in the brightness level from each flight. However, the night time thermal band suffers from a problem called 'gain effect' from different flights. This gain effect had created problems in identifying objects throughout the whole imagery. The use of ratio reduces the gain problem with different flights and hence it is recommended to use band ratio rather than absolute values (only for day time flights not for night time).

The cross-scan variation provides a comparison between the ATM and CASI scanners. The values represented are raw digital values, not radiances, and hence in both cases a similar pattern was expected and observed, but neither showed the same values nor exactly the same shape. This could be due to either the sensor possibly not responding in a linear fashion, or the ATM sensor not giving the same response to all wavelengths in the given wavelength range, and of course different IFOV. There is a discrepancy in the digital number (DN) based on its location across the image. If the variation of the averages of the DNs over 40,000 pixels is large, than this variation could be due to the chance of encountering more, for example, water at the centre of the image rather than at the edges. In addition to the quality analysis of Airborne Thematic Mapper, the distribution of DN values and its standard deviation were carefully studied across the swath of the image. These variations cannot be attributed to chance inclusions of particular land cover types and are a property of the sensor. This is of great concern in the quantitative application of the ATM data.

This chapter also looked at the frequency distribution of the DN values by considering the centre, east and west side of the image. There is a rises in DN value in the middle of the scan line, but it then drops un-expectantly at the edge of the scan line. The edge lines also have a larger number of high DN values, which cannot be explained by the land cover. In Band 1, because of its poor quality, it is difficult to interpret the distribution throughout the whole imagery and a high fluctuation was seen in the east, centre and west sides of the imagery.

Chapter 5 discussed the geometric accuracy on the ATM imagery. Geometric correction of airborne scanner imagery has conventionally been performed by parametric and a non-parametric techniques to acquire best accuracies between adjacent flights. The first aim of this chapter was to check how well the geo-correction software performs. Results showed a lesser distorted imagery and therefore linear features, such as the roads and field boundaries, showed reduced or almost no distortion in the datasets. The better the accuracy and resolution of the DEM, the better the parametric method performs. The images were corrected using the parametric and non-parametric correction techniques with a considerable number of GCPs selected from the imagery. The results of the affine transformation enabled the images to align very well and the mosaic functions seemed a lot more plausible. The large amount of miscalculations all over the images had been minimized; this was largely due to yaw rotation. The images line up well and can be mosaiced, especially for applications that require high accuracy, such as creating a map and multitemporal work. Almost all the features in the image maintain the same shape and size, which is an indication of less radial distortion.

The recommended future work plans for the ATM data are to investigate why there is a dip in values in visible, near and far infrared bands. A detailed explanation of why there is a dip in values happening in the centre of the image when compared to edges, and the dip is more skewed towards the east side relative to the west side is required. What are the causes in decreasing the degree and magnitude in the dip value as the wavelengths increase in all bands of the ATM image data? This requires a study of the sensor physics.

As a final conclusion, the main aims and objectives of the thesis are discussed as follows:

(a) Is the digital number (DN) obtained at different points across a scan line the same for the same land cover at all wavelengths,

- The digital number (DN) obtained at different points across a scan line was not the same for the same land cover at all wavelengths.

(b) What is the potential for the day and night time thermal imagery of the same area?

- As there is no correlation between the night time thermal and day time thermal bands. The information content of the night time thermal is very high and this could lead to a significant improvement in classification accuracy, particularly for manmade structures and open water.

(c) Are geo-rectification techniques suitable to mosaic images and co- registering night time and day time flights?

- The geo-rectification techniques were found to be suitable for mosaic images and co-registering of night time and day time flights of sufficient and significant accuracy.

(d) Is the ATM data in the form supplied suitable for land cover classification?

- Mosaiced raw DN imagery is inappropriate for classification and it was discovered that the same land cover on different parts of the imagery gave different spectral responses and their quantitative classification was not reliable and tangible. Therefore, the ATM data in the form supplied is not suitable for land cover classification

REFERENCES

Atkinson, P.M. and Curran, P.J., (1997), 'Selecting the spatial resolution of airborne MSS imagery for small-scale agricultural mapping', *International Journal of Remote Sensing*, **18**, No. 9, pp.1903–1917.

Avery, T.E., & G. L. Berlin., (1992), 'Fundamentals of Remote Sensing and Air Photo Interpretation', 5th Edition, Macmillan Publishing Company, New York.

Azimuth, (2005) '*AZGCORR User's manual* [Online], Airborne Remote Sensing Hyperspectral', Azimuth systems UK, Available: http://arsf.nerc.ac.uk/documents/azgcorr_v5.pdf, *Direct Georeferencing package,* [2005, July].

Barnsley, M.J. and Barr, S.L., (1993), 'Mapping urban areas using high spatial resolution remotely sensed images: 1.Data Processing', *Proceeding of the 1993 NERC Symposium on Airborne Remote Sensing*, December, Dundee, pp. 1-13.

Barnsley, M.J., Settle, J.J., Cutter, M.A., Lobb, D.R. and Teston, F., (2004), '*The PROBA/CHRIS Mission:A Low-Cost Smallsat for Hyperspectral Multiangle Observations of the Earth Surface and Atmosphere*, IEEE Transactions on Geoscience and Remote Sensing, 42(7), pp: 1512-1520.

Becker, F., and Li, Z. L., (1990), 'Temperature-independent spectral indices in thermal infrared bands', *Remote Sensing of Environment,* **32**, pp.17-33.

Becker, F & Li, Z.L., (1993), 'Surface temperature and emissivity at various scales: measurement and related problems', *Proc. Workshop on Thermal Remote Sensing, La Londe les Maures*, France, September 20-24th. Int. report by CEMAGREF, France and Penn State University, USA, pp.35-60.

Becker, F., and Li, Z. L., (1995), 'Surface temperature and emissivity at various scales: definition, measurement and related problems', *Remote Sensing Reviews,* **12**, pp.225-253.

Ben-Dor, E., Levin, N., and Saaroni, H., (2001), 'A spectral based recognition of the urban environment using the visible and near-infrared spectral region (0.4—1.1 µim)', A case study over Tel-Aviv, *Israel. International Journal of Remote Sensing*, **22**, pp. 2193-2218.

Blonda, P., la Forgia, V., Pasquariello, G. & Satalino, G., (1996), 'Feature extraction and pattern classification of remote sensing data by a modular neural system', Optical Engineering, **35**, pp. 536-542.

Bowers, D.G., Harker, G.E.L., Smith, P.S.D. and Tett, P., (2000), 'Optical properties of a region of freshwater influence (the Clyde Sea)', *Estuarine, Coastal and Shelf Science,* **50**, pp. 717-726.

Bowers, D.G., Evans, D., Thomas, D.N., Ellis, K. and Williams, P.J le B., (2004), 'Interpreting the color of an estuary', *Estuarine, Coastal and Shelf Science,* **59,** pp. 13-20.

Caselles, V., Sobrino, J. A., and Coll, C., (1992), 'A physical model for interpreting the land surface temperature obtained by remote sensors over incomplete canopies', *Remote Sensing of Environment,* **39**, pp.203-211.

Caselles, V., Coll, C., and Valor, E., (1997), 'Land surface emissivity and temperature determination in the whole HAPES Sahel area from AVHRR data', *International Journal of Remote Sensing*, **18**, 1009-1027.

Choudhury, B. J., Dorman, T. J., and Hsu, A. Y., (1995), 'Modeled and observed relations between the AVHRR split window temperature difference and atmospheric perceptible water over land surfaces', *Remote Sensing of Environment*, **51**, 281-290.

Crabtree, D.L., and Bown, M., (1989), 'A stabilization system for a large aperture reconnaissance camera', *SPIE Airborne Reconnaissance X*III , **1156**, pp.266-271.

Cracknell, A. P., and Xue, Y., (1996), 'Dynamic aspects study of surface temperature from remotely-sensed data using advanced thermal inertial model', *International Journal of Remote Sensing*, **17**, 2517- 2532.

Danson, F.M., (1986), 'Remotely sensed red and infra-red response to forest canopy cover', *Proceeding of the NERC 1985 Airborne Campaign Workshop*, 16th November, Ripton, Camps, UK.

Dana, K.J., Ginneken, B.V., Nayar, S.K.and Koenderink, J.J., (1999), 'Reflectance and texture of real-world surfaces', *ACM Transactions on Graphics,* **18**, pp. 1-34.

Dash, P., Gottsche, F-M., Olesen, F-S., and Fishcher, H., (2002), 'Land surface temperature and emissivity estimation from passive sensor data: theory and practice—current trends', *International Journal of Remote Sensing,* **23**, pp. 2563-2594.

Davies C. H., and Wang. X., (2001), 'Planimetric Accuracy of IKONOS 1-m Panchromatic Image Products', *Proceedings of the 2001 ASPRS Annual Conference,* St. Louis, MI, USA, April 23 - 27, CD-ROM.

Devereux, B.J., Fuller, R.M., Carter, L. and Parsell R.J., (1990), 'Geometric correction of airborne scanner imagery by matching delaunay triangles', *International Journal of Remote Sensing,* **11**, No. 12, pp. 2237-2251.

Diak, G. R., and Whipple, M. S., (1993), 'Improvements to models and methods for evaluating the land-surface energy balance and 'effective' roughness using radiosonde reports and satellite-measured 'skin' temperature data', *Agricultural and Forest Meteorology*, **63**, pp. 189–218.

Diner, D. J., Martonchik, J. V., Borel, C., Gerstl, S. A. W., Gordon, H. R.,Knyazikhin, Y., Myneni, R., Pinty, B., and Verstraete, M. M., (1999), 'Multriangle Imaging Spectro-Radiometer (MISR) level 2 surface retrieval (MISR-10) algorithm theoretical basis', *Jet Propulsion Laboratory*, California Institute of Technology.

Dowman, I.J., Coyle, J. and Ward, N., (1984), 'Geometric correction of airborne MSS data', *Report on NERC Contract G60/66/99.*

Doxaran, D., Froidefond, J.M. and Castaing, P., (2002), 'A reflectance band ratio used to estimate suspended matter concentrations in sediment-dominated coastal waters', *International Journal of Remote Sensing,* **23**, pp. 5079-5085.

Doxaran, D., Froidefond, J.M. and Castaing, P., (2003), 'Remote sensing reflectance of turbid sediment-dominated waters: Reduction of sediment type variations and changing illumination conditions effects using reflectance ratios', *Applied Optics,* **42**, pp. 2623-2634.

D'Sa, E.J., and Miller, R.L., (2003), 'Bio-optical properties in waters influenced by the Mississippi River during low flow conditions', *Remote Sensing of Environment,* **84**, pp. 538-549.

Edina Digimap Collections, (2005), '[Online] Available: http: //edina.ac.uk/digimap/'

Ehlers, M., (1997), 'Rectification and registration', *Integration of Geographical Information Systems and Remote sensing*, J. Star, J. Estes and K. McGwire, eds., Cambridge University Press.

Ehrlich, D., and Lambin, E. F., (1996), 'The surface temperature-vegetation index space for land cover and land-cover change analyses', *International Journal of Remote Sensing*, **17**, pp. 463–488.

Elachi, C., (1987), 'Introduction to the physics and techniques of remote sensing', John Wiley & Sons.

Ellis, R.J., (1997), 'Evaluation of remote sensing for monitoring landfill gas and leachate within an urban environment', PhD Thesis, Aston University, UK.

ERDAS, (1998), 'ERDAS User manual', Available from ERDAS UK limited, Telford House, Cambridge, CB1 5FB.

Fang, H., Liang, S., Chen, M., Walthall, C. and Daughtry, C., (2004) 'Statistical comparison of MISR, ETM+ and MODIS land surface reflectance and albedo products of the BARC land validation core site, USA', *International Journal of Remote Sensing*, **25:2**, 409–422.

Feldhake, C. M., Glenn, D. M., and Peterson, D. L., (1996), 'Pasture soil surface temperature response to drought', *Agronomy Journal*, **88**, pp. 652–656.

Franc, G. B., and Cracknell, A. P., (1994), 'Retrieval of land and sea surface temperature using NOAA-11 AVHRR data in northeastern Brazil', *International Journal of Remote Sensing*, **15**, 1695-1712.

Gillespie, A. R., Rokugawa, S., Matsunaga, T., Cothern, J. S., Hook, S., and Kahle, A. B., (1998), 'A Temperature and Emissivity Separation algorithm for Advanced Spaceborne Thermal Emission and Reflection radiometer ASTER images', *IEEE Transactions on Geoscience and Remote Sensing*, **36**, pp.1113-1126.

Gregory, S., (2001), 'The Geometric Correction and Registration of Airborne Line-Scanned imagery for Temporal Thermal Studies', PhD Thesis, Aston University, Birmingham, UK.

Gu, X. F., and Guyot, G., (1993), 'Effect of diffuse irradiance on the reflectance factor or reference panels under field conditions', *Remote Sensing of Environment*, **45**, 249–260.

Gupta, P.R., (2003), 'Remote sensing Geology', 2nd Edition Springer-Verlag, Berlin.

Hanley, H.B. and Fraser C.S., (2001), 'Geo-positioning accuracy of IKONOS imagery: Indications from two-dimensional transformations', *Photogrammetric Record,* **17,** No. 98, pp. 317-329.

Hautecoeur, O., and Leroy, M.M., (1998), 'Surface Bidirectional Reflectance Distribution Function observed at global scale by POLDER/ADEOS', *Geophysical Research Letters*, **25**, 4197–4200.

Herold, M., Roberts, DA., Gardner, M.E. and Dennison, P.E., (2004), 'Spectrometry for urban area remote sensing: development and analysis of a spectral library from 350 nm to 2400nm', *Remote Sensing of Environment,* **91**, pp. 304-319.

Hoffbeck, J.P. & Landgrebe, D.A., (1996), 'Classification of remote sensing images having high spectral resolution', *Remote Sensing of Environment,* **57**, pp.119-126.

Holland, S.E., Groom, D.E., Palaio, N.P., Stover, R.J., and Wei, M., (2003), 'Fully Depleted, Back-Illuminated Charge-Coupled devices Fabricated on High Resistivity Silicon', IEEE Trans. On Electron Devices, Vol. **50**, No1.

Holst, G.C., (1998), 'CCD Arrays, Cameras, and Displays, Second Edition', Winter Park, FL: JCD Publishing and Bellingham, WA, SPIE.

Hook, S., Gabel, A. R., Green, A. A., and Kealy, P. S., (1992), 'A comparison of techniques for extracting emissivity information from thermal infrared data for geologic studies', *Remote Sensing of Environment,* **42**, pp. 123-135.

Hook, S.J., (2000), 'ASTER spectral library', Available online at: http://speclib.ipl.nasa.gov/ (accessed October 2004).

Hughes, G.F., (1968), 'On the mean accuracy of statistical pattern recognizer', *IEEE Transactions on Information Theory,* **14**, 55-63.

Idrisi, (2001), ' Guide to GIS and image processing', *Available from* Clarks Lab, Clarks University , 950 main street, Worcester, MA, USA, **1 & 2**.

Ignatov, A. M., and Dergileva, I. L., (1995), 'Model approximation of angular dependence in AVHRR brightness temperature over a black surface', *International Journal of Remote Sensing*, **16**, 3687-3693.

Jackson, R. D., Reginato, R. J., and Idso, S. B., (1977), 'Wheat canopy temperature: a practical tool for evaluating water requirements', *Water Resources Research*, **13**, pp. 651–656.

Jacobsen, K., (1993), 'Experiences in GPS photogrammetry', *Photogrammetric Engineering and Remote Sensing*, **59**, pp. 1651–1658.

Janssen, L. L. F., and Van Der Wel, F. J. M., (1994), 'Accuracy assessment of satellite derived land cover data: a review', *Photogrammetric Engineering & Remote Sensing*, **60,** pp. 419-426.

Jensen, J. R., (1996), 'Introductory Digital image processing: A Remote Sensing Perspective', Upper Saddle River, N.J.: Prentice-Hall.

Jensen, J. R., (2000), 'Remote Sensing of the Environment: An Earth Resource Perspective', Upper Saddle River, N.J.: Prentice-Hall.

Jeon, B., and Landgrebe, D.A., (1999), 'Partially supervised classification using weighted unsupervised clustering', *IEEE Transactions on Geosciences and Remote Sensing,* **37**, pp.1073-1079.

Jia, X., (2003), 'On error correction and accuracy assessment of satellite imagery registration', *The Globe,* No. **54**, pp. 35-38.

Kerr, Y. H., Lagouarde, J. P., and Imbernon, J., (1992), 'Accurate land surface temperature retrieval from AVHRR data with use of an improved split window algorithm', *Remote Sensing of Environment*, **41**, 197- 209.

Kindelan, M., Moreno, V., Velverde , A., (1981), 'Geometric correction of airborne multispectral scanner images', *proceedings of the 15th International Symposium on Remote Sensing of the Environment*, Ann Arbor, Michigan, pp. 1539-1549.

Konecny, G., (2000), 'Mapping from Space', *Remote Sensing for Environmental Data in Albania: A Strategy for Integrated Management,* NATO Science Series, **72**, Kluwer Academic Publishers, pp. 41-58.

Kruse, F. A., and A. B. Lefkoff, (1992), 'Hyperspectral Imaging of the Earth's Surface-An Expert System-Based Analysis Approach', *Proceedings of the International Symposium on Spectral Sensing Research*, Maui, Hawaii.

Lacaze, R., and Roujean J. L., (2001), 'G-function and Hot Spot (GHOST) reflectance model Application to multi-scale airborne POLDER measurements', *Remote Sensing of Environment*, **76**, 67–80.

Lagourde, J. P., Kerr, Y., and Brunet, Y., (1995), 'An experimental study of angular effects on surface temperature for various plant canopies and bare soils', *Agricultural and Forest Meteorology,* 77, pp.167-190.

Lambin, E. F., and Ehrlich, D., (1997), 'Land-cover changes in sub-Saharan Africa (1982–1991): Application of a change index based on remotely sensed surface temperature and vegetation indices at a continental scale', *Remote Sensing of Environment*, **61**, pp, 181–200.

Li, Z. L., Becker, F., Stoll, M. P., and Wan, Z., (1999), 'Evaluation of six methods for extracting relative emissivity spectra from thermal infrared images', *Remote Sensing of Environment,* **69**, pp.197-214.

Liang, S., (2001), 'Narrowband to broadband conversions of land surface albedo: I, Algorithms', *Remote Sensing of Environment*, **76**, 213–238.

Liang, S., Fang, H., Chen, M., Walthall, C., Daughtry, C.,Morisette, J., Schaaf, C., and Strahler, A., (2002), 'Validating MODIS land surface reflectance and albedo products: methods and preliminary results', *Remote Sensing of Environment*, **83**,149–162.

Lillesand, T.M. and Kiefer, R.W., (1994), 'Remote Sensing and Image Interpretation', John Wiley & Sons.

Lillesand, T.M. and Kiefer, R.W., (2000), 'Remote Sensing and Image interpretation', John Wiley & Sons.

Lucht, W., (1998), 'Expected retrieval accuracies of bidirectional reflectance and albedo from EOS-MODIS and MISR angular sampling', *Journal of Geophysical Research*, **103**, 8763–8778.

Lytle, D., (1996), 'Imager Finds "Hot Spots" in Raging Blazes', *Photonic Spectra*, October, pp.16-18.

Ma, X. L., Wan, Z., Moeller, C. C, Menzel, W. P., Gumley, L. E., and Zhang, Y., (2000), 'Retrieval of geophysical parameters from Moderate Resolution Imaging Spectro radiometer thermal infrared data: evaluation of a two-step physical algorithm', *Applied Optics,* **39**, pp, 3537-3550.

Ma, X., Wan, Z., Moeller, C. C., Menzel, W. P., and Gumley, L. E., (2002), 'Simultaneous retrieval of atmospheric profiles and land-surface temperature and surface emissivity from Moderate Resolution Imaging Spectroradiometer thermal infrared data: extension of a two-step physical algorithm', *Applied Optics*, **41**, 909–924.

Madani, M., (1999), 'Real-Time Sensor-Independent Positioning by Rational Functions', *Proceedings of ISPRS Workshop on Direct Versus Indirect Methods of Sensor Orientation,* Barcelona, Spain, November, pp. 64-75.

Mather, P.M., (1999), 'Computer processing of Remotely Sensed Images', 2nd Ed., John Wiley & Sons.

Mather, P.M., (2004), 'Computer Processing of Remotely-Sensed Images'3rd Ed., Chichester,Wiley.

McCullagh, M. J., and Ross, C. G., (1980), 'Delaunay triangulation of a random data set for isarithmic mapping', *Cartographic Journal,* **17,** pp. 93-99.

McDaid, H., and Oliver, D., (1997), 'Smart weapons: top secret history of remote controlled airborne weapons', New York: Barnes & Noble.

McVicar, T. R., and Jupp, D. L. B., (1998), 'The current and potential operational uses of remote sensing to aid decisions on drought exceptional circumstances in Australia: a review', *Agricultural Systems*, **57**, pp. 399–468.

Meister, G., Rothkirch, A., Spitzer, H, and Bienlein, J., (2000), 'BRDF field studies for remote sensing of urban areas', *Remote Sensing Reviews,* **19**, pp. 37-57.

Menenti, M., Jia, L., LI, Z.-L., Djepa , V., Wang , J., Stoll, M. P., Su, Z., and Rast , M.,(2001), 'Estimation of soil and vegetation temperatures from directional thermal infrared observations: The HEIHE, SGP'97, IMGRASS experiments', *Journal of Geophysical Research,* **106,** pp.11997-12010.

NCSA, (2004), 'HDF 4.1r3 User's Guide', [Online], National Centre for Super Computing, Available:http://hdf.ncsa.uiuc.edu/UG41r3_html/UG_BookTOP.html.

Natural Environmental Research Council (NERC), (2004), ' Airborne Remote Sensing Facility (ARSF), Home page [Online], 'Available: http: *//www.nerc.ac.uk/arsf/home.htm'*.

Negahdaripour, S., (1998), 'Revised definition of optical flow: integration of radiometric and geometric cues for dynamic scene analysis', *IEEE Trans. O Pattern Analysis and Machine Intelligence,* Vol. 20, No. 3, pp. 961-975.

Norman, J. M., Castello, S., and Balick, L. K., (1994), 'Directional infrared temperature and emissivity of vegetation: measurements and models', *Proceedings of the 6th Symposium on Physical Measurements and Signatures in Remote Sensing, **17-21** January 1994, Val d'Isere, France* (CNES ED), pp.749-758.

Ottermann, J., Brakke, T. W., and Susskind, J., (1992), 'A model for inferring canopy and underlying soil temperatures from multi-directional measurements', *Boundary-Layer Meteorology,* **61,** pp.81-97.

Ottlé, C., and Vidal-Madjar,D., (1992), 'Estimation of land surface temperature with NOAA9 data', *Remote Sensing of Environment*, **40**, 27-41.

Pala V. and X. Pons, (1995), 'Incorporation of Relief in Polynomial-Based Geometric Corrections', *Photogrammetric Engineering & Remote Sensing,* **61,** No.7, pp. 935-944.

Perplant, F.P and McKeown, D.M., (1990), 'Scene registration in aerial image analysis', *Photogrammetric Engineering and Remote Sensing,* **56, No. 4**, pp. 481-493.

Petrie, G., (2002), 'Optical Imagery from Airborne & Spaceborne Platforms', *Geoinformatics,* **5,** No. 11, pp. 28-35.

Prata, A. J., and Platt, C. M. R., (1991), 'Land surface temperature measurements from the AVHRR', *Proceedings of the 5th AVHRR Data Users' Meeting. Tromso, Norway,* pp. 433- 438.

Prata, A. J., Caselles, V., Coll, C., Ottlé, C., and Sobrino, J., (1995), 'Thermal remote sensing of land surface temperature from satellites: current status and future prospects', *Remote Sensing Reviews*, **12**, 175- 224.

Ralf, W., Morley M.B., Alexander, W., Armin, R., and Erik, B., (2002), *'Temperature dependence of dark current in a CCD',* Proceedings of the SPIE Vol. **4669**, 193.

Ralf, W., Alexander, W., Morley, M.B., Albert, J.B., and Erik, B., (2003), *'PSF measurements on back-illuminated CCDs',* presented at Electronic Imaging.

Reutter, H., Olesen, F. S., and Fischer, H., (1994), 'Distribution of the brightness temperature of land surfaces determined from AVHRR data', *International Journal of Remote Sensing*, **15**, 95-104.

Richards, J.A., (1986), 'Remote Sensing Digital Image Analysis', Springer-Verlag.

Richards, J.A., (1993), 'An Introduction Remote Sensing Digital image Analysis', 2nd Edition, Springer-Verlag, Berlin.

Richards, J.A. and Jia, X., (1999), *'Remote Sensing Digital Image Analysis',* 3rd Ed., Springer-Verlag, Berlin.

Rowlands, A., and Sarris, A., (2007), 'Detection of exposed and subsurface archaeological remains using multi-sensor remote sensing', *Journal of Archaeological Science,* 34: 795-803.

Roy, D.P., Devereux, B., Grainger, B. and White, S.J., (1997), 'Parametric geometric correction of Airborne Thematic Mapper imagery', *International Journal of Remote Sensing*, **18**, No 9, pp.1865–1887.

Roy, D. P., Lewis, P. E., and Justice, C. O., (2002), 'Burned area mapping using multi-temporal moderate spatial resolution data bi-directional reflectance model-based expectation approach', *Remote Sensing of Environment*, **83**,No1, pp.263-286.

Sabins, F.F., Jr., (1987), 'Remote Sensing: Principles and Interpretation', 2^{nd} Edition, New York: W.H. Freeman & Co.

Salisbury, J.W. and D. M. D'Aria, (1992), 'Emissivity of Terrestrial Materials in the 8 – 14 μm Atmospheric Window', *Remote Sensing of Environment*, **42**, pp.83-106.

Sandmeier, S.,Muller, C., Hosgood, B., and Andreoli, G., (1998), 'Sensitivity analysis and quality assessment of laboratory BRDF data', *Remote Sensing of Environment*, **64**, 176–191.

Schultz, P. A., and Halpert, M. S., (1995), 'Global analysis of the relationships among a vegetation index, precipitation and land surface temperature', *International Journal of Remote Sensing*, **16**, 2755- 2777.

Scott, A., (1994), 'Low cost remote sensing techniques applied to drainage area studies', *Journal of the Institute of Water Environmental Managements*, **8**, pp. 497-501.

Seguin, B., Courault, D., and Guerif,M., (1994), 'Surface temperature and evapotranspiration: application of local scale methods to regional scales using satellite data', *Remote Sensing of Environment*, **49**, 287- 295.

Settle, J., and Drake, M., (1987), Digital ground reference maps. Report no. 4, Image and map processing software, NERC Unit for Thematic Information Systems (unpublished).

Shaker, A., Barakat, H., and Shi, W., (2002), 'The Use of Satellite Image Maps for Urban Planning in Turkey', *Third International Symposium Remote Sensing of Urban Areas Turkey*, 11-13.

Snyder, W.C., W. Zhengming, Y. Zhan and Y. Freng., (1997), 'Thermal infrared (3–14 μm) bi-directional reflectance measurements of sand and soils', *Remote Sensing of Environment*, **60**, pp.101-109.

Sobrino, J. A., Li, Z. L., Stoll, M. P., and Becker, F., (1994), 'Improvements in the split-window technique for land surface temperature determination', *IEEE Transactions on Geoscience and Remote Sensing,* **32**, pp. 243-253.

Strausz, A., (2001), 'Application of Photogrammetric Techniques to the Measurement of Historic Photographs', Oregon State University.

Tajudin, S. & Landgrebe, D.A., (2000), 'Robust parameter estimation for mixture model', IEEE *Transactions on Geoscience and Remote Sensing,* **38**, pp.439-445.

Tao V. and Y. Hu, (2001), '3-D Reconstruction Algorithms with the Rational Function Model and their Applications for IKONOS Stereo Imagery', *Proceedings of ISPRS Joint Workshop "High Resolution Mapping from Space",* Hannover, Germany, September, CD-ROM, pp. 253-263.

Ton, J. and Jain, A.K., (1989), 'Registering Landsat images by point matching', *IEEE Transactions on Geoscience and Remote Sensing,* **38**, No. 5, pp. 642-651.

Tonry, J.L., Onaka, P.M., Burke, B., and Luppino, G.A., (2005), 'Pan-STARRS and Gigapixel Cameras', Proc. Scientific Detector Workshop, Sicily, p. 53.

Toutin, Th., (1995), 'Multi-source data fusion with an integrated and unified geometric modelling', *EARSeL Journal Advances in Remote Sensing,* **4,** No.2, pp. 118-129 http://www.ccrs.nrcan.gc. ca/ccrs/eduref/ref/bibpdf/ 1223.pdf

Toutin Th., (2001), 'Geometric processing of IKONOS Geo images with DEM', *Proceedings of ISPRS Joint Workshop "High Resolution Mapping from Space"*, Hanover, Germany, September, CD-ROM, pp. 264-271. http://www.ccrs.nrcan.gc.ca/ccrs/eduref/ref/bibpdf/ 13116.pdf

Toutin, Th., (2004), '*Review Article: Geometric Processing of Remote Sensing Images': Models, Algorithms and Methods*, Int. J. Remote Sensing, **25(10)**, pp: 1893-1924.

Tso, B., and Mather, P.M., (2001), 'Classification Methods for Remotely Sensed Data', London, Taylor and Francis.

Vermote, E. F., and Roy, D. P., (2002) 'Land surface hot-spot observed by MODIS over Central Africa', *International Journal of Remote Sensing*, **23**, 2141–2143.

Vermote, E. F., El Saleous, N. Z., Justice, C. O., Kaufman, Y. J., Privette, J., Remer, L., Roger, J. C., and Tanre', D., (1997), 'Atmospheric correction of visible to middle infrared EOS-MODIS data over land surface, background, operational algorithm and validation', *Journal of Geophysical Research*, **102**, 17131–17141.

Vermote, E. F., El Saleous, N. Z., and Justice, C. O., (2002), 'Operational atmospheric correction of the MODIS data in the visible to middle infrared', *Remote Sensing of Environment*, **83**, No. 1, pp.97-111.

Vermote, E. F., and Vermeulen, A., (1999), 'Atmospheric correction algorithm: spectral reflectances (MOD09)', National Aeronautics and Space Administration.

Vidal, A., (1991), 'Atmospheric and emissivity correction of land surface temperature measured from satellite ground measurements or satellite data', *International Journal of Remote Sensing*, **12**, 2449-2460.

Vogt, J. V., (1996), 'Land surface temperature retrieval from NOAA- AVHRR data', In *Advances in the Use of NOAA± AVHRR Data for Land Applications*, edited by G. D'Souza *et al*., Dordrecht, The Netherlands: Kluwer Academic Publishers, pp.125-151.

Wadsworth, A., Looyen, W.J., Reuter, R., Petit, M., (1992), 'Aircraft experiments with visible and infrared sensors', *International Journal of Remote Sensing* , **13**, No. 6 and 7, pp 1175-1199.

Wan, Z., and Dozier, J., (1996), 'A generalized split-windows algorithm for retrieving land surface temperature from space', *IEEE Transactions on Geoscience and Remote Sensing*, **34**, 892- 905.

Wan, Z., and Li, Z. L., (1997), 'A physics-based algorithm for retrieving land-surface emissivity and temperature from EOS/MODIS data', *IEEE Transactions on Geoscience and Remote Sensing,* **35**, pp.980-996.

Wan, Z., Zhang, Y., Li, Z.-L., Wang, R., Salomonson, V. V., Yves, A., and Bosseno, R., (2002), 'Preliminary estimate of calibration of the Moderate Resolution Imaging Spectroradiometer (MODIS) thermal infrared data using Lake Titicaca', *Remote Sensing of Environment*, **80**, 498–515.

Wan, Z., Zhang, Y., Zhang, Q. and Li, Z. -L. (2004), 'Quality assessment and validation of the MODIS global land surface temperature', *International Journal of Remote Sensing*, **25:1**, pp. 261–274.

Wilson, A.K., (1994), 'The NERC integrated ATM/CASI/GPS system', *Proceedings of the First International Airborne Remote Sensing Conference and Exhibition*, Strasbourg, France, September, **2**, pp.249-260.

Wilson, A.K., (1995), 'NERC - scientific series Airborne Remote Sensing Facility User Guide handbook', CSS ARSF Faculty handbook Version **1**, National Environmental Research Council.

Wilson, A.K., (1997), 'An integrated Data System for Airborne Remote Sensing', *International Journal of Remote Sensing,* **18,** No.9, pp.1889-1901.

Winterbottom, S.J., and Dawson, T., (2005), 'Airborne multi-spectral prospection for buried archaeology in mobile sand dominated systems', *Archaeological Prospection,* **12**, pp.205-219.

Yamaguchi, Y., Kahle, A. B., T su, H., Kawakami , T., and Pniel , M., (1998), 'Overview of Advanced Spaceborne Thermal Emission and Reflection Radiometer (ASTER)', *IEEE Transactions on Geoscience and Remote Sensing,* **36**, pp.1062-1071.

Yao, J., (2001), 'Image registration based on both feature and intensity matching' In: *The Proceedings of IEEE International Conference on Acoustics, Speech, and Signal Processing,* Vol. 3, pp. 1693-1696.

Yu, B., Ostland, I.M., Gong, P. & Pu, R.L., (1999), 'Penalized discriminant analysis of in situ hyperspectral data for conifer species recognition', *IEEE Transactions on Geoscience and Remote Sensing,* **37**, pp.2569-2577

APPENDIX 1 – LAY OUT OF DAEDALUS AAD1268

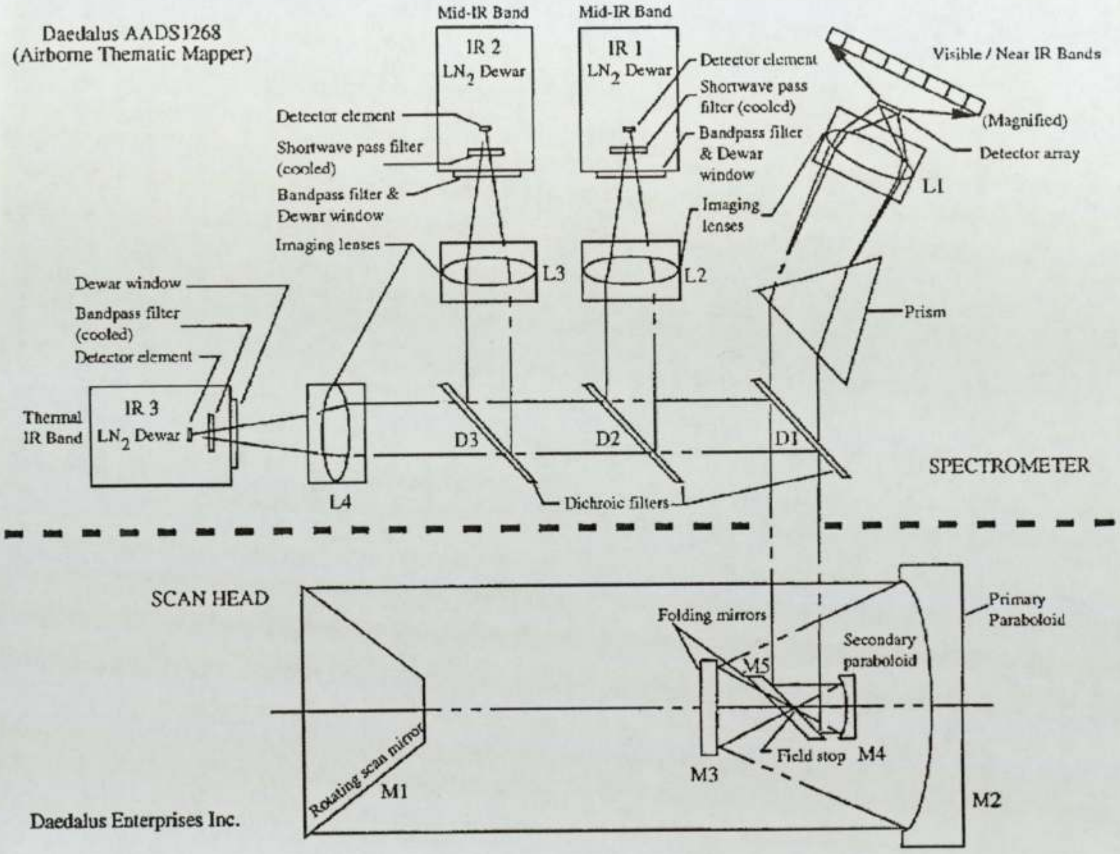

Figure A1-1: Layout of optics and detectors in the Daedalus AADS1268 (from NERC, accessed on 2005).

APPENDIX 2 – AZIMUTH HDF DOCUMENTATION

Extract from 'AZSPS User Guide HDF Contents'

VGroup: ATM / AZ16

Contains ATM scanner recording parameters and recorded, calibrated or geometrically corrected image data stored as 16 bit integer to level 1b and either 16 bit integer or 32 bit floating for level 2 and level 3. Level 1 data is inserted by AZATM. Data recorded with the DEI320 has 12 channels and from the AZ16 11 channels.

Vgroup name: ATM

Vgroup title: ATM

Data	itemtype	AT	Description
ATdesc	C8	64	Vgroup description: ATM scanner details, calibration
ATprog1	C8	40	Vgroup 1st processing program
ATprog2	C8	40	Vgroup 2nd processing program
ATprog3	C8	40	Vgroup 3rd processing program
ATprog4	C8	40	Vgroup 4th processing program
ATsbend	I32	1	Sbend correction applied in scanner flag 0= no, 1= yes
ATrgyro	I32	1	Roll gyro correction applied in scanner flag, 0= no, 1=
ATrmedia	C8	16	Aircraft data recording media
AThddt	C8	16	HDDT tape external label name (Note 1)
ATcct	C8	64	CCT tape external label name (Note 1)
ATtype	C8	8	Daedalus ATM type eg: 1268 or AZ16
ATid	C8	32	ATM ID owner (i.e. NERC)
ATfov	F32	1	Field of view (dec degs)
ATpixfov	F32	1	Pixel field of view (mradians)

ATpixrec	I32	1	Pixels per scan recorded
ATpixred	I32	1	Pixels per scan reduction method, 0= none, 1=average,
ATpixsav	I32	1	Pixels per scan saved
ATsscan	I32	1	Target start scan
ATescan	I32	1	Target end scan
ATchan	I32	1	Channels/bands recorded
ATbpix	I32	1	Bits per pixels recorded
ATgains	F32	var	Channel gains (ATM only)
ATwavu	F32	var	Channel upper wavelength limit
ATwavl	F32	var	Channel lower wavelength limit
ATscps	F32	1	Nominal scans per second recorded
ATbbtf	I32	1	Black body temperature saved type flag, 0= fixed for
ATbb1	F32	var	Set black body 1 temperature
ATbb2	F32	var	Set black body 2 temperature
ATbbscan	I32	var	scan at which temp applies for table option
ATsbb1	F32	var	Recorded blackbody 1 temperatures
ATsbb2	F32	var	Recorded blackbody 2 temperatures
ATvbb1	F32	var	Average sensor response to blackbody 1 temperatures
ATvbb2	F32	var	Average sensor response to blackbody 2 temperatures
ATsync	F32	var	Synchronisation flag
ATcal	C8	32	Calibration version
ATcalfmt	C8	32	Calibration format
ATcalfile	C8	32	Calibration file name
ATcaltab	F32	100	Calibration values table (100 for ATM, 20 for AZ16)
ATradsc	F32	var	Channel radiance scaling multiplier
ATrunits	C8	32	Radiance units
ATimgmin	F32	var	Channels minimum values (excluding zero)
ATimgmax	F32	var	Channels maximum values (excluding overflows)

ATimgzer	I32	var	Channels no. of zero values
ATimgovr	I32	var	Channels no. of overflowed values
SCimtype	I32	1	Image type flag, 0= as source, 1= resampled
SCorder	I32	1	Pixel order flag, 0= l to r, 1= r to l in direction of lines
SClndir	I32	1	Scan line direction flag, 0= flight direction, 1= north up
SCtiles	I32	1	Tiles in image, 0= not tiled single image, >0 = number
SCbands	I32	1	Bands in image
SCpixels	I32	1	Pixels in image
SClines	I32	1	Lines in image
SCpixfmt	I32	1	Pixel format flag, 0= 8bit unsigned, 1= 16bit unsigned
SCHDFfmt	I32	1	Pixel HDF number format flag, see HDF documentation
SCimover	F32	1	flag value indicating overflowed values, see general
SCimunder	F32	1	flag value indicating underflowed or missing values, see
SCpixbytes	I32	1	Bytes per pixel
SCposn	I32	1	Position data relation flag, 0= posns per scan, 1= posns

---

Remote Sensing Scanner processing System (C) Azimuth Systems 1999

Version: 1.2.0 4 011100

APPENDIX 3 – MATLAB PROGRAM USED

Read and Opening HDF File

```
% open the hdf file
hdf_file = 'C:\ATM1\a085031b.hdf';
sd_id = hdfsd('start', hdf_file, 'read');
if sd_id == -1
   fprintf('Error opening hdf file %s',hdf_file)
   break;
end
% get all the info needed to read in the image data
sds_index = hdfsd('nametoindex',sd_id,'ATdata');
if sds_index == -1
   fprintf('Error finding index of ATdata')
   break;
end
sds_id = hdfsd('select',sd_id, sds_index);
[name,rank,dimsizes,data_type,nattrs,status] = hdfsd('getinfo',sds_id);
start = zeros(1, rank);
stride = ones(1, rank);
% edge = dimsizes;
edge = [11 dimsizes(2) dimsizes(3)];
```

```
% read in the image data
fprintf('\nReading in the data ...')
[atm_data,status] = hdfsd('readdata',sds_id,start,stride,edge);
status = 1;
if status == -1
   fprintf('\nError reading in the data')
   break;
end
fprintf('\nData read in successfully.')
% close interfaces to hdf file
status = hdfsd('endaccess',sds_id);
status = hdfsd('end',sd_id);


% get some vgroup attribute information
file_id = hdfh('open',hdf_file,'read',0);
status = hdfv('start',file_id);
if status == -1
   fprintf('\nError error starting the vgroup interface')
   status = hdfh('close', file_id);
   break;
end
```

```
vgroup_ref = hdfv('find', file_id, 'ATM2');

if vgroup_ref == 0

   fprintf('\nError finding the vgroup reference')

   status = hdfv('end',file_id);

   status = hdfh('close', file_id);

   break;

end

% Retrive any vdata information needed from the vgroup

vgroup_id = hdfv('attach', file_id, vgroup_ref, 'r');

  vdata_scale_ref = hdfv('flocate',vgroup_id,'SCposimag');

  if vdata_scale_ref == 0

     fprintf('\nError finding the vdata reference')

     status = hdfv('end',file_id);

     status = hdfh('close', file_id);

     break;

  end

status = hdfv('detach',vgroup_id);

% get the vdata information

vdata_scale_id = hdfvs('attach',file_id,vdata_scale_ref,'r');

  [scale_field_names,count] = hdfvs('getfields',vdata_scale_id);

  status = hdfvs('setfields',vdata_scale_id, scale_field_names);
```

```
  [count,status] = hdfvs('Querycount',vdata_scale_id);

  [atm_data_scale,count] = hdfvs('read',vdata_scale_id,count);

  status = hdfvs('detach',vdata_scale_id);


status = hdfv('end',file_id);

status = hdfh('close', file_id);

%multiply the ATM image data by the scale factor

atm_double_data = double(atm_data);

clear atm_data;

%vgroup_id = hdfv('attach',file_id,1,'r');

%[vgroup_name,status] = hdfv('getname',vgroup_id)

%[n,interlace,fields,nbytes,vdata_name,status] = hdfvs('inquire',vdata_scale_id)
```

Padding Both Extreme Edges Of HDF File To One From The Original Value

```
function res = update_atm_bands(orig_hdf, left_pad, right_pad)

res =1;

TOTAL_NUM_BANDS = 11;

%open the original hdf file

sd_id = hdfsd('start', orig_hdf, 'rdwr');
```

```
if sd_id == -1
   fprintf('Error opening hdf file %s',orig_hdf)
   break;
end
% get all the info needed to read in the image data
sds_index = hdfsd('nametoindex',sd_id,'ATdata');
if sds_index == -1
   fprintf('Error finding index of ATdata')
 break;
end
sds_id = hdfsd('select',sd_id, sds_index);
[name,rank,dimsizes,data_type,nattrs,status] = hdfsd('getinfo',sds_id);
stride = ones(1, rank);
% edge = dimsizes;
row = dimsizes(2);
col = dimsizes(3);
all_bands = zeros(col,row,TOTAL_NUM_BANDS);
%loop
for x=1:1:TOTAL_NUM_BANDS
   start = [x-1 0 0];
   edge = [1 row col ];
```

```
  %read in one band at a time
  disp(['Reading in band ', num2str(x)]);
  [atm_data,status] = hdfsd('readdata',sds_id,start,stride,edge);
  if status == -1
     fprintf('\nError reading in the data')
     break;
   end
   %padd/trim this band
   atm_data(1:left_pad,:) = 1;
   atm_data(col-right_pad:col,:) = 1;
    %add this band to a 'big' array
   all_bands(:,:,x) = atm_data;
end %end loop
start = zeros(1, rank);
stride = []; % write every element
edge = [dimsizes];
write_status = hdfsd('writedata',sds_id, start, stride, edge, uint16(all_bands));
if write_status == -1
   disp('the data was not written successfully!');
end
%close original hdf file
```

```
status = hdfsd('endaccess',sds_id);

status = hdfsd('end',sd_id);
```

APPENDIX 4 – PROGRAMS USED

AZGCORR

Azgcorr is a geo-correcting program, run in UNIX. It takes the image data, with the information from the flight path (post processed navigation data). With this information it creates a map projection referenced output image. This image is corrected for aircraft position, altitude and ground surface separation, computed from aircraft spheroid separation estimates. It contains many options for selecting mapping details, images definition and interpolation techniques. Enabling it to handle many different types of scanner data and able to output the images on all of the main survey map projections.

There are 6 different levels of airborne or satellite image processed data defined as:

Level 0: No corrections

Level 1A: Radiometric correction

Level 1B: Radiometric correction with synchronised per scan geo-location

Level 2: Product derived from level 1

Level 3A: Level 1 data geo-corrected.

Level 3B: Geo-corrected with ground control pints used for precise location.

Idrisi 32

Idrisi is a window based Geographical Information Systems (GIS) or Digital Image Processing (DIP) package, developed by Clark Labs. It boasts an impressive importing, exporting, image processing, modelling and analytical functionality and it is easy to use. The program is the main package used for this project. It has all the capabilities to carry out all the accuracy tests needed and all the qualities needed to manipulate to improve the data. There are many special features included within the package: this includes change and time series analysis, land change prediction, multi-criteria and milti-objective decision supports, uncertainty analysis and simulation modelling. TIN interpolation, Kriging and conditional simulation are also offered .for image processing there full set of tools: restoration, enhancement, and transformation, signature development and classification, include hard and soft classifiers and hyper spectral image classification. All theses features make Idris a very usable tool for GIS and remote sensing.

Matlab

Matlab is a high-performance language for technical computing. It integrates computation, visualization, and programming in an easy-to-use environment where problems and solutions are expressed in familiar mathematical notation. Mat-lab provides a set of functions that enable you to access the HDF and importing HDF Data. Hierarchical Data Format (HDF) is a general-purpose, machine-independent standard for storing scientific data in files, developed by the National Centre for Supercomputing Applications (NCSA).

ArcGIS

ArcGIS is also a window bases GIS and remote sensing package, created by ERSI. It is a market leader for GIS, and so it is highly regarded it is very easy to use and is a single, integrated system for geographic data creation, management, integration and analysis. It is also use full when dealing the project points, vector or polygons data and very good in presenting a data.

APPENDIX 5 – RESAMPLING

```
Resample: Summary of Transformation a085043b

Computed polynomial surface: Quadratic (based on 19 control points)

Coefficient              X                         Y


     b0      179904.0254974365230000      1497933.8767127990700000

     b1         -2.1467582208933891          -9.1370439555612393

     b2          0.0832887107553688           1.2077473455792642

     b3          0.0000040975112327           0.0000111363010752

     b4          0.0000000203669696           0.0000001073078403

     b5         -0.0000001507656495          -0.0000000039802040

Note: Figures are carried internally to 20 significant figures.

    Formula shown is the back transformation (new to old).

Control points used in the transformation:


     Old X       Old Y        New X        New Y    Residual

-------------------------------------------------------------

 1159.184905 9161.568621 408936.780000 308202.350000    omitted

 1599.387198 9648.380130 409302.620000 308599.530000    4.286600

 1936.589099 9001.255249 409580.360000 308072.550000    2.825512

  676.963707 8535.436615 408541.230000 307706.080000    1.990518

 1225.166473 8630.297774 408994.590000 307783.190000    0.662978

  991.086674 8072.624030 408802.210000 307338.610000    2.701714

 1096.646692 7965.309653 408885.900000 307251.860000    1.966732

 1998.551935 7572.472237 409631.620000 306930.520000    1.376575

 1296.255850 7007.709434 409050.190000 306482.020000    3.350471
```

1719.992966	6661.648215	409400.090000	306204.510000	0.944310
1455.147487	6100.518293	409184.240000	305754.530000	4.019568
1166.566736	5487.638950	408942.470000	305261.730000	omitted
1440.718447	5498.857792	409061.650000	305278.750000	omitted
1837.074088	5389.127498	409485.430000	305175.800000	omitted
1805.540126	5074.755504	409471.840000	304933.900000	1.600851
754.789687	4189.672141	408603.410000	304230.530000	2.109127
1610.399055	3958.403721	409308.210000	304043.980000	3.827316
736.739361	3520.589304	408587.280000	303695.130000	2.757643
744.272027	2966.258297	408593.420000	303248.170000	2.139418
1353.873815	2502.354164	409099.550000	302876.650000	1.598217
1070.773687	1832.636854	408814.130000	302307.470000	omitted
1159.081807	1937.545047	408928.720000	302431.450000	omitted
2024.571484	2026.839500	409659.520000	302502.460000	omitted
1660.998616	1283.300235	409366.770000	301924.630000	omitted
1770.018010	1194.831651	409441.880000	301827.420000	0.494951
1911.999739	737.743966	409558.230000	301460.690000	0.883138
926.646791	1281.889832	408747.530000	301900.390000	2.271859

Overall RMSE = 2.456768

Note: RMSE Error is expressed in input image units.

With low RMSE errors, be careful that an adequate sample exists

(eg. 2-3 times the mathematical min).

```
Resample: Summary of Transformation a085053b

Computed polynomial surface: Quadratic (based on 24 control points)


Coefficient                  X                          Y


     b0    5194836.1402076482800000      532908.2304921150210000

     b1       -26.1484380882861842       -5.0199986419520428

     b2        -0.5503454602222178        2.0174659019066894

     b3         0.0000330443244845        0.0000065676519377

     b4         0.0000009061000764       -0.0000011553181259

     b5         0.0000002939460112       -0.0000004816995283


Note: Figures are carried internally to 20 significant figures.

    Formula shown is the back transformation (new to old).



Control points used in the transformation:


     Old X      Old Y       New X       New Y    Residual

----------------------------------------------------------------

  984.842207 8337.949404 409552.090000 307855.720000    0.251840

 1274.279826 8272.889599 409793.090000 307805.240000    3.698632

 1860.234484 7855.976742 410270.440000 307461.800000    3.147516

 1765.745862 7614.002468 410192.500000 307272.200000    2.189098

 1017.683866 7182.680059 409581.950000 306925.630000    5.667853

 1707.248520 6749.911888 410149.980000 306585.200000    omitted

 1548.858641 6585.850533 410021.200000 306456.950000    omitted
```

1757.352449	5986.312389	410185.810000	305969.130000	4.437062
1515.399940	5637.784616	409991.360000	305695.900000	omitted
983.123681	6024.047075	409547.610000	306004.340000	6.075825
2037.394396	5618.459826	410420.700000	305681.560000	omitted
1500.133930	5172.256542	409981.470000	305316.710000	1.960286
1869.814636	5026.850891	410283.940000	305198.860000	5.074756
934.512142	5077.742114	409512.570000	305248.330000	3.594099
1133.301853	4747.560598	409677.070000	304976.930000	4.509362
1633.707464	4156.450122	410105.170000	304513.470000	omitted
1866.979252	4175.275296	410275.320000	304513.440000	5.092715
1265.740030	3689.209276	409792.120000	304133.880000	5.464786
1177.126850	3368.187337	409715.320000	303875.560000	2.707815
1516.168582	3086.261522	409993.840000	303651.140000	2.358490
1325.939201	2095.846498	409831.440000	302861.400000	6.714759
1853.669219	1986.112770	410266.460000	302769.070000	3.279537
2046.306567	2042.016008	410422.260000	302808.020000	0.939795
733.106795	1556.703002	409341.370000	302432.790000	1.702899
1436.380468	816.789621	409930.720000	301836.080000	5.252825
1071.155234	360.599072	409622.780000	301478.020000	1.391672
1157.842041	216.021733	409693.410000	301358.940000	3.749465
871.293986	379.876051	409462.760000	301489.380000	omitted
855.084704	795.959996	409443.610000	301827.730000	2.619853
843.949734	887.490990	409432.620000	301899.070000	0.708000
1836.170211	84.314151	410246.770000	301238.220000	omitted

Overall RMSE = 3.869167

```
Note: RMSE Error is expressed in input image units.
With low RMSE errors, be careful that an adequate sample exists
(eg. 2-3 times the mathematical min).


Resample: Summary of Transformation a085063b
Computed polynomial surface: Quadratic (based on 30 control points)

Coefficient              X                              Y

     b0    -1209025.6001652479200000      -269021.9045658111570000
     b1          4.8154036642317806        -0.6326516420449480
     b2         -0.1750547223521153         1.3849295880636419
     b3         -0.0000041761868717         0.0000006202678460
     b4         -0.0000005790305423         0.0000004422302638
     b5          0.0000006776180000        -0.0000005207951749

Note: Figures are carried internally to 20 significant figures.
    Formula shown is the back transformation (new to old).


Control points used in the transformation:

     Old X       Old Y       New X        New Y    Residual
--------------------------------------------------------------
 1213.541594  8199.639624 410580.080000 307468.120000    4.017855
  841.123898  8197.884737 410270.180000 307460.580000    omitted
```

1853.423717	8730.563298	411106.850000	307887.890000	0.836732
1829.813840	8611.511729	411092.510000	307778.700000	omitted
752.254742	7958.164357	410191.390000	307274.280000	6.892089
1891.356630	7875.904005	411144.520000	307192.490000	omitted
1836.460156	7999.294533	411092.240000	307300.220000	2.310993
1318.374656	6881.924743	410655.730000	306413.430000	omitted
1373.271133	6748.251670	410700.680000	306299.320000	omitted
847.865182	7165.901182	410276.820000	306641.540000	0.916757
779.354379	7092.195907	410221.500000	306583.530000	1.987580
1875.964209	6409.295458	411128.160000	306026.650000	1.782389
1914.639435	6385.934396	411155.190000	306010.270000	omitted
1255.109735	6053.043202	410613.990000	305748.310000	3.768321
745.305910	6333.287770	410195.640000	305977.490000	4.897498
821.502224	5473.710950	410257.640000	305283.040000	2.105735
914.606648	5329.810174	410339.190000	305167.160000	6.097312
1290.537720	5421.064324	410645.480000	305240.270000	1.712558
1208.453770	4576.401309	410580.490000	304560.140000	5.431099
844.764613	4511.278530	410275.240000	304512.380000	2.879344
1198.160681	4795.762248	410565.620000	304736.970000	4.661673
1987.297531	4850.602483	411223.820000	304773.190000	4.558517
1962.799981	4601.970562	411203.900000	304576.860000	2.323201
1975.975136	3459.100056	411208.120000	303672.990000	omitted
1525.165268	3554.522062	410840.260000	303743.020000	1.666804
1528.678642	3324.631793	410845.780000	303566.910000	omitted
1985.768667	3147.388154	411216.300000	303416.290000	5.384696
1613.067933	2538.968644	410909.810000	302934.060000	4.369365
1843.545300	2585.016892	411103.270000	302971.680000	7.815185

```
1679.175589  1885.588914 410961.610000 302406.330000     3.519606
1817.426451  1701.508231 411078.800000 302261.170000     1.770894
1769.815027  1633.940849 411038.400000 302202.410000     4.929179
 708.897921  1959.720630 410161.050000 302475.730000     3.201393
1414.166687  1297.977220 410738.620000 301940.540000     5.746596
1791.579963  1215.716868 411055.060000 301870.220000     2.500406
1894.826512   733.163917 411143.460000 301485.860000     4.673299
1511.868691   389.205964 410821.370000 301214.730000     0.619877
 813.736475   419.847945 410248.270000 301242.970000     3.113543
1136.253275   574.086106 410504.420000 301360.590000     omitted

Overall RMSE =     3.997012

Note: RMSE Error is expressed in input image units.
With low RMSE errors, be careful that an adequate sample exists
(eg. 2-3 times the mathematical min).


Resample: Summary of Transformation a086073b
Computed polynomial surface: Quadratic (based on 28 control points)

Coefficient                   X                          Y

      b0    -306653.7773990631100000    -2003528.2355346679700000
      b1          0.1526556569115201           8.1359148782794364
      b2          0.1316914344265570           0.9188644197438407
      b3          0.0000017773460632          -0.0000102052639265
```

```
b4        -0.0000012043552035        0.0000009327707669
b5         0.0000005959111308       -0.0000000873348395
```

Note: Figures are carried internally to 20 significant figures.

Formula shown is the back transformation (new to old).

Control points used in the transformation:

```
     Old X       Old Y       New X        New Y    Residual
--------------------------------------------------------------
 1731.770422 9384.156979 411625.930000 308091.600000    0.397480
 1326.909454 9060.529796 411301.190000 307840.360000    1.899631
 1805.994936 9487.537885 411686.770000 308178.070000     omitted
  991.549609 8916.007220 411030.000000 307731.600000    2.914592
 1083.677971 9117.375245 411104.560000 307887.900000    1.747371
 1565.192622 8893.454003 411494.790000 307703.570000    4.075724
 1810.439968 8558.888105 411691.350000 307428.970000    1.669408
 1122.291270 8218.840883 411142.630000 307167.190000     omitted
 1345.610423 8336.669944 411316.650000 307258.880000    0.796326
 1853.914640 8319.884481 411731.350000 307236.650000     omitted
 1409.565665 7847.366320 411366.960000 306863.820000    4.071689
 2235.453926 7678.810495 412031.510000 306718.450000    3.191652
 1195.186159 7647.206278 411190.600000 306709.330000     omitted
 1751.518549 6878.872626 411641.470000 306087.440000    4.445313
 1169.530907 6774.929867 411180.560000 306008.940000    4.703984
 1105.103573 6792.607100 411127.660000 306026.180000    2.224237
```

1282.340918	5595.750524	411269.890000	305065.280000	1.507902
1554.778611	5729.449001	411488.790000	305174.370000	omitted
1229.765222	5276.701309	411221.920000	304808.280000	omitted
1912.124647	4765.134379	411774.030000	304389.080000	4.334780
2169.672102	4682.837472	411979.960000	304327.120000	3.910141
1434.539968	3086.493340	411389.020000	303055.730000	1.319086
1733.265509	3560.556596	411624.960000	303428.710000	4.548498
2246.370557	3655.369247	412036.560000	303500.420000	2.989893
2253.399393	3490.325003	412044.800000	303373.160000	4.362652
2214.531055	3813.569002	412013.680000	303630.430000	2.316437
1195.433008	3149.589394	411198.990000	303116.670000	omitted
1258.411381	3167.568682	411247.480000	303125.280000	3.663910
1152.247838	3264.656837	411163.010000	303201.150000	0.841246
1653.945372	1995.058062	411561.650000	302178.150000	0.835565
1020.155201	1598.558565	411052.540000	301869.980000	2.179850
1332.797838	1117.163127	411302.650000	301481.390000	1.025846
1348.542432	1222.791443	411315.410000	301566.470000	2.027412
2208.661129	759.684307	412000.980000	301184.000000	2.901746
1811.531880	1117.865434	411694.690000	301473.880000	omitted
1312.484505	801.823263	411287.210000	301227.750000	2.206202
1125.419051	1118.652028	411145.010000	301484.640000	omitted

Overall RMSE = 2.922208

Note: RMSE Error is expressed in input image units.

With low RMSE errors, be careful that an adequate sample exists

(eg. 2-3 times the mathematical min).

```
Resample: Summary of Transformation a085083b

Computed polynomial surface: Quadratic (based on 25 control points)


Coefficient                 X                              Y


    b0     2955428.6563744545000000      -2265450.4408130645800000

    b1        -16.1147951752318477            9.4561347535782261

    b2          0.7696548451003764            0.8188601361434849

    b3          0.0000218904472991           -0.0000120778065988

    b4         -0.0000023762150195            0.0000017335019822

    b5          0.0000003449525006           -0.0000004658942518


Note: Figures are carried internally to 20 significant figures.

    Formula shown is the back transformation (new to old).



Control points used in the transformation:


    Old X        Old Y        New X          New Y       Residual

-------------------------------------------------------------

 1614.606974 7622.566877 413192.500000 307411.430000    omitted

 1941.766809 7766.020271 413465.170000 307522.070000   4.609797

 1610.125333 6757.363593 413192.500000 306723.830000    omitted

 1869.634610 8010.855755 413409.360000 307724.150000   3.985046

 2156.000751 7841.925058 413631.520000 307589.580000   5.491937

 1263.900460 8144.086108 412917.200000 307829.640000   4.479853
```

965.317867	7909.944914	412680.730000	307649.520000	5.622067
1386.950706	7803.789403	413011.600000	307565.180000	omitted
1988.207742	6789.215263	413490.940000	306760.470000	omitted
948.466897	6886.763565	412661.340000	306827.430000	2.724696
1212.895504	6032.869856	412877.110000	306142.980000	2.370480
1804.255360	5807.530965	413347.600000	305958.380000	omitted
1845.191034	5482.853469	413388.270000	305701.960000	4.700242
2025.087712	5714.215103	413527.970000	305880.570000	4.620094
1941.659970	5874.570239	413463.560000	306013.290000	1.451673
1198.099161	4946.385529	412862.070000	305273.930000	5.502907
1551.073252	4861.407314	413145.810000	305201.510000	omitted
1487.971738	4824.109432	413100.840000	305169.650000	4.427866
1740.377792	4410.963657	413304.170000	304840.300000	4.400527
1978.442592	5056.503930	413493.190000	305350.080000	omitted
1183.937174	4471.214082	412857.160000	304893.180000	3.246688
1014.710388	4453.999675	412716.830000	304881.720000	1.761602
1486.681021	4034.900573	413090.110000	304539.190000	omitted
1397.048190	3728.627574	413015.950000	304289.950000	omitted
812.642129	3408.726496	412549.270000	304046.870000	3.497812
902.274960	3849.845683	412624.520000	304396.810000	2.303788
780.374309	4004.058081	412527.910000	304524.670000	3.027947
1475.796585	3141.355184	413086.970000	303831.740000	4.610169
2015.926615	2850.133316	413516.930000	303594.280000	2.177701
1682.853880	1105.220010	413247.940000	302204.750000	2.991268
1010.607644	1181.429625	412714.980000	302264.930000	5.462059
840.305264	1486.268088	412568.850000	302518.510000	omitted
719.300942	858.659489	412474.500000	302010.100000	1.307506

```
1050.458398   921.918301 412741.490000 302053.950000     5.189270

1162.499437   400.779018 412829.680000 301643.560000     3.568916

1638.673854   608.114002 413219.710000 301799.580000      omitted

1229.724061  1599.959734 412877.160000 302586.430000      omitted


Overall RMSE =     3.966447


Note: RMSE Error is expressed in input image units.
With low RMSE errors, be careful that an adequate sample exists
(eg. 2-3 times the mathematical min).




Resample: Summary of Transformation a085093b
Computed polynomial surface: Quadratic (based on 25 control points)


Coefficient                    X                          Y


      b0      2360005.0295085907000000       -1632834.0154714584400000
      b1         -13.1845295703933516           5.3465739972634765
      b2           0.6589458304644609           2.2492860086106248
      b3           0.0000182189900889          -0.0000053787121878
      b4          -0.0000019086402773          -0.0000029562634467
      b5           0.0000002095561353           0.0000003609247798


Note: Figures are carried internally to 20 significant figures.
      Formula shown is the back transformation (new to old).
```

Control points used in the transformation:

```
      Old X       Old Y       New X         New Y    Residual
--------------------------------------------------------------

 1521.390178 8383.233629 411473.030000 306452.890000    omitted

 1203.308532 8678.271278 412022.470000 307877.370000   3.374343

 1222.470077 7229.904641 412029.250000 306717.440000    omitted

 1291.451638 7367.844321 412090.300000 306829.360000   3.594322

 1927.614932 7743.346782 412598.720000 307131.890000   1.829418

 1988.931876 7375.507636 412662.840000 306831.230000    omitted

 1751.328718 7371.675978 412455.470000 306837.520000   6.664347

 1624.491554 6937.500089 412358.940000 306487.320000   1.023372

 1732.801803 6689.527459 412443.440000 306287.600000   1.582956

 1883.494325 6772.708151 412566.810000 306351.250000   5.611130

  733.300666 6433.362679 411641.010000 306090.820000   1.839876

 1875.328747 5720.674334 412567.160000 305512.500000    omitted

 1124.150187 4499.371713 411949.740000 304538.340000    omitted

 1065.285921 4469.944581 411912.280000 304519.610000   1.655289

  842.092245 4940.778688 411752.040000 304729.790000    omitted

 1249.044269 4380.919162 412057.840000 304442.510000   4.302534

 1177.716475 4177.016605 412002.060000 304283.230000   0.536771

 1192.785727 4240.296709 412012.570000 304334.980000   2.005016

 1282.196623 4170.989929 412084.520000 304284.850000    omitted

 1242.510337 3213.381514 412054.320000 303512.220000   1.015666

 1170.303504 3343.645617 411994.430000 303616.370000   1.951892

 1311.577743 3495.881978 412106.400000 303740.060000   4.327956
```

```
1594.253762 2716.455340 412335.650000 303110.310000    3.064260
1538.999838 2436.465992 412289.470000 302886.330000    1.432913
1927.003648 2440.909486 412595.240000 302886.330000    1.658364
1186.371612 1252.559143 412012.320000 301939.440000    7.852793
1429.904730 1720.723346 412204.760000 302318.690000    5.012529
1360.837324 1530.820256 412145.710000 302168.720000    5.642799
1095.016109 1763.932182 411934.150000 302354.580000    1.139459
1186.914882  304.453728 412003.630000 301183.390000    5.452569
1432.182657  733.599399 412199.810000 301526.000000    4.461764
2072.178259  875.370736 412715.000000 301635.610000    omitted
1186.102200 1249.233248 412012.860000 301941.780000    6.524801

Overall RMSE =    3.929155

Note: RMSE Error is expressed in input image units.
With low RMSE errors, be careful that an adequate sample exists
(eg. 2-3 times the mathematical min).


Resample: Summary of Transformation a085103b
Computed polynomial surface: Quadratic (based on 24 control points)

Coefficient                  X                          Y

        b0    -1947652.2511539459200000     213048.0445842742920000
        b1          9.1110723915808194       -3.4126916307795909
        b2         -1.2620775190897575        2.0136919502583623
```

b3	-0.0000107472872071	0.0000050881900627
b4	0.0000033549978935	-0.0000025988537779
b5	-0.0000002082274753	0.0000005106566367

Note: Figures are carried internally to 20 significant figures.

Formula shown is the back transformation (new to old).

Control points used in the transformation:

Old X	Old Y	New X	New Y	Residual
1344.679800	8225.642634	413776.230000	306928.740000	4.060753
1499.030509	9185.794850	413903.090000	307700.280000	3.048749
1174.687104	9003.542935	413642.930000	307552.660000	1.052869
1950.714075	8970.334360	414271.850000	307523.760000	6.556410
1984.888156	8965.204642	414045.100000	307605.640000	omitted
1966.434156	8412.392073	414281.990000	307081.550000	4.400977
2174.896052	8506.436895	414445.000000	307150.030000	5.936535
930.545659	8766.048696	413448.550000	307362.790000	1.031353
866.791702	8140.824067	413389.510000	306864.650000	omitted
2125.693193	7957.741026	414401.710000	306706.960000	omitted
2121.318911	7832.548559	414403.360000	306607.690000	omitted
1624.491599	7718.251879	414010.010000	306507.460000	omitted
973.632202	7499.671133	413475.410000	306337.210000	omitted
1644.432040	6781.310290	414016.820000	305765.150000	omitted
908.659259	6730.362998	413427.630000	305737.480000	1.359552

952.132790	7076.844642	413463.360000	306013.480000	0.847918
1744.475852	6669.794927	414095.200000	305684.100000	6.210935
2248.410058	6646.417307	414494.740000	305657.850000	omitted
2135.349924	7487.312678	414414.870000	306340.270000	3.069350
1051.783242	6153.142589	413542.180000	305268.890000	omitted
1682.535328	5882.630138	414050.220000	305045.930000	omitted
1128.541432	5612.117688	413603.720000	304833.340000	omitted
858.676883	5911.506079	413386.290000	305077.500000	5.612775
1625.917472	5469.810031	414022.180000	304795.380000	omitted
1922.938295	5002.257647	414244.330000	304343.010000	omitted
1410.979694	5109.201779	413834.540000	304437.070000	6.169258
1703.509830	5035.333846	414065.380000	304379.360000	2.510382
1743.151764	4797.314950	414097.760000	304187.930000	1.974312
2139.282763	4804.881284	414422.620000	304189.380000	1.147778
2091.225461	4652.592793	414384.580000	304066.480000	3.082201
1524.216046	4211.757689	413916.880000	303718.110000	5.746707
1333.788988	4267.102525	413768.340000	303766.860000	3.023490
1224.859103	4239.316555	413679.380000	303747.520000	5.574392
2269.688254	4532.271513	414528.350000	303974.190000	5.410895
1660.628700	3780.848039	414026.000000	303370.010000	omitted
1598.054088	3366.312745	413986.050000	303038.210000	6.568435
1710.688389	2973.902709	414077.030000	302731.930000	omitted
1981.845040	2304.718348	414295.360000	302183.060000	3.225659
1172.025273	1239.471194	413634.290000	301340.040000	2.272617

Overall RMSE = 4.222610

```
Note : RMSE Error is expressed in input image units.
With low RMSE errors, be careful that an adequate sample exists
(eg. 2-3 times the mathematical min).


Resample: Summary of Transformation a086013b
Computed polynomial surface: Quadratic (based on 25 control points)

Coefficient                X                          Y

     b0    2360005.0295085907000000     -1632834.0154714584400000
     b1       -13.1845295703933516          5.3465739972634765
     b2         0.6589458304644609          2.2492860086106248
     b3         0.0000182189900889         -0.0000053787121878
     b4        -0.0000019086402773         -0.0000029562634467
     b5         0.0000002095561353          0.0000003609247798

Note: Figures are carried internally to 20 significant figures.
    Formula shown is the back transformation (new to old).


Control points used in the transformation:

    Old X       Old Y       New X        New Y     Residual
-------------------------------------------------------------
1521.390178 8383.233629 411473.030000 306452.890000    omitted
1203.308532 8678.271278 412022.470000 307877.370000   3.374343
```

1222.470077	7229.904641	412029.250000	306717.440000	omitted
1291.451638	7367.844321	412090.300000	306829.360000	3.594322
1927.614932	7743.346782	412598.720000	307131.890000	1.829418
1988.931876	7375.507636	412662.840000	306831.230000	omitted
1751.328718	7371.675978	412455.470000	306837.520000	6.664347
1624.491554	6937.500089	412358.940000	306487.320000	1.023372
1732.801803	6689.527459	412443.440000	306287.600000	1.582956
1883.494325	6772.708151	412566.810000	306351.250000	5.611130
733.300666	6433.362679	411641.010000	306090.820000	1.839876
1875.328747	5720.674334	412567.160000	305512.500000	omitted
1124.150187	4499.371713	411949.740000	304538.340000	omitted
1065.285921	4469.944581	411912.280000	304519.610000	1.655289
842.092245	4940.778688	411752.040000	304729.790000	omitted
1249.044269	4380.919162	412057.840000	304442.510000	4.302534
1177.716475	4177.016605	412002.060000	304283.230000	0.536771
1192.785727	4240.296709	412012.570000	304334.980000	2.005016
1282.196623	4170.989929	412084.520000	304284.850000	omitted
1242.510337	3213.381514	412054.320000	303512.220000	1.015666
1170.303504	3343.645617	411994.430000	303616.370000	1.951892
1311.577743	3495.881978	412106.400000	303740.060000	4.327956
1594.253762	2716.455340	412335.650000	303110.310000	3.064260
1538.999838	2436.465992	412289.470000	302886.330000	1.432913
1927.003648	2440.909486	412595.240000	302886.330000	1.658364
1186.371612	1252.559143	412012.320000	301939.440000	7.852793
1429.904730	1720.723346	412204.760000	302318.690000	5.012529
1360.837324	1530.820256	412145.710000	302168.720000	5.642799
1095.016109	1763.932182	411934.150000	302354.580000	1.139459

```
1186.914882  304.453728 412003.630000 301183.390000    5.452569
1432.182657  733.599399 412199.810000 301526.000000    4.461764
2072.178259  875.370736 412715.000000 301635.610000    omitted
1186.102200 1249.233248 412012.860000 301941.780000    6.524801

Overall RMSE =    3.929155

Note: RMSE Error is expressed in input image units.
With low RMSE errors, be careful that an adequate sample exists
(eg. 2-3 times the mathematical min).


Resample: Summary of Transformation a086023b
Computed polynomial surface: Quadratic (based on 17 control points)

Coefficient                    X                            Y

      b0    -4241632.1646270752000000     -3154053.6973075866700000
      b1          20.4656821393291466           13.8998198419285473
      b2          -1.5283059793227949            0.6586970218195347
      b3          -0.0000247319167622           -0.0000175538696450
      b4           0.0000038526839841            0.0000019301267302
      b5          -0.0000000982802638           -0.0000003339745451

Note: Figures are carried internally to 20 significant figures.
    Formula shown is the back transformation (new to old).
```

```
Control points used in the transformation:

      Old X       Old Y       New X        New Y    Residual
-------------------------------------------------------------
1304.687725 8501.600335 412254.300000 307489.020000    3.453759
1409.193529 8303.306740 412340.640000 307332.030000    4.853942
 540.714259 8386.229516 411657.760000 307414.450000    5.428242
 728.554437 9199.683920 411799.040000 308062.010000    2.629607
2246.591336 8591.733788 413011.750000 307559.660000    1.712861
 688.013392 7757.999353 411763.720000 306904.250000    5.903961
 633.958666 7526.356365 411744.100000 306731.560000    omitted
1106.937521 7670.569888 412093.390000 306833.600000    6.704592
1377.211153 7057.662412 412313.680000 306345.090000    omitted
1183.406213 1445.548045 412158.000000 301851.190000    2.343419
1601.429431 1673.405413 412491.170000 302031.290000    4.591426
1523.590625  949.453524 412415.780000 301452.520000    omitted
1869.180508 1965.005161 412717.290000 302265.900000    4.369398
1525.752817 1893.619473 412430.610000 302207.600000    2.980652
1370.075205 2101.286947 412310.410000 302374.140000    4.676359
1174.036731 1876.313850 412145.760000 302196.250000    3.568287
1557.464923 2177.143268 412457.430000 302432.940000    1.858698
1480.816045 7359.609478 412396.270000 306583.920000    omitted
 543.867455 6731.379299 411639.400000 306087.760000    omitted
1404.238516 6361.832144 412333.830000 305767.810000    omitted
 944.773342 5314.481411 412000.410000 304827.230000    omitted
1773.612480 4638.480519 412621.720000 304398.330000    omitted
```

```
1210.542414  5215.334614 412180.790000 304863.300000     3.600926
 854.682132  3459.534938 411892.180000 303464.360000     2.328725
1242.074337  1034.945029 412188.810000 301520.280000     omitted
1453.788682  1080.011755 412365.180000 301552.340000     omitted
 599.084707   965.471606 411690.900000 301476.440000     1.831144

Overall RMSE =     3.977579

Note: RMSE Error is expressed in input image units.
With low RMSE errors, be careful that an adequate sample exists
(eg. 2-3 times the mathematical min).


Resample: Summary of Transformation a086033b
Computed polynomial surface: Quadratic (based on 21 control points)

Coefficient                    X                          Y

     b0      96164.0207343995571000     -428218.5546650886540000
     b1         -1.5013477564282312        0.1726647162704467
     b2         -0.2284064378011692        1.3462765169458635
     b3          0.0000032756685393        0.0000000336646402
     b4          0.0000000781003708       -0.0000006129545661
     b5          0.0000003217447756        0.0000002524092772

Note: Figures are carried internally to 20 significant figures.
    Formula shown is the back transformation (new to old).
```

Control points used in the transformation:

```
   Old X      Old Y       New X       New Y    Residual
------------------------------------------------------------
 785.212565  8085.930506 409588.670000 306922.000000   omitted
 778.472711  9512.024438 409581.960000 308071.600000   3.598243
 984.038253  9363.683698 409752.900000 307940.890000   omitted
1219.933137  9612.491578 409943.940000 308152.040000   3.891257
1747.747940  8484.343394 410376.300000 307233.700000   omitted
 441.901260  9091.191876 409297.080000 307733.090000   7.303597
2159.131773  8299.440027 410721.200000 307086.060000   6.556931
 536.933199  8175.120364 409379.550000 307010.260000   6.857488
1312.016390  7496.630047 41003.850000 306456.930000   0.000063
1429.963832  7724.198228 410119.960000 306635.480000   1.696432
1986.001773  7062.564814 410662.500000 306404.800000   omitted
 987.660924  5937.366569 409750.730000 305201.170000   omitted
1581.610543  6211.291231 410245.100000 305427.910000   4.272732
1796.443384  6531.572374 410423.520000 305684.390000   6.523227
1362.939355  6562.565475 410065.460000 305708.770000   1.412126
1383.644186  6654.051255 410083.570000 305781.210000   1.709490
1611.097403  5997.208569 410272.170000 305276.160000   omitted
 393.711305  6009.851245 409263.060000 305271.310000   3.299470
 646.455824  5588.428689 409472.970000 304933.310000   1.937128
 886.563116  5651.642072 409679.330000 304976.010000   omitted
1573.185726  5089.464370 410234.370000 304520.590000   omitted
```

```
1979.986461  5089.110375 410565.490000 304521.350000     omitted
1740.586853  5311.351775 410376.480000 304702.900000    1.063658
1725.489580  5143.052463 410363.200000 304566.720000    2.398573
1372.304381  4233.976562 410076.760000 303840.650000    5.858272
 614.070825  2834.853655 409438.820000 302730.180000    5.203703
1393.366424  2594.642798 410074.230000 302537.420000     omitted
1486.039415  2535.643621 410163.230000 302478.180000    4.120375
 774.142354  1132.306508 409574.230000 301360.870000    2.987300
 769.929945  2084.721486 409577.800000 302121.210000     omitted
 479.273748  1705.441185 409320.780000 301828.500000     omitted
 951.063517  1052.236222 409720.590000 301296.620000    0.877956
1005.824829   795.168463 409774.130000 301093.140000     omitted
 955.275925   761.454658 409724.160000 301068.160000    5.397557
1186.958401  1697.012734 409117.310000 301757.110000     omitted

Overall RMSE =     4.247019


Note : RMSE Error is expressed in input image units.
With low RMSE errors, be careful that an adequate sample exists
(eg. 2-3 times the mathematical min).



Resample: Summary of Transformation a086043b
Computed polynomial surface: Quadratic (based on 17 control points)

Coefficient                    X                    Y
```

b0	-3044834.0499839782700000	-936200.8735656738280000
b1	11.4777049924305175	2.1835952262626961
b2	2.7975254357370432	1.9630514969758224
b3	-0.0000092347852071	-0.0000022275324706
b4	-0.0000086698179353	-0.0000011140198343
b5	0.0000012879580811	-0.0000004157129386

Note: Figures are carried internally to 20 significant figures.

Formula shown is the back transformation (new to old).

Control points used in the transformation:

```
     Old X       Old Y       New X        New Y      Residual
--------------------------------------------------------------
1815.292636 8559.895434 413462.330000 307526.640000   2.196351
1743.805572 8388.465304 413404.460000 307385.760000   2.818829
1859.312353 7586.172335 413490.170000 306779.300000    omitted
1529.906062 6887.538004 413231.710000 306186.680000    omitted
1554.892602 6846.967730 413249.850000 306153.190000   2.216343
1692.318571 6747.102442 413362.890000 306073.650000   2.333582
1625.167245 6745.542047 413308.460000 306069.460000   2.089170
1889.087572 6467.791713 413530.350000 305847.580000   1.093490
1925.005723 6506.801591 413558.260000 305879.670000   1.984099
1461.217628 5592.980240 413172.770000 305147.990000   0.937638
1437.480415 5630.429723 413154.390000 305178.900000   2.849297
1698.589756 5509.343061 413366.580000 305081.160000   4.040294
```

791.388338	4653.230983	412618.060000	304397.180000	2.507322
2028.114548	4384.657105	413644.300000	304178.720000	2.505472
1575.363144	1907.015501	413244.280000	302201.380000	omitted
1503.876083	1830.824332	413201.040000	302138.490000	0.622845
1665.913425	1778.442904	413332.060000	302097.880000	1.991597
893.853135	1987.968618	412712.080000	302261.460000	omitted
903.384744	1187.485139	412713.850000	301643.880000	omitted
550.137977	1993.480285	412429.440000	302274.930000	2.704349
559.507929	2015.325817	412434.600000	302291.290000	0.833674
937.851796	1722.724300	412740.140000	302053.230000	2.597925
1152.312988	1022.717938	412910.570000	301485.340000	omitted

Overall RMSE = 2.296062

Note: RMSE Error is expressed in input image units.

With low RMSE errors, be careful that an adequate sample exists

(eg. 2-3 times the mathematical min).

Resample: Summary of Transformation a086053b

Computed polynomial surface: Quadratic (based on 30 control points)

Coefficient	X	Y
b0	2338853.6818104982400000	-1540757.5889077186600000
b1	-12.2383724612291189	5.2266763912375609
b2	-0.4894796421499450	1.8262004796633846

```
b3        0.0000159432987145        -0.0000059124736110

b4        0.0000011836112348        -0.0000011541788006

b5        0.0000000051954502        -0.0000001661108291
```

Note: Figures are carried internally to 20 significant figures.

Formula shown is the back transformation (new to old).

Control points used in the transformation:

```
   Old X       Old Y       New X        New Y    Residual

---------------------------------------------------------------

1965.712808 9072.432653 411303.450000 307838.460000    omitted
1672.527923 9237.223731 411054.540000 307970.450000    1.612804
1324.370871 9478.917313 410775.470000 308166.550000    4.805921
1775.142632 8270.449404 411137.980000 307196.970000    0.602729
1976.707241 8387.634171 411299.510000 307293.010000    4.541658
 536.436492 7542.805231 410119.350000 306633.390000    6.251661
 829.621377 7242.519266 410356.190000 306390.640000    omitted
1092.571571 6888.218439 410577.560000 306095.750000    5.475093
1761.399591 6952.303858 411126.040000 306143.710000    2.277366
1830.114798 6792.090310 411182.980000 306008.840000    6.392109
 762.738575 6119.193406 410310.810000 305487.330000    2.351384
1165.867793 6306.872134 410637.500000 305640.190000    omitted
 423.744566 6288.562014 410026.080000 305625.200000    4.024062
1928.185146 5933.840042 411263.330000 305327.600000    1.345872
1916.457750 5964.308081 411256.110000 305351.300000    3.433339
1902.384876 6088.523934 411248.900000 305447.130000    omitted
```

1172.940881	5811.967884	410646.110000	305238.980000	3.426382
1205.777589	6109.617192	410673.930000	305477.010000	3.722320
725.862386	5757.297024	410283.370000	305198.910000	6.317757
676.085696	4911.219250	410234.690000	304523.980000	2.095458
679.017545	4940.515441	410235.900000	304544.490000	4.712726
828.541836	4966.882014	410364.410000	304565.610000	1.807595
840.269231	5057.700208	410374.060000	304635.590000	3.513465
1071.885291	4914.148869	410564.100000	304520.360000	0.396409
1018.888458	4330.704214	410521.180000	304055.380000	1.711875
599.912593	3024.885035	410173.130000	303019.740000	2.595867
661.728161	3041.557150	410222.980000	303030.580000	0.728463
661.737545	2390.347334	410225.560000	302507.940000	3.983297
638.682795	2513.636206	410202.010000	302610.760000	3.184510
1614.277328	2247.194136	411010.040000	302382.240000	1.858723
1619.906478	2322.192387	411011.070000	302443.040000	2.937820
1674.321592	2040.948946	411057.440000	302214.270000	2.752533
1787.955365	1226.704254	411145.120000	301565.730000	6.452623
1987.602544	1226.704254	411316.520000	301561.740000	5.174099

Overall RMSE = 3.782730

Note: RMSE Error is expressed in input image units.

With low RMSE errors, be careful that an adequate sample exists

(eg. 2-3 times the mathematical min).

Resample: Summary of Transformation a086063b

```
Computed polynomial surface: Quadratic (based on 23 control points)

Coefficient                  X                          Y

     b0      -45710.4156341552734000     -864496.9538307189940000
     b1          -0.5218169443432998           1.5863481125416001
     b2          -0.6775497493126750           2.2896590698437649
     b3           0.0000021085263265          -0.0000010788769556
     b4           0.0000000820604118          -0.0000022465939855
     b5           0.0000010553492158          -0.0000001805789616

Note: Figures are carried internally to 20 significant figures.
    Formula shown is the back transformation (new to old).


Control points used in the transformation:

     Old X       Old Y       New X        New Y    Residual
-----------------------------------------------------------------
  864.276072 8355.027801 413458.770000 307524.930000   3.306897
  808.482566 8140.236471 413412.150000 307346.900000   5.313826
  812.774374 8505.381733 413416.390000 307639.370000   4.237395
 1405.043895 7508.749958 413878.410000 306846.730000    omitted
 1304.969782 8539.199171 413808.770000 307672.810000   5.373553
 2061.580540 7931.091570 414420.170000 307181.680000   2.668110
 1018.258457 6910.248502 413578.980000 306375.270000    omitted
 1272.464655 6783.081724 413791.710000 306263.410000   2.673345
```

1562.522215	7089.247006	414020.760000	306504.650000	3.479135
1589.487672	7304.175803	414043.170000	306680.050000	1.296415
2004.938964	7198.068886	414375.170000	306591.210000	2.808846
723.297788	6553.809670	413353.340000	306082.670000	4.642189
948.312138	6301.839162	413527.980000	305883.180000	5.659585
979.251611	6335.622917	413553.270000	305907.320000	2.815138
1761.261463	5905.003587	414164.270000	305556.560000	omitted
892.706793	5645.127541	413491.890000	305351.640000	7.498892
1563.945584	4950.578284	414023.070000	304796.820000	2.670533
1278.969525	4885.281720	413793.270000	304737.520000	omitted
513.544423	5406.210846	413181.610000	305167.130000	2.225202
1318.190471	4373.826784	413827.050000	304335.750000	0.885445
1304.127074	4576.529315	413814.020000	304497.140000	2.894106
2057.606528	4195.681260	414416.240000	304189.720000	3.971757
1818.638652	4082.958770	414218.660000	304103.600000	omitted
2008.164899	4047.217492	414378.250000	304068.130000	2.321918
2139.786066	3714.462759	414487.350000	303790.420000	omitted
1431.637725	3607.067094	413917.740000	303716.520000	5.664453
1908.028427	3834.745905	414287.370000	303899.000000	omitted
1633.352707	2361.277355	414077.790000	302723.860000	2.443592
1573.267393	3160.301106	414021.660000	303371.310000	omitted
1865.110346	2713.535138	414264.920000	303004.540000	3.619770
603.318757	1695.424214	413246.960000	302199.910000	1.536100

Overall RMSE = 3.819920

Note: RMSE Error is expressed in input image units.

```
With low RMSE errors, be careful that an adequate sample exists
(eg. 2-3 times the mathematical min).


Resample: Summary of Transformation a086073b
Computed polynomial surface: Quadratic (based on 36 control points)

Coefficient                 X                          Y

      b0    318472.7166152000430000      -59787.4416522979736000
      b1       -2.6973648711718852        -1.9589173916756408
      b2       -0.1220581566494730         1.7949416892843146
      b3        0.0000047587409792         0.0000026807243794
      b4        0.0000000891862604        -0.0000007498608640
      b5        0.0000001392256718        -0.0000003862780644

Note: Figures are carried internally to 20 significant figures.
    Formula shown is the back transformation (new to old).


Control points used in the transformation:

     Old X      Old Y       New X       New Y    Residual
-------------------------------------------------------------
 1229.471321 9011.954238 411489.390000 307836.880000    omitted
 843.878505 8675.382719 411187.740000 307574.640000    1.010362
 1420.051679 8480.525523 411651.090000 307409.160000    5.310287
```

790.693288	8161.668294	411144.710000	307160.930000	4.755067
515.903005	9423.811493	410926.280000	308173.680000	5.921342
1922.705162	9380.836634	412051.140000	308129.340000	1.763535
1505.215497	8251.242798	411719.970000	307227.450000	2.300951
1547.042053	8287.463619	411756.210000	307257.330000	5.034701
1451.305714	8270.746317	411674.190000	307244.620000	1.723352
786.303516	8992.238667	411140.250000	307832.940000	4.331820
745.638809	9061.894091	411107.350000	307886.700000	2.060648
712.235657	8896.462458	411080.080000	307757.520000	5.284593
796.469693	8973.373656	411148.270000	307816.890000	3.462137
1241.848090	8762.840134	411507.980000	307641.770000	0.751204
1219.772964	8794.185075	411490.440000	307666.740000	0.817449
1227.905905	8838.300177	411494.300000	307703.310000	2.967645
1563.761275	7795.074090	411768.820000	306873.430000	omitted
722.442200	6745.560398	411088.440000	306034.090000	3.129709
832.817833	6719.439614	411180.950000	306008.930000	2.907445
768.916151	6729.597696	411128.210000	306018.670000	0.873417
911.242626	6691.867675	411244.250000	305985.400000	3.652813
1407.372943	6818.036751	411644.190000	306083.920000	5.036280
940.331340	5867.605526	411262.740000	305328.910000	3.443737
919.999044	6018.525613	411247.810000	305448.390000	1.601269
1338.264603	5816.815112	411590.070000	305304.020000	omitted
1573.436874	4705.525379	411776.070000	304391.590000	3.982317
1851.191346	4498.735837	411994.030000	304226.320000	5.327702
851.143651	4853.795368	411194.410000	304519.940000	2.271145
1012.323361	3532.014553	411319.200000	303454.200000	omitted
1854.890655	3740.618038	411993.160000	303615.650000	5.708705

```
1880.306096  3758.757472 412013.300000 303628.240000     6.489257
1186.146828  2807.648861 411466.800000 302875.520000     omitted
 628.308735  2874.790156 411017.290000 302941.120000     5.530706
 667.811593  2627.513399 411044.350000 302741.990000     0.737892
 849.060002  2822.548588 411189.360000 302894.580000     2.450301
 999.923780  1161.356113 411318.810000 301566.090000     omitted
 797.819959  1157.813255 411145.210000 301568.570000     3.512588
1475.045044  1051.527512 411693.390000 301476.790000     3.548191
1794.156341  1072.784661 411948.880000 301486.710000     1.987187
2064.707697  1496.986650 412166.780000 301819.240000     4.341523
1626.690700  1453.452010 411810.320000 301790.180000     5.477321
2020.266979  1569.544384 412129.920000 301882.020000     3.398904

Overall RMSE =     3.797801

Note: RMSE Error is expressed in input image units.
With low RMSE errors, be careful that an adequate sample exists
(eg. 2-3 times the mathematical min).
```

APPENDIX 6 – RMSE FROM INDEPENDENT CHECK POINTS

Rectified ATM		OS Map		Square of X difference	Square of Y difference	Sum of X & Y
X	Y	X	Y			
411026.25	307732.10	411028.50	307731.00	5.07	1.21	27.21
410943.97	307165.52	410948.13	307167.60	17.38	4.34	320.76
410304.29	307018.50	410304.69	307018.01	0.16	0.24	0.08
410674.79	306230.82	410674.19	306232.02	0.36	1.44	2.20
411185.43	306707.97	411187.90	306705.50	6.12	6.11	74.82
410425.92	305636.97	410420.97	305634.03	24.48	8.67	674.57
410272.53	305698.78	410276.48	305699.08	15.59	0.09	242.95
410097.40	305642.01	410093.93	305642.91	12.07	0.81	146.31
410357.70	305360.49	410354.17	305358.59	12.43	3.61	167.61
410591.70	304808.26	410593.20	304805.79	2.25	6.11	42.42
410391.28	304531.86	410388.01	304532.96	10.72	1.21	116.36
410702.13	304204.98	410698.06	304207.98	16.60	9.00	356.47
410595.62	304109.65	410594.15	304111.07	2.17	2.01	8.75
411063.80	303221.04	411066.68	303222.88	8.26	3.39	79.69
411160.69	303201.26	411163.16	303201.73	6.12	0.22	37.51
410678.26	302737.46	410673.32	302735.46	24.48	4.00	615.39
410225.52	302507.53	410226.92	302510.01	1.96	6.11	41.20
410406.83	301952.47	410404.53	301953.99	5.29	2.31	33.28
411034.53	302021.40	411035.83	302024.63	1.69	10.48	112.71
410968.35	301405.67	410967.85	301404.00	0.25	2.79	7.84
410195.30	301297.69	410193.00	301295.01	5.29	7.18	79.54
410731.02	301113.89	410732.32	301114.99	1.69	1.21	4.31
				Independent RMSE		**12.05**

Table A6-1: RMS errors calculated by using independent checkpoints for a085073b, band 7.

Rectified ATM		OS Map		Square of X difference	Square of Y difference	Sum of X & Y
X	Y	X	Y			
411107.58	308303.27	411109.18	308299.66	2.56	12.99	175.29
411975.43	308017.43	411978.03	308021.93	6.77	20.29	457.32
411178.19	307582.56	411179.86	307579.95	2.80	6.78	53.83
410946.00	307173.72	410947.90	307171.91	3.62	3.28	23.85
411551.41	307101.85	411549.81	307102.95	2.56	1.21	8.04
410833.44	307013.32	410836.43	307012.11	8.92	1.46	81.66
411713.02	306201.38	411712.69	306200.01	0.11	1.88	3.53
412072.97	306318.56	412074.28	306318.01	1.71	0.30	3.02
411801.14	305564.70	411804.74	305566.30	12.97	2.57	174.83
411840.16	305220.97	411841.97	305223.00	3.28	4.14	27.91
411187.22	305075.14	411184.62	305077.00	6.77	3.44	57.61
412000.44	304826.46	411998.84	304827.99	2.56	2.34	12.06
411743.31	304511.37	411741.31	304513.98	4.00	6.78	61.98
412063.87	304448.88	412061.67	304447.27	4.85	2.57	30.16
411794.34	304012.70	411795.93	304010.37	2.53	5.45	36.10
411493.89	303640.33	411491.58	303642.93	5.36	6.78	74.75
411221.04	303416.38	411218.44	303417.99	6.77	2.59	52.51
411673.67	302769.28	411675.02	302770.49	1.83	1.46	5.48
411005.13	302708.18	411003.93	302709.14	1.45	0.92	2.94
411626.85	301910.48	411628.45	301913.82	2.56	11.17	131.25
411608.64	301193.07	411612.24	301195.67	12.97	6.78	214.19
411173.61	301210.78	411169.01	301209.17	21.17	2.57	454.88
				Independent RMSE		**9.87**

Table A6-2: RMS errors calculated by using independent checkpoints for a085063b band 7.